ADVANCED FLAME MONITORING AND EMISSION PREDICTION THROUGH DIGITAL IMAGING AND SPECTROMETRY

A Thesis Submitted to the University of Kent

For the Degree of Doctor of Philosophy

In Electronic Engineering

By

JAMES CUGLEY BEng

November 2019

Abstract

This thesis describes the design, implementation and experimental evaluation of a prototype instrumentation system for burner condition monitoring and NOx emissions prediction on fossil-fuel-fired furnaces.

A review of methodologies and technologies for burner condition monitoring and NOx emissions prediction is given, together with the discussions of existing problems and technical requirements in their applications. A technical strategy, incorporating digital imaging, UV-visible spectrum analysis and soft computing techniques, is proposed. Based on these techniques, a prototype flame imaging system is developed. The system consists mainly of an optical and fibre probe protected by water-air cooling jacket, a digital camera, a miniature spectrometer and a mini-motherboard with associated application software. Detailed system design, implementation, calibration and evaluation are reported.

A number of flame characteristic parameters are extracted from flame images and spectral signals. Luminous and geometric parameters, temperature and oscillation frequency are collected through imaging, while flame radical information is collected by the spectrometer. These parameters are then used to construct a neural network model for the burner condition monitoring and NO_x emission prediction.

Extensive experimental work was conducted on a 120 MWth gas-fired heat recovery boiler to evaluate the performance of the prototype system and developed algorithms. Further tests were carried out on a 40 MWth coal-fired combustion test facility to investigate the production of NOx emissions and the burner performance.

The results obtained demonstrate that an Artificial Neural Network using the above inputs has produced relative errors of around 3%, and maximum relative errors of 8% under real industrial conditions, even when predicting flame data from test conditions not disclosed to the network during the training procedure. This demonstrates that this off the shelf hardware with machine learning can be used as an online prediction method for NO_x.

Acknowledgements

The author wishes to express grateful thanks to the following:

University of Kent

Dr G. Lu My first supervisor, whose advice, encouragement, and contributions made it possible for me to complete this work.

Professor Y. Yan My second supervisor for his advice, support and encouragement, which allowed the project to progress at all times.

Mr Ivan Searle and Mr Gary Bearpark at British Sugar plc for their technical advice and assistance throughout the project, in particular, system trials on the gas-fired heat recovering boiler at Wissington Factory.

The Biomass and Fossil Fuels Research Alliance, who provided a research grant for the project.

A number of academic staff, technicians, colleagues and friends at the University of Kent, in particular, Dr Md. M. Hossain, Mr T Brazier, Mr D O'Connell, Mr E. Catley and Ms L. Drake who made various contributions to the project and supported me.

This thesis is dedicated to my parents Ian and Josephine Cugley without whom, none of this would have been possible.

Content

List of Tables

List of Figures

Nomenclature

Acronyms

ANN	Artificial Neural Network
ARX	Auto-Regressive model with EXogenous Inputs
ARMAX	Auto-Regressive Moving-Average model with EXogenous Inputs
BF2RA	Biomass and Fossil Fuels Research Alliance
CCD	Charge-Coupled Device
CEMS	Continuous Emission Monitoring System
CFD	Computational Fluid Dynamics
CMOS	Complementary Metal–Oxide–Semiconductor
CTF	Combustion Test Facility
CUSUM	Cumulative Sum
DL	Deep Learning
EMCCD	Electro-Multiplying Charge-Coupled Device
eVQ	Evolving Vector Quantization
EWMA	Exponentially Weighted Moving Average
FAAS	Flame Atomic Absorption Spectrometry
FES	Flame Emission Spectroscopy
FFT	Fast Fourier Transform
FLEXFIS	FLEXible Fuzzy Inference Systems
GUI	Graphical User Interface
GHL	Generalized Hebbian Learning
GNARX	General Nonlinear Auto-Regressive model with EXogenous Inputs
GT	Gas Turbine
HSI	Hue, Saturation, Intensity

HSW	Henke Sass Wolf
ICCD	Intensified Charge-Coupled Device
KPCA	Kernel Principal Component Analysis
LII	Laser Induced Incandescence
LIF	Laser Induced Fluorescence
LIMS	Laser Ionization Mass Spectrometry
MBMS	Molecular Beam Mass Spectrometry
MSE	Mean Squared Error
MSPC	Multivariate Statistical Process Control
OFA	Overfire Air
PA	Primary Air
PCA	Principal Component Analysis
PCB	Printed Circuit Board
PF-LIF	PhotoFragmentation Laser Induced Fluorescence
PLIF	Planar Laser Induced Fluorescence
PLS	Partial Least Square
PSD	Power Spectral Density
RBF	Radial Basis Function
RGB	Red, Green, Blue
RME	Rapeseed biodiesel/Methyl Esters
SPC	Statistic Process Control
SVM	Support Vector Machine
1-D	One-Dimensional
2-D	Two-Dimensional
3-D	Three-Dimensional

Abbreviations

B	Blue channel of a RGB image
G	Green channel of a RGB colour image
G	Gun (Burner Configuration)
H	Hue channel of an HSI colour image
I	Intensity channel of an HSI colour image
IR	Infrared
NIR	Near Infrared
Norm	Normalising Term to bound between [0 - 1]
R	Red channel of a RGB image
Rel Irr	Relative Irradiance
S	Saturation channel of an HSI colour image
S	Spud (Burner Configuration)
UV	Ultraviolet
VIS	Visible

Greek

π	Pi Constant
λ	Light Wavelength
β	*C*oefficients estimated from Training Data
ε	Emissivity

Symbols

A	Flame Area (Pixels)
$B(\lambda)$	Theoretical Shape of Reference Blackbody
c	Speed of light

°C	Degrees Celsius
°K	Degrees Kelvin
h	Explicit/Fixed Basis Function
h	Planck's First constant
k	Boltzmann's constant
C_2	Planck's Second constant
D	Data Set
D(λ)	Dark spectrum (counts)
ε_g	Gaussian Matrix
e	Base of the Natural Logarithm
f	Frequency Component
F	Weighted Power Spectral Density
$G(\lambda_R, T)$	Grey-level intensity of the R channel of a RGB image at temperature T
$G(\lambda_G, T)$	Grey-level intensity of the G channel of a RGB image at temperature T
Hz	Hertz
K_1	Instrumentation Factor First Variable
K_2	Instrumentation Factor Second Variable
L_1	Calculated Length 1
L_2	Calculated Length 2
ln	Natural Logarithm
$\mathbb{M}$	Horizontal Length of Matrix
M	Neural Network Model
MW_{th}	Megawatts thermal
N	Total Number of Components
$\mathbb{N}$	Vertical Length of Matrix
nm	Nano Meters

σ	Standard Deviation
σ^2	Variance
P_{xx}	Power Density
R	Flame Region
r	R-Value (correlation coefficient)
R(λ)	Reference Spectrum (counts)
$\mathbb{R}$	Real Numbers
S	Instrumentation Factor
S(λ)	Sample Spectrum (counts)
T	Temperature
T_c	Colour Temperature of Reference Light Source
V	Volts
%w/w	Percentage Moisture Content
W	Watts
W	Vector of Network Weights
x_i	Training data (predicted value)
y_i	Training data (actual value)

Chemical symbols

Ar	Argon
C_2	Dicarbon radical
C_2^*	Excited-state C_2
CH	Methylidyne radical
CH^*	Excited-state CH
CN	Cyanogen radical
CN^*	Excited-state CN

CO	Carbon Monoxide
CO_2	Carbon Dioxide
H	Hydrogen
H_2	Dihydrogen radical
H_2O	Water
K	Potassium
Na	Sodium
NH	Imidogen
NH_3	Azane
NO	Nitrous Oxide
NO_x	Nitrous Oxides
O_2	Oxygen
OH	Hydroxyl radical
OH^*	Excited-state OH

Chapter 1

Requirements for Burner Condition Monitoring and Emission Prediction

1.1 Introduction

Fossil fuel fired utility boilers are firing a range of fuels (e.g., natural gas, oil, pulverised coal and biomass) under variable operation conditions, and it is of importance that the boilers operate safely, efficiently and cleanly. It is known that flame properties such as size, shape, temperature, oscillation frequency, colour/spectrum, etc. have a close correlation to burner conditions, and consequently, the overall performance of the boiler. The flame size and its variation depends on many factors such as; fuel type, furnace load, fuel and air ratio, as well as burner settings [1, 2]. Flame temperature is crucial for the understanding of the energy conversion, combustion efficiency and emission formation process [3–5]. Flame oscillation frequency is another important indicator of the flame stability [6, 7].

The spectral characteristics of the flame over a wide spectral range from the UV (ultraviolet) to near IR (infrared), in particular, the detailed information about free radicals (such as OH^*, CH^*, CN^* and C_2^*) in the flame. It is believed that the spectral information of these flame radicals is closely linked to pollutant emission (e.g., NO_x, CO) formation of the combustion process [8, 9]. NO_x is used to define nitrogen oxides, oxygen and nitrogen do not react at ambient temperature, but high temperatures such as the ones seen in furnaces cause endothermic reactions producing aa variety o nitrogen oxides. The

potential damage these gasses cause will be defined in 1.3. The present industrial standard of boiler operation uses only single flame scanners that offer only a single point detection of the flame, offering only on/off state of the flame. Emission analysis within the industrial setting currently only studies the flue gas output and is therefore intrusive and not an online analysis. It is therefore highly desirable to develop an advanced flame monitoring technique that is capable of quantifying flame properties and using such information to assess and optimise the overall performance of the boiler.

Significant progress has been made in developing advanced sensing techniques for flame visualisation and characterisation on lab-scale and practical furnaces. At the University of Kent, the Instrumentation and Control Research Group, supported by the external funding body BF2RA (Biomass and Fossil Fuel Research Alliance), has been conducting pioneering work in the use of digital imaging technique for two-dimensional (2-D) and three-dimensional (3-D) flame monitoring and characterisation over the past two decades [1, 3, 6–9]. Several prototype systems have been developed [1–6], and substantial trials of the systems have been undertaken on laboratory test rigs [7, 10, 11] and industrial-scale combustion test facilities operated by British Sugar and Doosan Babcock [8, 9, 12–14].

The author joined the Group in September 2015 for undertaking an BF2RA funded project with the aim of developing a methodology for burner condition monitoring and NO_x emission prediction. This thesis reports the work which has been done during the course of the project.

1.2 Importance of Burner Condition Monitoring and its Technical Requirements

In a multi-burner boiler, all burners need to be balanced to ensure that the fuel burns safely, efficiently and cleanly. Most previous work, however, focuses mainly on the flame monitoring of a single-burner combustion system. There has been a growing interest in developing techniques for monitoring flames in a multi-burner boiler to understand how each burner performs with regard to the overall performance of the boiler. In previous studies, imaging sensors such as CCD cameras have been used alongside image processing to gain characteristic information such as size, shape, location, luminosity, temperature and oscillation frequency. The systems developed, however, are still largely limited on the uses on lab-scale combustion test facilities or single-burner boilers. Previous research was also conducted where intensified imaging devices incorporating with band-bass filters were used to capture images key flame radicals. Based on the information provided by these images, machine learning techniques were applied to predict emissions (e.g., NO_x) in flue gas [7–9]. However, these prediction models developed were mainly based on lab-scale combustion test facilities and never evaluated in industrial environment. The imaging techniques used for these models (ECCD) requires a complex array of mirrors and expensive hardware, making the process unsuitable for industrial trials.

The technical requirement for the advanced burner condition monitoring is that the system should be capable of providing direct, temporal and spatial measurement, which is essential to observe the dynamic nature of a flame. It should also be capable of giving the assessment of flame stability in general cases without ad-hoc adaptation. In addition, the system should be operational under hostile plant conditions including high ambient temperature, dusty air and mechanical vibrations. It is envisaged that optical sensing,

embedded image and signal processing, as well as a miniature industrial computer would meet the requirements.

1.3 Importance of NO_x Emission Prediction and its Technical Requirements

NO_x is a known precursor to the formation of pollutant ozone and acid rain, which has a significant impact on air quality, human health, and climate change [16]. 80% of the total NO_x emissions is believed to be from fossil fuel combustion processes. In view of the increasingly strict environmental rules, and the fact that fossil fuels will continue to be utilised in the production of energy, the reliable, on-line monitoring of NO_x emissions is essential for the future of power generation.

An unstable flame can result in high NO_x emissions but also many other combustion problems such as low combustion efficiency, and unburnt fuel [17, 18], particularly where low quality fuel and variations in diet are applied. Currently NO_x measurement techniques (e.g., emission analysers) have a number of disadvantages such as slow system response, requirements for frequent system calibration, and high system and maintenance cost [19]. It is clear that new technologies for the predication of NO_x emissions based on online measurements of flame characteristics can be very useful for the reduction of the NO_x emissions.

The essential requirements for the on-line NO_x emission monitoring and prediction include a fast, realisable and robust. It should also be capable of giving the assessment of NO_x emission production in general cases without/ or with minimal manual aid. It is envisaged that spectrometric and digital imaging techniques would meet the requirements. The information provided by the solutions to the above-mentioned issues

can be used either by a boiler operator to manually regulate the combustion process, or by a boiler control system to automatically adjust the combustion process. In addition, in order to explore the relationship between the noisy optical sensorial information captured from a flame and combustion process, machine learning algorithms such as ANN and SVM should be employed to tackle these complex and ill-defined problems.

1.4 Aim and Objectives of the Research Programme

The research programme aims to develop a methodology for the prediction of NO_x emissions and individual burner condition on fossil-fuel-fired furnaces. The objectives of the research programme are as follows:

- To define the state-of-the-art in the field. Study the existing flame monitoring techniques, especially spectrometric and digital imaging methods, to review and identify suitable flame sensing methods for burner condition monitoring and emission (e.g., NO_x) prediction in industrial boilers.

- To design and implement a prototype instrumentation system for on-line burner condition monitoring as well as the emission prediction based on digital imaging, spectrometric, and embedded computing techniques.

- To develop novel algorithms (machine learning) to indicate burner performance and to predict NO_x emissions and flame characteristics, such as geometrical/luminous parameters, temperature, oscillation frequency, and radical spectral intensities should be quantified. Dedicated software should be developed to acquire, processing and present flame parameters online.

- To evaluate the techniques developed on lab-scale experiments and then industrial-scale boilers under a range of operation conditions.

1.5 Major Technical Challenges

The development of the methodology as proposed in section 1.4 faces a number of technical challenges, including:

- **Multiple parameters**: Due to the complexity of a flame, the reliable burner condition monitoring and prediction of NO_x emissions demands the concurrent measurement of multiple parameters through different means (e.g., high resolution and high speed digital imaging, and spectroscopic). These sensing techniques must be used simultaneously and not impact each other's sampling. For example, the measurement of flame oscillation frequency, temperature distribution through a digital camera could potentially lead to high processing demand from the CPU that could hinder the processing of the flame radical species through a spectrometer.
- **Fast system response**: The system must be capable of processing a large amount of 2-D data (i.e., flame images and spectra) in order to keep track of the dynamic nature of the flame. Specifically, 900 FPS s
- **Variable operational conditions**: The system should be able to operate effectively at different sites and different conditions. Furnaces may have a diet of wide range of fuels and operate under different burner configurations such as variable fuel supplies, air-to-fuel ratios, etc. Thus, it is important to ensure that the system is functional for these operation conditions.

- **Predication of NOx emissions**: There is no effective means for emission (NO_x) predication. Appropriate techniques should be employed such that these measurements can be gained effectively.
- **Hostile environment**: The spectrometric and digital imaging components of the system along with the optical probes should be protected from the heat radiation from the flames. Power plants are also dusty environments therefore the optical probes should also be able to keep themselves clean.

- **Multiple flame measurement**: The system should be able to monitor flames in multi-burner combustion systems. In practical furnaces, it is impossible to visualise all burners from a given view-point. The optical probe should have the maximum field of view so that primary combustion zones of flames can be viewed and acquired.

1.6 Thesis Outline

The main contributions of this thesis to the state-of-the-art can be summarised as (1) the development and fabrication of a flame monitoring system, which incorporates spectrometric and digital imaging techniques capable of measuring and monitoring simultaneously a range of flame characteristic parameters (e.g., size, shape, temperature, oscillation frequency, colour/spectrum, and the flame radicals OH^*, CH^*, CN^* and C_2^*); (2) the monitoring of burner condition through flame parameters; (3) the use of ANN (Artificial neural network) training with flame characteristics for predicting NO_x emissions.

The thesis is composed of seven chapters including:

- Chapter 1 introduces the importance of burner condition monitoring, emissions (i.e., NO_x), the aim and objectives of the project, and technical requirements and challenges.
- Chapter 2 reviews the existing techniques that could be potentially used for burner condition monitoring and emission predications.
- Chapter 3 gives the detailed descriptions of the design, implementation and evaluation of the flame monitoring instrumentation system.
- Chapter 4 presents the theories of digital imaging, image processing, spectral analysis techniques as required for the burner condition monitoring and emission. The theories of machine learning which have been used in this project are also included.
- Chapter 5 presents the experimental results obtained from a 120 MW_{th} gas-fired boiler.
- Chapter 6 presents the experimental results obtained from a 40 MW_{th} coal-fired CTF (Combustion Test Facility).
- Chapter 7 draws conclusions from the work that has been presented and provides suggestions for future work.

Chapter 2

Review of Techniques for Flame Monitoring and Emission Prediction

2.1 Introduction

A complete literature review was conducted to examine all existing techniques that might be used for flame monitoring and emission prediction in industrial combustion systems. The state-of-the-art techniques within this field of study are defined following the analysis of all relevant references and materials in the field. The following survey of current literature was completed not only to acquire the necessary knowledge to fulfil the aim and objectives of the project at hand, but also to ascertain that the contribution of this work is also state-of-the-art.

Flames in both the laboratory- and industry-scale facilities have been studied across a wide variety of disciplines for decades, including the theoretical and experimental studies on the structural properties and the chemical mechanisms of various fuel combustion and their applications. Moreover, with the improved understanding of combustion and progress of computing technologies, mathematical modelling, such as CFD (Computational Fluid Dynamics), has formed another important branch of flame research. The studies in these areas are very useful for simulating combustion processes and thus an in-depth understanding of flames. These techniques have provided the research community an in-depth understanding of flames under a multitude of different possible conditions through simulating combustion processes. Such simulations are, however,

beyond the scope of this research programme. In a similar fashion, there has been in recent years great efforts in developing the 3-D (three-dimensional) flame imaging techniques. As such systems hold very little practical uses in industry-scale boilers due to the complexity of the systems and high equipment cost, these are also excluded in this review.

This chapter reviews firstly the existing flame monitoring techniques, especially visualisation methods, which could potentially be used for industry-scale flame monitoring, including laser-based imaging techniques, chemiluminescence imaging, imaging-based pyrometry, and broadband imaging. Optical flame scanners and photo detectors are also included due to their wide availability and simple implementation for essential flame failure detections. The basic principle, and the advantages and disadvantages of the techniques are discussed.

Secondly, a comprehensive survey regarding burner condition monitoring including flame stability monitoring, have been previously conducted [8, 9]. These two surveys contribute to the key techniques laid out within this review. In addition, the work that has been reported regarding the emission (mainly NO_x) prediction is included, focusing on the algorithms, data processing and analysis.

2.2 Flame Detection

Flame detection is the simplest form of flame monitoring which is often referred to as flame failure detection which is essential in the safe operation of a boiler [12]. The purpose of flame failure detection is to provide a continuous indication of ‘on’ or ‘off’ of the flame and an alarm if any abnormal state occurs. A flame detector must correctly detect the supervised flame, discriminate against spurious signals from noise. It should

also be reliable, easily maintained, and low cost. This requirement has been raised considerably in recent years due to the use of fuels from variety of sources with unknown combustion characteristics which often cause the problem of flame instability. Table 2.1 summarises the flame detection techniques which have commonly been used in fossil fuel fired boilers.

Figure 2.1 shows an example of the industrial installation of a flame detector. The photodetector can also be used for studying the flame oscillatory characteristics through power spectral density analysis [3, 13, 14, 17]. The photodetector is, however, regarded as the one-dimensional measurement, and thus the information provided is limited.

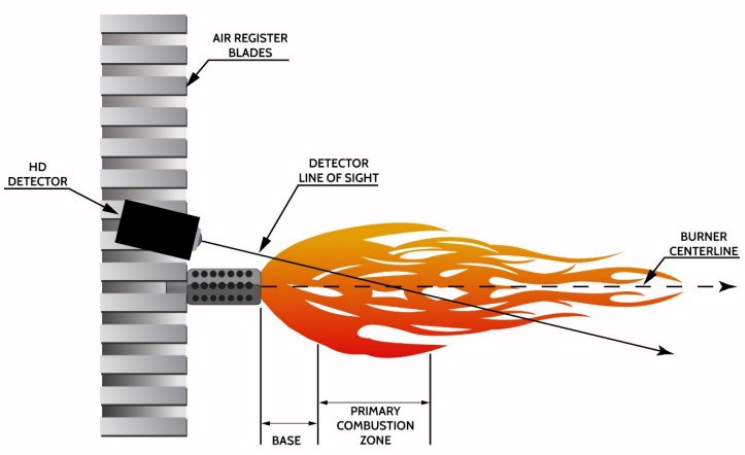

Figure 2.1 Sensing arrangement of 3-D multi-wavelength flame detector [18].

2.3 Vision-based Flame Monitoring

The most conspicuous aspect of a flame is its luminosity. The luminous region of the flame is the zone of chemical and thermal reactions of combustibles, relating to many factors such fuel type, air and fuel flowrates, air-to-fuel ratio, temperature, oscillation

frequency and emissions. Visualisation techniques use electric or optical means to visualise the flame to obtain qualitative and quantitative 2-D information of the flame,

Table 2.1 Summary of common flame detection techniques.

Name	Brief working principle and applications	References
Thermal detector	Thermocouples, pyrometers and heat flux meters, etc., having been used to monitor flames based on existence of heat at the base of the burner.	[20–22]
Ionisation detector	Measuring the ionisation level and reliably detect arrival of a flame, for monitoring flames in gas and oil burners of small heat release.	[22]
Acoustic/pressure detector	A pair of transmitter and receiver, speaker and microphone, or transceivers working for different frequency ranges depending upon the working distances and media, having been used to monitor the signal generated by a flame. Only suitable for single burner combustion systems.	[20–22]
UV detector	Consisting of an optical lens, a photocell and an associated circuit, for monitoring the UV radiation of the combustion. Ideal for discriminating between a flame and the background within gas and oil fired furnaces.	[16, 19, 23]
IR detector	Similar to the UV detector, but having a narrow frequency in the IR region. Ideal of low NO_x coal furnaces with a weaker UV signal.	[16, 19, 20]
Cross-correlation based detector	Two IR detectors which are used to monitor the flicking of a flame when the flame is ignited. The two detectors receive a similar signal from the flame front making correlation between the two very high. If no flame is present, the detectors receive very different signals from the furnace wall.	[20, 24, 25]

Transmitter-Receiver detector	Detecting the changes in the signal strength of either sound waves or electromagnetic radiation beam directed through a flame field. This beam is absorbed and scattered by the flame, therefore the changes of the straight through energy can be monitored by suitably positioned detectors. It suffers practical difficulties such as the size and positioning of the transmitter and receiver.	[20, 26, 27]

such as the geometrical and luminous profiles, temperature distribution and soot concentration. With the developments of optical sensing (particularly, CCD/CMOS imaging sensors) and computing techniques (including image processing and machine learning) in the last two decades, the applications of visualisation techniques to flame monitoring and characterisation have considerably been enhanced.

2.3.1 Flame Imaging

Passive imaging is regarded to be a natural option for flame visualisation as the radiation of the flame gives strong enough signals that imaging sensors can acquire without an assistance of external illumination and other optics/electronics (e.g., expensive laser sources and synchronisation devices). The passive imaging techniques can be further divided into three categories based on the radiation bands used, i.e., broadband imaging, imaging-based pyrometry, and chemiluminescence imaging. [3] Active imaging on the other hand can also be further divided into the same three subcategories as well as many others which will be discussed within this section. However, such techniques use more than the flame's natural illumination in order to capture enhanced images. [28]

2.3.1.1 Broadband Flame Imaging

CCD and CMOS cameras have a broadband spectral response across the all Visible spectral range (400 nm – 700 nm) and thus been used widely nowadays for flame visualisation and monitoring in both research and industrial applications. In comparison to other flame visualisation techniques (such as laser-based imaging systems, refer to section 2.3.1.2), a broadband flame imaging system is simple, easy to use and maintain, and generally low cost. It can be a monochromatic or colour system, depending upon the camera chosen. Figure 2.2 shows a typical schematic diagram of a broadband imaging system [29]. The system consists of a lens, an image guide, and a colour CCD Camera. The image guide is fixed in the centre of a stainless steel pipe that is inserted into the water-wall of the furnace. The optics of the system are kept cool and clean by purging compressed air.

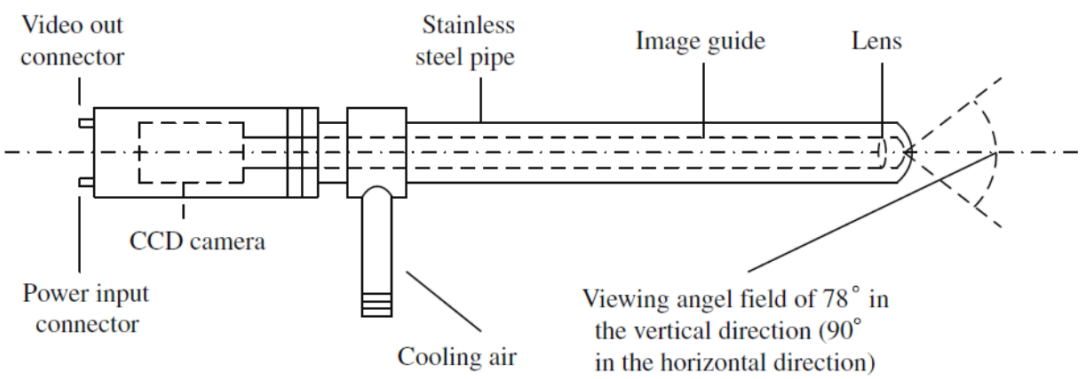

Figure 2.2 Schematic diagram of a broadband imaging system [30].

Sun et al [3] combined three different spectra of photodiodes and an imaging sensor in order to acquire high resolution flame images in a visible spectral range as well as flame signals in UV and IR though the visible spectral ranges for oscillation analysis. Figure

2.3 shows the schematic of the system whilst Figure 2.4 illustrates the physical implementation of the system. Within industrial environments, the use of the broadband imaging does not have problems such as system complexity and high equipment and maintenance costs. Figure 2.5 demonstrates some example flame images captured by the system during an industrial trial.

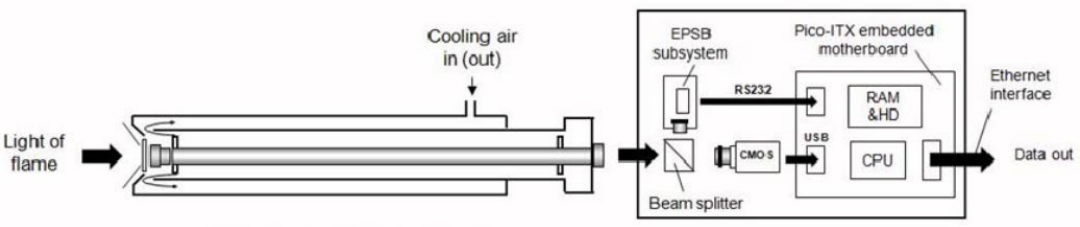

Figure 2.3 Schematic diagram of flame monitoring system [3].

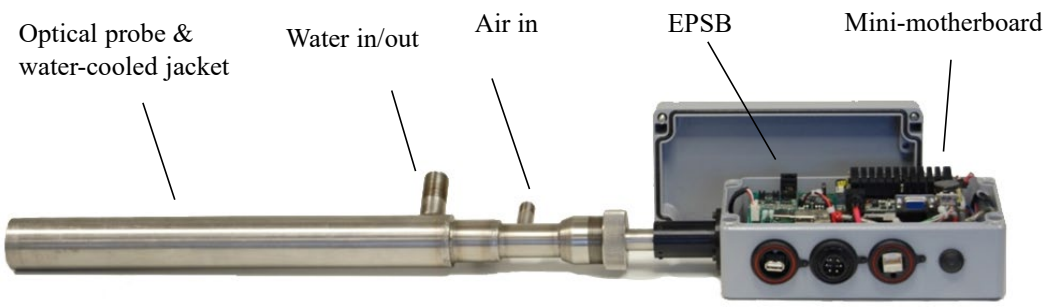

Figure 2.4 Physical implementation of the flame imaging system [14].

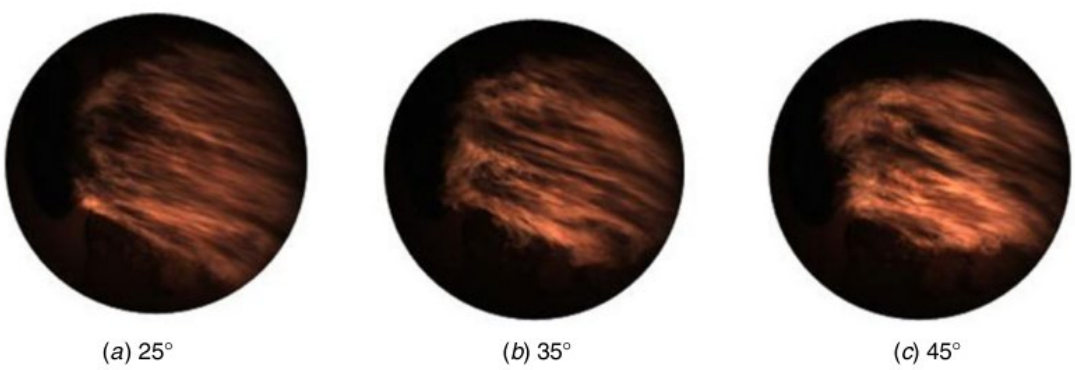

Figure 2.5 Example flame images captured by the flame imaging system [14].

However, the broadband imaging system corresponds to a certain bandwidth (generally Visible) rather than a specific wavelength (i.e., narrow bands) which poses difficulties in interpreting the data in some applications. Significant efforts have been made to convert the raw non-filtered images into meaningful, usable information through image processing techniques [31–34] and soft-computing (e.g., neural network) techniques [30, 35].

2.3.1.2 Optical-Based Flame Pyrometry

The temperature distribution of a flame is one of the most important characteristic parameters to evaluate the performance of a combustion system, including fuel conversion, emission formation process, furnace slagging and fouling [6, 9].Current devices for measuring flame temperature in industrial furnaces such as thermocouples and gas-sampling probes give only a single-point, intrusive measurement and only measure the gas temperature of the flame. In the last two decades, non-intrusive optical techniques were successfully developed and used for the measurement of flame temperature in both fossil-fuel-fired furnaces and internal combustion engines [36–39], ranging from active laser-based methods (such as PLIF, refer to section 2.3.2), flame emission spectroscopy (FES) and image-based pyrometric techniques. While laser-based methods are commonly used in laboratories, however, these techniques are not suitable for operation in industry due to the complexity and high cost of the system.

The image-based pyrometric technique is essentially based on the two-colour method, in which the temperature is derived from the ratio between intensity of the signal collected form two different wavelengths simultaneously. The two-colour method is mainly used for measuring the temperature of a flame whose radiation bands are dominated by black-

body emission. The main advantage of the two-colour method is that the emissivity of soot particles contained in the flame is not required [38]. Figure 2.6 depicts a two-colour imaging system which incorporates a monochromatic CCD camera and a set of optical filters to acquire images of two different wavelengths (700nm and 650nm) for the flame temperature measurement in an industry-scale combustion test facility.

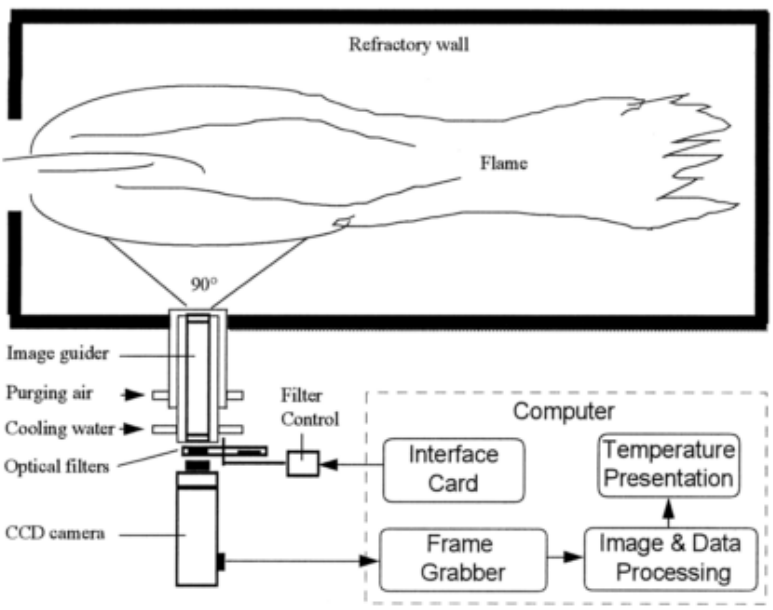

Figure 2.6 Schematic of a two-colour imaging system for flame temperature measurement in an industry-scale combustion test facility [40].

Parameswaran et al. [37] incorporated a miniature commercial spectrometer propagated within a pilot scale entrained flow gasification facility to obtain a UV-Visible bandwidth of the combusting carbon based fuels. Once obtained, a pair of close wavelengths are used to calculated the ratio and therefore the temperature measurement is found. Han et al [39] used a high-speed RGB camera to visualise the flame and its temperature distribution in a model engine (Figure 2.7) where the red and green channels of the RGB image at 550 nm and 750 nm were separated to act as the two band-pass images so that the two-colour

method was applied for producing the flame temperature distribution (Figure 2.8). Sun et al [41] also presented the two-colour pyrometric imaging techniques for the monitoring and characterisation of soot particles in heavy oil flames in an industry-scale combustion test rig.

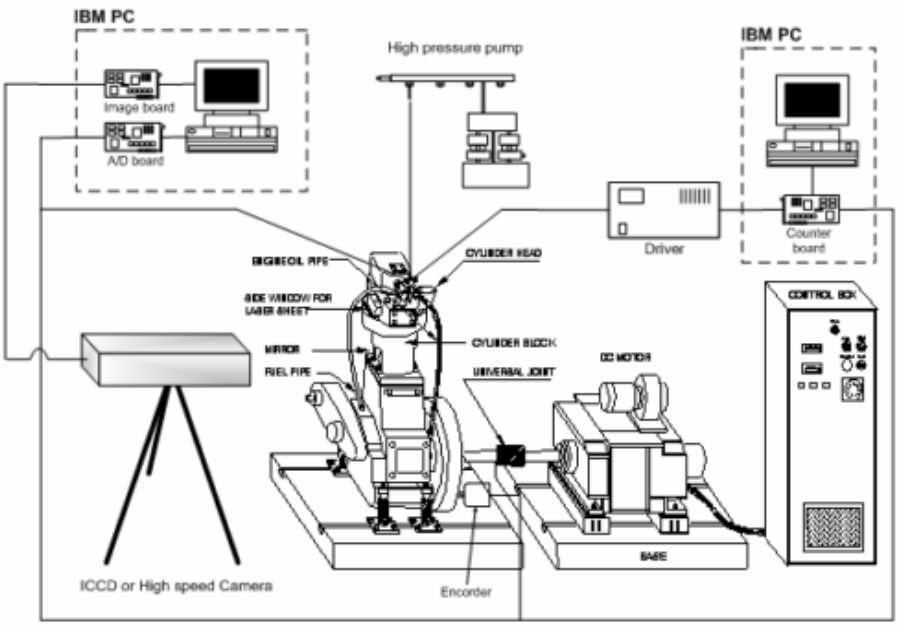

Figure 2.7 Schematic of experimental set-up for diesel engine combustion visualisation [39].

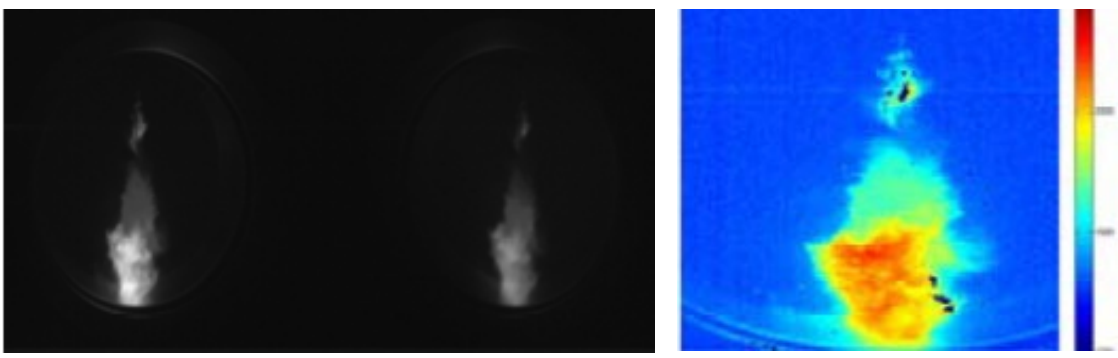

(a) Images at 550 nm (left) and 750 nm (right) (b) Temperature distribution

Figure 2.8 Filtered flame images and temperature distribution [39].

2.3.1.3 Flame Chemiluminescence Imaging

The investigation into the physical and chemical nature of the light emitted by a flame, particularly intermediates (or free radicals) of the flame, has been an important area in fuel and combustion research for decades. This is commonly regarded as the flame chemiluminescence detection. Chemiluminescence imaging captures radiative emission from electronically excited species formed by thermal excitation and chemical reactions, such as OH^* (282.9 nm, 308.9 nm), CH^* (387.1 nm, 431.4 nm), C_2^* (513 nm, 516.5 nm, 568 nm, 590 nm) [42].

Comprehensive reviews of spectroscopic techniques for flame chemiluminescence analysis were previously conducted by Suet al [43] and Liu et al [44]. A number of image systems have been developed and applied to flame chemiluminescence detection. The principle of such a system is to apply a dedicated optical filtering mechanism (e.g., a set of beam splitters and narrow bandpass filters) which allows only the light of flames emitted at the spectral bands of interest (such as the radicals mentioned above). In addition, an ICCD (Intensified CCD) or EMCCD (Electro-Multiplying CCD) camera should be used to capture the filtered images as the image signals can be very weak through the filters in some cases [39, 45, 46]. Krabicka et al. [47] developed an EMCCD-based system for measuring multiple flame radicals simultaneously. The system, as shown in Figure 2.9, comprised of a set of beam-splitters, mirrors, bandpass filters and an EMCCD camera. Four images corresponding to OH^*, CN^*, CH^*, C_2^* (Figure 2.10) can be acquired concurrently. The experimental data obtained by this system have been used in various studies within the research group, including fuel tracking and NO_x prediction [11].

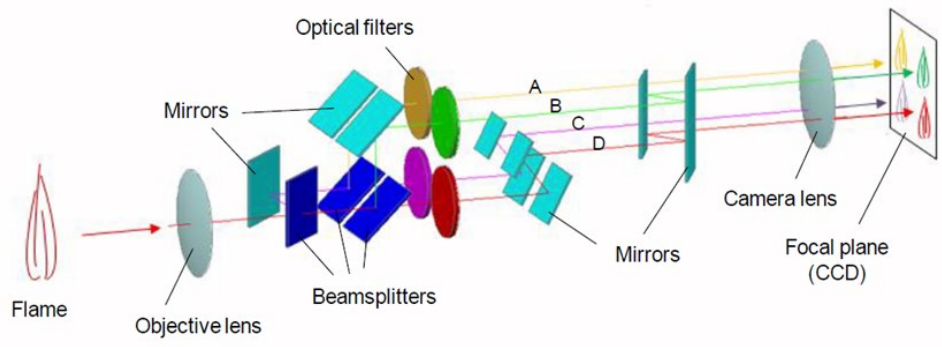

Figure 2.9 Sensing arrangement of a chemiluminescence imaging system [47].

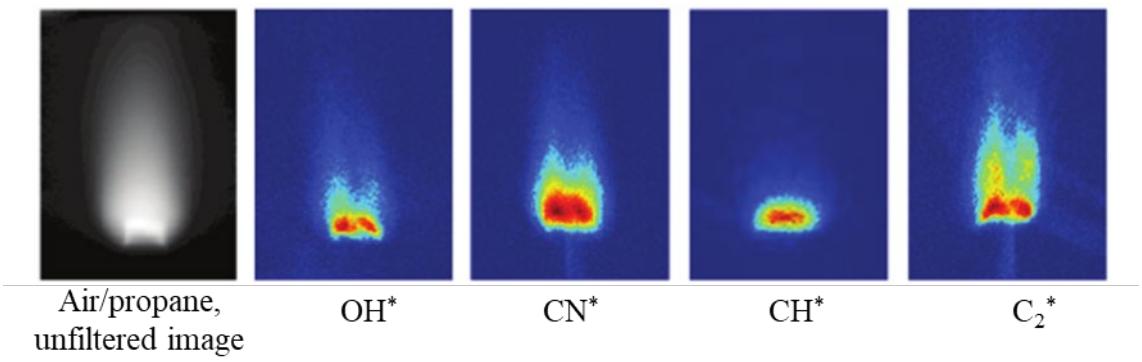

Figure 2.10 Unfiltered flame image and chemiluminescence images produced by an EMCCD camera system [47].

The chemiluminescence signal of the flame is directly related to the concentration of the corresponding excited species within the flame. Hence, chemiluminescence imaging techniques have been mostly successful when determining the location of flame reaction zone, giving detailed information of the heat release pattern and radical formation. Due to the technique requiring the flame chemiluminescence, however, it is normally only suitable for the study of gaseous flames where only the low soot content and blackbody radiation present. With appropriate filtering and removal of the blackbody radiation, there has been success in monitoring the chemiluminescence emissions in sooting flames with the mentioned imaging techniques [48]. Similar to laser-based imaging

chemiluminescence imaging is not selected as the sensing method for this study due to the complexity and expense of the system setup.

2.3.2 Laser-based Flame Imaging

Laser-based flame imaging is considered to be another branch in flame visualisation and measurement. There are a number of laser-based imaging techniques which have been developed in the last decades for studying the physical and chemical properties of flames. Those include LIF (laser-induced fluorescence) [28, 49], PF-LIF (photofragmentation laser-induced fluorescence) [50], and PLIF (Planar Laser Induced Fluorescence) [12, 51–53]. Among them, the PLIF is regarded to be the most common tool to study flame temperature, heat release, and free radicals (e.gg., OH and CH) due to its capability of detecting narrow bandwidths of spectra [54]. Figure 2.11 shows a typical sensing arrangement of CH-PLIF. The PLIF uses a laser usually within the green spectrum accompanied with a cylindrical beam splitter to fan out the light into a thin ‘sheet’ that passes through the flame to excite atomic or molecular species from a lower energy state to an upper excited state. Once excited the atoms (or molecules), these revert back to the lower energy state, then spontaneously emit photons causing emission known as fluorescence. This fluorescence can be then captured with an intensified camera (e.g., ICCD). The brightness intensity of the images is directly related to the density of the species.

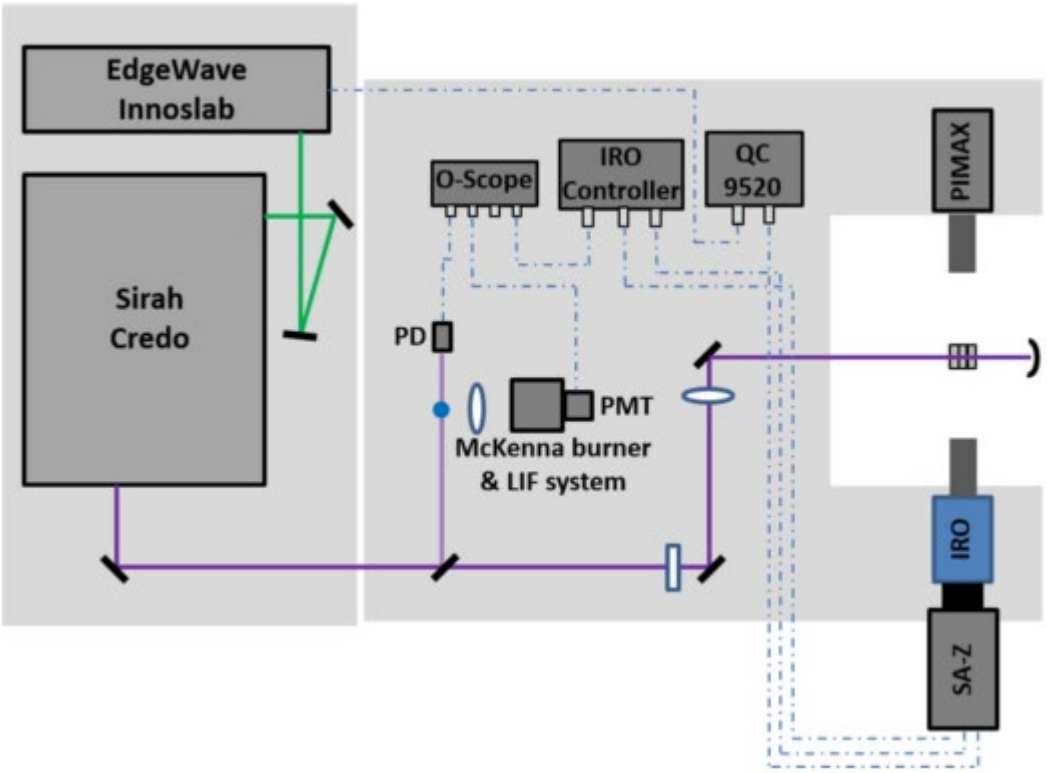

Figure 2.11 Schematic diagram of a kHz CH-PLIF system [51].

The laser-based techniques have been extremely useful for precisely observing the mechanisms and the chemical reactions of combustion processes. However, the complexity, high cost of the equipment and size makes such systems unsuitable for industrial environments.

2.4 Flame Spectrometry

The chemiluminescence imaging techniques reviewed in Section 2.3.1.3 target for measuring the emissive patterns of a few flame radicals using either 2-D ICCD or EMCCD imaging sensors. Flame spectrometry focuses on the measurements of light emissions of flames across a much wide spectral range from UV to IR through Visible by employing spectrometers. A spectrometer uses a one-dimensional CCD sensor, being

capable of detecting spectral intensities of flame across a wide spectra with a very high resolution (down to 0.1 - 1 nm). Generally fibre optic cables are used to collect light from a source to be transmitted down to the CCD sensor, due to the ability to change the exposure time of the sensor through software much like a CCD camera the probe can be placed anywhere that has a direct line of sight to the flame. Kathrotia et al [55] denoted a one-dimensional simulation of premixed laminar freely propagating flames performed by means of the coding flame simulation environment INSFLA. It was discovered that OH^* and CH^* are important heat release markers. Lamoureux et al [56] incorporated Molecular Beam Mass Spectrometry (MBMS) to quantify species $CH_4/O_2/N_2$ within flames doped with NO, NH_3 and NH_3+NO. Zhang et al [57] also showed the effectiveness of MBMS in detecting fuel species such as CO, CO_2, H_2, O_2, H_2O and Ar, as well as 30 intermediates within acetone–butanol–ethanol flames. Other similar spectrometric techniques which have been used to monitor flame radicals include Laser Ionization Mass Spectrometry (LIMS) [58], dual-resolution laser based Raman spectroscopy [59], Fluorescence-Assisted Gamma Spectrometry [60], and flame atomic absorption spectrometry (FAAS) [61]. Although these studies showcase the effectiveness of those techniques in quantifying the chemical emissions of the flames and predicting flame stoichiometric states, such apparatus are very expensive and not suitable for industrial retrofitting.

Far more relevant to the study present within this programme is the recent adoption of Flame Emission Spectroscopy (FES) with inexpensive miniature spectrometers. Romero et al [36] detailed a dual-spectrometer system, for high resolution data collection across a wide bandwidth, where the first spectrometer works on a bandwidth between (200 nm and 410nm) and the second UV to near IR light (200 nm–850 nm). The system was used to measure real-time combustion stoichiometry and temperature of a burner flame in a natural gas fired glass furnace (as shown in Figure 2.12). The results (Figure 2.13) showed

that from the emission band of the hydroxyl flame radical, OH^* correlated, to that of burner stoichiometry, through the excess O_2 and NO_x emission in flue gas, FES can be a powerful tool to monitor burner stoichiometry, which in turn, can be used to predict the NO_x emission in flue gas.

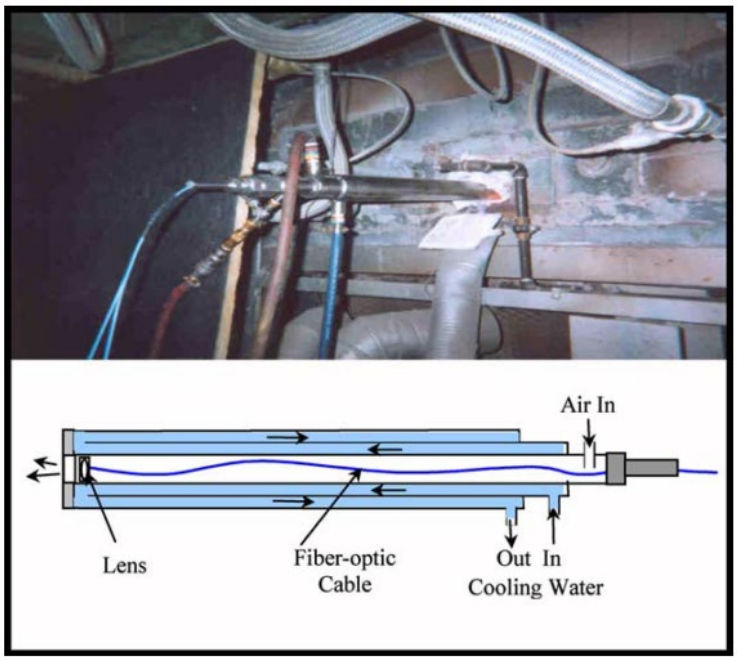

Figure 2.12 Physical implementation and schematic of fibre-optic cable probe [36].

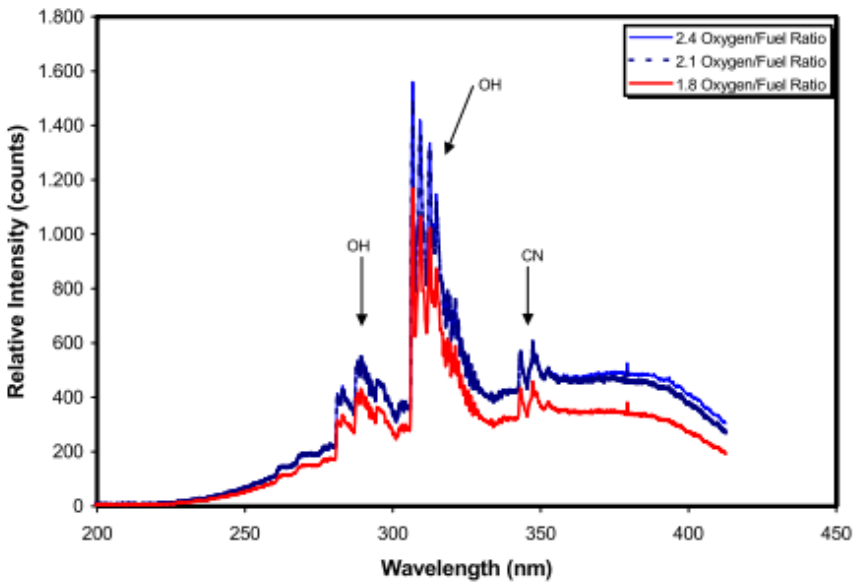

Figure 2.13 Typical UV spectrum for a range of oxy-fuel ratios captured with fibre-optic and spectrometer [36].

Parameswaran et al [62] also detailed the use of a spectrometer (a spectral range from 200 nm to 800 nm) in conjunction with a water-cooled and air purged fibre-coupled probe for measuring temperatures and species emissions during oxy-fired petroleum coke gasification with steam in a pilot-scale facility. The system setup is shown in Figure 2.14. The measured intensities of OH^*, CH^* and C_2^* under two different air to fuel ratios captured with this system can be seen in Figure 2.15. Chong et al [63] applied an spectrometer (Ocean Optics USB2000+) in model gas turbines where rapeseed biodiesel/methyl esters (RME), and 50% RME/diesel blend were used detected strong flame emission spectral peaks including OH^*, CN^*, CH^* and C_2^*.

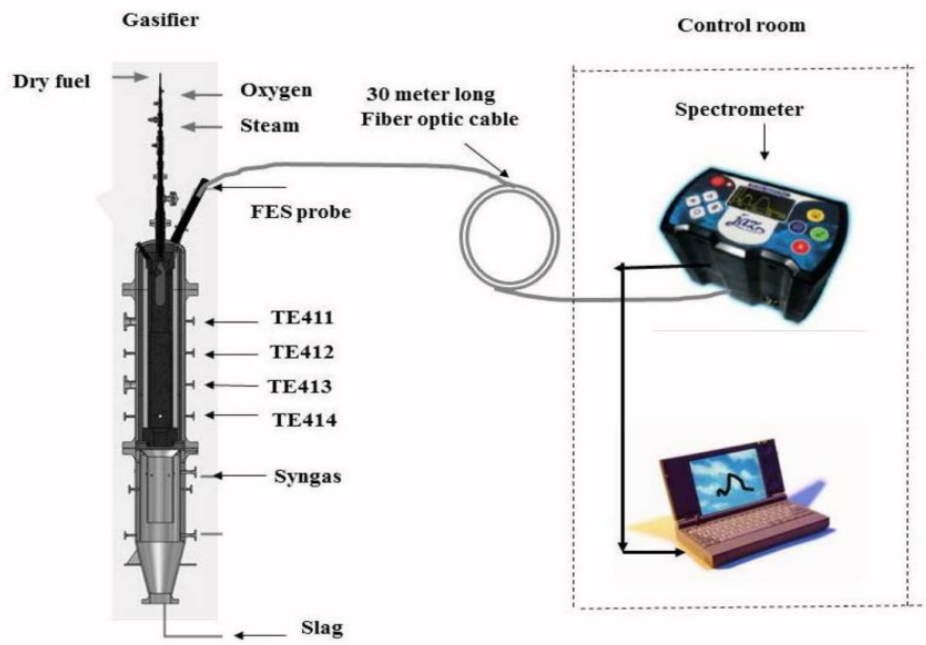

Figure 2.14 Schematic diagram of FES in the CanmetENERGY gasifier [62].

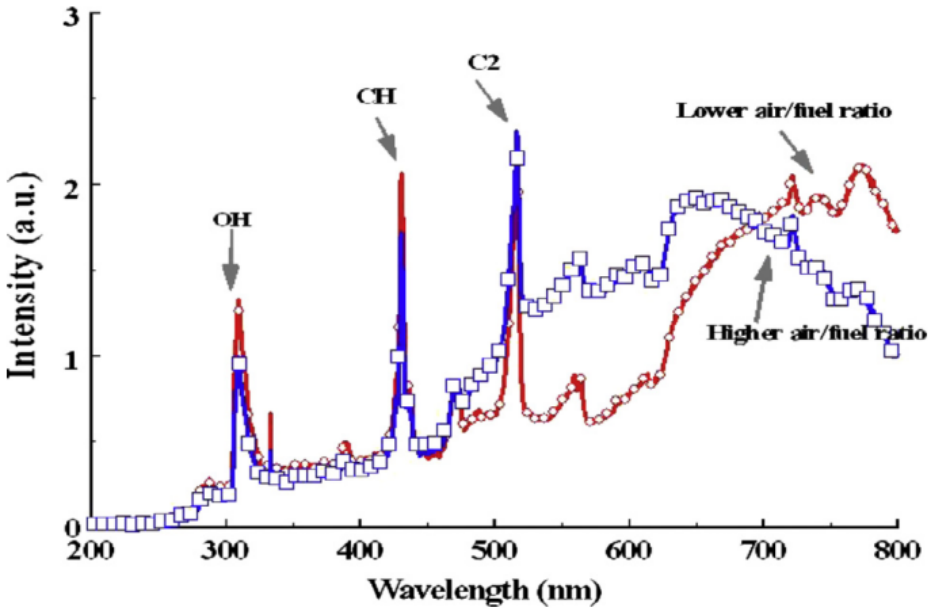

Figure 2.15 Natural gas flame spectra: spectral features vary with air/fuel ratio [62].

2.5 Condition Monitoring of a Combustion Process

This section reviews the existing techniques that have been used for the detection of abnormal conditions in combustion processes, the identification of flame state, and the prediction of NO_x emissions.

2.5.1 Burner Condition Monitoring

Traditional Statistical Process Control (SPC) techniques can be used to detect abnormal behaviour when it occurs in a process [64]. In the SPC technique, the control charts present thresholds that would not be surpassed under normal operating conditions. Therefore, control charts are crucial for determining if a process is still working under normal operating conditions or not. There are three main categories of control charts including [65]:

- Shewhart control chart [66]: in which the mean of a variable with upper and lower limits is expressed as an evolution over time. If any of the variable thresholds is exceeded, a fault is detected. It is usual to require a determined number of abnormal values to activate an alarm in order to avoid false alarms.

- Cumulative Sum (CUSUM) charts [67, 68]: this method is able to detect small variations faster than Shewhart charts by representing the cumulative addition of deviations across every observation. This technique requires a determined amount of past observations to calculate the normal cumulative sum at a current time.

- Exponentially Weighted Moving Average (EWMA) control chart [69]: this method computes a decision function for each observation based on the current data and the past average values through filtered data.

Unfortunately, these techniques are only capable of charting a small number of process variables and then analysing them individually, making these techniques inadequate for the online monitoring of the process such as a combustion process as studied in this research programme. It is desirable to analyse hundreds or thousands of simultaneous data processes to determine if an abnormal occurrence takes place. Approaches such as MSPC (Multivariate Statistical Process Control), in particular, Principal Component Analysis (PCA), Partial Least Squares (PLS), etc. have been used to monitor different industrial processes [70, 71]. Kernel PCA (KPCA) [72], is another form of the MSPC where a non-linear mapping within the high dimensional feature space is used to transform non-linear data into linear data, and to calculate the principal components in the feature space [73]. These MSPC techniques are based on the principle that dynamic

processes have a unique variation signature. Changes in these signatures may indicate that a significant change in the process has occurred.

2.5.2 Flame State Identification and Classification

Various algorithms alongside hardware monitoring techniques have been used to successfully classify and identify flames to specific groups. Huang et al [74] used digital image processing techniques for the characterising of radiation emission features from partially premixed syngas flames varying H_2, CO and/or CO_2 and different equivalence ratio at a constant 2 kW thermal power. Sbarbaro et al [75] processed flame images acquired by a CCD camera via the PCA and a generalised Hebbian learning (GHL) algorithm to characterise the flames produced by a laboratory-scale gas burner over a range of combustion conditions.

In more recent years, machine learning techniques such as Artificial Neural Networks (ANN) and Support Vector Machine (SVM) have been used to classify flame through its images. Hernandez et al [76] presented multiple approaches for condition monitoring of combustion systems based on flame images and demonstrated that, with limited image processing and neural network training, flame images under different swirl level percentages were successfully categorised. John et al [77] developed a novel flame edge detection algorithm to accurately determine flame parameters such as volume, spread speed and surface area, and used these parameters as inputs in a feed forward neural network to classify flames.

Zhou et al [2] developed a regression based SVM where flame parameters were used as the input nodes for predicting the type of coal fed into a 0.3 MW coal combustion furnace. Similarly, Xu et al [78] detected various type of fuels in a coal-fired boiler by extracting flame features in both time and frequency domains using three photodectors covering the UV, Visible and IR spectra in conjunction with a hybrid neural network against a fuzzy inference system. The results show that the neural network had a higher correct identification success rate of above 90% per trial.

2.6 Prediction of NO_x Emission

The monitoring and control of NO_x emissions to reduce the environmental impact has increasingly become a world-wide concern, and with the more stringent standards regarding the NO_x emissions for industrial sites, now more than ever this effort is of great importance. Many methods have been researched to understand the mechanisms of NO_x and minimise its emissions from fossil fuel fired power plants. Currently within the industrial environment, the measurement of NO_x emissions is achieved by using emission sensors or analysers, such as Continuous Emission Monitoring System (CEMS). However, the CEMS has a number of disadvantages such as high capital cost, drifts in measurements and often off-line maintenance due to harsh working environments (e.g., humidity and high temperature) [7, 79].

Machine learning has also been regarded as a promising technique to predict pollutant emissions and other flame conditions linked to the production of pollutant emissions [7, 10, 47, 78, 80]. Li et al. [7] described a three-layer back-propagation neural network where the ratios of the six radical pairs (CN^*/C_2^*, CN^*/OH^*, CN^*/CH^*, C_2^*/OH^*, C_2^*/CH^*, OH^*/CH^*) obtained using an EMCCD based chemicluminescence imaging system, and

flame temperature obtained using a spectrometer as the inputs of the network. The output of the neural network is the predicted value of NO_x emission. Li et al. [10] incorporated a technical approach for NO_x emission predication, where flame radical images, Contourlet Transform and Radial Basis Function (RBF) network were employed. The features extracted from the flame radical images through Contourlet Transform and the measured NO_x emissions (by a gas analyser) were used to train the RBF network. The average errors of NOx predicted are all less than +/-10% showing the success of the algorithm. Hao et al. [81] combined a simple three-layer back propagation neural network with generic algorithms, in an attempt to predict NO_x emission in a 600 MW coal-fired boiler. In their network, 29 input neurons were taken from the input parameters of the furnace, such as the fuel rate, total air flow rate, as well as the measurements from standard Oxygen and Hydrocarbon devices.

Regression analysis has also been used to predict NO_x emissions from combustion reactions with a 660 MW coal-fired boiler [71], a diesel engine [76] and a laboratory scale propane rig [77]. Ma et al [82] presented a method of NO_x prediction in diesel engines through the use of a general linear, and non-linear auto-regressive model with exogenous inputs (GNARX) such as the net engine torque, turbo speed, and accelerator pedal position. Lv et al [79] introduced an adaptive least squares SVM for predicting NO_x emission in an industrial furnace, where variables including model boiler load, coal quality, total fuel rate, total air rate, coal-feed rate, primary air rate, secondary air rate, circumferential air rate, OFA (Overfire air) air rate, and O_2 concentration in the flue gas were used as the inputs of model. The maximum relative errors of the five tests conducted within this study are 22.5%, 16.1%, 16.3%, 12.9%, and 11.6%, respectively indicating a reliable NO_x emission estimating.

Lughofer et al. [84] incorporated an FLEXFIS (FLEXible Fuzzy Inference System) approach to predict the NO_x emission in a diesel engine. They can automatically extract an appropriate number of rules and fuzzy sets by an evolving version of vector quantization (eVQ), offering the benefit that the trained models are further updated, such that with new incoming samples the prediction can evolve and improve. Smrekar [85] also presented an auto-regressive model in the form of the multi-step-ahead prediction of NO_x emissions. With the aid of pre-processing and resampling and feature selection analysis the model was trained with 32 inputs acquired from the plant's operator comprehended categorised into three groups, depending on their relevancy to the NO_x formation.

Finally, Li et al. [15] and Wang et al [86] developed a novel model architecture based on deep learning (DL) techniques for predicating NO_x emissions. Although these techniques are very powerful, due to their complexity to be trained and implemented they are not suitable for the daily running of boilers in industrial environments.

2.7 Summary

This chapter has reviewed firstly the existing flame monitoring techniques within the industrial environment. Then taken a look at the current state flame analysis research, including laser-based techniques, passive imaging such as chemiluminescence imaging, optical-based pyrometry, photodetectors. Secondly, the work that have been reported on abnormal burner condition monitoring, flame state identification and classification and finally NO_x prediction.

As can be seen from the cited work (Section 2.6), although a variety of NO_x prediction techniques have been developed, very limited work has focused on predictions suitable for the industrial environment. The main challenges of developing NO_x prediction suitable for such practical uses reside in two aspects. First, there are many different parameters that have been affectively linked to the production of NO_x emissions PLIF images, chemiluminescent images, optical based temperature maps, non-filtered images, and flame spectral analysis, the best method to produce a quantities analysis of the NO_x emissions is not clear. Second, challenges are also associated with the system installation, ensuring the system is simple to implement and use daily as well as protecting the system within the harsh environments of the combustion chamber. A variety of soft computing techniques have also been widely used to classify flame states and predict NO_x emissions. However, much of the existing work used burner and furnace combustion process data as the input to train the models, which could be different from the actual flame state, rather than direct information from the flame. Moreover, there have been no efforts to study the effectiveness of combining different successful hardware techniques (e.g., CCD camera and miniature spectrometer) with soft computing techniques for the NO_x predication and flame state identification.

The literature review has demonstrated that there is a certain gap between the existing technology for effective NO_x prediction and the requirements of industry. Based on the literature review, an instrumentation system incorporating broadband imaging and UV-Visible spectrum analysis techniques is thought to be a promising and feasible solution. Unlike active imagining techniques, there is no requirement for any external illuminations and due to the ease and cost effectiveness of the installation is much more suitable for industrial use.

Chapter 3

System Description

3.1 Introduction

In this chapter, the design, implementation and evaluation of the instrumentation system produced under this research programme will be given in detail. A digital RGB camera is used to capture the individual images of burner flames, from where a number of flame parameters is derived, including geometric and luminous parameters, temperature and its distribution and oscillation frequency. The system is calibrated by using a blackbody furnace as a standard temperature source for the temperature measurement. The accuracy of the temperature measurement is also verified by applying the system to measure the true temperature of the blackbody furnace. A standard frequency-varying light source is used as an idealised flame to evaluate the performance of the system for the oscillation frequency measurement.

A miniature spectrometer is also used as part of the system for the flame spectral measurement in a working wavelength ranging from 180 nm to 876 nm. The spectral signal of the flame is captured with a focus on obtaining the overall flame spectral information, but specifically, the spectral characteristics related to the key flame radicals such as CH^* (432 nm) and C_2^* (568 nm) to establish a predication modelling of emissions (e.g., NO_x).

3.2 System Design

3.2.1 System Overview

Figure 3.1 is the block diagram of the flame monitoring system developed under this research programme, whilst figure 3.2 gives the schematic of the system. The system consists of a rigid optical probe; an optical fibre; an RGB digital camera; a miniature spectrometer; and an embedded computer with associated application software. The optical probe and fibre transmit the image and spectral signals to the camera and the spectrometer. To prevent the probe/fibre from overheating due to the high temperature, and to maintain positive pressure inside the furnace, a water/air cooled jacket with a single-valve isolating unit was designed as an integrated part of the system. The objective of the probe/fibre has a tilted view angle of 75º with the reference to the optical path of the probe. The cooling jacket and the probe/fibre are installed penetratingly into the boiler through the viewport at the back of the sidewall, in order that the burners at the front wall of the boiler can be fully visualised. Such a system configuration allows both the camera and spectrometer to capture flame images and spectroscopic data concurrently. The application software permits the system to acquire flame signals, process the data and present the measurement results.

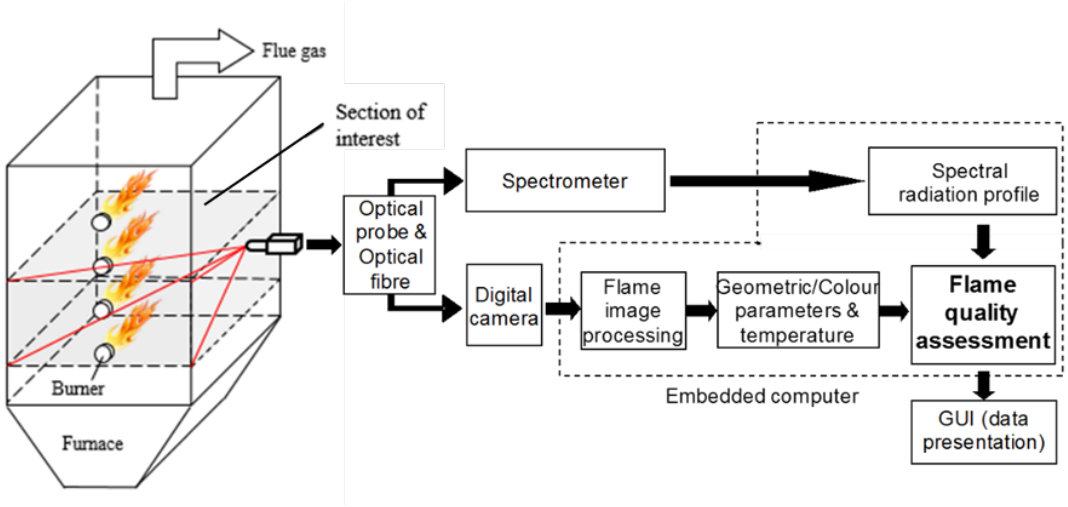

Figure 3.1 Block diagram of the flame monitoring system.

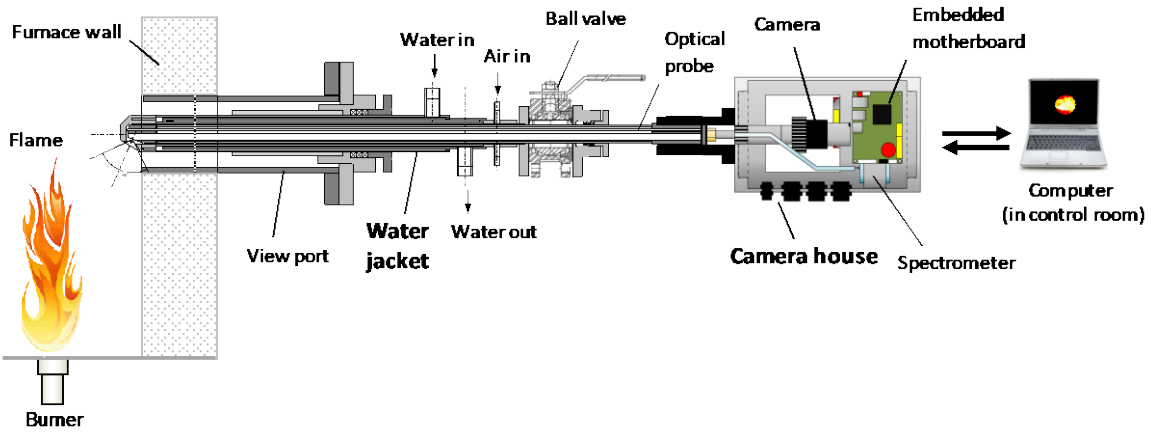

Figure 3.2 Schematic of the flame monitoring system.

The system can be divided into four hardware subsystems and associated application software:

- Light transmission subsystem: an integrated probe including an optical probe, an optical fibre, and a thermocouple enveloped in a stainless steel tube to transmit light of flame in the boiler to the sensing and computing subsystem.

- Sensing and computing subsystem: an instrumentation unit including an optical lens, a digital camera, a miniature spectrometer, and a mini-motherboard to acquire and process the flame signals, and transmit the processed flame data to the main computer system for the data presentation and storage.
- Water/air cooling subsystems: a stainless structure including supporting/sealing flanges, sealing glands and an isolation valve to prevent the light transmission subsystem in the harsh environment inside the boiler.
- Water/air flow control and alarm subsystem: a cabinet housing power supply (for the instrument), water and air flow meters and regulators, and probe temperature monitoring).
- System application software: programmes software including a GUI (Graphic User Interface) based on C language.

The following sections are detailed descriptions of the subsystems:

3.2.2 Light transmission subsystem

In the system design, an optical probe and optical fibre are employed to transmit flame light into the imaging sensor (a digital camera) and the spectrometer. The light transmission subsystem is essentially an integrated probe to accommodate and secure the two crucial sensing elements; i.e., the optical probe (for imaging); optical fibre (for spectroscopic detection), in a single, rigid and robust unit. This is necessary as it is crucial to collect flame visual and spectroscopic information from a furnace through two sensing elements concurrently. For this to be achieved, the optical probe and optical fibre must penetrate through the furnace wall and be positioned in such a way that the primary areas

of flames can be visualised. The working temperature of the probe should also be monitored by a thermocouple continuously, to ensure all the optical components work under a safe environment. There are a number of technical challenges in the design:

- to ensure the optical probe, optical fibre and thermocouple are fixed securely in the limited space of a long (up to 1.4 m) and rigid stainless tube.
- to ensure that the fields of view of the optical probe and optical fibre cover the primary areas of flames at the viewport located restrictedly at the back-end of the boiler sidewall.
- to ensure the all optical components are prevented from the harmful environment, particularly the high temperature, positive flue gas pressure, and flue gas dust.

The complete assembly of the light transmission subsystem is shown in Figure 3.3 whilst Figure 3.4 shows the relationship between the probe and the furnace. All the dimensions were either provided by the industrial collaborator or measured in site. DAs can also be seen, several other important additions, including the sealing block that tighten a packed graphite seal around the integrated probe and the jacket.

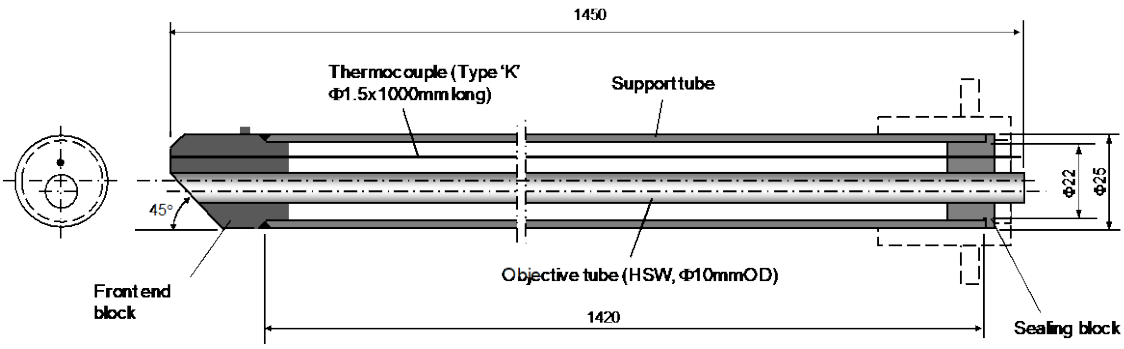

Figure 3.3 Assembly and dimensions of the light transmission subsystem-integrated probe (Unit: mm).

Given the fact that the probe has to be installed at the viewport located at the back-end of the boiler sidewall with a 6750 mm distance (L_1+L_2, as shown in Figure 3.4) from the viewport and the front wall of the boiler, the view angle of the probe has to be tilted to a suitable angle with a reference to the burner central axis, so as to achieve the maximum field of view of the system. Based on the dimensions of the boiler, a trigonometric calculation was performed to determine the distance from the lens to the closest visible point of the flame (L_1). The resulted tilted view angle of the probe is determined to be 70° with an angle of view of 90°, resulting in that the estimated length of visible flame from the burner (L_2) is 5900 mm.

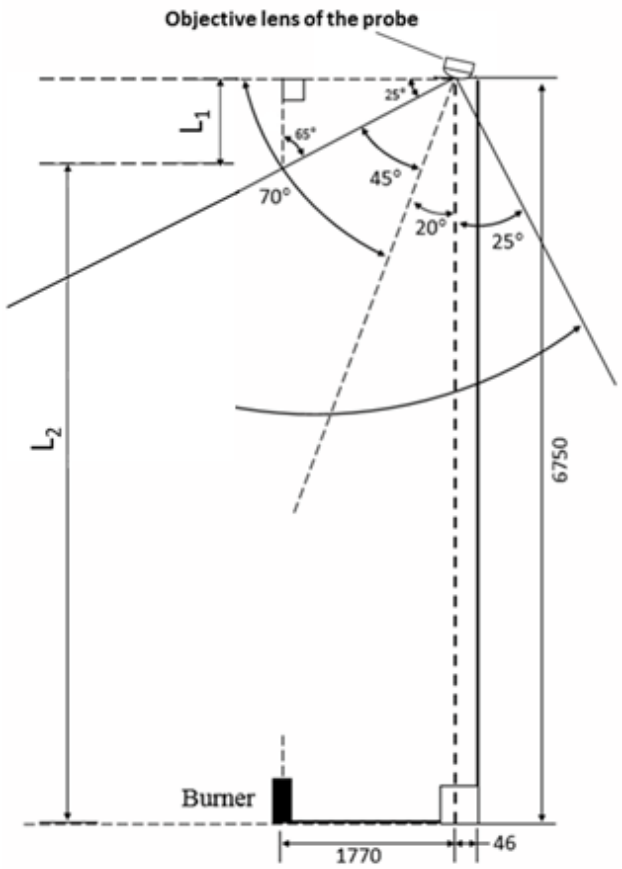

Figure 3.4 Sketch of layout of the inside of the furnace, with relative angle and distance from the viewport (Unit: mm).

3.2.2.1 Optical Probe

Based on the dimensions of the boiler, the thickness of boiler wall and the length of the required isolation assembly of the cooling jacket, all possible specifications of commercially available optical probes were studied. The key technical requirements of choosing the optical probe are that it should be capable of transmitting a high-resolution image signal, and to be robust and suitable for industrial environment. A borescope probe from HSW (Henke Sass Wolf) [87], as shown in Figure 3.5(a) was chosen. The full specifications of the probe are listed in Table 3.1. The probe has an outer diameter of 8 mm with a 70° tilted objective lens and a 90° angle of view.

(a) Overview of the optical probe (with the camera attached).

(b) Close up view of the objective lens.

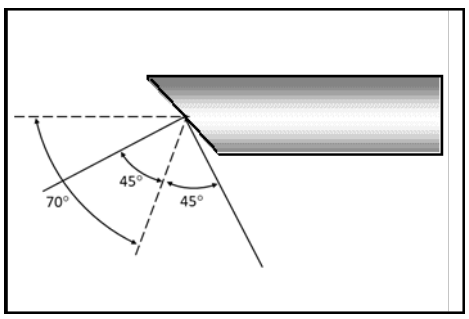

(c) Tilted angle and field of view.

Figure 3.5 The HSW optical probe.

Table 3.1 Specifications of the optical probe.

Name	Description
Model	R10-1450-70-90, HSW
Diameter (mm)	10
Working length (mm)	1450
Direction of view	70°
Angle of view	90°
Eyepiece	Rotation and focusing C-Mount eyepiece

3.2.2.2 Optical Fibre

The optical fibre cable (Figure 3.6) was determined once the spectrometer was selected (Section 3.2.3.2). The optical fibre was capable of transmitting the light of the flame in a spectral range from UV to near Infrared, i.e., 300 nm-2100 nm. It is a flexible cable with a length of 1600 mm and an outer diameter of 4.5 mm. The optical fibre itself was 1.5 mm in diameter with a 7° angle of view and was connected to the spectrometer via a standard SMA-905 connector.

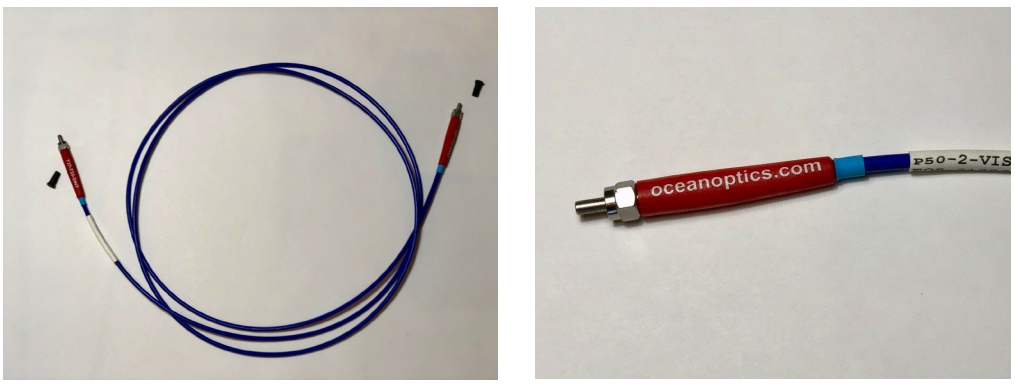

(a) Optical fibre (b) SMA-905 connector.

Figure 3.6 Layout of the optical fibre.

3.2.2.3 Thermocouple

A thermocouple is incorporated into the design of the integrated probe to measure the working temperature of the optical probe and fibre during system operation. A warning alarm will be trigged if the working temperature excesses the threshold set the system. Considering the temperature of the boiler around the viewport can be up to 700 °C (based on the on-site measurement), a Type K thermocouple with working temperature ranging from -50 °C to +800 °C was chosen. The thermocouple conforms to IEC 584 standards, having a durable construction and featuring an Iconel Alloy 600 mineral insulated flexible sheath around the probe. It also has an ungrounded hot junction to reduce electrical interference. Figure 3.7 shows the layout of the thermocouple, where Lp is the length of the cable out to the system and L is the length of the probe transmitting into the furnace. Table 3.2 is the brief summary of the technical data of the thermocouple.

Table 3.2 Specifications of thermocouple.

Attribute	Description
Type	K
Probe diameter (mm)	1.5
Probe length (mm)	16
Maximum Temperature Sensed (°C)	+800
Probe Material	Inconel 600
Termination Type	Bare Wire Tail

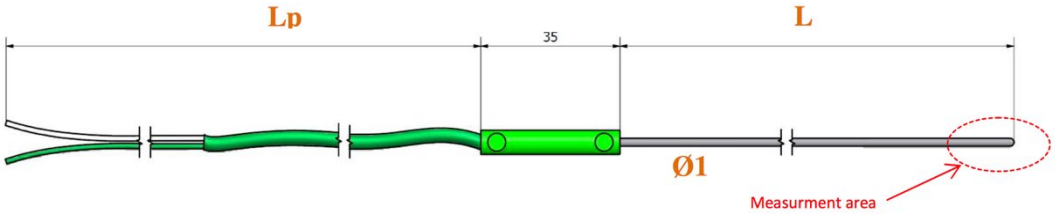

Figure 3.7 Layout of the thermocouple.

3.2.2.4 The body of the Integrated Probe

Figure 3.8 shows the mechanical drawing of the completed integrated probe including the probe head, base and protective tube, capable of housing the optical probe fibre, and thermocouple. The design of the integrated probe assembly allows the three sensing parts [i.e., the rigid optical probe (for flame imaging), optical fibre (for spectrometer); and thermocouple (for probe temperature monitoring)] being secured within the probe head and enveloped in a single stainless steel tube, ensuring that the viewing angle of the optical fibre is lined up with the flames inside the boiler.

Figure 3.9 shows the mechanical drawings of the integrated probe head, which is the most crucial part of the integrated probe's design as it allows the optical probe, fibre and thermocouple to all capture data simultaneously.

To achieve this with very limited space to meet the required direction of view of the fibre optics it was chosen to place an opening into the top of the head, allowing the fibre and the thermocouple to have more room to bend upward and to helix around the optical probe, to then be secured at the necessary 70°.

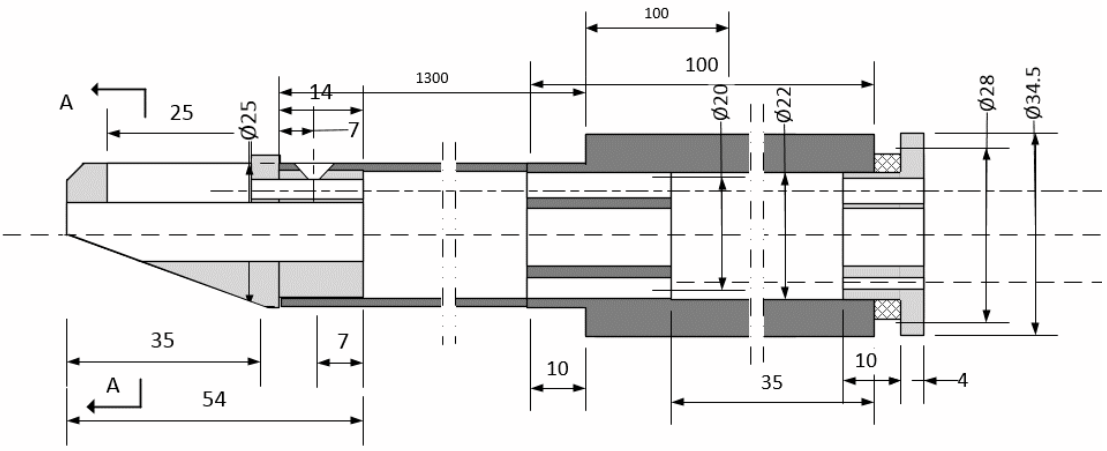

Figure 3.8 Complete mechanical drawing of the integrated probe.

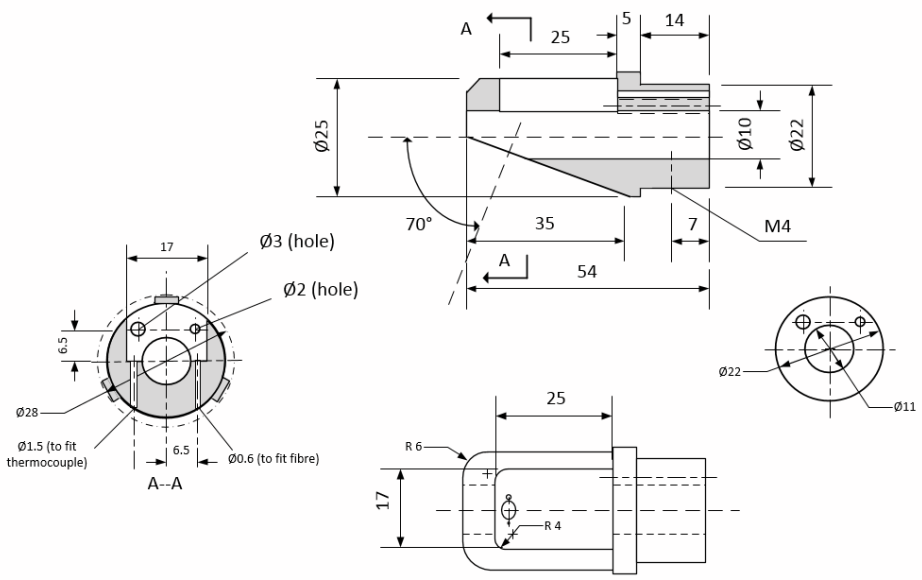

Figure 3.9 Mechanical drawing of the integrated probe head.

Figure 3.10 shows a mechanical drawing of the integrated probe base, as mentioned, the furnace functioned at positive pressure, and therefore all three of the main sensing transmissions within the probe must be sealed for a safety purpose.

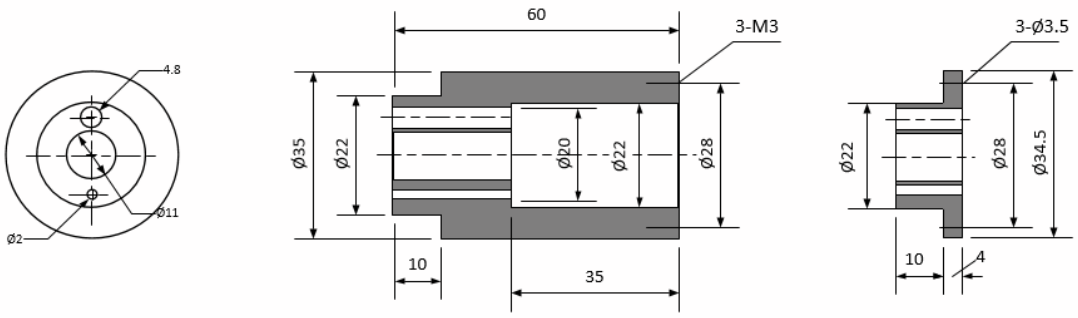

Figure 3.10 Mechanical drawing of the integrated probe base.

3.2.3 Sensing and computing subsystem

The sensing and computing subsystem acquires and processes the flame signals transmiting the processed flame data to the main computer system for presentation and storage. It includes a digital camera with a coupling camera lens, a miniature spectrometer, a thermocouple processing circuit board, and a mini-motherboard.

3.2.3.1 Digital Camera

The camera receives the light of the flame transmitted by the optical probe and convert it to digital images. A cost effective and high performance digital camera (UI-3130CP Rev 2, IDS Ltd.) was selected in the system. It is an industrial CMOS RGB camera, as illustrated in Figure 3.11, featuring two different modes, programmable via application software, i.e., a high-resolution mode (up to 1280(H)×1024(V) at a frame rate of 25 fps (frames per second)), and a high-speed mode (up to 900 fps with a reduced image resolution of 400(H)×300(V)), which is achieved by a subsampling setting. The full specifications of the camera are listed in Table 3.3. The capability of switching the two

different modes makes this digital camera very powerful for capturing the images of the flame for both high resolution and high-speed.

Table 3.3 Specifications of the camera [88].

Attribute	Description
Model	UI-3130CP Rev 2
Sensor type	CMOS
Frame rate (fps)	Normal: 25
	High-speed: up to 900
Resolution (h x v) (pixels)	800 x 600
Optical area (mm)	3.840 x 2.880
Shutter	Global Shutter
Resolution (MPix)	0.48
Pixel size (μm)	4.80
Lens mount	C-Mount
Dimensions H/W/L (mm)	29.0 x 29.0 x 29.0
Weight (g)	52

Due to the inclusion of an eyepiece fitted to the end of the HSW optical probe, a coupling lens (Figure 3.12) is used to connect the optical probe and the CCD camera. The coupling lens is designed with a specific focal length (25 mm) which allows images to focus on the camera imaging sensor correctly. An image of the coupling lens is shown in Figure 3.12 with the 32 mm borescope eyepiece adaptor and a standard C-mount to attach to the camera.

Figure 3.11 Physical layout of the digital cameras. [88]

Figure 3.12 Physical layout of the coupling lens.

3.2.3.2 Miniature Spectrometer

A miniature spectrometer (USB2000+, Ocean Optics Ltd) was chosen, which has a commensal 2048-element linear silicon CCD array with a detection range of 180 nm to 876 nm capturing 2048 pixels. The layout of the spectrometer is shown in Figure 3.13, and the full specifications for the spectrometer are listed in Table 3.4. The spectrometer also features an adjustable integration time of 1 ms – 65 sec, allowing for a wide range of light to be absorbed by the sensor, which was very important as the intensity of the industrial flame could vary significantly. This is crucial as the 500nm-800nm spectrum intensity of a flame provides a much stronger signal than the single UV-VIS wavelengths of the flame radicals usually found in the 200nm-500nm range. The ability to change which characteristic is being focused on, easily and online, provides much more data, describing the flame state even better.

Figure 3.13 Physical layout of the spectrometer (USB2000+, Ocean Optics Ltd) [89].

Table 3.4 Specifications of the spectrometer [89].

Attribute	Description
Model	(USB2000+, Ocean Optics Ltd.)
Interface & power supply	USB 2.0
Sensor type	Linear Silicon CCD Array
Detector range (nm)	200-1100
Pixels	2048
Pixel size (µm)	14 x 200
Integration time	1 ms – 65 seconds
Signal-to-noise ratio	250:1 (full signal)
A/D resolution	16-bit
Power consumption	250 mA@5VDC
Dimensions H/W/L (mm)	89.1 x 63.3 x 34.4
Weight (g)	190

3.2.3.3 PCB for the Thermocouple

The thermocouple is very important in maintaining the safe operating conditions of the probe and whole instrumentation system, as temperatures above 70°C could pose a threat to the optical probes and even propagate through to the components within the camera housing. Data processing circuit board (PCB) was required to transmit the temperature signal to the computer system. The PCB has a microcontroller (Teensy 2.0), a thermocouple amplifier breakout board (MAX31855) and a simple transistor switch. Figure 3.14 shows the circuit diagram of the PCB and Table 3.5 details the full specifications of the custom thermocouple monitoring PCB. The simple design of the PCB allows for a microcontroller to easily interoperate the signal from off-the-shelf thermocouples to the thermocouple amplifier breakout board, monitoring the temperature.

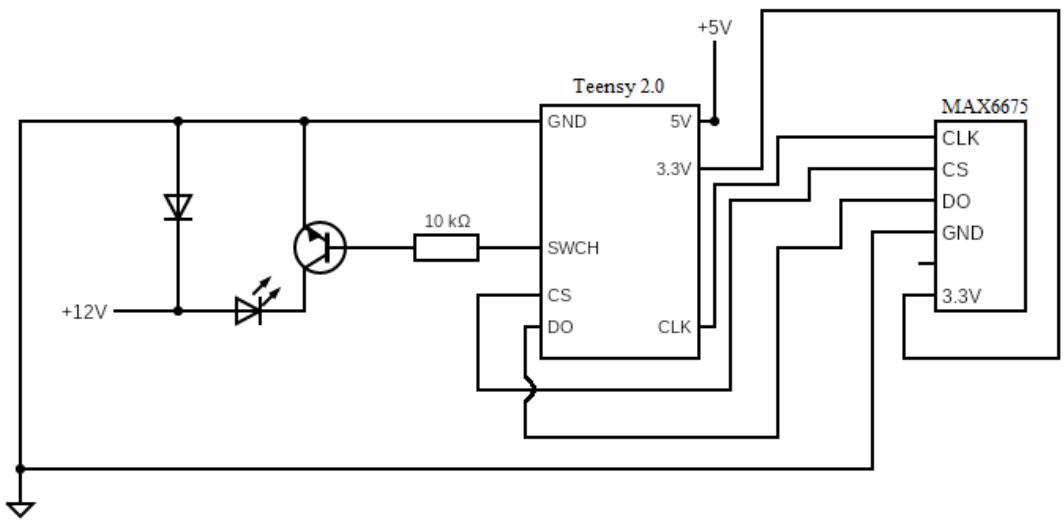

Figure 3.14 Circuit diagram of the custom thermocouple PCB.

Table 3.5 Specifications of the custom thermocouple PCB.

Name	Description
Microcontroller	Teensy 2.0
Thermocouple breakout	MAX31855
Interface	USB 2.0
Power supply	5V DC
Alarm trigger	Transistor Switch

3.2.3.4 Mini-Motherboard

For a fast data acquisition, processing and transmission, it was necessary to integrate embedded computing technology and associated software with the optical systems. It was also crucial to ensure that the system worked reliably, safely and robustly during the operation, giving warnings wherever necessary. A Pico-ITX embedded motherboard (Figure 3.15) is used to acquire and store the images and spectral data from the camera and spectrometer. The motherboard features an Intel Celeron J1900 2.42GHz Processor, 1333MHz SO-DIMM 8GB memory, 250GB SSD drive, USB 3.0 for fast on-board data processing connection, Ethernet was used as the transmission source between the user and the main computer system. A full list of the motherboards specifications can be seen in Table 3.6.

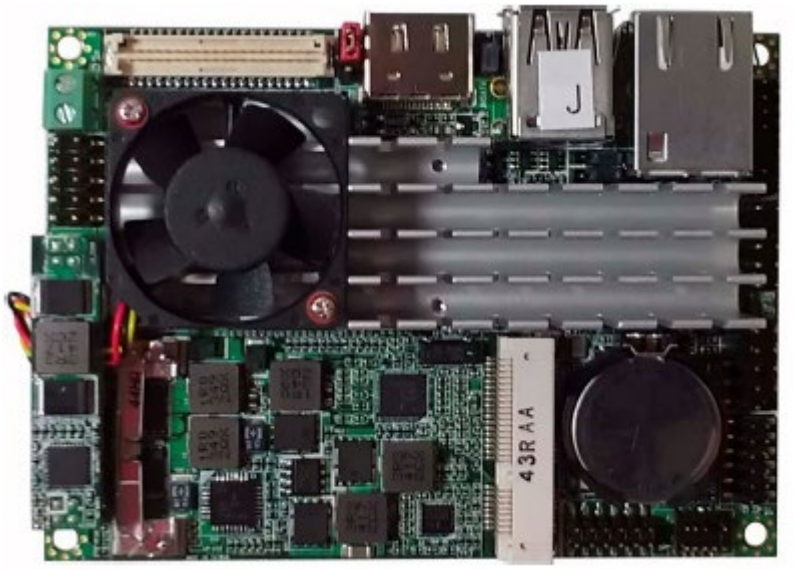

Figure 3.15 Pico ATX Motherboard LP-173 [90].

Table 3.6 Specifications of the motherboard [90].

Name	Description
Model	LP-173, Taiwan Commate Computer Inc.
CPU	Intel® Celeron™ J1900
Memory	DDR3L 1333 SO-DIMM up to 8GB
Integrated Graphics	Intel® Clear Video integrated HD Graphics
Serial ATA	1x SATAII with 300MB/s (3Gb/s)
LAN Interface	Intel® I210 Gigabit LAN
Extended interface	One PCIE mini card socket or mSATA
External I/O Port	1x HDMI, 1x RJ45, 1x USB 3.0, 1x USB2.0
Power	DC 6~30V input.

3.2.4 Cooling Jacket

Although the cooling jacket is separate from the sensing and computing systems, it is absolutely essential to allow the developed flame monitoring system to be functional under the hostile working environment of the boiler. The jacket should meet the following technical requirements:

- to house the integrated probe, providing support to the instrumentation box and securing the connection between the instrumentation system and the boiler at the identified viewport.
- to prevent all the optical components to fall out of safe working temperatures and to keep the objective lenses of the optical probe and fibre free from dust.
- to allow the integrated probe to be installed and removed during the boiler operation and to ensure that the flue gas does not escape due to a positive pressure inside the boiler when the probe is installed or removed.

A high temperature resistance stainless steel structure with combined water and air cooling mechanisms with an isolation facility were implemented in the design. A supporting and sealing flange was designed, which is attached to the flange of the viewport on the boiler. An isolation valve was also attached to the end of the jacket to provide the isolation of the system. This design has advantages, including to be small in size (a decreased overall working distance) and easy for system manoeuvre. It allows that the integrated probe can be extracted from the jacket if required whilst the boiler is still in operation. Figure 3.16 illustrates the complete design of the cooling jacket and its relation to the integrated probe and the view port of the boiler, whilst Figure 3.17 shows the general assembly and dimensions of the cooling jacket.

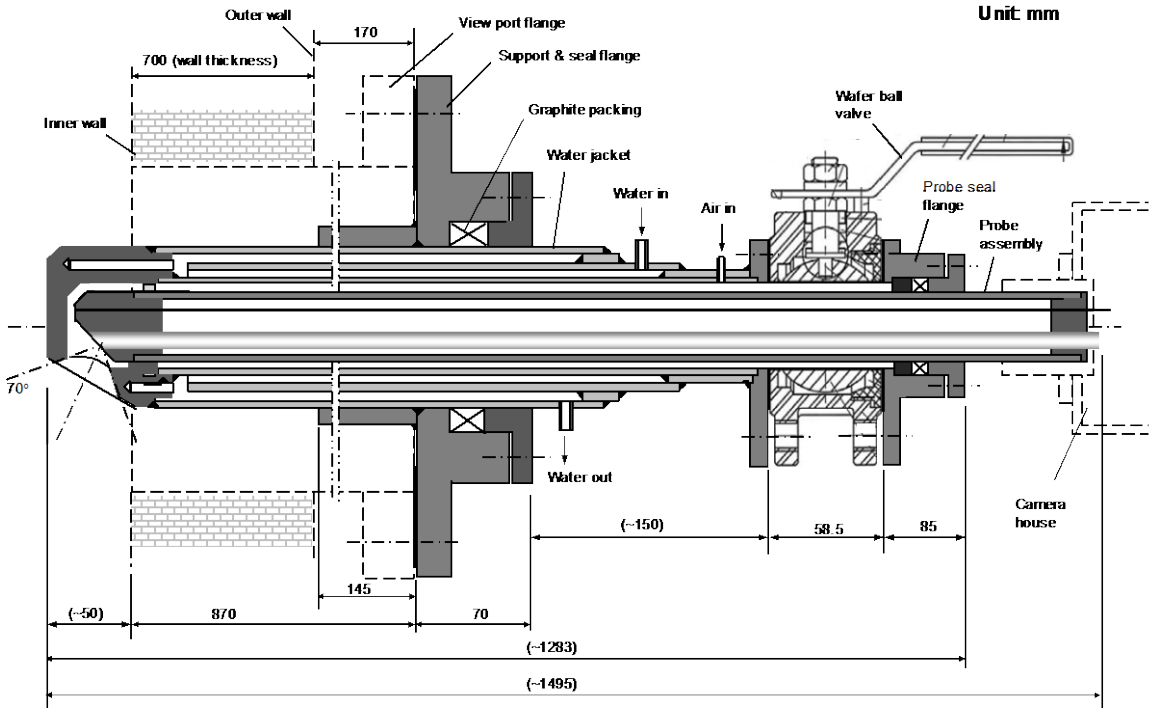

Figure 3.16 The complete design of the cooling jacket and its relation to the integrated probe and the viewport.

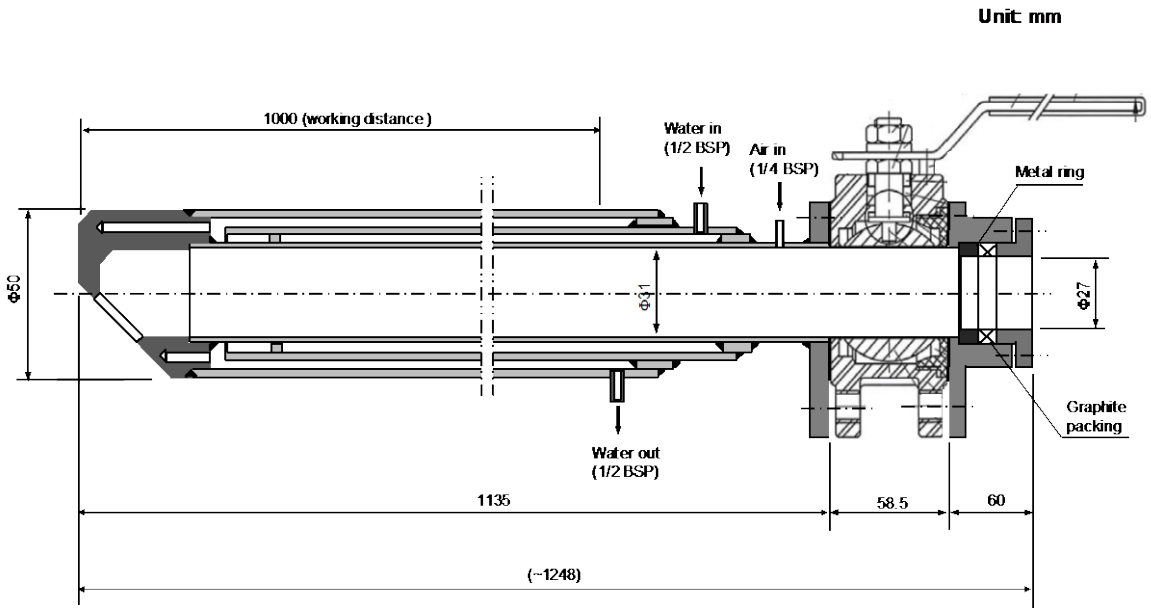

Figure 3.17 General assembly and dimensions of the cooling jacket.

3.2.4.1 The Main Structure

The layout of the main structure of the cooling jacket is given in Figure 3.18, which is made of three stainless tubes, and this creates two channels for water-in and water-out to allow the cool water circulating inside the chambers of the jacket, preventing the probe from the thermal radiation. The third channel is formed between the inner tube and the integrate probe so that a jet air flow can introduced, cleaning continuously the working optical surfaces of the optical probe/fibre. At the front end, a view window is designed to allow the optical probe/fibre to visualise the flames with an appropriate view angle. At the back end, a flange Figure 3.18 is constructed to allow the isolation valve to be attached to the jacket and create the entrance of the integrated probe.

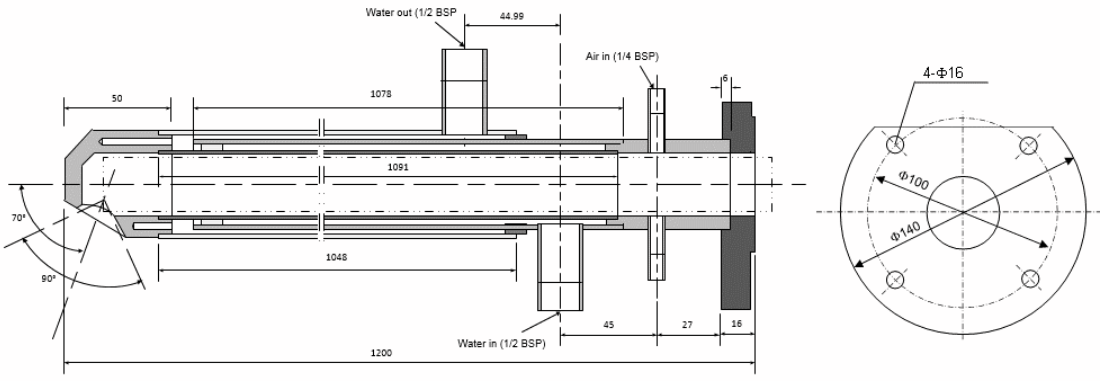

Figure 3.18 Schematic of the main structure of the cooling jacket.

3.2.4.2 The Supporting/Sealing Flange

The supporting/sealing flange, as shown in Figure 3.19, was also designed to be mounted on the existing flange of the viewport. This arrangement also ensures that the jacket can be installed and sealed securely during the service of the boiler.

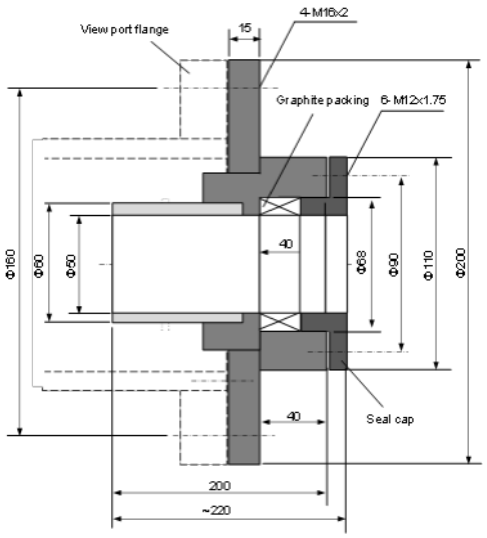

Figure 3.19 Assembly of the supporting/sealing flange and sealing gland.

3.2.4.3 Isolation Valve

The isolation valve is needed to block a possible flue gas leakage when the integrated probe is required to be extracted from or pushed into the boiler during the boiler operation. This is particularly crucial due to the positive pressure inside the boiler (25 mbar). The technical requirements for the isolation valve are that it should be:

- suitable for a high working temperature (up to 150 °C);
- suitable for frequent operation;
- compact in size

Considering the above factors, a stainless-steel Wafer ball valve from Leengate Valve [91] was selected. Figure 3.20 gives the layout of the isolation valve and Table 3.7 summarises the technical data of the valve. With such a configuration of the cooling jacket, the optical probe can be extracted from the jacket if required whilst the jacket

remains in the boiler, making it easier to manoeuvre the probe on the platform with a constrained operation space.

Figure 3.20 Layout of the isolation valve. [91]

Table 3.7 Technical data of the valve. [91]

Name	Wafer Ball Valve PN16
Material	Stainless steel
Diameter (Inner/Outer) (mm)	32/135
Width (mm)	58.4
Fitting	4-M16x2
Temperature (°C)	-10 to 180
Weight (kg)	3.6

3.2.5 Water/Air Flow Control and Alarm Subsystem

The water/air flow control subsystem is used to control the water and air flow supplies as required for the cooling jacket. It also accommodates the power supply for the instruments. Figures 3.21 and 3.22 show the schematic of the water/air flow control unit and the layout of the cabinet. The key components are documented in Table 3.8. All components for water/air flows metering and water flow/temperature failure alarms, as well as the power supply are enclosed in a steel cabinet, preventing exposure to dust. The temperature alarm collects the signal from the PCB of the thermocouple to monitor the working temperature of the probe in the boiler. This ensures that if unmanageable temperatures were sensed, the probe would be removed to prevent a possible damage of the highly sensitive optical probe and fibre. The water flow alarm was connected to a

water flow sensor placed inline of the cooling water fed to the jacket. In the event that a lack of water flow to the system exists, operators will be alerted. The power supply provides the electric power to the camera house, water flow sensor and alarms.

Table 3.8 Technical specifications of the main components for the water/air control subsystem.

Component	Model	Technical Specifications
Water flow sensor	Dwyer Series SFI-800	Sight Flow, Indicator/Transmitter
Float flow meter	Key Instruments polycarbonate gas flow indicator MR3000	1/8" FNPT inlet and outlet, 100psi, 65°C max, 100 L/min.
Air filter pressure regulator		Dimensions (HxWxD): 210x53x53 (mm).
Power supply	SDS60UD01	63W, 5V, 7A, 12V, 3A
Alarm	Banshee Excel Lite Xenon	9VDC – 30VDC, 90mA at 12VCD
Signal board	Custom	Signal taken from thermocouple and flow meter. O/P to alarms.

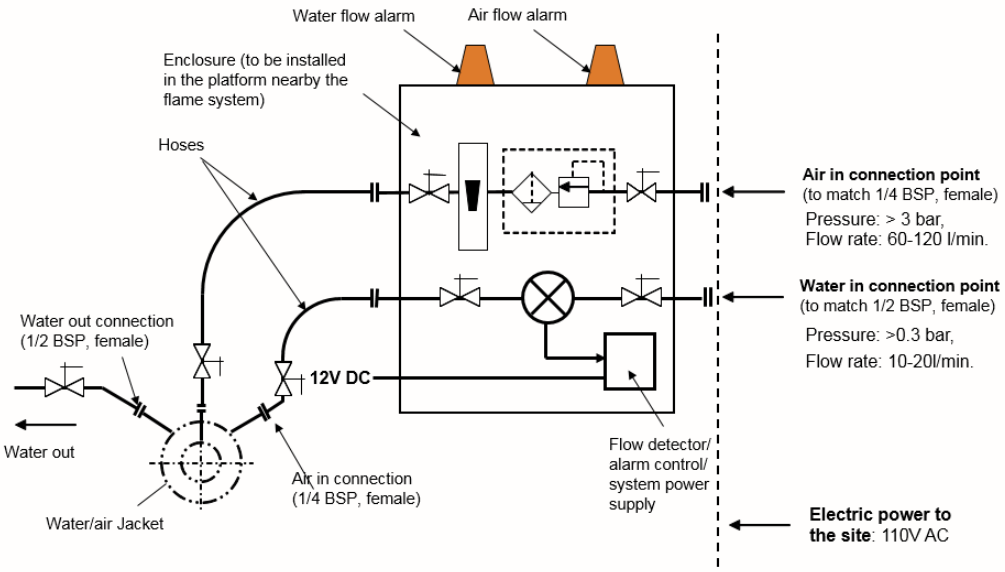

Figure 3.21 Schematic of the water/air flow control and alarm subsystem.

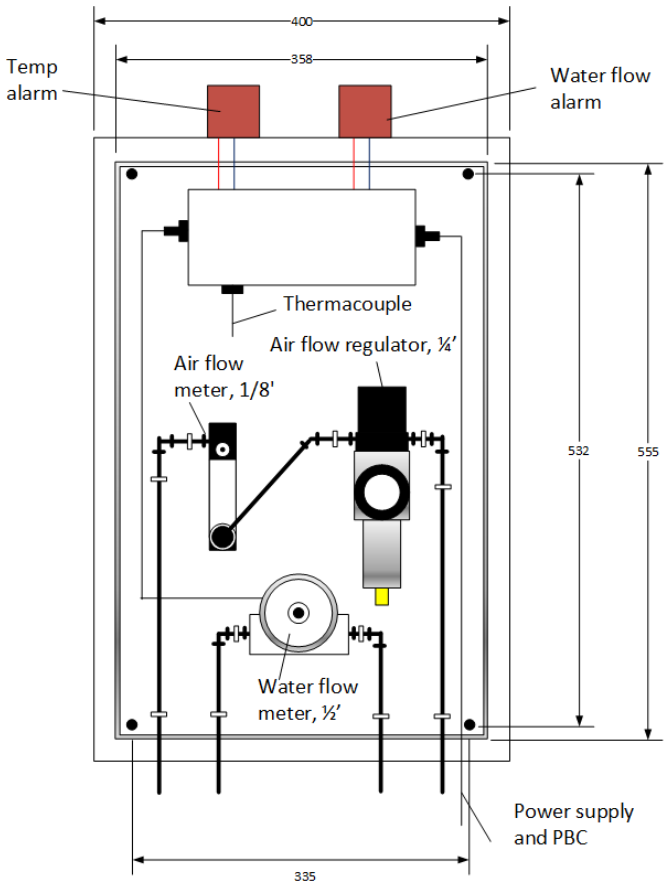

Figure 3.22 Layout of the water/air flow control subsystem.

3.2.6 System Application Software

Two separate instances of software were designed in C++ and C# in order to visualise and capture flame data online. The first was written to control the camera and acquire the images of the flames for the computation of flame characteristic parameters (e.g., area, brightness, temperature, and oscillation frequency). The second was also written for operating the miniature spectrometer to perform flame spectral analysis (i.e., flame radical information).

3.2.6.1 Image Acquisition and Analysis Software

Figures 3.23 and 3.24 present the screenshot of the GUI and the flowchart of the software, respectively. The program is capable of capturing flame images and conducting data processing for both off- and on-line measurements.

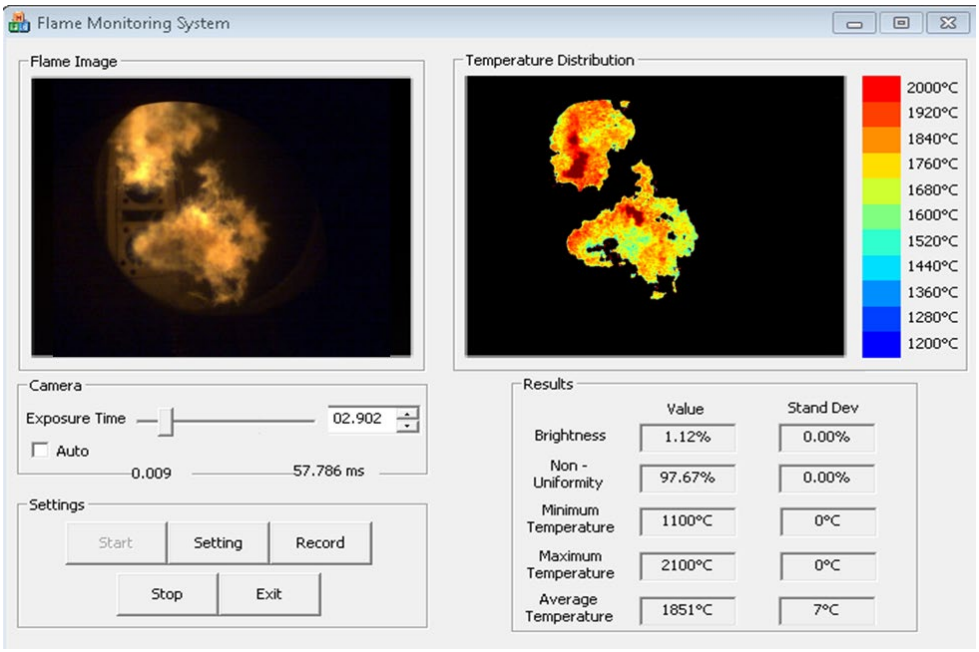

Figure 3.23 Screenshot of the system GUI.

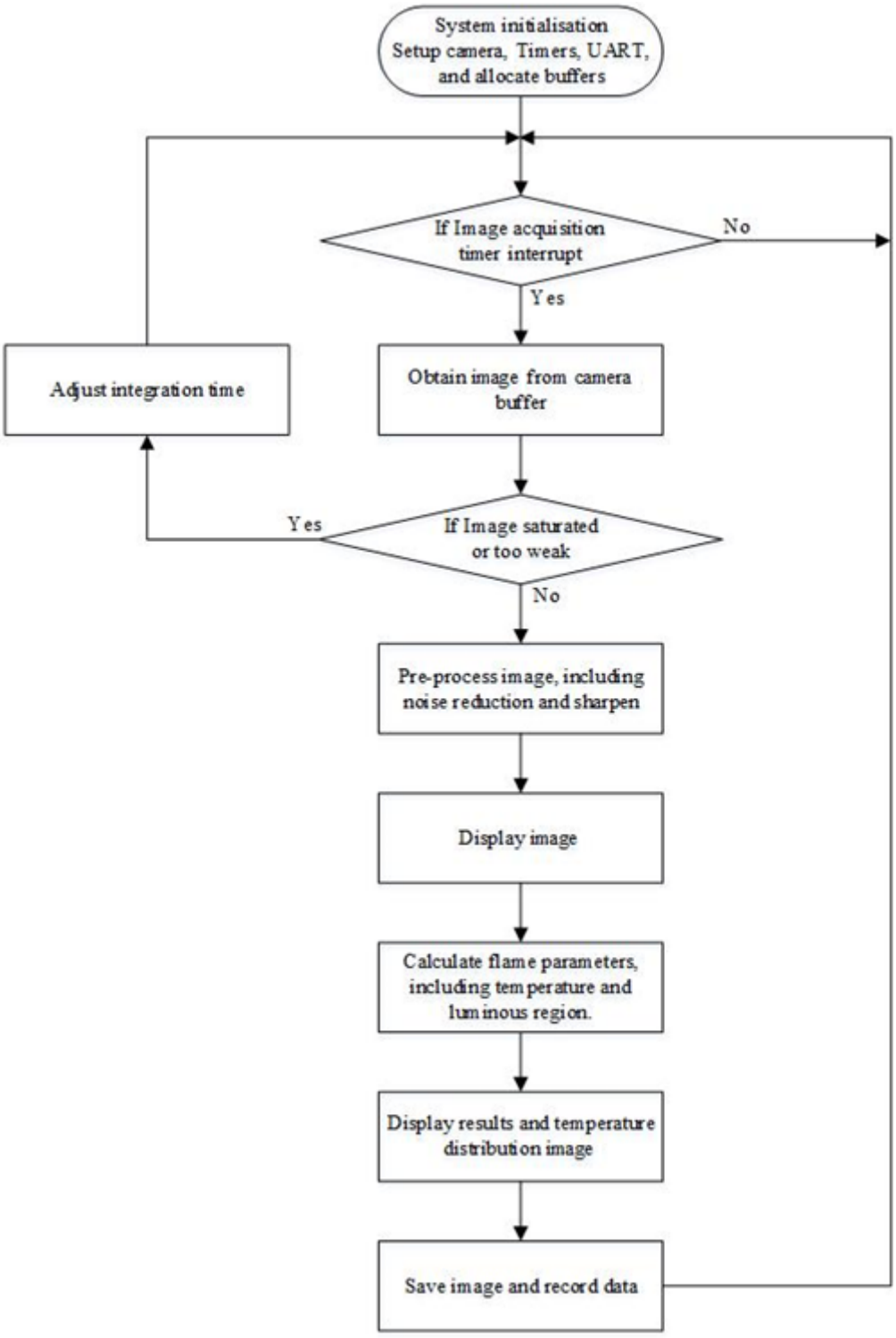

Figure 3.24 Software flowchart of C++ for imaging capture.

3.2.6.2 Spectrum Analysis Software

The development of the spectrum analysis software was based on the open source programs provided by the spectrometer supplier (Ocean Optics Ltd) [92]. A screenshot of the updated GUI is shown in Figure 3.25 and full software flowchart is presented in Figure 3.26. Software parameters can have great effects on the operation of the spectrometer, the integration time functions similarly to that of the shutter speed of a camera. Boxcar averages a group of adjacent detector elements. A value of N, for example, averages each data point with N points to its left and N points to its right. Scans to average specifies the number of acquisitions that the device driver accumulates before sending a spectrum. Trigger mode allows the user to synchronise the sending and receiving of acquisition data with a number of different hardware of software events. The program is capable of capturing flame spectra for both off- and on-line measurements. The program also allows the spectrometer to acquire a single wavelength so that the key free flame radicals, such as OH^*, CN^*, CH* and C_2^*, can be monitored.

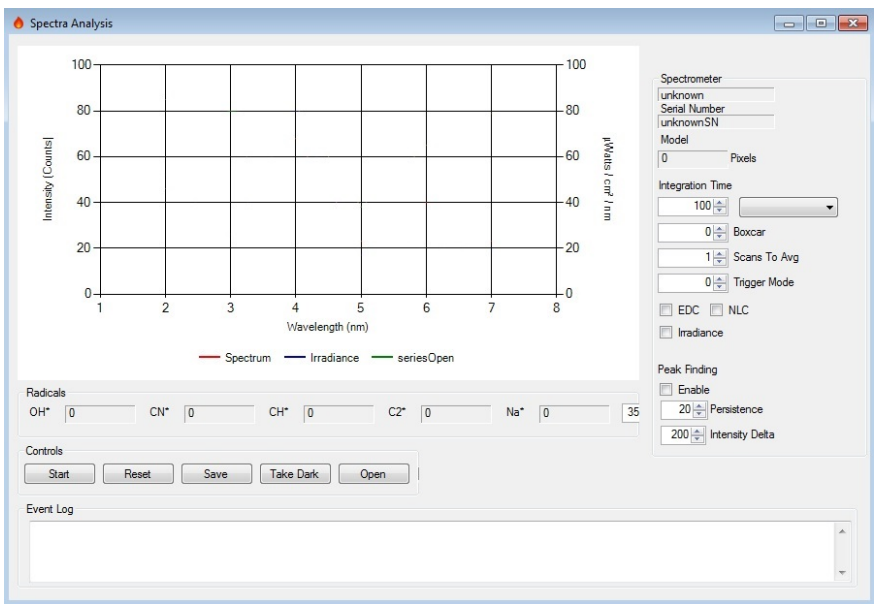

Figure 3.25 GUI of C# for spectra capture.

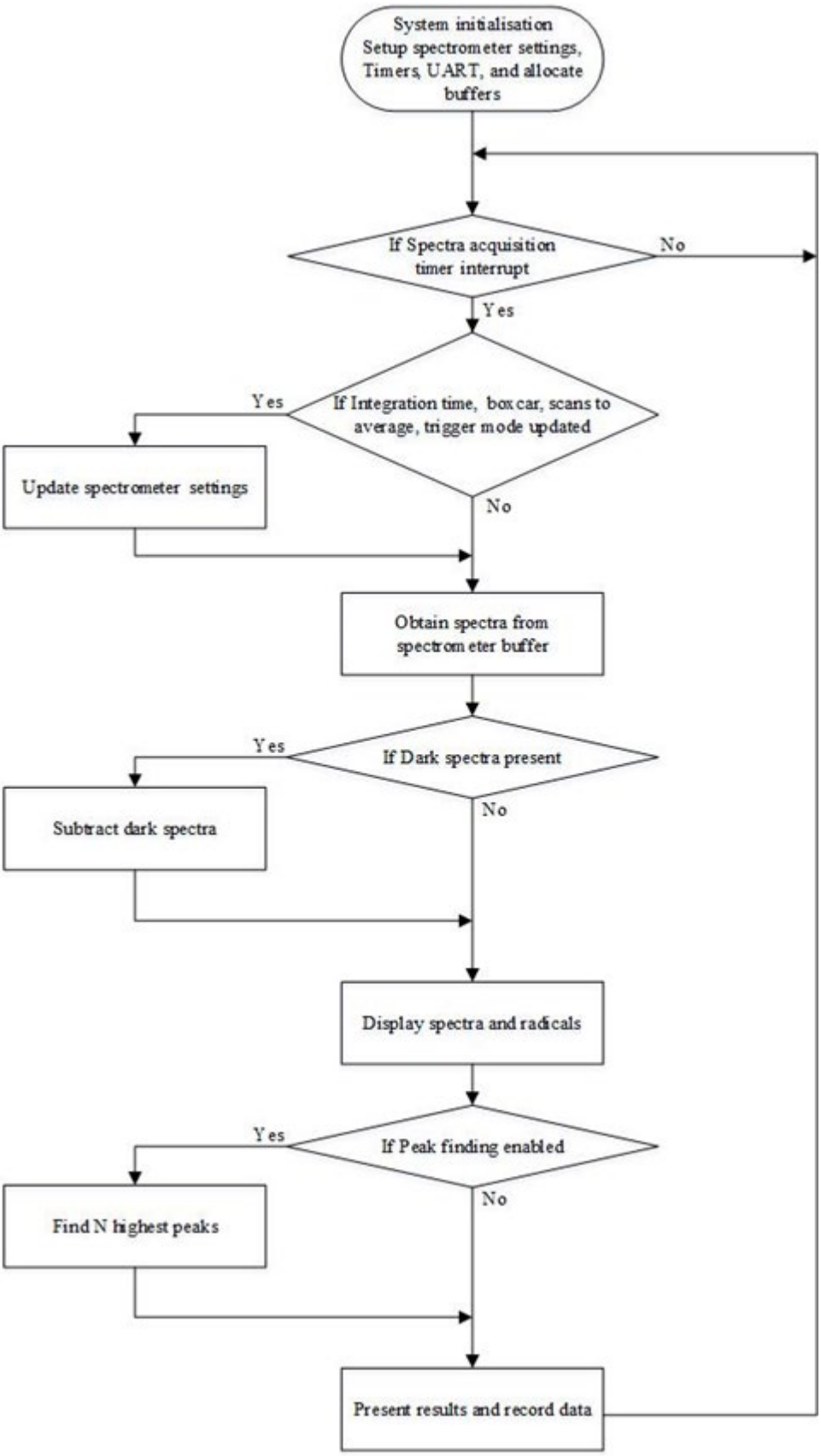

Figure 3.26 Flowchart of C# for spectra capture.

3.2.6.2 Thermocouple Measurement Software

Figure 3.27 presents the flowchart of the Arduino software allocated to run on the microcontroller and monitor the temperature of the probe through the thermocouple and send a signal to the alarm if the probe temperature is above 65 °C.

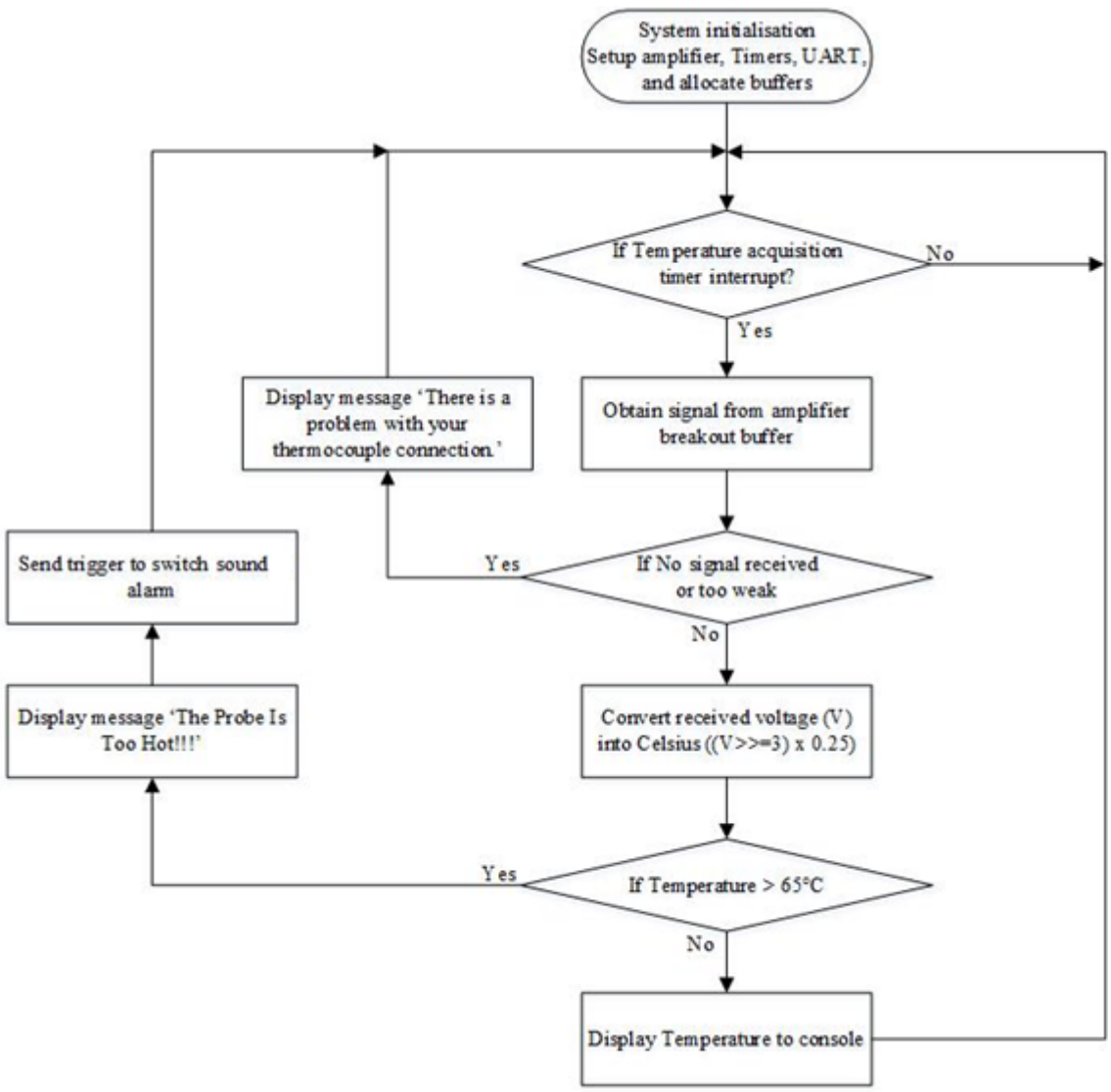

Figure 3.27 Flowchart of the Arduino program for the thermocouple.

3.3 System Implementation

3.3.1 Light transmission subsystem

Figure 3.28 is the overview of the integrated probe which was finally fabricated. The probe head was carefully made to ensure that the three sensing parts [i.e., the rigid optical probe (for flame imaging); optical fibre (for spectrometer); and thermocouple (for probe temperature monitoring)] being secured within the probe head and enveloped in the single stainless steel tube. It ensures that the flame information is collected through the digital camera and spectrometer concurrently from the same perspective which is essential for the real-time analysis of all the flame parameters.

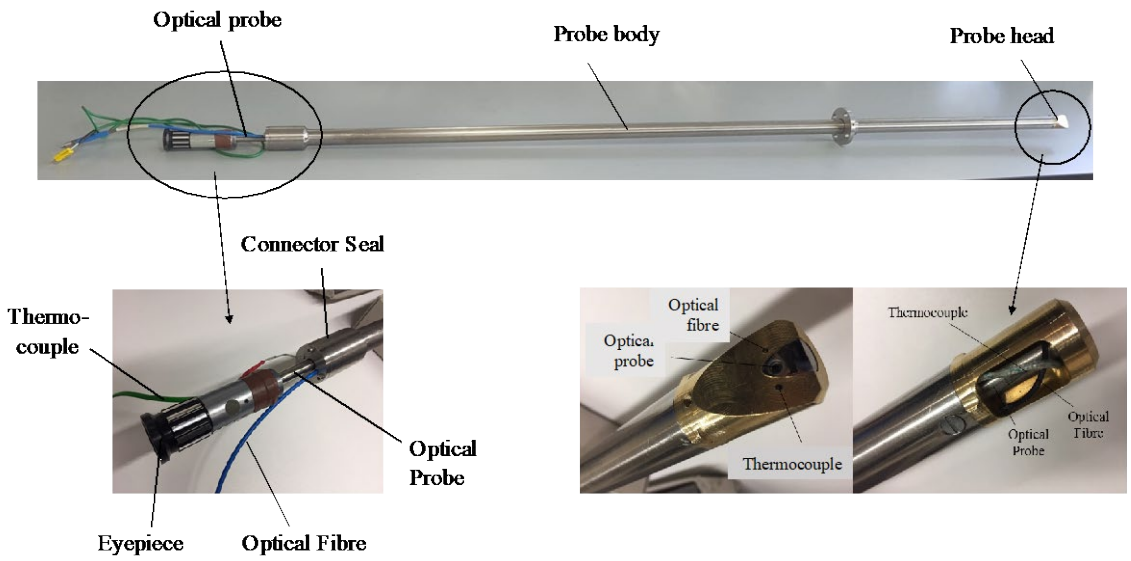

Figure 3.28 The complete integrated probe (including the optical probe, optical fibre and thermocouple).

3.3.2 Sensing and Computing Subsystem

The fabricated and assembled camera housing can be seen in Figure 3.29, which was implemented based the design as given in section 3.2.3. All the components are placed securely within a single cased aluminium enclosure with an IP rate of 65.

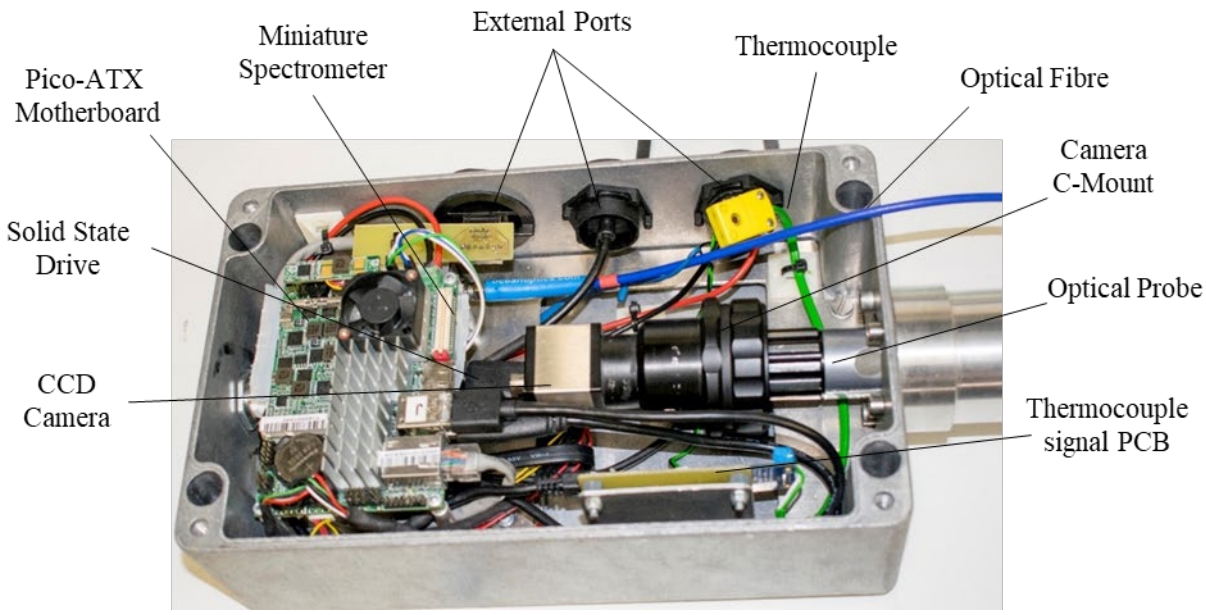

Figure 3.29 Overview of the complete camera/spectrometer house.

Figure 3.30 shows the final fabricated single layer custom PCB and its integration into the camera housing. It can be seen that the PCB has been fitted to an aluminium mounting bracket and then to the camera housing itself to ensure that the construction is stable and secure during industrial use. The microcontroller is powered through USB 2.0 from the embedded pico-ITX LP-173 motherboard.

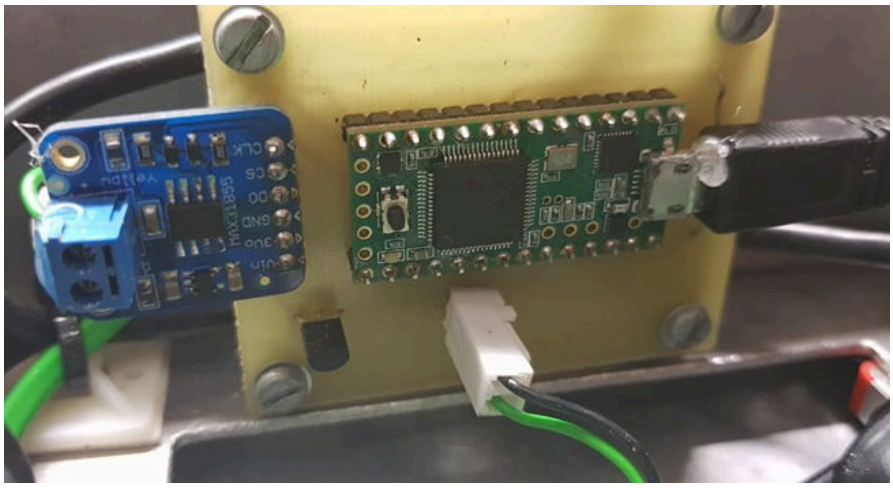

Figure 3.30 Layout of the custom thermocouple PCB.

3.3.3 Cooling Jacket

The cooling jacket was fabricated and assembled based on the design as described in section 3.2.4. The complete jacket is shown in Figure 3.31. The jacket was fitted with a supporting/sealing flange in order to connect the exiting flange of the viewport on the boiler. The ball valve was also attached to the back of the jacket. After the completion of the fabrication, the jacket was taken of a leakage test before it was transported to the site for the installation.

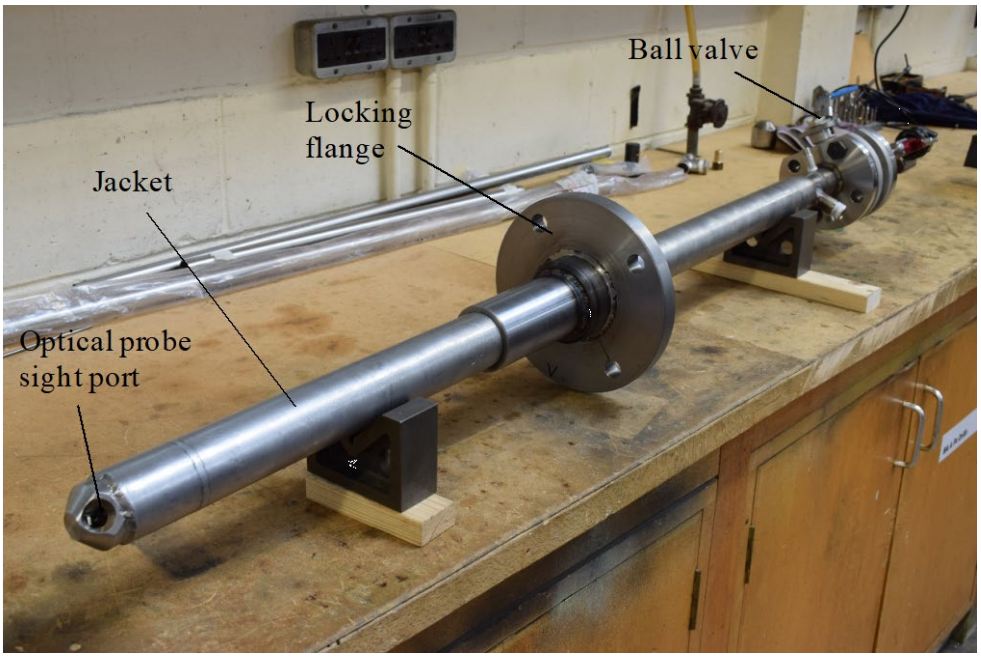

(a) Complete assembly of the cooling jacket.

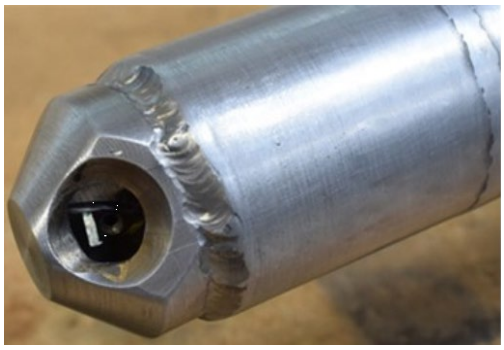

(b) Close up of the view window

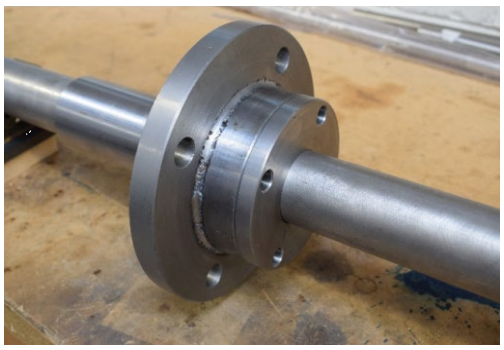

(c) Supporting/sealing flange (to be attached the existing flange of the boiler)

Figure 3.31 Complete assembly of the cooling jacket (including the supporting/sealing flange and isolation ball valve).

3.3.4 Water/air flow Control Subsystem

Figure 3.32 illustrates the layout of the water/air flow control subsystem which was constructed based on the design detailed in Section 3.2.5. All components for water/air flows metering and flow/temperature failure alarms, as well as the power supply are enclosed in an off-shelf steel cabinet, preventing from dust. The water flow and temperature alarms were fixed in the top of the cabinet, giving the best warning sign if any fault event occurs. The power supply was enclosed in an IP65 rated casted aluminium enclosure, providing electrical power to the camera house, water flow sensor and alarms.

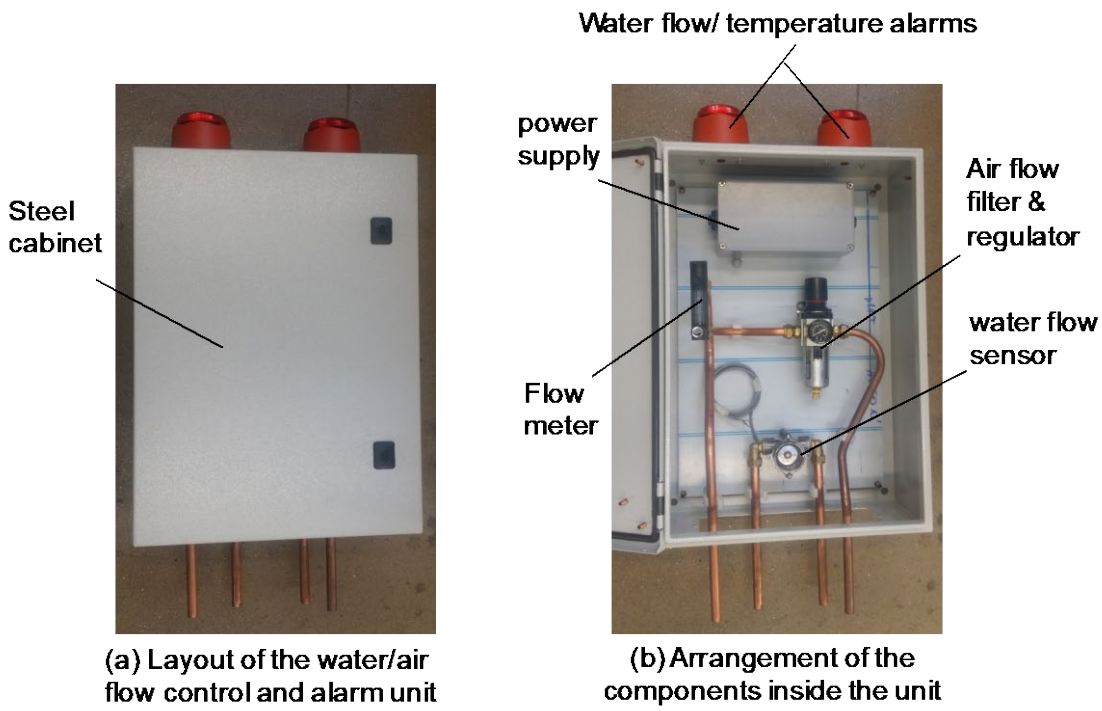

Figure 3.32 Layout of water/air flow control subsystem.

3.4 Summary

A digital RGB camera and a miniature spectrometer have been built into an effective housing suitable for industrial use in order to derive a number of flame parameters including geometric and luminous parameters, temperature and its distribution, oscillation frequency, overall flame spectral information, and the spectral characteristics related to the key flame radicals such as CH^* (432 nm) and C_2^* (568 nm).

The instrumentation system specifically designed for the safe and effective monitoring of the flames in an industrial boiler has been designed and implemented. Great efforts have been made to ensure that the custom-built system is suitable for this industrial installation, including the construction of an integrated probe to house the optical transmission elements. The design and fabrication of the water cooling jacket and its water/air flow control and alarm have also been made to protect the probe from intense temperatures.

System software has also been developed to aid in the online and offline measurements of the flame parameters, using automation to assist in the collection of good quality flame images and complete spectra. For this to be feasible, settings such as exposure time, integration time, gains and different resolutions have been added. Software was also developed to monitor the online temperature of the probe to ensure that the working temperature is never exceeded.

Chapter 4

Theories of Flame Characterisation and Emission Prediction

4.1 Introduction

This chapter presents the detailed theories which are used in flame monitoring and characterisation, and the emission (NO_x) prediction in this research programme. The premise of these theories and relevant techniques have already been discussed (Chapter 2), but now a detailed approach will be taken to explain how and why these processes have been conducted.

Firstly, the chapter presents algorithms for flame image processing and measurement, covering the following topics:

- Separating flame regions within a multi-burner flame image and determining the flame boundary and area.
- Measurement principles of flame temperature and oscillation frequency.
- Transformation of HSI (Hue, Saturation, Intensity) colour space.

Secondly, the feature extraction of the spectral parameters and spectral analysis techniques, covering:

- Processing of flame spectra to remove noises from blackbody radiation and dark current of the CCD sensor.
- Analysis of the spectroscopic characteristics of flame radical species.

Finally, the theory of machine learning algorithms used for NO_x prediction is given, specifically covering ANN (Artificial Neural Network).

4.2 Pre-processing of Flame Images and Spectra

4.2.1 Basic of a Flame Digital Image

A 2-D monochrome flame image can be represented by a luminous intensity function of each colour channel *g(x, y)*, where the value of *r* represents the luminosity of that channel at the point *(x, y)*. If *g* is continuous, it can be approximately transferred into discrete form of $\mathbb{N} \times \mathbb{M}$ matrix, *G*, through a digitisation process, i.e.,

$$G = \begin{pmatrix} B_{00} & B_{01} & \dots & B_{0(\mathbb{M}-1)} \\ B_{10} & B_{11} & \dots & B_{1(\mathbb{M}-1)} \\ \vdots & \vdots & \vdots & \vdots \\ B_{(\mathbb{N}-1)0} & B_{(\mathbb{N}-1)1} & \cdots & B_{(\mathbb{N}-1)(\mathbb{M}-1)} \end{pmatrix} \tag{4-1}$$

where B_{ij} is the greyscale, i.e., grey-level, at the row of I ($0 \leq i < \mathbb{N}$) and the column of j ($0 \leq j < \mathbb{M}$). In an 8-bit digitising system B_{ij} varies from 0 (black) to 255 (bright white). Therefore, the digital image of the flame can be expressed as a matrix of digital numbers each represented by a finite number of bits. The image is typically composed of a number of non-divisible image elements, called pixels. The grey-level of each pixel represents the luminous intensity, i.e., the brightness of the correspondent area in the image. Obviously, the pixels representing the luminous region of a flame have higher grey-levels than those outside the luminous region. The total quantity of the grey-levels depends upon the number of bits a digitising system provides.

A 2-D RGB (Red, Green, Blue) flame image can therefore be represented by three of these grey-scale matrices, each corresponding to a colour channel (i.e., R, G, or B) overlapping each other. Three 8-bit channels of RGB data, also called 24-bit "colour depth" supplies up to 16.7 million possible colour combinations ($256 \times 256 \times 256$).

A binary flame image can also be described as the same matrix. However, rather than expressing the pixel values in a grey-scale form, the image is only represented in single 1-bit form, i.e., a pixel within a binary image is represented only by 0 (black) or 1 (bright white).

It must be stressed that the 2-D image of a 3-D object, such as a flame, by directly photographing has an inherent limitation due to the superposition effects along the line-of-sight at each pixel. Information along the optical path at each pixel within the flame will not be spatially resolvable. However, this information is analogous to those that occur with most techniques used for measuring 3-D flow fields (shadowgraping and schlieren imaging, for example), does not affect the statistical properties of the flame [93]. However, such an image comprehends quantitative information about geometrical and luminous profiles over the entire flame region. Of course, to investigate the spatially resolved characteristics of a flame, the multiple views of the flame using tomographic reconstruction techniques have to be utilised [94].

4.2.2 Image Segmentation

When analysing the images and thus the characteristic parameters of flames in a multi-burner combustion system, such as British Sugar's boiler, it is important to distinguish between the flames of different burners where possible, as this will give a much more precise analysis of the boiler performance. An effective method is required for separating the flame regions of individual burners in the images captured by the flame image system before the characteristics parameters (e.g., temperature, area and HSI characteristics) are computed. The procedures are described below.

Firstly, contiguous regions are detected within the binary image, all sections equalling to '1' are assigned to a different region. Once all regions within the image are detected, they are assigned a bounding box (defined as the smallest rectangle containing the region) and centroid (defined as the centre of mass of the bounding box). If a region of grey-level pixels is smaller than a determined threshold, they are deemed to be the broken sections of one of the main burner flames. These are then assigned to either of the burner flames based on the bounding box and the centroid. Figure 4.1 illustrates the bounding box (green) and centroid (red) for a discontinuous region (pixels in white). Once only the number of regions matching the number of visible burners determined remain (either contiguous or dis contiguous), individual binary images are masked containing only that flame region. Figure 4.2 shows a typical output of these masked binary images. Once the masked images containing only data from a single flame, the images are treated as two unique samples from which, the geometric and luminous parameters are extracted. The definitions of these parameters are given in Section 4.3.

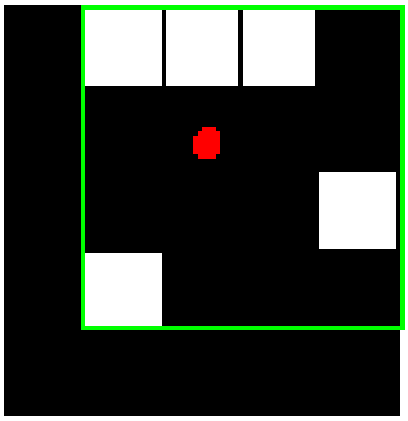

Figure 4.1 Illustration of the bounding box and centroid of a binary image.

Figure 4.2 Typical images of multi-burner flames and their separation.

4.2.3 Flame Spectra

Flame spectral signals can be represented similarly to that of a flame image but with only one dimension instead of two. A luminous intensity is a function of each wavelength $\lambda(x)$, where the value of λ represents the intensity of that wavelength (x). If λ is continuous, it can also be approximately transferred into discrete form of vector, λ, through a digitisation process, i.e.,

$$\lambda = \left(B_0 \;\; B_1, \; \ldots, \;\; B_{(V-1)}\right), \tag{4-2}$$

where B_i is the intensity, i.e., counts, at the wavelength λ_i. In an 11-bit digitising system B_i varies from 0 (no light) to 2048 (saturated light). Therefore, the digitalised spectral signal of the flame can be expressed as a vector of digital numbers, each represented by a finite number of bits.

4.3 Characteristic Parameters of a Flame

Since a flame is the variation of its characteristic parameters, it is natural to consider using these parameters as an indication of burner condition. A number of flame characteristic parameters can be extracted through digital imaging and image processing techniques, such as flame area, temperature distribution and oscillation frequency. Furthermore, the flame spectra and production of radical emissions such as OH^*, CN^*, CH^* and C_2^* can be monitored through the use of a spectrometer. These parameters characterise a flame in terms of its nature of geometry, luminance, and thermodynamics.

4.3.1 Flame Area

Flame area, *A* (pixels), is computed from a binary image using an appropriate threshold to determine the outer contour of the flame region within the image matrix. The area is then the total number of pixels within the flame region, *R*, defined by the outer contour. i.e.,

$$A = \sum_{i=1} 1, \quad i \in R. \tag{4-3}$$

With the known geometric relationship between the optical probe and the flame, the flame area in pixels can be easily converted and presented with absolute dimensions. The flame area is then isolated when performing all other measurements to ensure that only the flame is being processed to eliminate noise and light reflections within the furnace.

4.3.2 Flame Temperature

In the present study, the flame temperature is computed based on the relationship between two primary colours of the images captured by an RGB camera, known as the two-colour method which is widely used to measure the temperature of sooting flames the emissivity of which is unknown. Since the fundamental aspects of the two-colour method were comprehensively discussed elsewhere [40, 94], only a brief introduction and how it is implemented in this study is given below.

The flame image system developed uses an RGB camera to generate three separate images of the flame through the three channels corresponding to primary colours Red (R), Green (G) and Blue (B) (Section 4.3.4.1). The transient temperature distribution of the flame is calculated from the ratios of grey-levels pixel by pixel within the coloured banded R, G and B images.

In this study, the R and G colour channels are represented with the central wavelengths of 620 nm and 540 nm, respectively, these were chosen for the temperature calculation instead of other combinations (e.g., R and B, or G and B) as these two channels give a better signal-to-noise ratio due to the higher spectral sensitivities found in these channels. The flame temperature is thus computed by using [40].

$$T = \frac{C_2\left(\frac{1}{\lambda_G} - \frac{1}{\lambda_R}\right)}{ln\left(\frac{G(\lambda_R, T)}{G(\lambda_G, T)}\right) + ln\left(\frac{S_{\lambda_R}}{S_{\lambda_G}}\right) + ln\left(\frac{\lambda_R}{\lambda_G}\right)^5} \tag{4-4}$$

where T is the soot (solid particles) temperature inside the flame, C_2 is the second Planck's constant 1.438777×10^{-2}; $G(\lambda_R, T)$ and $G(\lambda_G, T)$ are the grey intensities of images from the R and G channels, respectively, λ_R and λ_G are the peak wavelengths of the R and G channels, and are 620 nm and 540 nm and $S_{\lambda R}/S_{\lambda}$ refers to the instrument factor, determined through a calibration procedure using a standard temperature source (Section 4.4.1).

4.3.3 Flame Oscillation Frequency

Within the present study, a digital camera with a high-speed capability is incorporated into the system (Section 3.2.3.1) such that the images of the flame can be captured at a frame rate up to 900 fps. These images are then converted into a continuous 1D signal that contains geometric and luminous information of the flame. The PSD (Power Spectral Density) estimates are then performed through the FFT (Fast Fourier Transform) [96] i.e.,

$$P_n(f) = \frac{1}{N}\left|\sum_{N=0}^{N=-1} x_N(n)e^{-j2\pi f_n}\right|^2 = \frac{1}{N}|X_n(f)|^2, \tag{4-6}$$

where, P_n is the power density of the n_{th} frequency component, $X_N(f)$ is the Fourier Transform of N-point sampling data sequence $x_N(n)$ of the flicker signal. N is the total number of frequency components.

It was suggested that the PSD estimates of the flame radiation signal are linked to the flame stability and various frequency components are present in the radiation signal [20]. The low frequency components and a low oscillation frequency are attributed to the geometrical fluctuations of the flame due to aerodynamic or the effects of heat transfer. A high amplitude within these low components can be indicative of an unstable flame [96]. The high frequency components are closer linked to the production rate of the reacting species or flame radicals and therefore reflect kinetic variations in the heat release. The DC component (mean amplitude of the waveform) is believed to depend on the volatility of the fuel, the size of the flame, and the intensity of the surrounding blackbody radiation.

It has previously been documented that a premixed flame contains multiple dominant frequencies and extends over a wide range ofhigher frequencies. Whereas, A diffusion flame appears to have a single dominant frequency and takes on a relatively lower frequency range. Therefore to obtain a quantitative oscillation frequency from the PSD estimates, the signal must be computed in such a way that factors in the weightings of the frequency across the entire available spectrum, to ensure no flame data is missed. It is therefore defined as the power-density-weighted average frequency [96], i.e.,

$$F = \frac{\sum_{n=1}^{N}[P_n(f_n)\times f_n]}{\sum_{n=1}^{N} P_n(f_n)}, \tag{4-7}$$

where, F is the weighted power spectral density, f_n is the n^{th} frequency component, P_n is the power density of the i^{th} frequency component and N is the total number of frequency components.

4.3.4 Colour Characteristics

4.3.4.1 RGB Space

It is known that flame light emission is closely related to the flame colour [97, 98] and that an RGB camera outputs images in the RGB model which functions similarly to that of the human eye. The additive RGB colour model is created by mixing three primaries (Red, Green and Blue) in specific proportions to produce a vast various of colours. This colour model is the most commonly used in modern day. The images captured by an RGB camera are composed of three layers also known as channels corresponding to Red, Green and Blue primaries. As shown in Figure 4.3, these three channels are each represented as a coordinate for each pixel within the image. When describing the Red channel, it does not necessarily refer to a colour we might represent as red, but perhaps hints of red or a reddish colour. As depicted in Figure 4.3 The range for each individual channel is 0-255, therefore 24-bit RGB can encode 256×256×256 or a total of 16,777,216 colours Figure 4.4 demonstrates an RGB image taken of a flower and the images separated into R, G, and B individual channels.

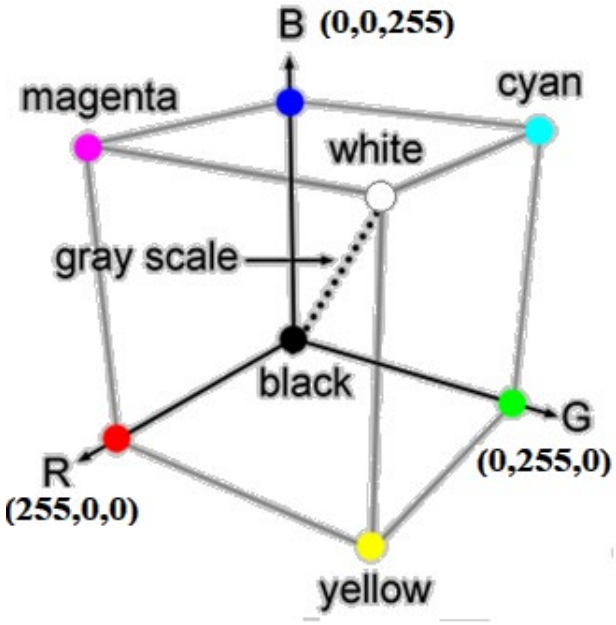

Figure 4.3 Visual representation of the RGB colour space [99].

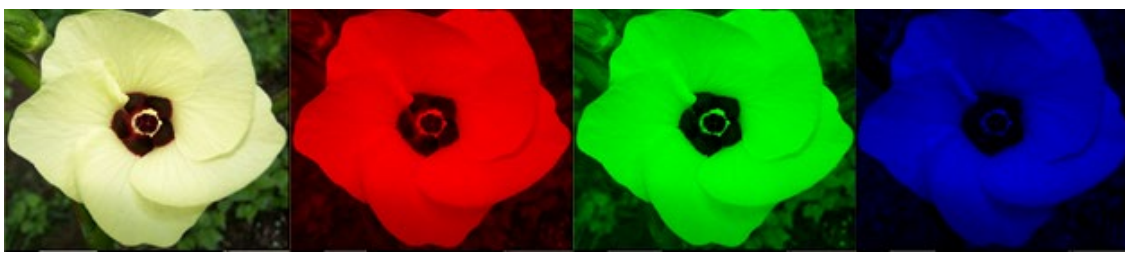

(a) RGB (b) R (c) G (d) B

Figure 4.4 An original RGB image separated into the R, G and B channels.

Whilst the RGB images useful for colour display, they are good enough for colour analysis due to the high correlation among R, G, and B components [100]. In the RGB colour space, the colour and intensity are inseparably stored in the three primary colour components. When the intensity changes, all the three components will change accordingly.

4.3.4.2 HSI Space

The HSI model is another commonly used colour space in image processing, which separates the colour information of an image from its intensity information. Similar to the RGB model, the HSI model has three separate channels, corresponding to Hue (H), Saturation (S), and Intensity (I). The H component represents the dominant wavelength in the spectral distribution of light wavelengths, indicating basic colours. The S component is the measure of the purity of the colour, denoting the amount of white light mixed with the hue. The I component is determined by the amount of light, describing the brightness of an image. The HSI model is described geometrically in Figure 4.5 [101].

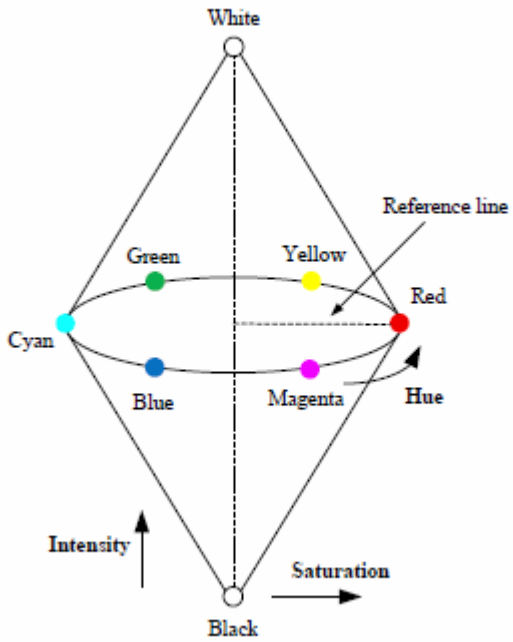

Figure 4.5 Relationship between RGB and HSI [101].

As can be seen in Figure 4.5, H is described in the form of an angle around the centre point. H ranges from 0° to 360°, in this example, Red is 0°, Yellow is 60°, Green is 120°, and Magenta is 300°, and therefore the H value is normalised by 360°. S is represented by the perpendicular distance from the colour point to the axis in the range [0, 1] with the darker colour depicted further away from the centre point. The intensity component (I) is the height of the colour point in the axis direction, ranging from 0 (black) to 1 (white).

An image in the RGB can easily be converted to the HIS space using the following transformation [9]:

$$H = \begin{cases} cos^{-1}\left\{\dfrac{\frac{1}{2}[(R-G)+(R-B)]}{[(R-G)^2-(R-B)(G-B)]^{\frac{1}{2}}}\right\}/360° & \text{if B} \leq \text{G} \\ 1 - cos^{-1}\left\{\dfrac{\frac{1}{2}[(R-G)+(R-B)]}{[(R-G)^2-(R-B)(G-B)]^{\frac{1}{2}}}\right\}/360° & \text{if B} > \text{G} \end{cases} \tag{4-8}$$

$$S = 1 - \frac{3}{R+G+B}[min(R,G,B)] \tag{4-9}$$

$$I = \frac{R+G+B}{3}. \tag{4-10}$$

Figure 4.6 demonstrates the three H, S and I channels once an RGB image is converted into the HIS space, displaying information of the image that could not be seen in the RGB form or any of its individual RGB channels.

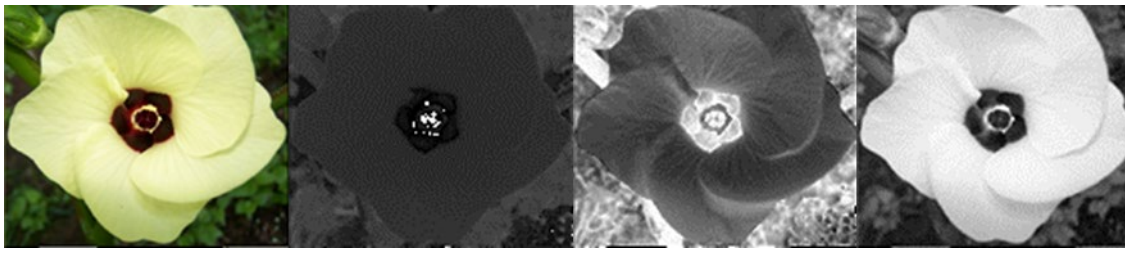

(a) RGB (b) H (c) S (d) I

Figure 4.6 An original RGB image separated into the separated H, S and I channels.

4.3.5 Flame Spectra

4.3.5.1 Relative Irradiance

The light of flame collected by the spectrometer includes information about the flame spectroscopic characteristics across the spectral range that can be detected by the spectrometer. To remove background information from the furnace and to see the true characteristics of the flame spectra, relative irradiance can be performed on the signal received. The relative irradiance is much more flexible than another technique, i.e., absolute irradiance, which requires much stricter calibration techniques that may not be suitable for an industrial environment. For the relative irradiance computation, the dark current of the spectrometer and the blackbody radiation are firstly removed using a blackbody furnace as a blackbody radiation reference[102] (also refer to section 4.4.1), i.e.,

$$\text{Rel Irr}(\lambda) = Norm\ \ B(\lambda)\left(\frac{S(\lambda) - D(\lambda)}{R(\lambda) - D(\lambda)}\right) \tag{4-11}$$

$$B(\lambda) = \frac{2\,h\,c^2}{\lambda^5\, e^{\frac{h\,c}{\lambda\,k\,T_c}} - 1} \tag{4-12}$$

where, $B(\lambda)$ is the theoretical reference of blackbody radiation, $S(\lambda)$ is the sample spectrum (counts), $D(\lambda)$ is the Dark spectrum (counts), $R(\lambda)$ is the Reference light source spectrum (counts), $Norm$ is the normalising term to bound into the range 0-1, h is Planck's First constant (J s), c is the speed of light (m/s), k is the Boltzmann's constant joule's per kelvin (J/K^{-1}) and T_c is the colour temperature of the reference light source (K).

Figure 4.7 shows the radiation spectra of a blackbody for a range of temperatures in the range of 100 K to 10000 K. There are several important features that should be notes. Firstly, the emitted radiation varies continuously with wavelength. Secondly, for the temperature range 1000 K~3000 K, the emitted radiation increases significantly with wavelength in the visible region, i.e. the rate of change of spectral radiance with respect to wavelength, in the visible region is higher than in the infrared region. Finally, for a temperature 1000 K~3000 K, the magnitude of the emitted radiation in the visible region increases significantly with temperature, i.e. the rate of change of spectral radiance with temperature, in the visible region is also greater than that in the infrared region.

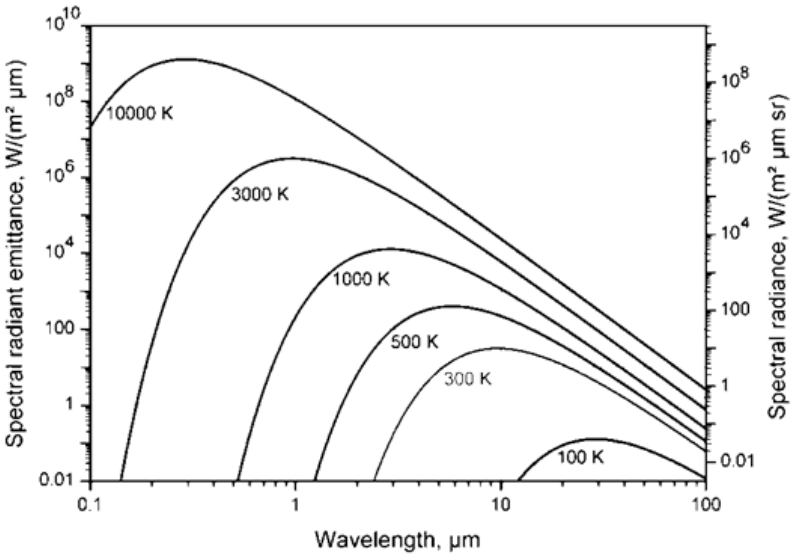

Figure 4.7 Emitted radiation and the temperature of a blackbody [103].

4.3.5.2 Flame Radicals

Electronically excited species formed by thermal excitation and chemical reactions, such as OH^*, CN^*, CH^*, C_2^* are known as flame radicals. The production of these excited species takes place during the combustion process, and is directly related to the location of flame reaction zones, giving detailed analysis of the heat release pattern. This study will focus on the radicals produced during the prompt and thermal NO_x formations in order to predict the NO_x production.

The radiative intensity of free radicals OH^* (308 nm), CN^* (350 nm), CH^* (400/432 nm) and the well documented C_2^* Swan bands (430-600 nm) [36, 83, 104–106], the C_2^* Swan band was the focus of this study, as it is easily obtainable within the visible region. UV signals can be obtained through a high integration time of the spectrometer. The overall intensity of the signal can be used very effectively to gain insight into the state of the flame under different combustion conditions. Figure 4.8. illustrates the production of

these flame radicals and their corresponding wavelengths, measured with an Ocean Optics spectrometer with similar specifications to the one used in this study under combustion conditions within the laboratory environment.

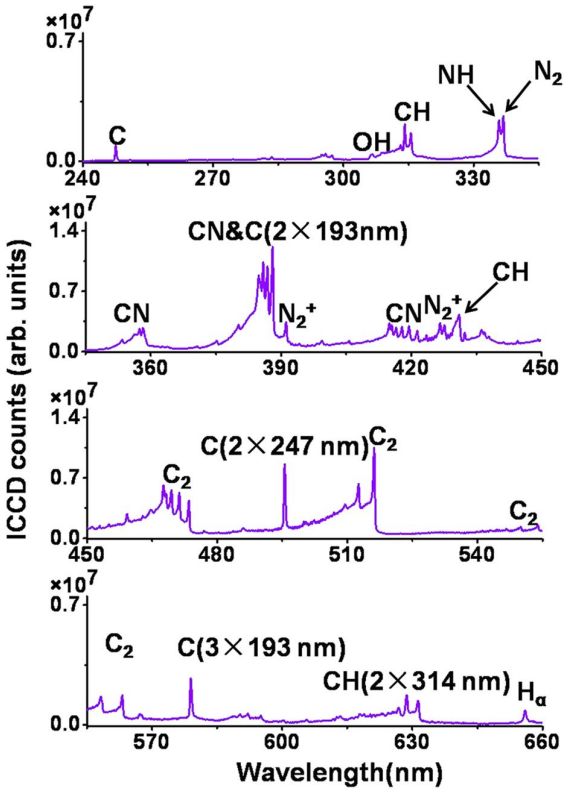

Figure 4.8 Filament-induced nonlinear spectra of a n-pentanol-air flame on an alcohol burner in the spectral range of 240–660 nm [42].

4.4 System Calibration and Evaluation

4.4.1 Calibration for Temperature Measurement

In order to calibrate the temperature readings of the system, the instrument factor, $\frac{S_{\lambda_R}}{S_{\lambda_G}}$, in eq (4-4) needs to be determined using a blackbody furnace as a standard temperature source, as shown in Figure 4.9, to reproduce the geometrical relationship between the

imaging system and the flame to be measured. The blackbody furnace has a working temperature range from 500 to 1500 °C, emissivity of 0.99, and a temperature stability of ±0.33 °C/10 min [107]. Further information on the temperature calibration can be found elsewhere [3].

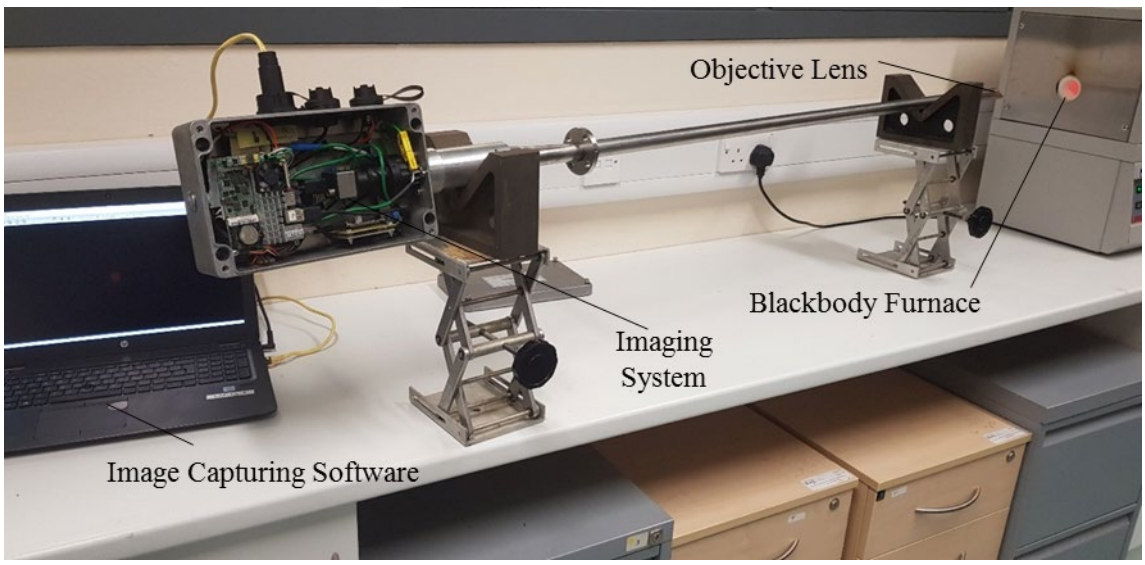

Figure 4.9 Experimental set-up for the system calibration of temperature measurement.

Figure 4.10 shows the example images over the temperatures range as given in Table 4.1. It should be noted that none of the images contain any under or over exposure. Once these images were captured, they were first cropped to eliminate the gradient area of the outer ring of the blackbody port, and then the average grey-level ratio of the red and green channel was obtained for this area. This ratio is then used to calculate the instrument factor (4-13).

Table 4.1 Blackbody temperature settings for system calibration and assessment.

Temperature settings of blackbody furnace (°C)	Used for Instrument Factor calibration	Used to assess the temperature measurement
1000	✓	
1050		✓
1100	✓	
1150		✓
1200	✓	
1250		✓
1300	✓	
1350		✓
1400	✓	
1450		✓
1500	✓	

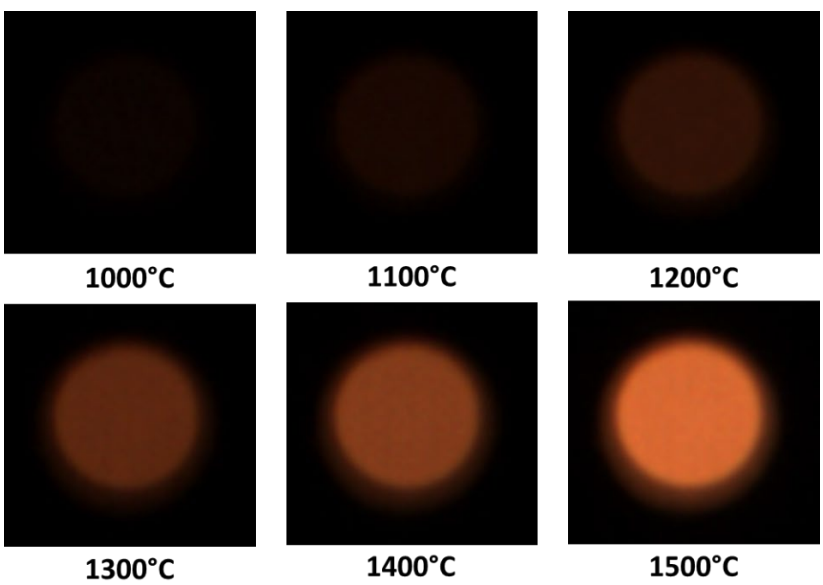

Figure 4.10 Example images of the blackbody furnace at different temperatures.

The values of grey-level ratio obtained for every second temperature reading are used to compute the instrument factor using a polynomial equation (4-13).

$$S = 0.309 \times \left(\frac{R}{G}\right)^2 - 1.123 \times \left(\frac{R}{G}\right) + 1.872 \tag{4-13}$$

The coefficients of this equation are then used with the greyscale ratio of the R and G channel to give then Instrument Factor to be substituted into equation 4-4. Figure 4.11 shows the results of the instrument factor plotted against the grey-level gained.

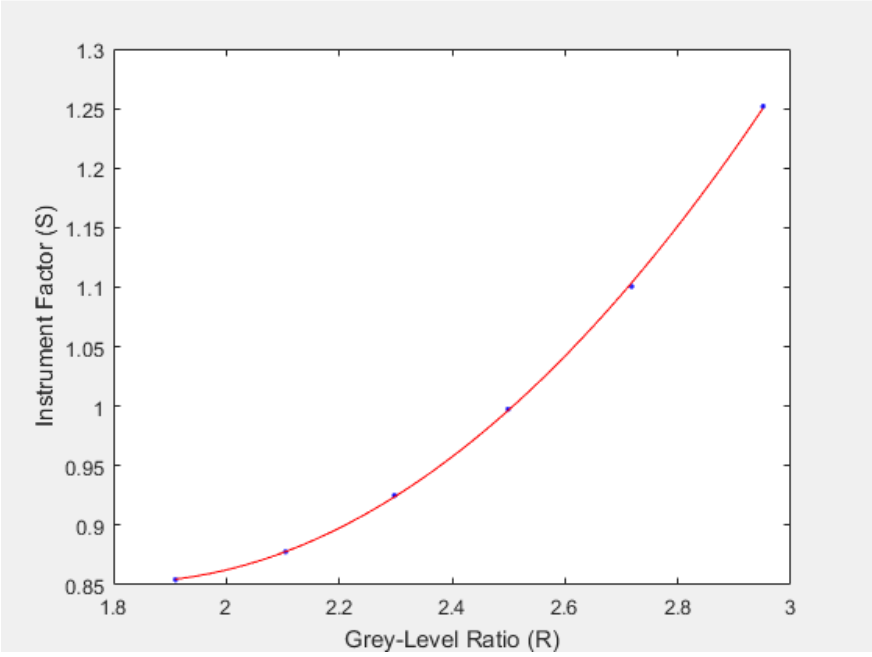

Figure 4.11 Instrument Factor against grey-level ratios.

Once the temperature from an image can be determined through this process, the known temperature of the blackbody furnace can be used to assess the accuracy of the system alternating temperatures such that the same temperatures used to calibrate the system are not used for the assessment (Table 4.1). The maximum relative error is found to be 1.2% at 1350 °C, as shown in Figure 4.12, and the maximum standard deviation was 4.1 °C.

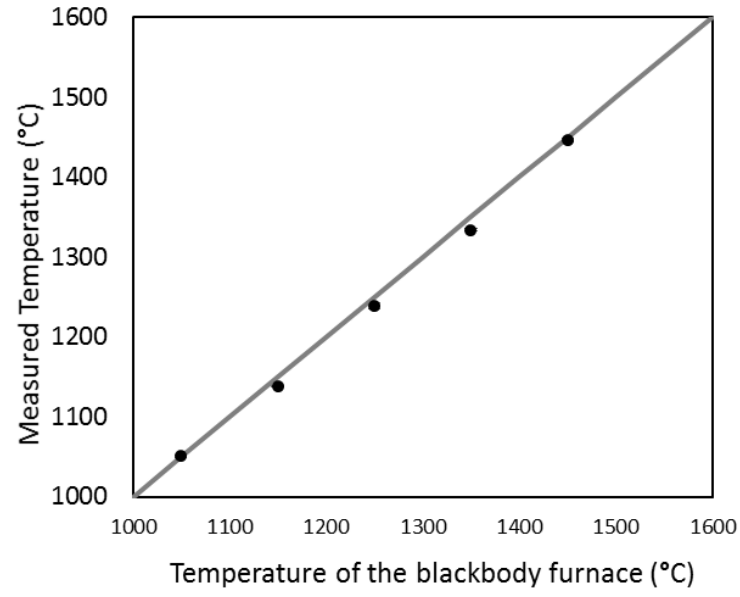

Figure 4.12 Blackbody setting temperature versus measured temperature.

4.4.2 Evaluation of Oscillation Frequency Measurement

Although the measuring of the flame oscillation frequency does not require a system calibration, it is important to ensure the measurement of the system is accurate. This was achieved in the lab test using a LED (light emitting diode) as an alternating light source, as shown in Figure 4.13. In the evaluation, the LED was powered by a signal generator which generated an oscillating signal with a frequency range from 50 Hz to 300 Hz.

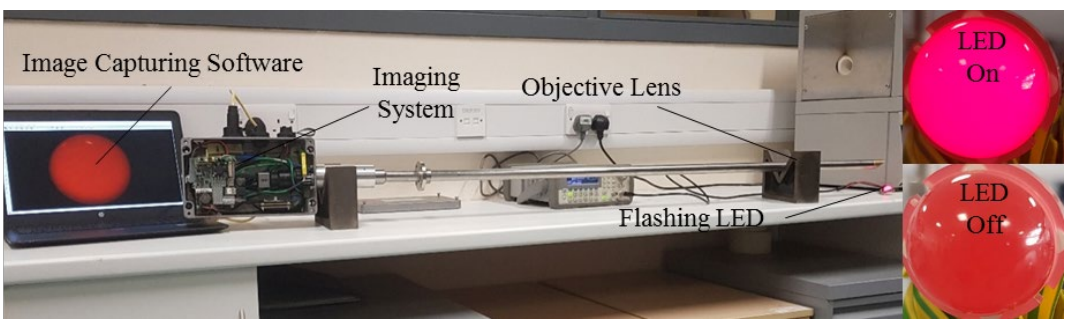

Figure 4.13 Experimental set-up for the evaluation of oscillation frequency measurement using an LED.

Figure 4.14 shows the example of the measured LED signal in the time domain whilst Figure 4.15 the PSD of the signal computed using (4-7). It is noted that the fluctuation of the signal in Figure 4.14 does not repeat perfectly continuously, with some delayed times turning on and off the LED due to electrical noise from the signal generator. This creates transient frequency components as shown in Figure 4.15.

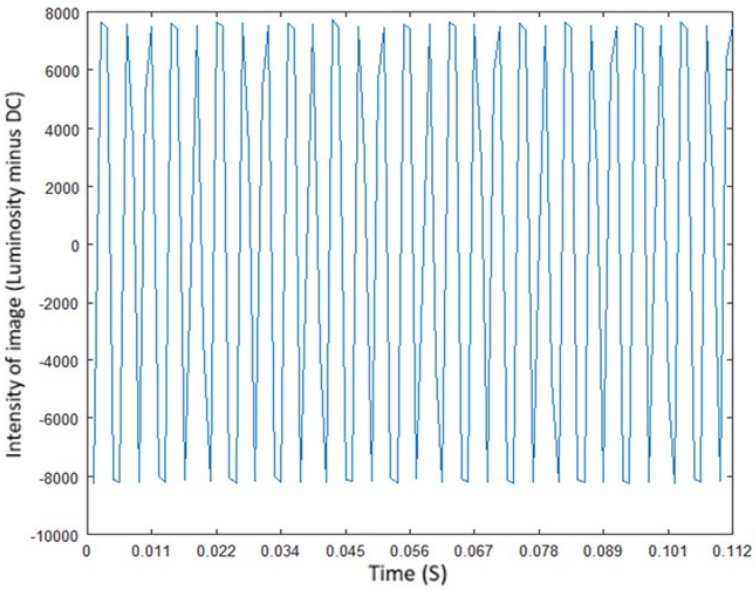

Figure 4.14 Processed signal in time domain for a 250 Hz LED.

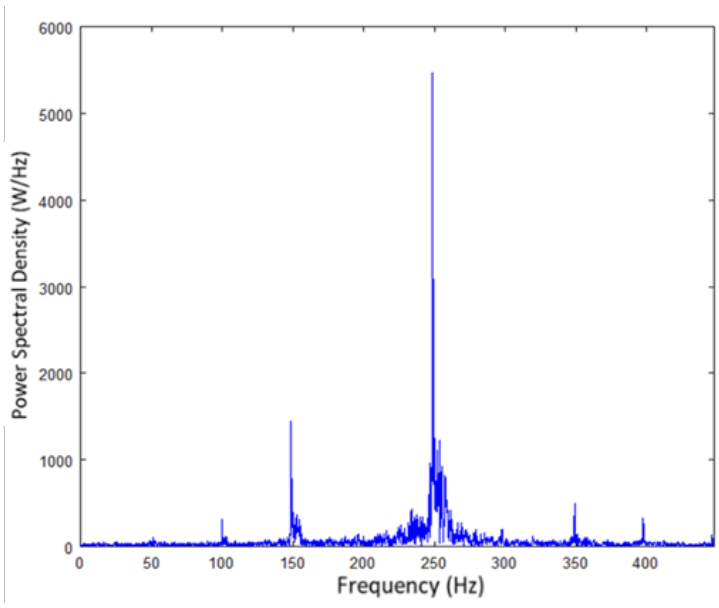

Figure 4.15 PSD signal for the LED signal as shown in Figure 4.14.

In the evaluation, the light of the LED was captured by the camera with the high-speed mode and the signal was processed based on the proposed method. Figure 4.16 gives the measured and reference frequencies for the LED signals. The relative errors of the oscillation frequency measurement have been found to have a maximum value of 0.93% at 50 Hz.

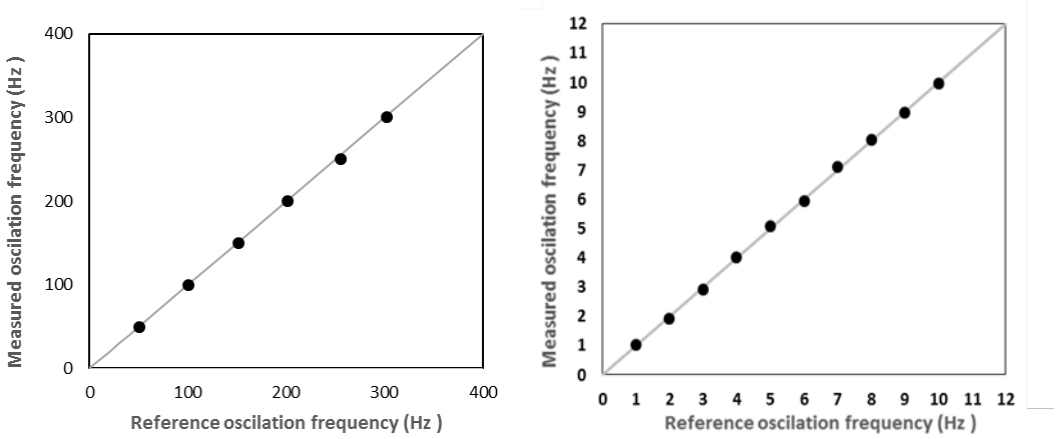

(a) frequency range 0-400 Hz (b) frequency range 0-12 Hz

Figure 4.16 Measured and reference frequencies for the LED signals.

4.5 Artificial Neural Network for NO_x Prediction

This section firstly gives the definitions of the machine learning techniques that are used in this study for the NO_x prediction, including the motivation and advantages. Then, it presents the theory of the artificial neural network (ANN) used for NO_x prediction.

ANN models are computing systems inspired by biological neural networks (a diagram of a typical neural network is shown in Figure 4.17). They are built as a framework for many different machine learning algorithms. Although there are many types of artificial neural networks, the basic concept often remains the same or similar. The data set enters

through the input layer as probabilistic signals, and converts them within the hidden layer corresponding to the biological neuron's axon and the weightings of the input. The network used in this present study is the Bayesian regularization backpropagation. Bayesian regularization was chosen to prevent overfitting in the model, and the backpropagation refers to the network feeding results of the estimations back into the process of learning in order to improve the performance of the model.

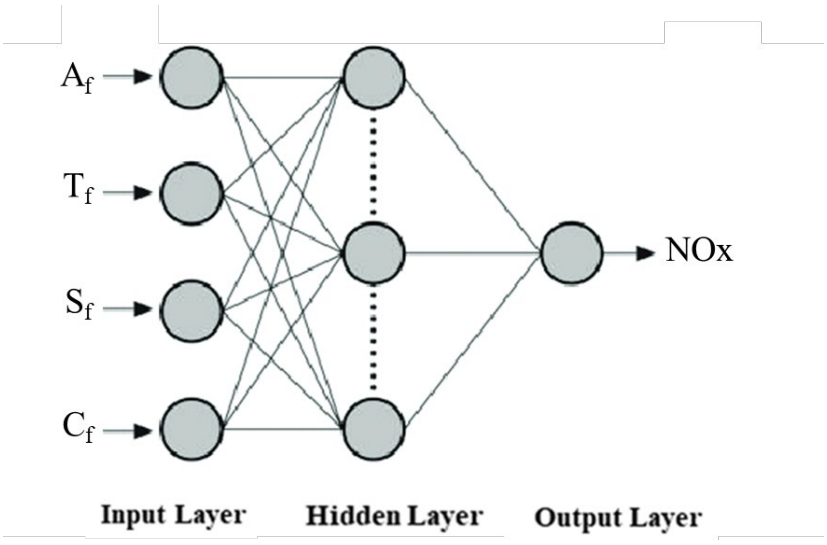

Figure 4.17 Structure of ANN for NO_x predication.

The Bayesian optimisation of the regularisation parameters requires the computation of the Gauss-Newton approximation to Hessian matrix of F(w) at the minimum point, where F is the regularized objective function and w is the weights [110]. The Levenberg-Marquardt algorithm framework is used with Bayesian regularization to reduce the computational overhead, typically, training aims to reduce the sum of squared errors $F=E_D$. However, regularisation also adds objective functions, and therefore, becomes,

$$F=\beta E_D+\alpha E_W, \tag{4-14}$$

where α and β are objective function parameters, and E_W, the sum of the squares of the network weights.

Therefore, if the training algorithm errors are smaller if $\alpha<<\beta$, and inverse accordingly there will be an emphasis on weight size reduction at the expense of network errors, thus a smoother network response will be produced.

Regularisation attempts to cut down computational time by making a selection of safe assumptions. Firstly, for example, the noise in the training set data and the prior distribution for the weights are both Gaussian.

Secondly, a uniform prior density $P(\alpha, \beta|M)$ for the regularization parameters α and β is assumed then the posterior density maximisation is achieved by maximizing the likelihood function P(D|α, β, M). where D represents the data set, M is the particular neural network model used.

The prior density expressed as $P(w \mid \alpha, M)$ denotes weights before any data is collected. The constants are either known or can be estimated, since the objective function has the shape of a quadratic in a small area surrounding a minimum point, F(w) is expanded where the gradient is zero.

For further information a comprehensive study of Bayesian optimisation and Gaussian processes can be found at [110] and [111] respectively.

For the purposes of this study the ANN model build and trained to predict the NO_x emissions of the furnaces incorporates four input parameters as follows: flame area; flame temperature; normalised average spectral intensity across the whole broadband of the miniature spectrometer and the normalised average peak value of wavelength 568 nm related to C_2^*, where chosen based on the repeatability data presented in 5.3 and 6.3. While the ANN model only has one output parameter, NO_x emission. The first step of building the ANN model is to scale the attributes of training data to fall in the range [-1, 1]. As the model constructed to be trained to predict NO_x with both data sets presented in this thesis during this study centre around Bayes' theorem, previous experiences have suggested that the data set can be made more efficient if proper scaling is performed. This scaling both avoids attributes with greater numeric ranges dominating those in smaller numeric range, and secondly avoids complications during the calculations. Once a scaling factor is selected for the training data, this factor should be used for any data further used as an input of this model.

For the regression problem (e.g., the prediction of NO_x), the Mean Square Error (MSE) and correlation coefficient are used to assess the quality of the trained model, i.e.,

$$MSE = \frac{1}{N}\sum_{i=1}^{N}(f(x_i) - y_i)^2 \tag{4-15}$$

$$r = \frac{N\left(\sum_{i=1}^{N} f(x_i)\, y_i\right) - \sum_{i=1}^{N} f(x_i)\ \sum_{i=1}^{N} y_i}{\sqrt{\left[N\, f(x_i)^2 - \left(\sum_{i=1}^{N} f(x_i)\right)^2\right]\left[N\ \sum_{i=1}^{N} {y_i}^2 - \left(\sum_{i=1}^{N} y_i\right)^2\right]}} \tag{4-16}$$

where $\{x_i, y_i\}$, $I = 1$ are the training data, and (X_i) is the predicted value of y_i.

4.6 Summary

This chapter firstly established the methodology for the characterisation and monitoring of the burner flame through the image processing and spectral analysis. Flame parameters including; flame area; brightness; temperature; oscillation frequency; and spectral properties, are defined and the methods of computing those parameters are established. Techniques for region segmentation over flame images, removing the blackbody radiation noise from flame radical spectral signals are also described in detail.

The performance of the oscillation frequency measurement of the system has been evaluated by using a standard frequency-varying light source. The relative error is no greater than 0.93% (frequency range: 50 Hz to 300 Hz). The accuracy of the temperature measurement has been verified by applying the system to measuring the true of a commercial blackbody. The maximum error of the temperature measurement of 0.76% occurred at 1225 °C. This same blackbody light source has also been used to remove background blackbody radiation from the signal and to relate the intensity of the industrial flame images to each other more systematically.

In addition, the machine learning techniques, specifically ANNs, for NO_x prediction are introduced, and the criteria for assessing the performance of the soft-computing models are established. The advantages of the Bayesian forms of ANN over other widely algorithms are the reduction of computational time (mainly the training time for construction of the models), and the ability to lean more heavily towards errors, therefore reducing the risk of overfitting.

Chapter 5

Industrial Trials on a 120 MW_{th} Gas-Fired Heat Recovery Boiler

5.1 Introduction

The instrumentation system and associated computational software were installed and tested on a 120 MW_{th} gas-fired heat recovery boiler at Wissington Factory, British Sugar. The objectives of the test were:

- to assess the performance of the flame imaging system as described in Chapter 3.
- to evaluate the effectiveness of the methods presented in Chapter 4, including; flame area, temperature, oscillation frequency, flame spectral analysis, and Artificial Neural Networks (ANN) based NO_x prediction.
- to investigate the characteristics of natural gas-fired flames under different burner settings.

Two different Gas Turbine (GT) loads were monitored during the tests. The GT loads were adjusted by varying the burner settings (i.e., Gun and Spud), as well as the flow rate of natural gas to the tested burners. The flue gas emissions, such as NO_x flue gas, were also acquired concurrently through the boiler data log system. It is understood that the burner settings affect the structure and stability of the flame. The instrumentation system and associated computational algorithms as described in Chapters 3 and 4 were employed to monitor these effects, and therefore gave insight into the operation of the boiler under different conditions. The effectiveness of the ANN for NO_x emission prediction are examined.

5.2 Experimental Set-up

5.2.1 Boiler Structure and System Installation

Figure 5.1 shows the structure of the test boiler and the location of the flame monitoring system. The boiler has four front-wall fired burners, each having a capacity of 30 MW_{th}. There are also viewports around the boiler house at four different levels. The viewport selected for the system installation is at the back-end of Burner 1 (Figure 5.1). This is considered to be the most suitable location of the measurement in terms of field of view (FOV) and working environment of the optical probe and fibre. From this viewport, the integrated probe and the cooling jacket were positioned perpendicularly to the burner axis, and 7 meters away from the front wall of the boiler. As described in Chapter 3, the probe has a tilted angle of 70°, which gives the best view of the primary regions of the flames.

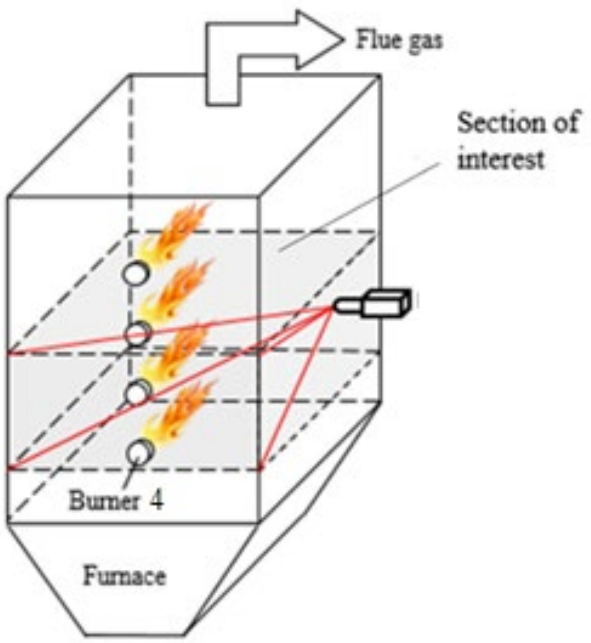

Figure 5.1 Schematic of the boiler structure and system installation.

Figure 5.2 illustrates the on-site installation of the flame imaging system where the cooling jacket was secured and sealed onto the supporting/sealing flange of the boiler. As described in Chapter 3, this design ensures that the integrated probe, as well as the instrumentation system, can be inserted and removed during the normal operation of the boiler which operates under a positive pressure.

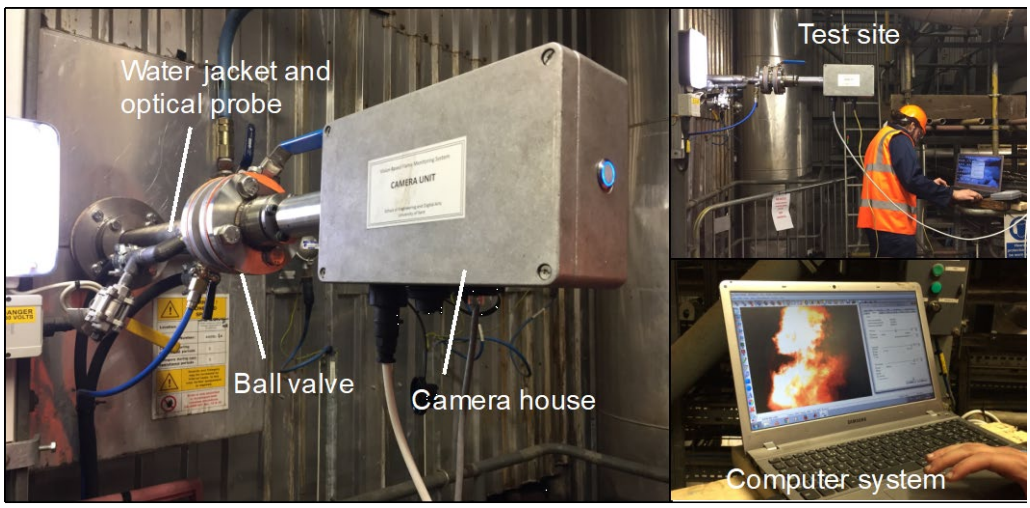

Figure 5.2 Site installation of the flame monitoring system.

Figure 5.3 shows the on-site cooling water and air supplies and control unit. A water chiller was purchased and installed especially for the operation of the image system. This ensures that, at all times, chilled water flows through the cooling jacket and maintains the working temperature below the maximum working temperature (below 70 °C) through the cooling water and air control unit.

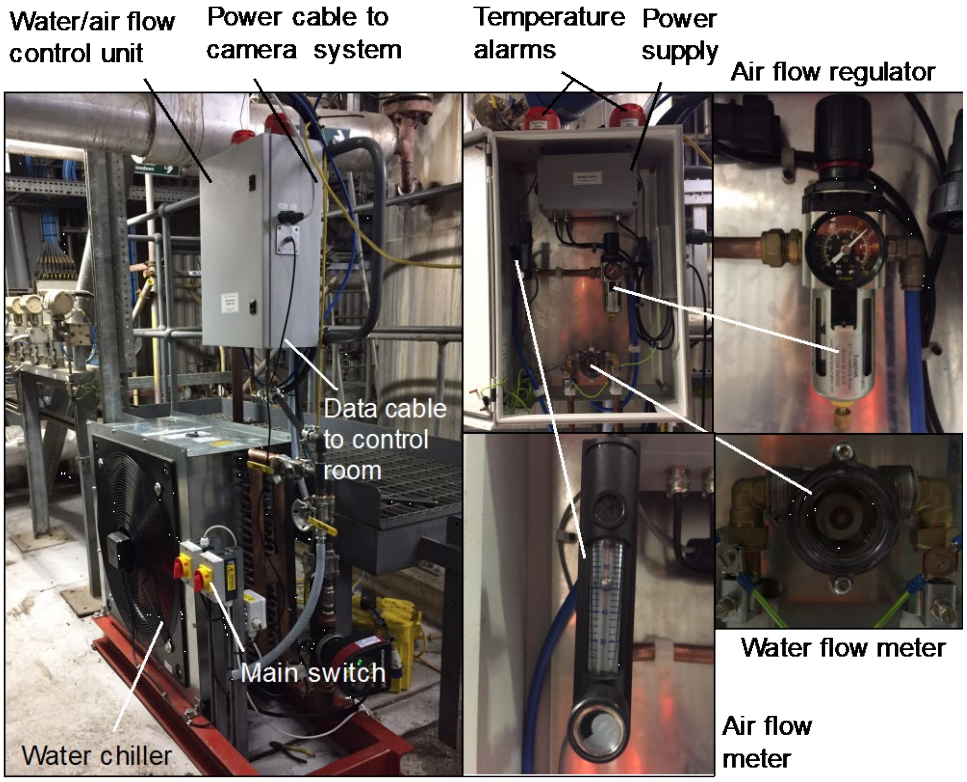

Figure 5.3 Site installation of the water/air flow control and alarm subsystem.

5.2.2 Test Programme

The setting of each individual burner was configured as Gun (at the centre, 10 MW_{th}) or Spuds (eight, allocated around the outer ring of the burner, 30 MW_{th} each) as illustrated in Figure 5.4, as well as two different GT outputs, i.e., 25 MW_{th} and 33 MW_{th}, giving a total of 16 test conditions. The Gun and Spud settings for all the 16 test conditions are summarised in Table 5.1 where 'G' means that only the Gun was ignited, and 'S' dictates that the eight Spuds were ignited. Note that these Spud burners cannot be ignited without the Gun.

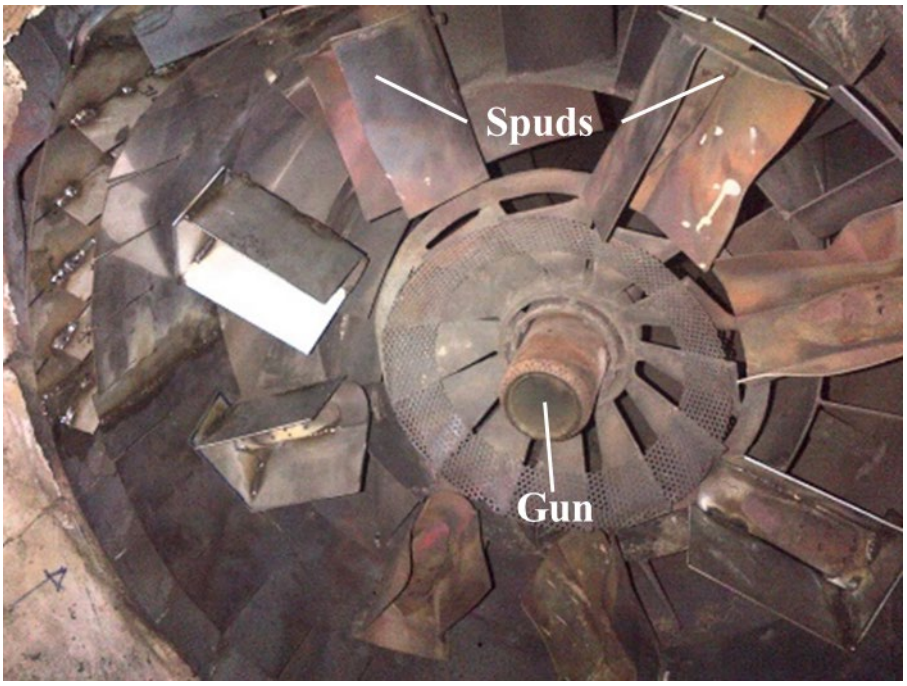

Figure 5.4 Burner structure including the locations of Gun and Spuds.

For each condition, a total of 240 flame images were acquired. The flame images captured were then processed for determining flame the parameters (i.e., area, temperature, and oscillation frequency). Integrated spectral intensity, peak spectra of key radicals (CH^*, CN^* and C_2^*) are also determined from the spectral data. The 240 processed data points were first averaged and then their standard deviation was calculated. To examine the repeatability of the imaging system and the ANN, two repeat tests were also carried out under each GT load and denoted with 'Rep X' in this chapter, so that the results of the repeat tests can be compared with the results of the experimentation under the same conditions.

Table 5.1 Test matrix.

Test No		**1**	**2**	**3**	**4**	**5**	**6**	**7**	**8**	**Rep*. 1**	**Rep*. 4**
GT load		33 MW_{th}									
Burner load	1	Not in use									
	2	*G*	*S*	*S*	*S*	*G*	*G*	*G*	*S*	*G*	*S*
	3	*S*	*S*	*G*	*G*	*S*	*G*	*G*	*S*	*S*	*G*
	4	*S*	*G*	*S*	*G*	*G*	*S*	*G*	*S*	*S*	*G*
Test No		**9**	**10**	**11**	**12**	**13**	**14**	**15**	**16**	**Rep.* 9**	**Rep.* 12**
GT load		25 MW_{th}									
Burner load	1	Not in use									
	2	*G*	*S*	*S*	*S*	*G*	*G*	*G*	*S*	*G*	*S*
	3	*S*	*S*	*G*	*G*	*S*	*G*	*G*	*S*	*S*	*G*
	4	*S*	*G*	*S*	*G*	*G*	*S*	*G*	*S*	*S*	*G*

Note: Rep.- Repeatability

Figures 5.5 and 5.6 show examples of the unprocessed flame images captured under the test conditions. The changes in the flame shape, size and brightness can already be seen across the different conditions. For instance, Flames under Test 5 (*G/S/G*) and Test 16 (*S/S/S*) show very bright regions in comparison to that under Test 8 (*S/S/S*) and Test 9 (*G/S/S*).

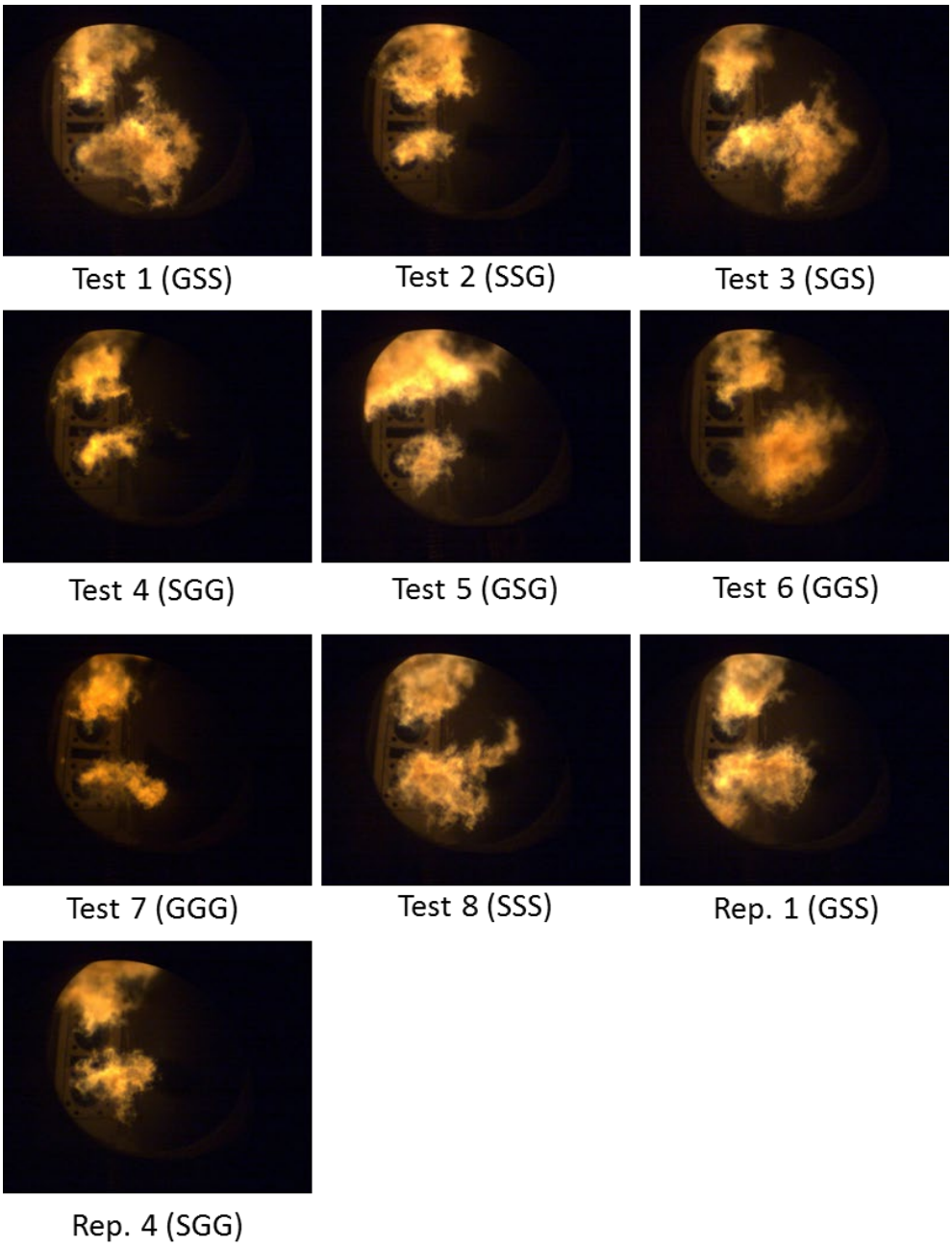

Figure 5.5 Example of unprocessed flame images for the GT load of 33 MW_{th}..

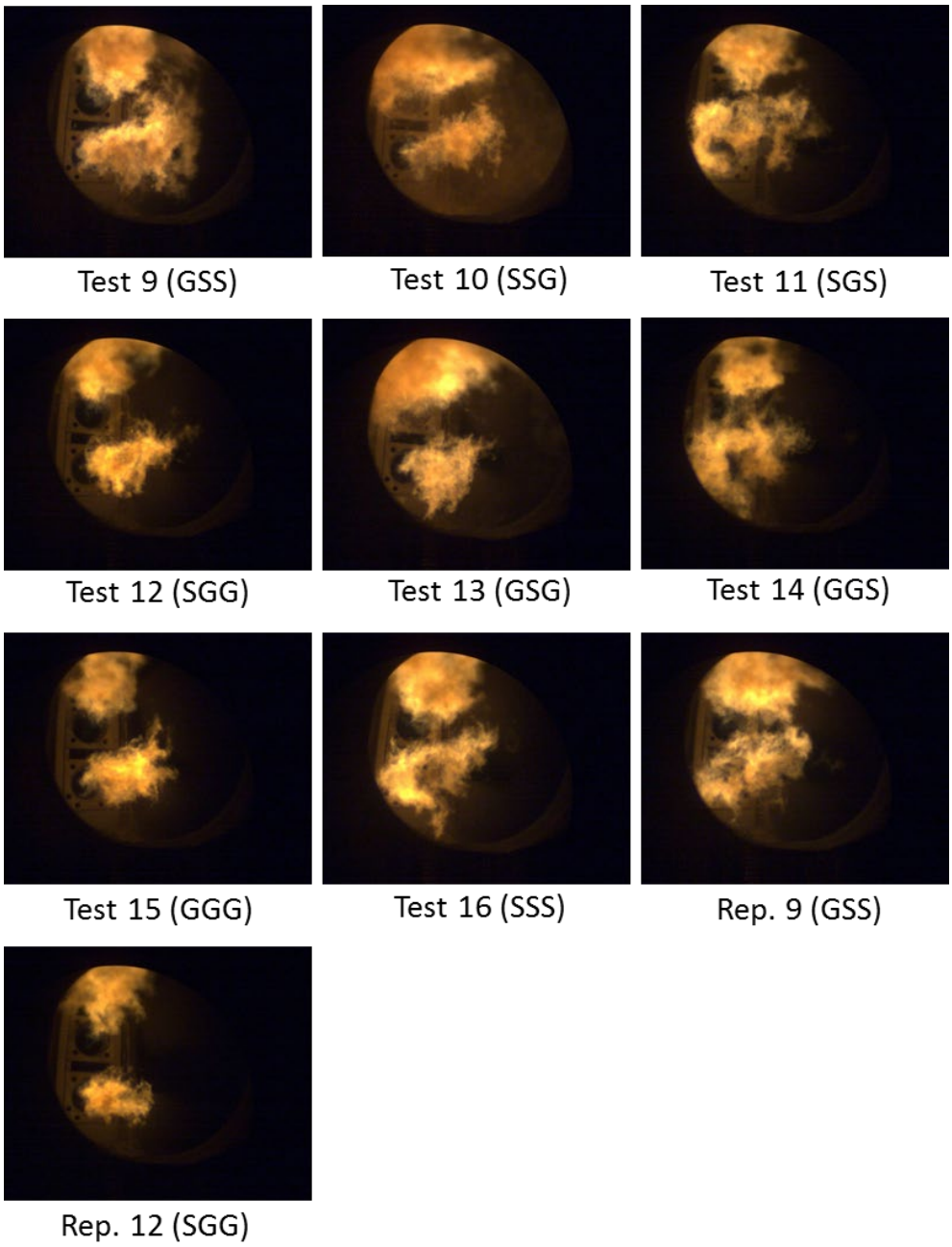

Figure 5.6 Example of unprocessed flame images for the GT load of 25 MW_{th}.

5.3 Results and Discussions

5.3.1 Repeatability Test

In order to examine the repeatability of the imaging system, two operation conditions were repeated for each GT load so that the flame measurement results can be compared under the same/similar test conditions for different operation times of the boiler. As shown in Table 5. 1, Rep. 1 (*G/S/S*) and Rep. 4 (*S/G/G*) are the repeated operations for Test 1 (*G/S/S*) and Test 4 (*S/G/G*) under the GT load of 33 MW_{th}. Rep. 9 (*G/S/S*) and Rep. 12 (*S/G/G*) are the repeated operations for Test 9 (*G/S/S*) and Test 12 (*S/G/G*) under the GT load of 25 MW_{th}.

Figures 5.7 and 5.8 show the flame parameters under repeated conditions for Burners 3 and 4 for the GT loads of 33 MW_{th} and 25 MW_{th}, respectively. More repeatable results were shown for the same boiler operation conditions under the GT loads of 33 MW_{th}, in comparison to the GT loads of 25 MW_{th}. Under the GT loads of 33 MW_{th}, the average flame temperatures at Burners 3 are 1741.2 °C and 1755.5 °C, respectively, for Test 1 and Rep. 1 (*G/S/S*), 1667.1 °C and 1671.4 °C, respectively, for Test 4 and Rep. 4 (*S/G/G*). Under the GT loads of 25 MW_{th}, in contrast, the average flame temperatures at Burners 3 are 1724.8 °C and 1745.4 °C, respectively, for Test 9 and Rep. 9 (*G/S/S*), and 1730.1 °C and 1704.5 °C, respectively, for Test 12 and Rep. 12 (*S/G/G*). Most notably, the flame temperatures have a standard deviation of 31.15 °C and 31.21 °C, respectively, for Test 12 and Rep 12 (*S/G/G*), and 16.19 °C and 18.48 °C, respectively, for Test 12 and Rep. 12 (*S/G/G*).

To compute the oscillation frequency of the flame, a 9-second video was captured for Burner 4 at the frame rate of 750 fps. The oscillation frequency of the flame was computed based on the method as introduced in Section 4.3.3. Figures 5.7(c) and 5.8(c) illustrate the flame oscillation frequency for Burner 4 under repeated conditions for the GT loads of 33 MW_{th} and 25 MW_{th}, respectively. It should also be mentioned, that due to the relative spatial resolution caused by the long observing distance of the optical probe to the burners (around 7 meters), the oscillation frequencies computed appear to be lower than expected. However, this is not a problem while comparing the oscillation frequencies of flames under different operation conditions. The average values of the oscillation frequency are once again less repeatable across the 25 MW_{th} conditions firstly showing repeatability with a frequency of 4.65 Hz and 5.18 Hz across Test 9 and Rep 9 (*G/S/S*), respectively.

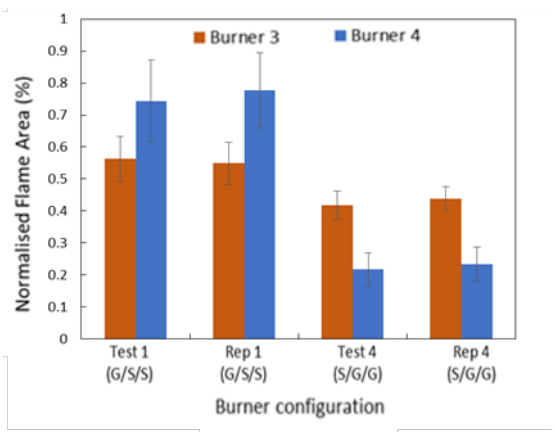

(a) Normalised flame area.

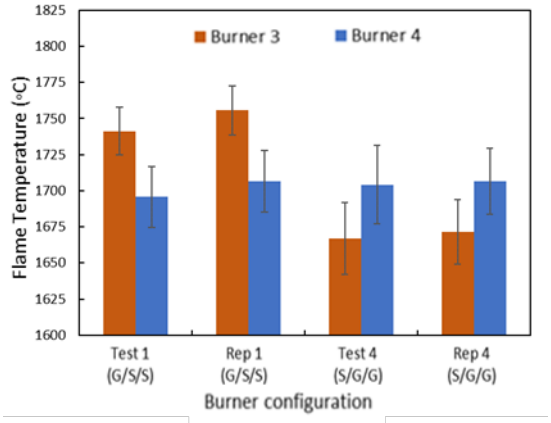

(b) Mean flame temperature.

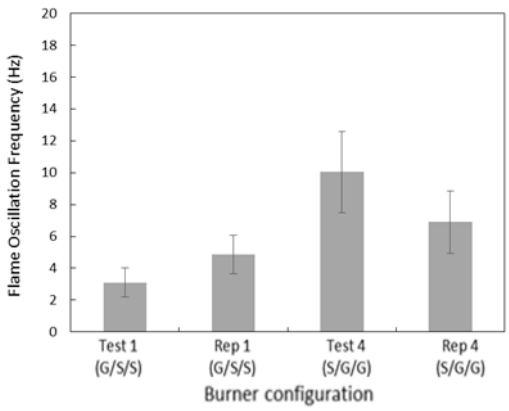

(c) Flame oscillation frequency.

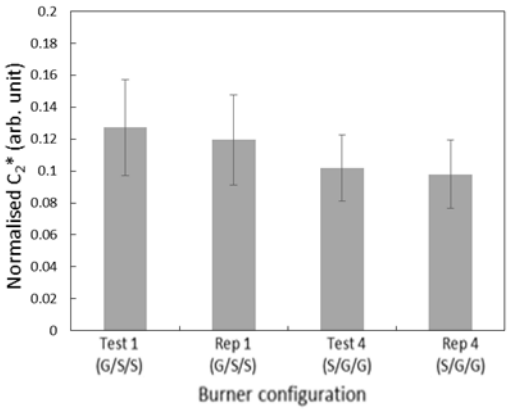

(d) Normalised C_2^*.

Figure 5.7 Flame parameters under the GT load of 33 MW_{th}.

The flame spectra taken from the furnace are normalised to a baseline signal taken from the boiler with the purpose of removing the background noise as well as the blackbody radiation from the boiler walls, such that the spectral distributions taken are only associated with the light of the flame. Full description of spectra normalisation is given in Section 4.3.5.1. The value from 240 data was taken and averaged and the standard deviation was calculated. Figures 5.7(d) and 5.8(c) also shows the variation of the intensity of radical C_2^* (568 nm), which was extracted from the normalised flame spectral data for the GT loads of 33 MW_{th} and 25 MW_{th}, respectively.

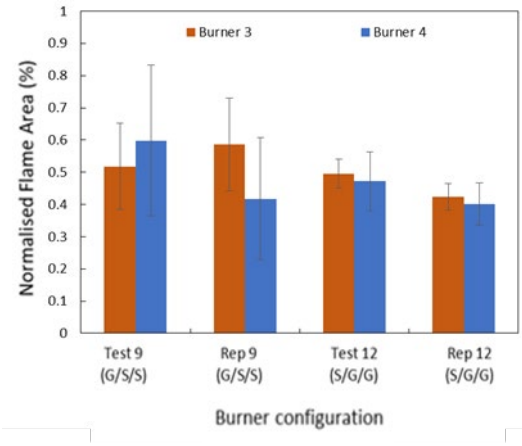

(a) Normalised flame area.

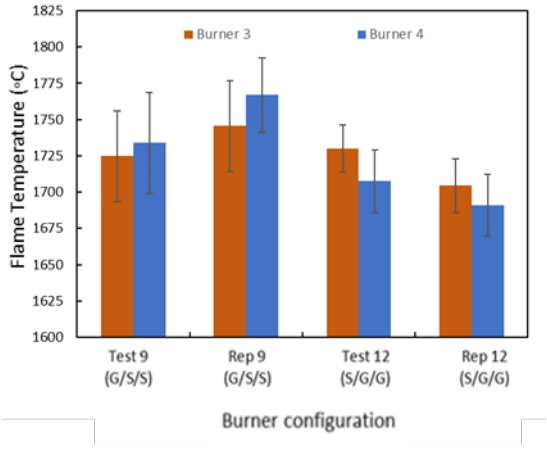

(b) Mean flame temperature.

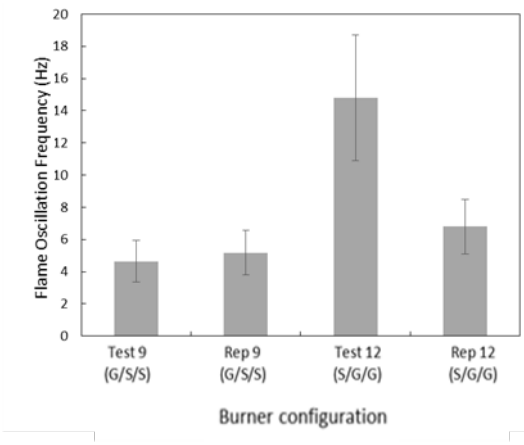

(c) Flame oscillation frequency.

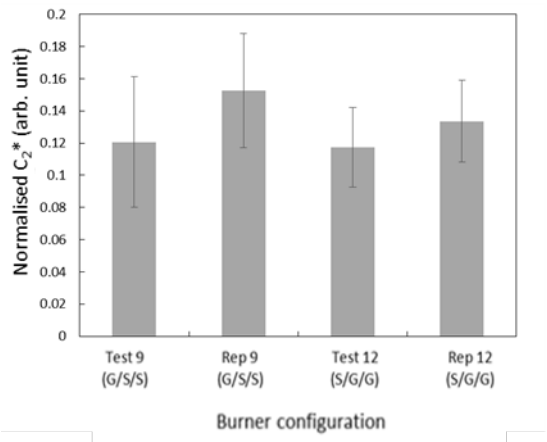

(d) Normalised C_2^*.

Figure 5.8 Flame parameters under the GT load of 25 MW_{th}.

5.3.2 Flame Characterisation

5.3.2.1 Flame Area

Figure 5.9 shows the binary images of flame area under the GT load of 33 MW_{th}, computed by applying global thresholds over the images in the HIS colour space with

setting: 0.213<H <0.927, 0.317<S<0.859 and 0.392<I<1.000. Figure 5.10 shows the binary images of flame area under the GT load of 25 MW_{th}, which were processed in the same way as the images presented for the 33 MW_{th} results on this occasion. However, the global image threshold was set to 0.4 rather than 0.24, as consistently the burner walls were brighter within these images. The areas were normalised by the maximum image area (i.e., 85000 pixels).

As can be seen from Figure 5.9, the flame area is affected significantly by the burner setting. This is particularly notable under Test 7 (*G/G/G*) and Test 8 (*S/S/S*) where even a visual inspection shows that the flame area has increased dramatically. Figure 5.10 also suggests that the flame area is much more similar over these testing conditions. For example, looking at Test 15 (*G/G/G*) and Test 16 (*S/S/S*), indicating that changing the burners between the Spuds and Gun has a much less significant effect on the flames under a low furnace load.

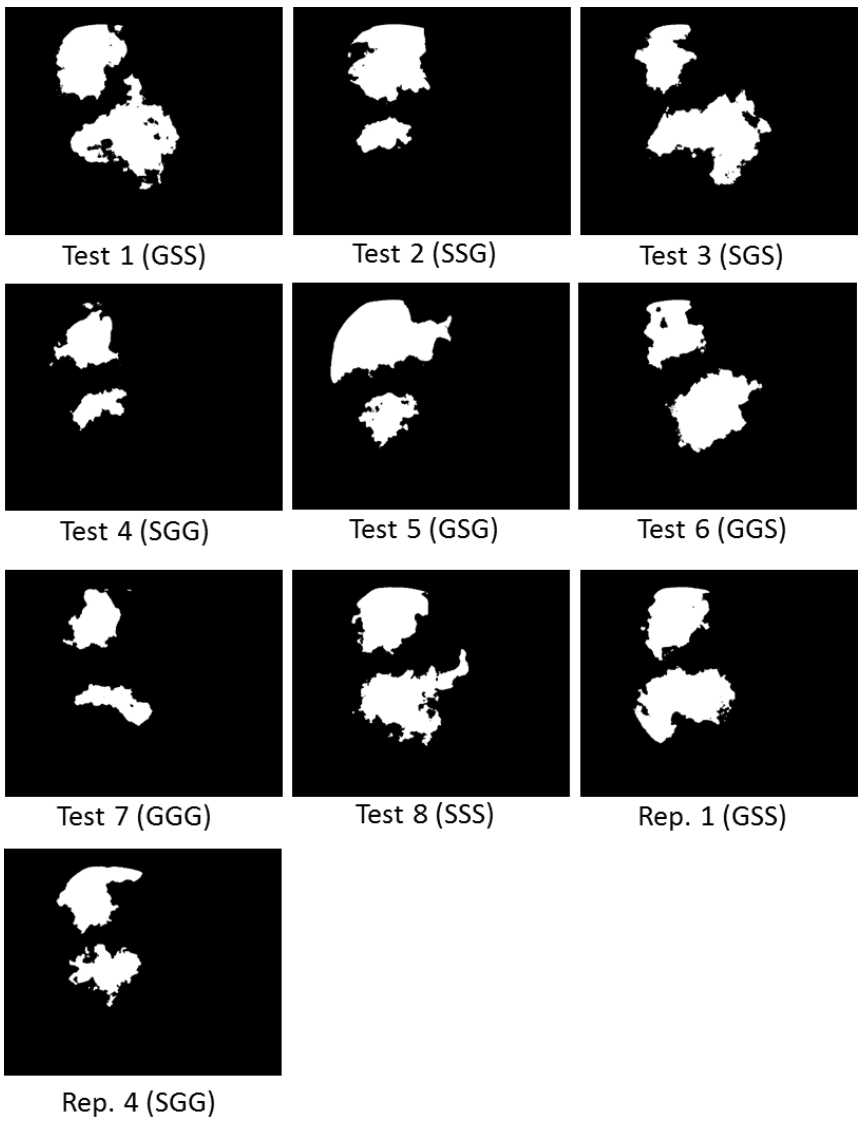

Figure 5.9 Flame area for different burner settings under the GT load of 33 MW_{th}.

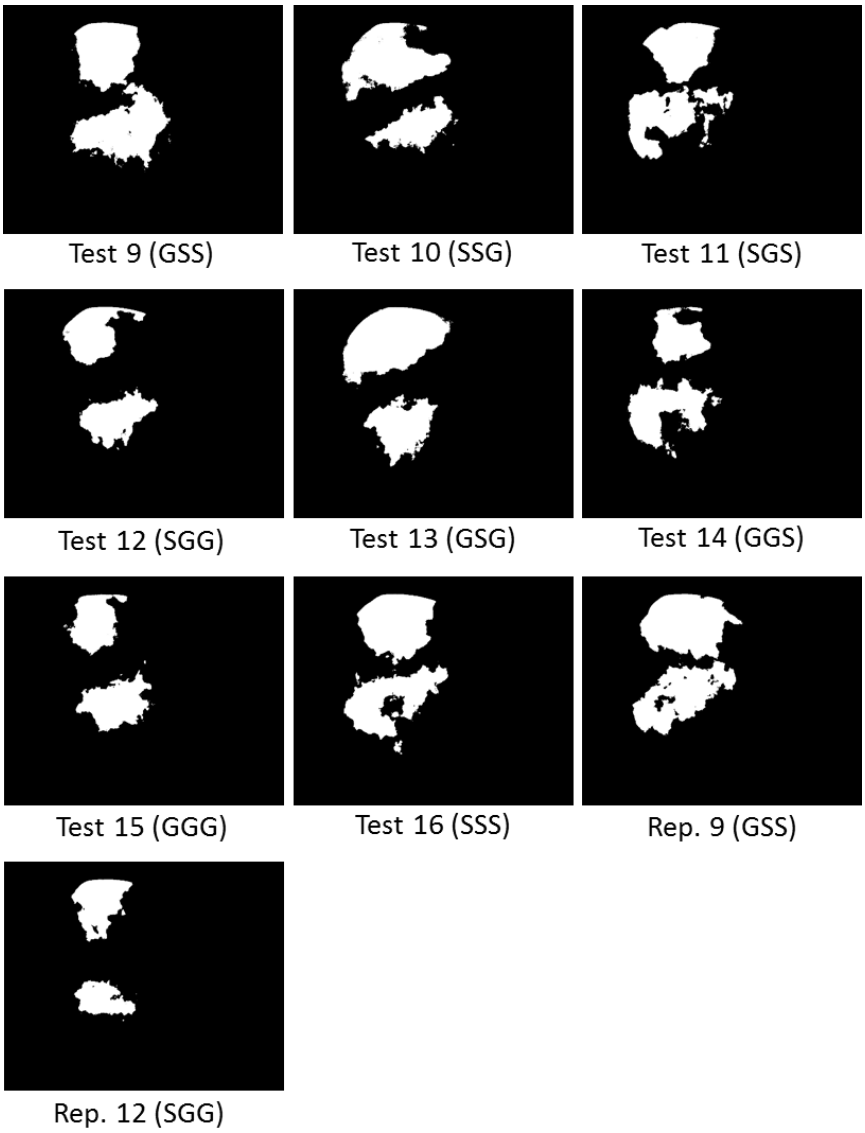

Figure 5.10 Flame area for different burner settings under the GT load of 25 MW_{th}.

Figure 5.11 shows the variation of flame area for different burner settings under the GT loads of 33 MW_{th} and 25 MW_{th}. An average value from 240 images was used in each data point and the standard deviations of the values are presented as error bars. It is noted from Figure 5.11(a), that Burner 3 has the smallest flame that occurs under Test 7 (*G/G/G*), with the averaged normalised flame area of 0.36, and the largest flame under Test 5 (*G/S/G*) with the averaged normalised flame area of 0.74. Burner 4 has the smallest flame in Test 4 (*S/G/G*) with an averaged normalised area of 0.22, and the largest flame in Test

1 (*G/S/S*) with an averaged normalised area of 0.74. The greatest standard deviation (18%) occurs on Burner 4 within Test 6 (*G/G/S*), whilst the smallest standard deviation (4%) occurs on Burner 3 in Test 7 (*G/G/G*). An unstable flame can be characterised by a large variation in many parameters [14] including geometry. Therefore, these results indicate that the flame is most unstable when Burner 4 was operated under the Spud configuration.

Figure 5.11(b) shows the variation of flame area for different burner settings under a GT load of 25 MW_{th}. The results across all test conditions are more similar than the 33 MW_{th}. Burner 3 has the smallest flame in Test 15 (*G/G/G*) with an averaged normalised area of 0.41, and the largest flame in Test 13 (*G/S/G*) with an averaged normalised area of 0.76. Burner 4 has the smallest in flame in Test 16 (*S/S/S*) with an averaged normalised area of 0.50, and the largest flame in Test 9 (*G/S/S*) with an averaged normalised area of 0.60. The highest standard deviation (23%) occurs is on Burner 4 under Test 9 (*G/S/S*), whilst the lowest standard deviation (4%) occurs on Burner 3 in Test 15 (*G/G/G*). These results are similar to that under the 33 MW_{th}, indicating that the flame is mostly unstable when Burner 4 was operated under Spuds. This could indicate an operational problem with the Spud surrounding the gun burner within Burner 4.

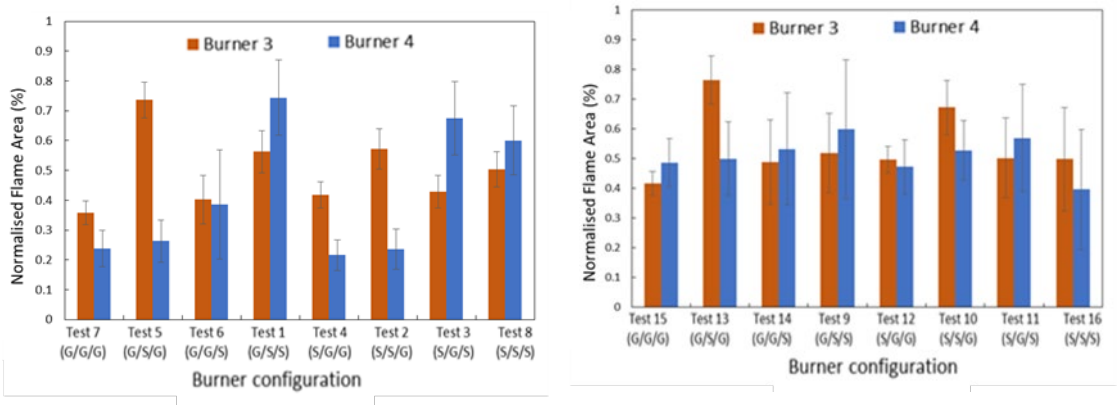

(a) 33 MW_{th} (b) 25 MW_{th}

Figure 5.11 Variation of flame area under different burner settings for the different GT loads

5.3.2.2 Flame Temperature

Figures 5.12 and 5.13 show the flame temperature distributions for different burner settings under the GT load of 33 MW_{th}, and 25 MW_{th}, respectively. It can be seen that the temperature distributions have clear changes but no clear patterns under the variation of the Gun and Spud settings under both GT loads. From Test 7 (*G/G/G*) and Test 8 (*S/S/S*), for example, it shows an increase in flame temperature, indicating when more fuel is fed into the burner, the temperature of the flame increases. Figure 5.13 also shows a more even temperature distribution across all burner configurations under the GT load of 25 MW_{th}.

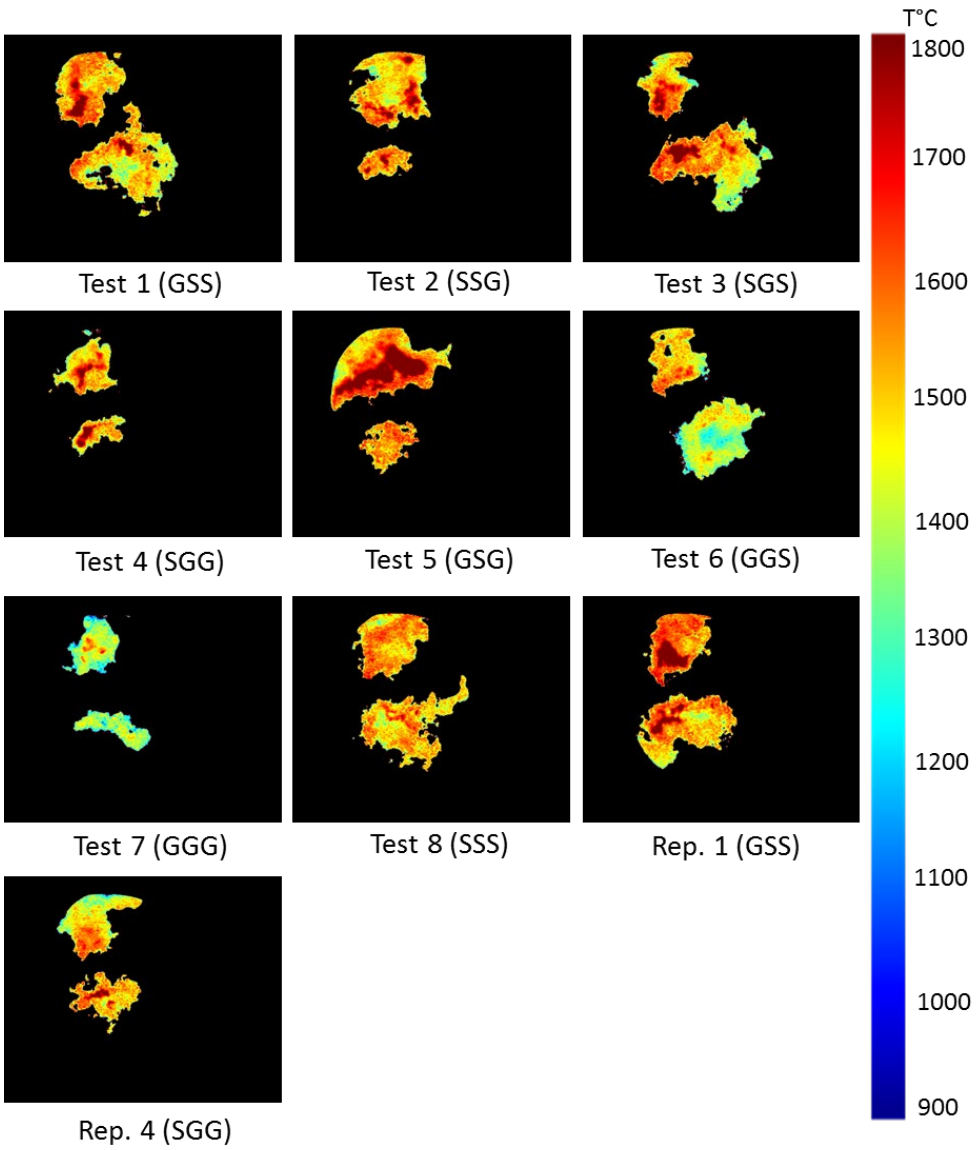

Figure 5.12 Flame temperature distribution for the GT load of 33 $MW_{th.}$

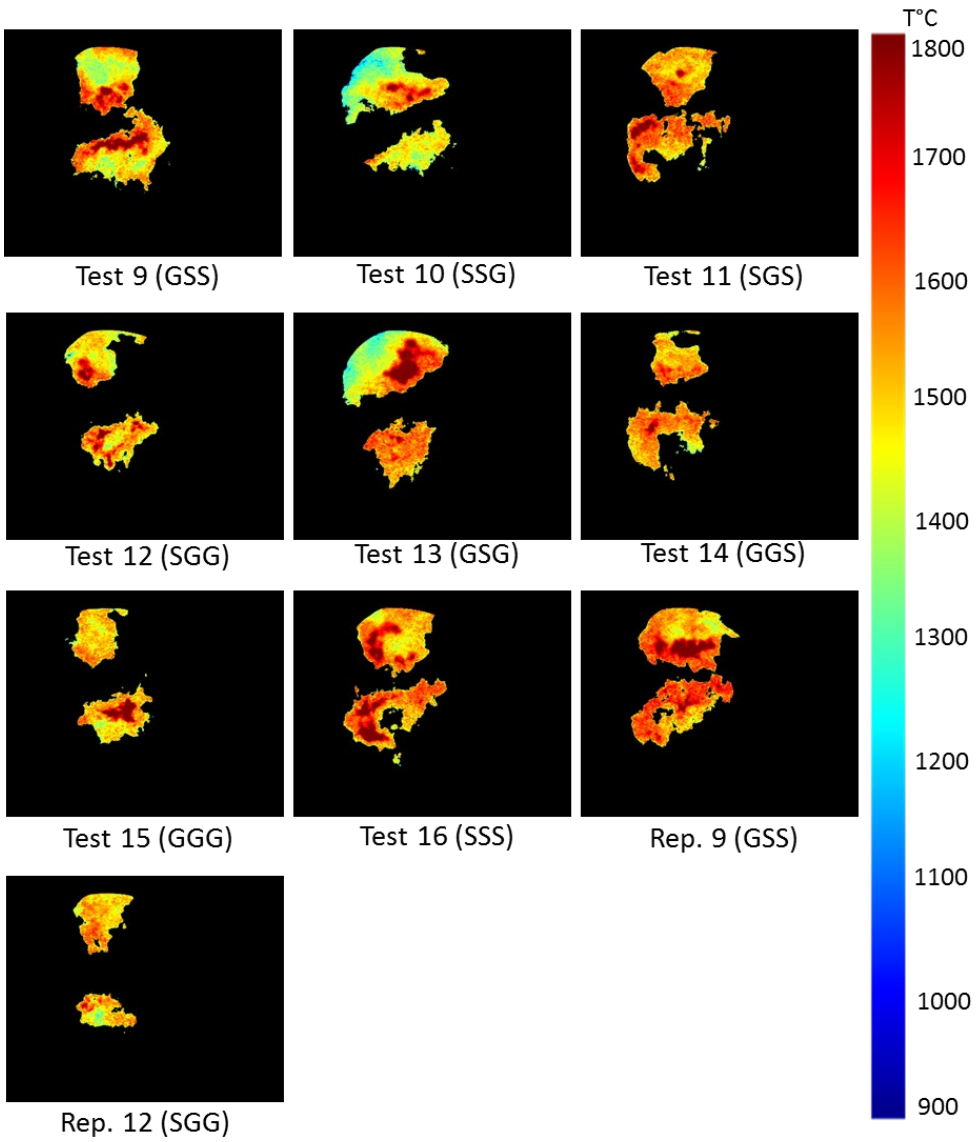

Figure 5.13 Flame temperature distribution for the GT load of 25 MW_{th}..

Figure 5.14(a) shows the variation of flame temperature for different burner settings under the GT load of 33 MW_{th}. Previous experiments [2] have shown that as the amount of fuel decrease so too should the flame temperature. This can be seen within the results here for Burner 3 as the flame temperature increases as the fuel increases (i.e., from Gun to Spuds). This effect is most evident in Burner 3 where the smallest flame in Test 7 (*G/G/G*) has an averaged flame temperature of 1658 °C, and the largest flame in Test 1 (*G/S/S*) 1741 °C. Burner 4, however, contradicts this most evidently between Test 7 (*G/G/G*) and Test 5 (*G/S/G*), where the average temperature increases to 1732 °C from 1659 °C. Burner 4 also shows inconsistent results within Test 6 (*G/G/S*), where the temperature is dropped to 1655 °C (on the Gun setting) and has a large standard deviation of 30.2 °C. Together with the analysis put forward in Section 5.4.1, it could be an indication of issues with the performance of Burner 4.

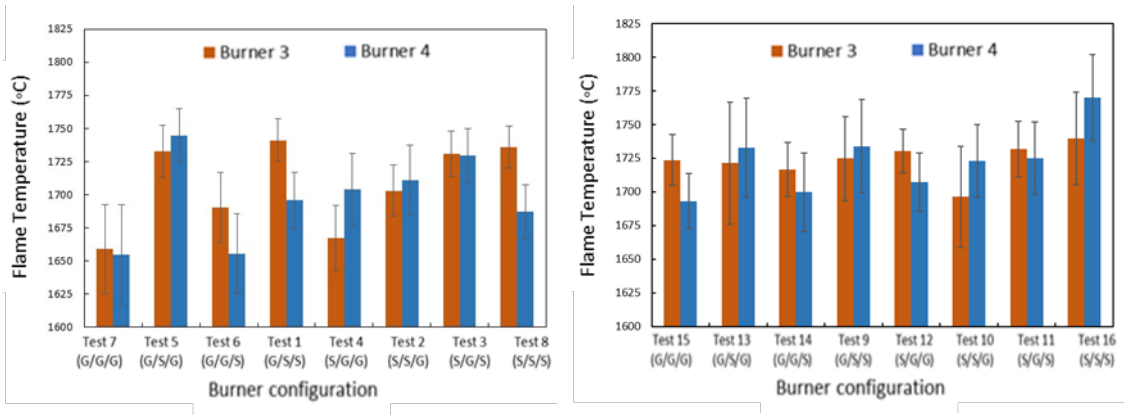

(a) 33 MW_{th} (b) 25 MW_{th}

Figure 5.14 Variation of flame temperature under different burner settings for the different GT loads

Figure 5.14 (b) shows the variation of flame temperature for different burner settings under the GT load of 25 MW_{th}. Differing from that under the GT load of 33 MW_{th}, the flame temperatures appear to be more similar under such a GT load. The average flame

temperatures of Burners 3 and 4 are 1739 °C and 1770 °C, respectively, under Test 16 (*S/S/S*). Burner 4 in Test 13 (*G/S/G*) shows a high standard deviation (36.70 °C), indicating the instability of the flame. It can also be seen that, under Test 14 (*G/G/S*), an unexpectedly low temperature of 1699 °C with a standard deviation of 29.25 °C is detected, which is consistent with the results from Burner 4 under the 33 MW_{th} conditions.

It is of note that there are some unexpected temperature results, for instance, the measured average temperatures exceed 1750 °C, meaning that it is likely some temperatures were over the maximum threshold of 1800°C. This however, does not affect the direct comparisons between test conditions. In addition, it can be seen that the average temperatures of the flames under 25 MW_{th} are greater than that of the 33 MW_{th} (as seen in Figures 5.14). This may be caused by the fact that as the 33MW_{th} tests were conducted early in the morning, and the 25 MW_{th} tests later in the day so that the overall burner zone stoichiometry of the furnace could increase over the test time. It is also however possible that the average temperatures are higher under the 25MWth conditions because the furnace is performing better under these conditions given that the flame size is also larger (Section 5.3.2.1).

5.3.2.3 Oscillation Frequency

For the oscillation frequency analysis, only the flame images of Burner 4 (bottom) were acquired due to the reduction of the image resolution in order to increase the frame rate of the camera. Figure 5.15 shows the examples of flame signals in both the time domain and frequency domain, respectively, under the GT loads of 33 MW_{th} [Figures 5.15(a-c)] and 25 MW_{th} [Figures 5.15(c-d)]. It can be seen from Figures 5.15(a-b) that the flame signals of Burner 4 have larger peaks between 8000 a.u and 17000 a.u and troughs of

between -6000 a.u and -10000 a.u when the Spuds were activated. The high peeks are signs of highly fluctuating flames and therefore a unstable combustion.

Figures 5.15(c-d) also suggest that, on Burner 4, the flame intensity variations (relating to both the geometric and luminous variations) are more uniform under the GT load of 25 MW_{th}. Figure 5.15(d) shows clearly that the flame under Test 13 (*G/S/G*) has the strongest intensity with peaks between 7000 a.u and 10000 a.u. These inconsistent high peaks can be evident of a high standard deviation, and therefore an unstable combustion rate [13]. These results in relation to the other test corresponds with the Spuds activated such as Test 9 (*G/S/S*) and Test 16 (*S/S/S*) with few peaks above 5000a.u are not expected from a Gun setting.

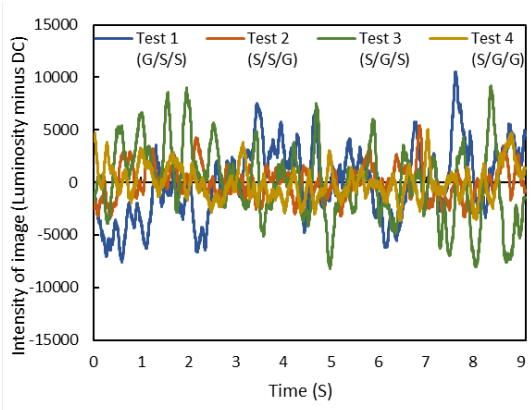

(a) Tests 1-4 for 33 MW_{th}.

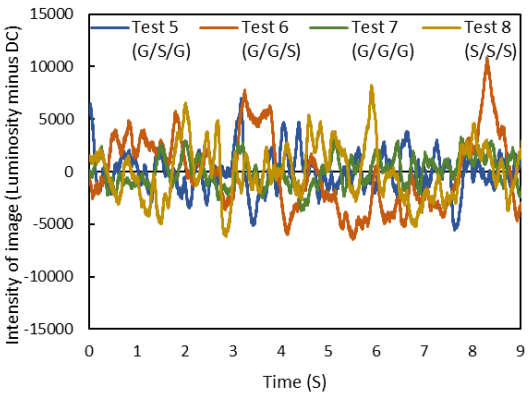

(b) Tests 5-8 for GT 33 MW_{th}.

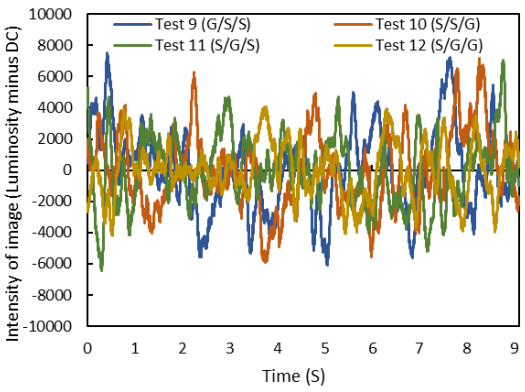

(c) Tests 9-12 for 25 MW_{th}.

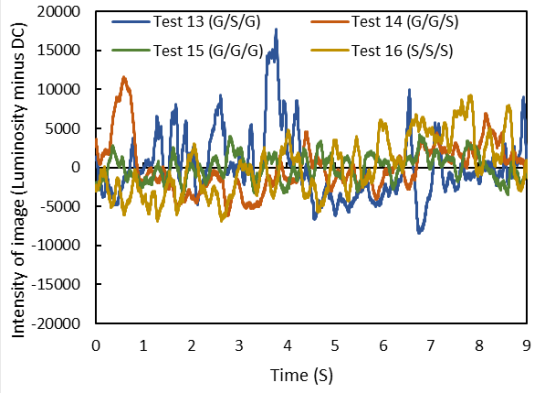

(d) Tests 13-16 for 25 MW_{th}.

Figure 5.15 Flame signals in time domain.

Figures 5.16(a-b) illustrates that the power spectral densities of the flame signals of Burner 4 have peaks between 1000 W/Hz and 2500 W/Hz, particularly, between 0 and 3 Hz when the Spuds were activated. Figures 5.16(c-d) shows that the power spectral density of the flame images of Burner 4 have again fewer differences in burner performance at 25 MW_{th}. The results from all test conditions are far more uniform. Once more Test 13 (*G/S/G*) within Figures 5.16(b) is the strongest signal throughout the bandwidth, with only Test 16 (*S/S/S*) with burner 4's Spud burners ignited giving similar peaks between 1000 – 2000 W/Hz between 0 – 3 Hz.

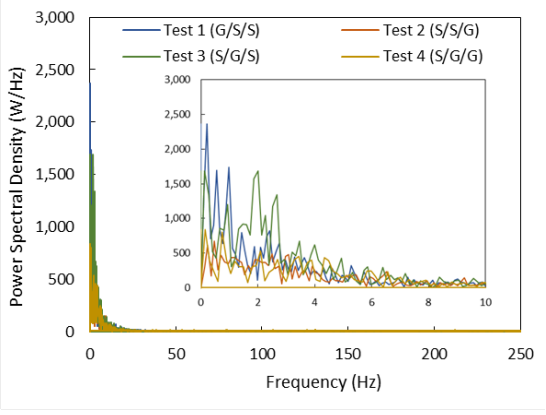

(a) Tests 1-4 for 33 MW_{th}.

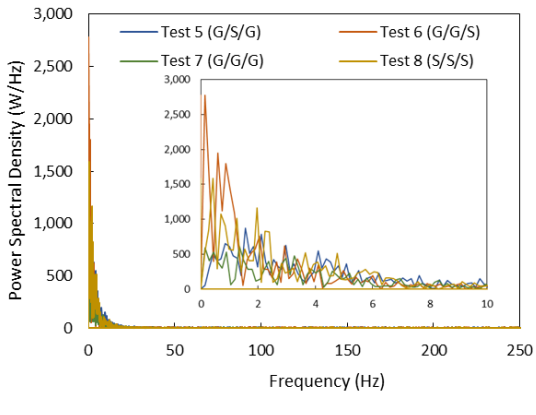

(b) Tests 5-8 for 33 MW_{th}.

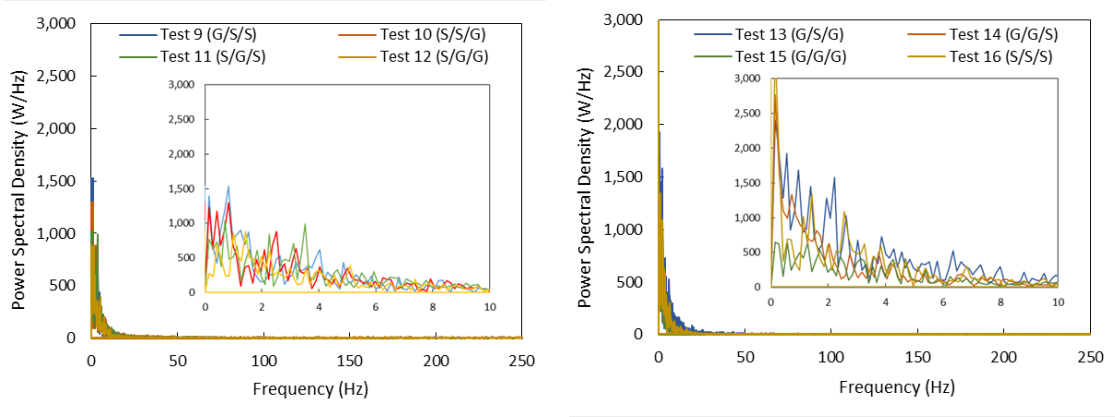

(c) Tests 9-12 for 25 MW_{th}.

(d) Tests 13-16 for 25 MW_{th}.

Figure 5.16 Flame signals in frequency domain.

Figure 5.17(a) illustrates that the oscillation frequency for different burner settings under the GT loads of 33 MW_{th}. Previous experiments have shown that as the fuel flow rate increases, so long as the fuel is properly combusted the radiation intensity of the combusting particles is increased resulting in an increase in the measured oscillation frequency [96]. However, the results from this experiment show the inverse as Burner 4 always has a lower perceived oscillation frequency with the Spuds ignited. This can be seen the oscillation frequency (5.84 Hz) in Test 5 (*G/S/G*) and 1.75 Hz in Test 1 (G/S/S). It can also be seen that although the flames in Test 5 (*G/S/G*) and Test 4 (*S/G/G*) have the highest average oscillation frequencies of 10.67 Hz and 10.03 Hz, respectively, indicating a combustion rate which is undesirable for a stable combustion.

Figure 5.17(b) shows the variation of oscillation frequencies for different burner settings under the GT load of 25 MW_{th}. The variation of the oscillation frequencies at this load shows a simlar pattern as that under 33 MW_{th}. It can be seen, however, that the lowest oscillation frequencies are observed in the tests with the Spuds ignited. This can be seen within Test 14 (*G/G/S*) and Test 9 (*G/S/S*) with average frequencies of 1.77 Hz and 2.91

Hz, respectively. In additoin, high standard deviations are also seen in the same burner configurations, as evident in the 33 MW_{th} with the flame in Test 13 (*G/S/G*) having a standard deviation of 2.92 Hz and Test 12 (*S/G/G*) 3.90 Hz.

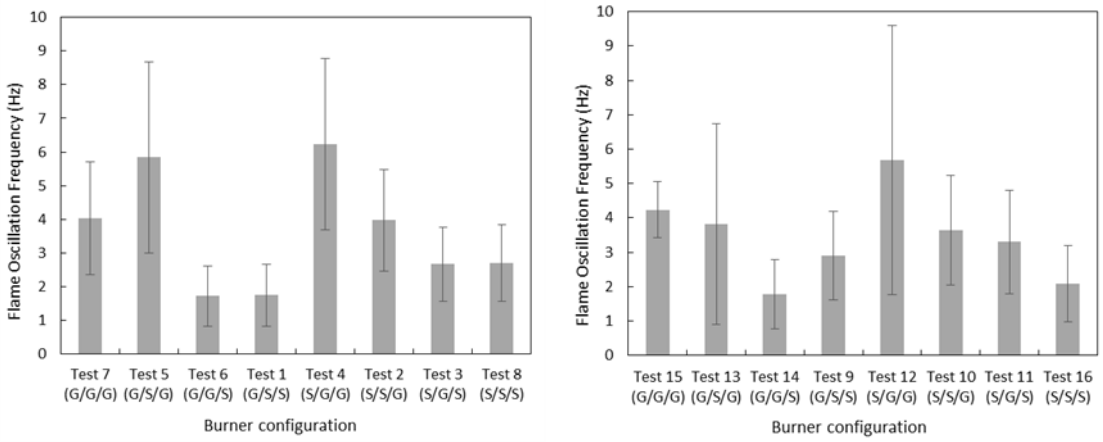

(a) 33 MW_{th} (b) 25 MW_{th}

Figure 5.17 Variation of oscillation frequency under different burner settings for the different GT loads.

5.3.2.4 Flame Spectra

The spectral characteristics of the flame have previously been studied with miniature spectrometers [36]. In this study, two different analyses were taken. Firstly, the overall spectral intensities of the flame were studied. This was achieved by averaging 120 radiative intensities of the flame across the visible range. The signals were then normalised to that of a blackbody signal which were collected on a blackbody furnace in the research lab. Secondly, the radiative intensity of the flame at a wavelength of 568 nm, which has been proven to correspond to flame radical C_2^*, was extracted from the normalised flame spectral signal (with a bandwidth of 2 nm) in order to obtain the true peak intensity of that radical.

Due to the single point measurement of the spectrometer, no distinctions can be drawn between the individual burners. It was decided that Burners 3 and 4 are the main focus of the analysis. Figures 5.18(a-d) show the normalised flame spectra under different burner settings at 33 MW_{th} and 25 MW_{th}. A single straight line is shown across these graphs in grey to represent the baseline values taken from the blackbody furnace.

As can be seen in Figure 5.18(a-b), the normalised intensity of the light emitted by the flames seems to meet the expectations with ignited Spud configurations on Burners 3 and 4 demonstrate an overall stronger intensity. This is most evident between Test 1 (*G/S/S*) peaking at 1.11 a.u and at almost half the intensity Test 7 (*G/G/G*) only reaching 0.56a.u. Likewise, Test 8 (*S/S/S*) having a peak value of 1.18a.u while Test 4 (*S/G/G*) only at 0.71a.u.

Figures 5.18(c-d) show that the flame spectral signals under the 25 MW_{th} have different distributions in comparison to that under the 33 MW_{th}, given that Test 13 (*G/S/G*) has a much larger peak value (1.04 a.u) than Test 9 (*G/S/S*) (0.72 a.u).

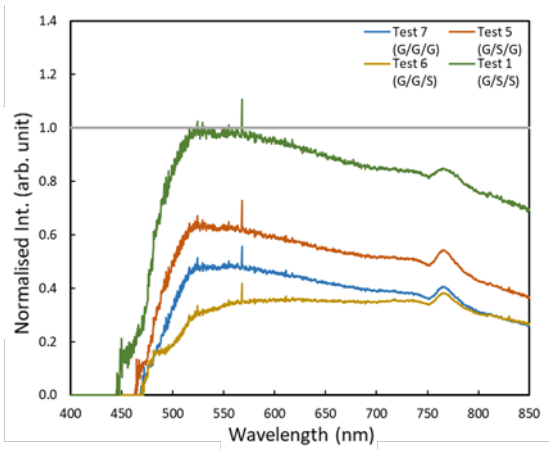

(a) Burner 1 set to G for 33 MW_{th}

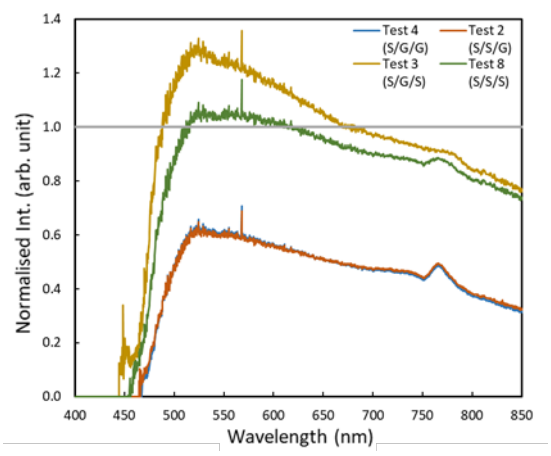

(b) Burner 1 set to S for 33 MW_{th}

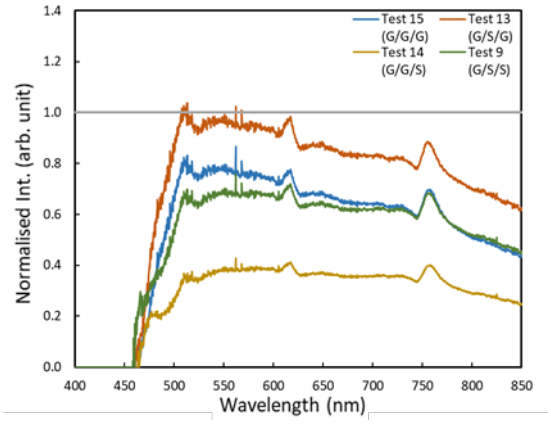

(c) Burner 1 set to G for 25 MW_{th}

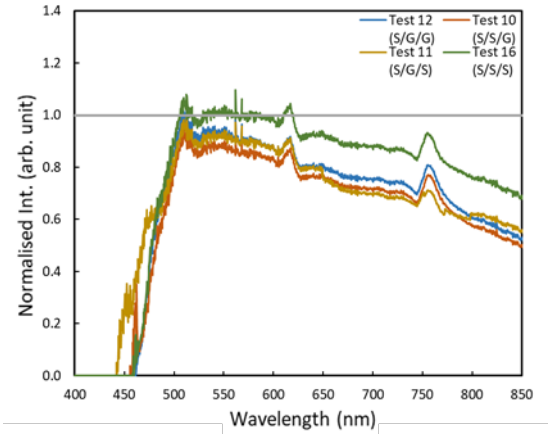

(d) Burner 1 set to S for 25 MW_{th}

Figure 5.18 Flame spectral distribution under different burner settings.

Figures 5.19(a-b) show the variations of average peak intensity of C_2^* (568 nm) under the 33 MW_{th} and 25 MW_{th}. Previous study suggests that the emissive intensity of C_2^* is low in air rich combustion mixtures, and the value increases significantly with the equivalence ratio approaching and passing beyond stoichiometric conditions [112]. Therefore, it can be estimated that the lowest stoichiometric condition is that of Test 6 (*G/G/S*) where the averaged C_2* peak is 0.057 a.u. It can also be seen that the highest value of 0.136 a.u occurs under Test 3 (S/G/S), also exhibiting a sign of fuel rich combustion.

These results suggest that the lowest stoichiometric condition also occurs under Test 14 (*G/G/S*) with an averaged C_2* peak of 0.096a.u under the 33 MW_{th}. Results under Test 6 (*G/G/S)* also featured with the same boiler configuration) also exhibited the lowest average C_2* peak. Test 16 (*S/S/S*) has the highest averaged C_2* peak (0.192 a.u). results under Test 8 (*S/S/S*) also had one of the highest averages with a value (0.131 a.u). It can also be seen that Test 9 (*G/S/S*), Test 11 (*S/G/S*) and Test 16 (*S/S/S*) have the high standard deviations over the test conditions (4.1%, 4.2% and 3.1%, respectively), with each of these containing at least two burners with the Spuds ignited.

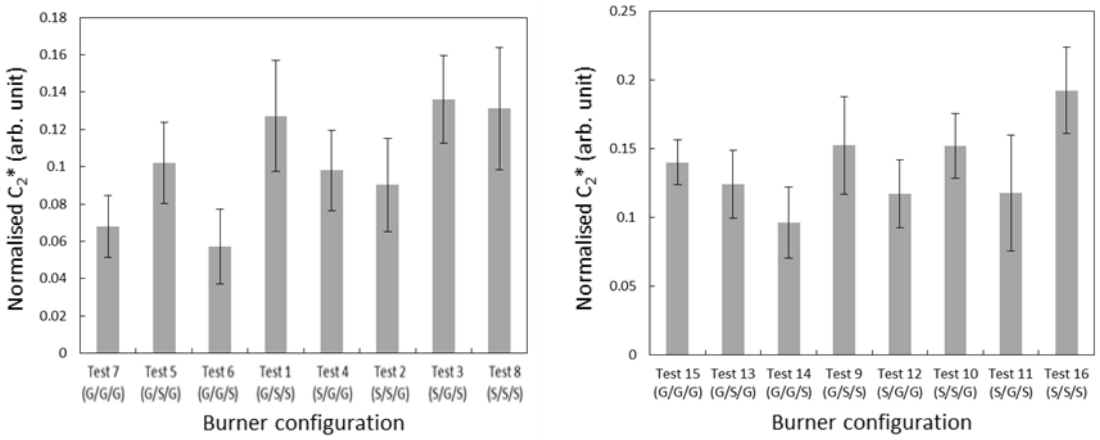

(a) 33 MW_{th} (b) 25 MW_{th}

Figure 5.19 Flame radical C_2^* under different burner settings for the different GT loads.

5.4 Prediction of NO_x Emission through ANN

Table 5.2 shows the NO_x emissions from the boiler data log system. These data were used to train the following ANN model (Section 4.5.2) and to assess the RMS of the predicted NO_x emissions for Rep. 1 (G/S/S), Rep. 4 (S/G/G), Rep. 9 (G/S/S), and Rep. 12 (S/G/G) which were unknown to the model during all training aspects.

Table 5.2 NO_x emissions collected under different burner settings for two GT loads.

Test No	**1**	**2**	**3**	**4**	**5**	**6**	**7**	**8**	**Rep. 1**	**Rep. 4**
GT load	33 MW_{th}									
NO_x Emissions (ppm)	32.62	31.38	30.70	29.97	30.94	31.68	32.69	30.72	31.73	30.72
Test No	**9**	**10**	**11**	**12**	**13**	**14**	**15**	**16**	**Rep. 9**	**Rep. 12**
GT load	25 MW_{th}									
NO_x Emissions (ppm)	31.90	31.20	30.99	30.87	32.58	31.69	32.95	31.44	31.93	32.14

Li et al [7] described Artificial Neural Network (NN) model to predict the NO_x emissions of premixed air-propane flames on a laboratory-scale test rig comprising of a Bunsen-type burner sealed within a cylindrical chamber. They extracted radical features from images of flame radicals (OH^*, CH^* C_2^* and CN^*) captured by an EMCCD camera, and used the extracted radical features as the input of the ANN. The results are very positive, although it has been noted that the work is preliminary in industrial uses. For the present study, a backpropagation ANN model for the purpose of NO_x prediction was built and trained. In the model, four flame parameters as discussed in Section 4.5.2 were used as the inputs (temperature, area, normalised average spectral intensity across the whole broadband of the miniature spectrometer and the normalised average peak value of wavelength 568 nm related to C_2^*). Both temperature and area have unique values for burner 3 and burner 4 giving a total of 6 input parameters. The network only has one output NO_x emissions (ppm) as this is the only flame emission being predicted at this time. 240 data points were selected for each input and output parameters. Eight tests from each of the 33 MW_{th} and 25 MW_{th} (the repeatability tests were excluded from the training data) were used to train the model, giving a total number of 1920 data points, and therefore, 11520 total inputs when all six parameters are considered.

To evaluate the capabilities of the ANN model for the NO_x emission prediction, the data from the inputs were divided into a training set (80%) and a performance set (20%). The performance set was divided further into 50% for validation and 50% for testing. The training set was used to compute the gradient, the network weights and biases, while the validation and testing sets were not included in the initial network development. They were used in two unique ways to ensure there is no overfitting, i.e., the validation set (10% of the overall data size) used to measure the network generalisation, and to stop training when the generalisation stops improving. While the testing set (10% of the

overall data size) was used only after all training is completed to assess the performance of the network against a set of blind data (the testing set). In this study, flame data of the repeatability tests which were excluded from the training were used as an independent data set for the performance evaluation of the ANN model.

Figure 5.20 shows the performance of the trained model for the emission prediction under the GT load of 33 MW_{th} and 25 MW_{th}. The data presented represents the predicted results from the two subsets of the performance data, i.e., Testing and Validation, Rep 1 (G/G/S) and Rep. 4 (S/G/G), with MSEs (Mean Squared Errors) of 0.35, 0.39, 1.03 and 1.54, respectively at 33 MW_{th}; and Testing and Validation, Rep. 9 (G/G/S) and Rep. 12 (S/G/G), with MSEs of 0.14, 0.14, 0.59 and 0.11, respectively at 25 MW_{th}. It can be seen that the predicted results from the tests disclosed to the model (Test 1-8, 9-16) are more accurate than the tests that were not disclosed to the network during training (Rep 1,4,9,12), but the MSE results from the predictions of Rep 1 (*G/G/S*) and Rep 4 (*S/G/G*) are still low. The results show that the predicted results from the 25 MW_{th} experiments are more accurate than the 33 MW_{th} experiments with all the results falling far below the 3% error margin, shown in the figure with the upper and lower dotted line. However, all predictions are close to the ideal line and all are either in line with or lower than 3% error margin.

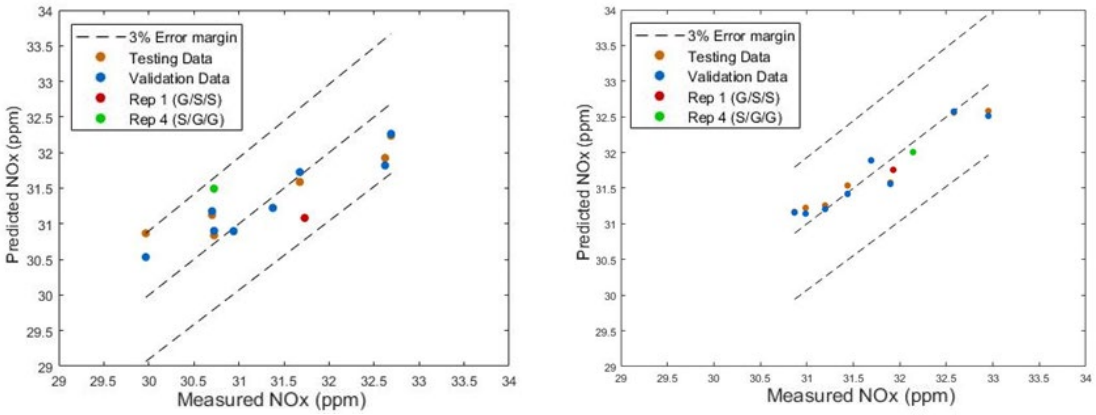

(a) GT load of 33MW_{th} (b) GT load of 25MW_{th}

Figure 5.20 Predicted NO_x (average) and measured NO_x for all condtions.

The 192 relative errors of each data point within the testing and validation subsets, each totalling 10% for the overall data size of 1920 are shown in Figure 5.21 for the GT load of 33 MW_{th} and 25 MW_{th}. It can be seen that the two subsets are very uniform, with the relative errors of each subset raising and falling together. The majority of the data points fall below 2% with only a small minority of the errors for the validation, testing data increasing above this, and that the maximum relative error is 8% and 5% or 33 MW_{th} and 25 MW_{th} respectively.

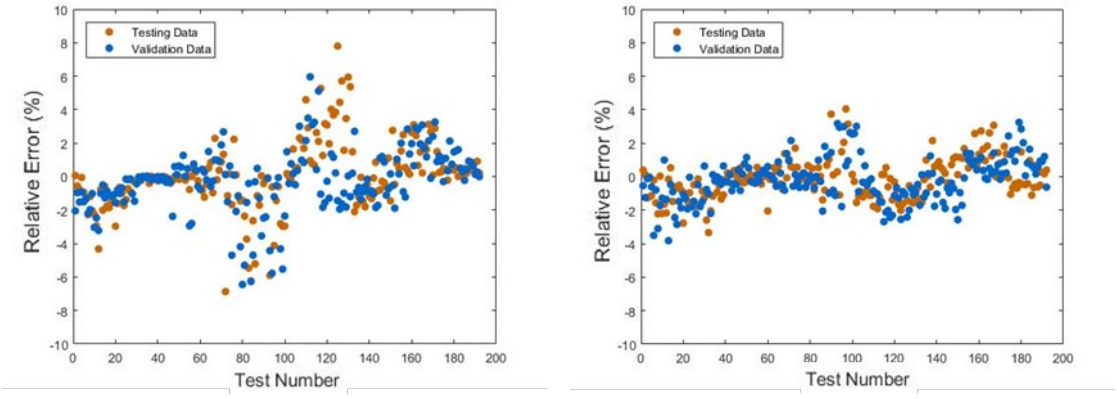

(a) GT load of 33MW_{th} (b) GT load of 25MW_{th}

Figure 5.21 Relative error of NO_x prediction of the training and validation data subsets.

The 240 relative errors of the predicted NO_x values for a set of inputs for Rep. 1 (*G/S/S*) and Rep. 4 (*S/G/G*) are shown below in Figure 5.22 (a) and Rep 9 (*G/S/S*) and Rep 12 (*S/G/G*) Figure 5.22 (b). It can be seen that the majority of the data points fall between 2-3% with only a small minority of the relative errors for Rep 1 (*G/S/S*) and Rep. 4 (*S/G/G*) being larger than this, and that the maximum relative error is 6%. Unlike the data subsets of testing and validation which were uniform in the relative errors presented it can be seen that for the majority of the data Rep. 1(*G/S/S*) is predicted under the measured value while the majority of the relative errors from the NO_x predictions of Rep. 4 (*S/G/G*) is predicted over the measured value. Once more the NO_x emissions predicted at 25 MW_{th} are closer to the measured values with the majority of the data points falling below 2% with only a very small minority of the errors being larger than this, and that the maximum relative error is 4%.

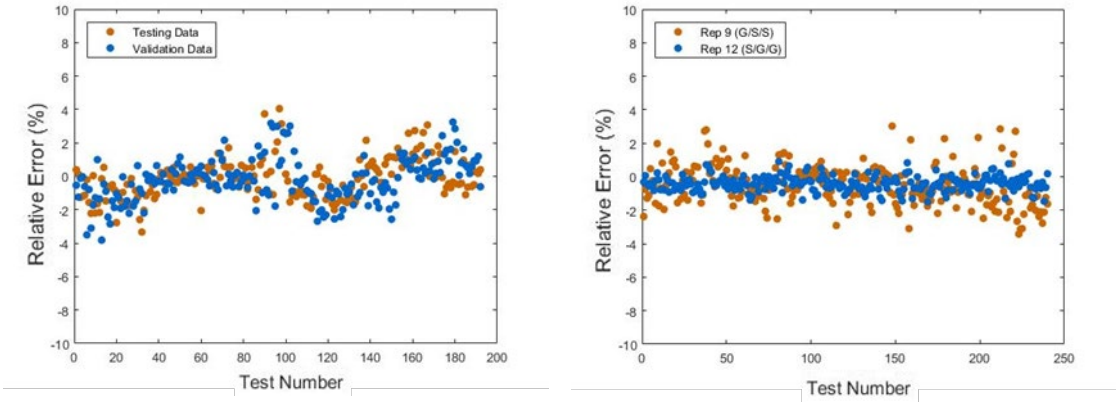

(a) GT load of 33MW_{th} (b) GT load of 25MW_{th}

Figure 5.22 Relative error of NO_x prediction of Rep 1,9 (G/S/S) and Rep 4,12 (S/G/G) data subsets.

5.5 Summary

A range of different burner configurations under two gas turbine power inputs have been explored on the 120 MW_{th} boiler run by British Sugar. The tests have demonstrated the ability for flame characteristics with the developed system and the computational algorithms. It has also been demonstrated that the temperature, oscillation frequency and flame radicals such as C_2^* can give a reasonable assessment of the flame. The relationship between the captured parameters of both the digital camera and the spectrometer with that of the NO_x emissions readings from the site have been investigated.

In addition, the test results obtained have also shown the effectiveness and potential of modest ANN implementation with such detailed flame data, such as the oscillation frequency and C_2^*. The performance of the ANN for flame NO_x prediction has also been evaluated and shown that once trained, even flame data that was not ever shown to the

network during the training procedure, can demonstrate relative errors of around 3%, and maximum relative errors of 8%.

Chapter 6

Trials on a 40 MW_{th} Coal Fired Combustion Test Facility

6.1 Introduction

Despite increasing use of renewable energy worldwide, coal remains to be the primary energy resource to meet the increasing demand for electric power in many countries. However, coal-fired power plants have to cope with coals with different properties, including those with high moisture content. It is known that moisture content in coal does not only affect coal handling but also burner performance, and thus combustion efficiency and emission formation process. Trials were carried out to investigate the impact of moisture content in coal on the burner performance using the flame imaging and spectroscopic techniques, which were developed partly under this research programme. The objectives of the trials were:

- to assess the performance of the flame imaging and spectra prototype system presented in Chapter 3.
- to evaluate the effectiveness of the methods presented in Chapter 4, including flame imaging, spectrum analysis and machine learning, such as ANN based NO_x prediction.
- to investigate the characteristics of coal flames under different combustion conditions including steam injection, burner zone stoichiometry and air-to-fuel ratio.

It should be mentioned that, due to the different structure of the test furnace, the hardware system as described in Chapter 3 was not used in the trial. Instead, a single camera system and a spectrometer were installed and used as separate instruments for the trials. Computer algorithms as described in Chapter 4 were used to process the flame data acquired.

6.2 Experimental Set-up

6.2.1 Combustion Test Facility and System Installation

The 40 MW_{th} CTF is specifically designed to accommodate investigations of various coal combustion characteristics. It uses a full-scale burner of a typical power plant with operational conditions close to real plant situations (either conventional air or Oxy combustion). The burner is fitted horizontally on the front wall of a rectangular combustion chamber with an inner cross-section of 5.2 x 5.2 m and a length of 17.0 m. A water jacket layer is fitted to the outside of the furnace that removes the input energy. The combustion chamber fits with a number of viewing/measurement ports on the centre line of the sidewall. A number of instruments (e.g., thermocouples; probes; and gas analysers) are also installed around the chamber and the flue gas exit to continuously monitor the temperature and other operation data of the furnace.

The flame imaging system consists of a water jacket, an optical probe (with an objective lens of a 90° direct view angle), a camera unit and a laptop PC. Two CMOS cameras were used in the tests: one is a wide dynamic range camera (IDS UI-3130CP Rev 2) with an image resolution of 1936 x 2160 (pixels) and frame rate of 25 fps, acquiring images for

the measurements of the flame ignition point and temperature. Another is a high-speed camera (IDS UI-3060CP Rev 2) with a frame rate up to 900 fps, acquiring videos for the measurement of flame oscillation frequency. A commercial spectrometer (Ocean Optics USB 2000) with air-cooled jacket was also used to acquire flame spectral characteristics along with the imaging system.

Figure 6.1 shows the block diagram of the system installation whilst Figure 6.2 shows the on-site installation of the systems. The optical probe and camera was located on the sidewall of the furnace at Port 2 to allow for visualisation of the flame at the exit of the quarl. The resulting maximum viewing field is about 4m long along the burner axis. The optical probe and spectrometer was located at Port 1. Cooling water and air supplies to the jackets of the camera optical probe and spectrometer optical fibre.

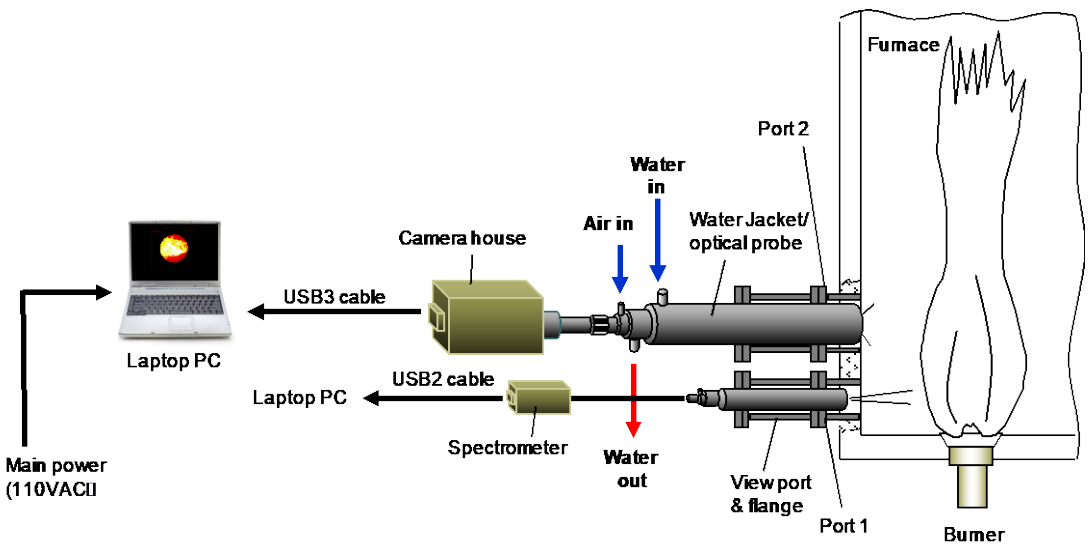

Figure 6.1 Block diagram of the system installation.

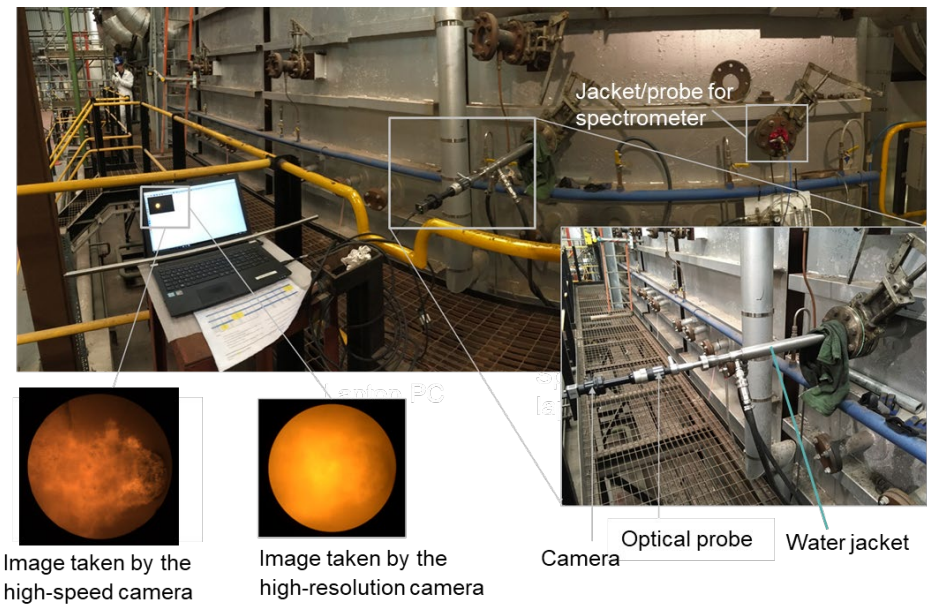

Figure 6.2 Overview of the system installation.

6.2.2 Trial Programme

Tables 6.1 and 6.2 summarise the trial programmes. The primary purpose of the test was to examine a typical high moisture coal under different air combustion conditions (as part of an enterprise project run within the Kent Team). Using coal with very high moisture contents is common in power plants, it is desirable to discover how the moisture effects on the combustion performance of such a coal. During the test, it was attempted to maintain the CTF under a constant load of 40 MW_{th}. was added to the coal to simulate the moisture content in the coal (Table 1). The burner zone stoichiometry (BZS) was varied, giving a total of 4 test conditions (refer to Table 6.2).

Table 6.1 Test matrix for PF moisture test.

Test No	Load (MW_{th})	PA: Fuel ratio (Burner outlet)	BZS	PA steam injection (kg/h)	**PF Moisture (%w/w)**
1	40.2	3.21	0.81	797	**20.1**
2	40	3.64	0.79	2015	**34.4**
3	40	3.97	0.8	2696	**40.3**
4	40	4.07	0.79	3373	**46.2**
5	40	4.33	0.78	4125	**49.8**
6	40	4.80	0.80	5169	**55.0**

Note: PF: Primary flow; PA: Primary air; BZS: Burner Zone Stoichiometry

Table 6.2 Test matrix for BZS test.

Test No	Load (MW)	Burner outlet PA: Fuel	**BZS**	PA steam injection (kg/h)	PF Moisture (%w/w)
7	40.2	3.88	**0.69**	2700	40.3
8	40.2	3.86	**0.81**	2700	40.3
9	40.2	3.90	**0.83**	2700	40.3
10	40.2	3.83	**0.89**	2700	40.3

For each condition, a total of 400 images and spectral readings were acquired. The flame images captured were then processed for determining flame parameters including; area; temperature; oscillation frequency; image intensity. The spectral data for integrated spectral intensity, peak spectra of key radicals such as CH^*, CN^* and C_2^*. The 400 processed data points were first averaged and then the standard deviation was calculated

and is shown with an error bar. The developed machine learning algorithm for NO_x prediction (Chapter 4) was also examined using the data acquired on the CTF under the realistic industrial operation condition.,

6.3 Results and Discussion

6.3.1 Variation in Steam Injection

6.3.1.1 Flame Area

Figure 6.3 shows the images of the flame under the six steam injection conditions whilst Figure 6.4 gives the variation of flame areas under such conditions. The area was computed by applying a global threshold over the images to segment the flame region (in pixels) in the HIS colour space of $0.109<H<0.986$, $0.482<S<0.882$ and $0.590<I<1.000$ in the range 0 to 1. The flame areas are then normalised by 640000 pixels (the total amount of pixels in the image). As can be seen, the moisture content of the coal has a significant impact on flame size (area). This can be more observed in more detail, which shows clearly that the flame area decreases with the moisture content. For instance, for 49.8%w/w and 55%w/w, the flame areas are 6% and 1%, respectively, decreased by 5%. The standard deviation of 49.8%w/w and 55%w/w are also high with values of 0.9% and 0.4%. Test 4 also has a high standard deviation of 0.8%. A large variation in geometric parameters can regarded to be a sign of unstable flame [1].

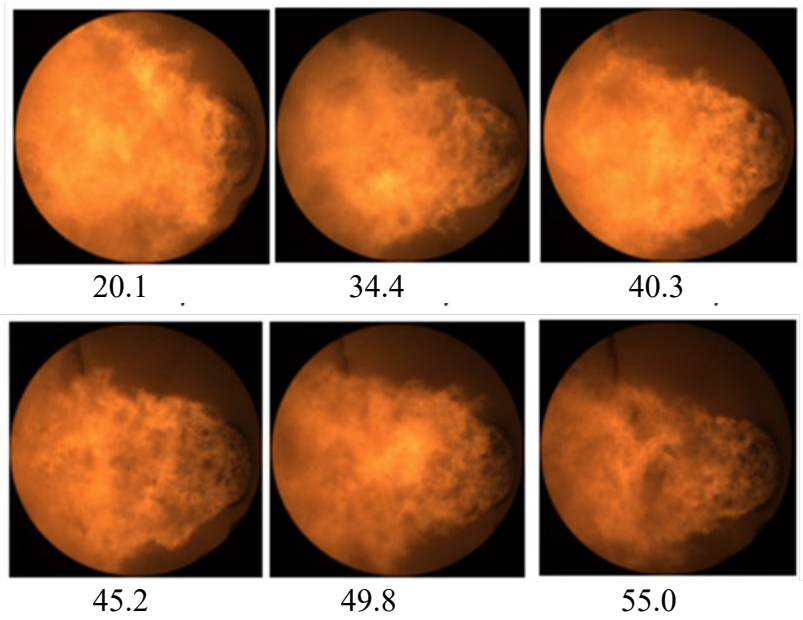

Figure 6.3 Example flame images for different steam injunctions (%w/w).

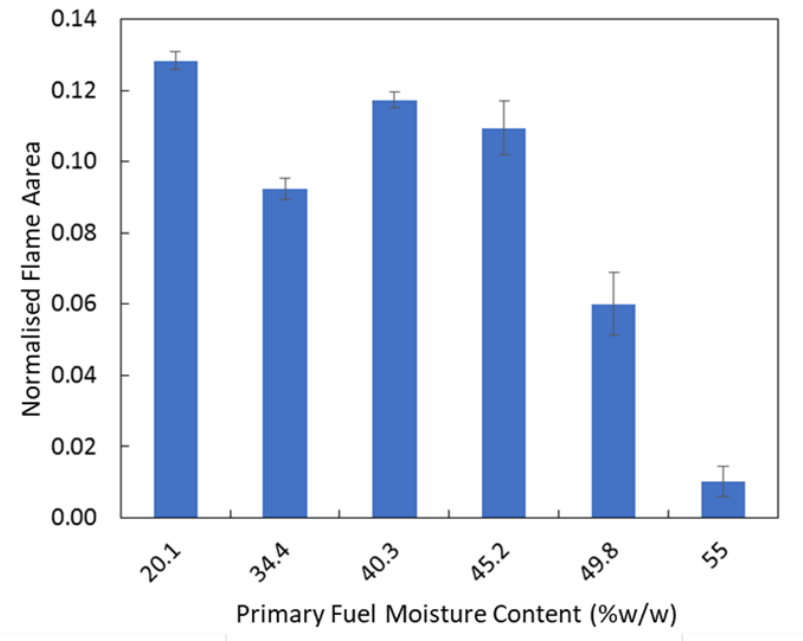

Figure 6.4 Variation of flame area under different steam injections.

6.3.1.2 Flame Temperature

Figure 6.5 shows the flame temperature distributions whilst Figure 6.6 illustrates the variation of flame temperature under different steam injections. The temperature decreases in general with the moisture content. The highest flame temperature (1547 °C) is found when the moisture content is 20.1%w/w and the lowest temperature 1450 °C when the moisture content 55%w/w. In addition, this moisture content has the highest standard deviation (21.76 °C), indicating an unstable flame.

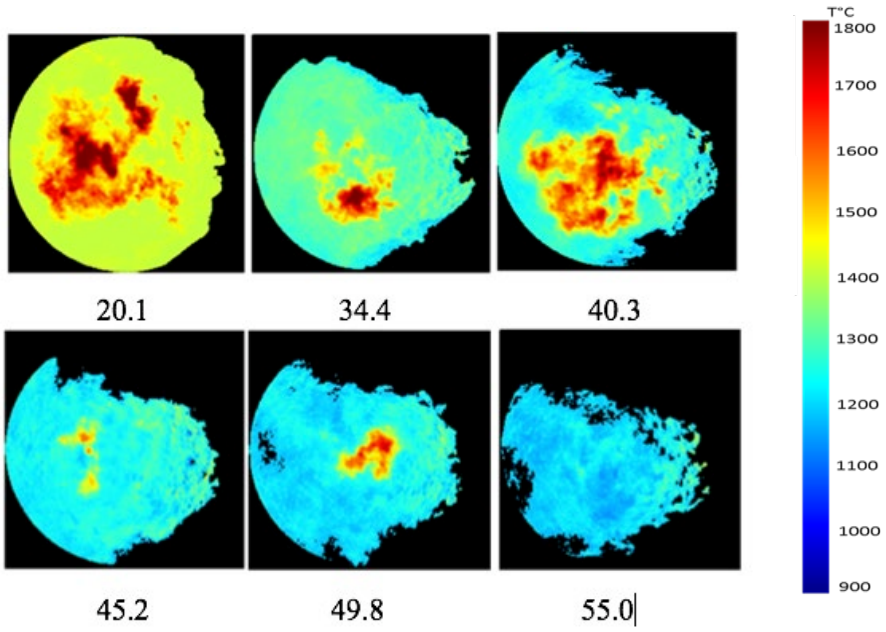

Figure 6.5 Temperature distributions of flame for different steam injections (%w/w).

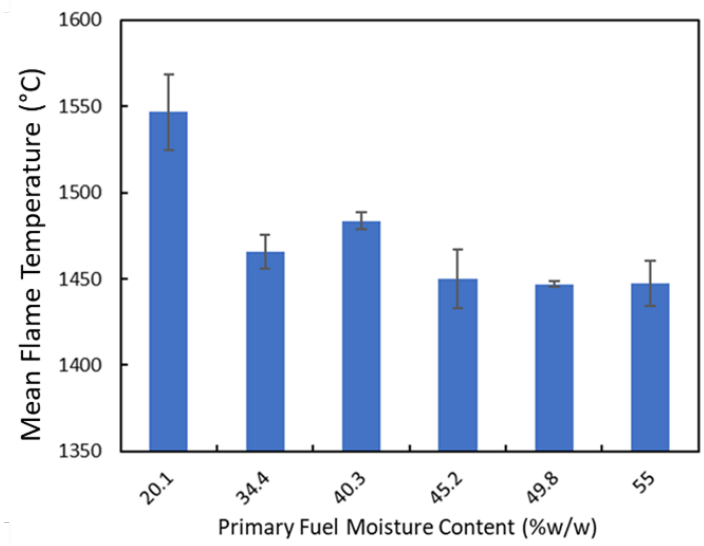

Figure 6.6 Variation of lame temperature under steam injections.

6.3.1.3 Flame Oscillation Frequency

The oscillation frequency of the flames was computed using a high-speed flame videos (image resolution of (400×300) recorded at a frame rate of around 750 fps for a total of 9 seconds. Figure 6.7 shows flame signals in time domain generated from the flame videos, showing that the intensities of the flame with higher moisture contents appear more uniform and have smaller peaks between 100 a.u and 2000 a.u and troughs of between -2000 a.u and -4000 a.u. Stronger peaks are evident of more dramatic flame fluctuation under such conditions.

Figure 6.8 gives the power spectral densities of the flame signals through the FFT for different steam injections. The flames appear to have frequencies dominated between 0 and 50 Hz. The quantified oscillation frequency (Figure 6.9) suggests that the flame under the lowest steam injection (20.1%w/w) has the highest oscillation frequency whilst the flames with the steam injection 34.4-55.0% appear to be similar. This is a very similar trend found in the flame temperatures (Section 6.3.1.2). There is a sharp frequency drop off from 20.1%w/w to 34.4%w/w, showing that once the steam injection is reduced to this level there would less impact on the flame oscillation frequency. Other studies have shown that a lower oscillation frequency of a flame indicates a less stable flame [96].

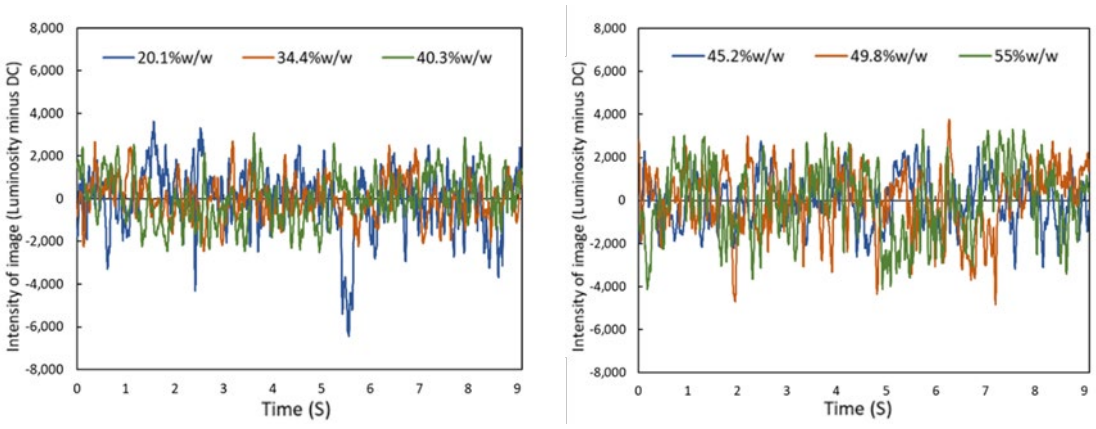

(a) 20.1w/w – 40.3w/w steam injection (b) 45.2w/w – 55w/w steam injection

Figure 6.7 Flame signals in time domain for different steam injections

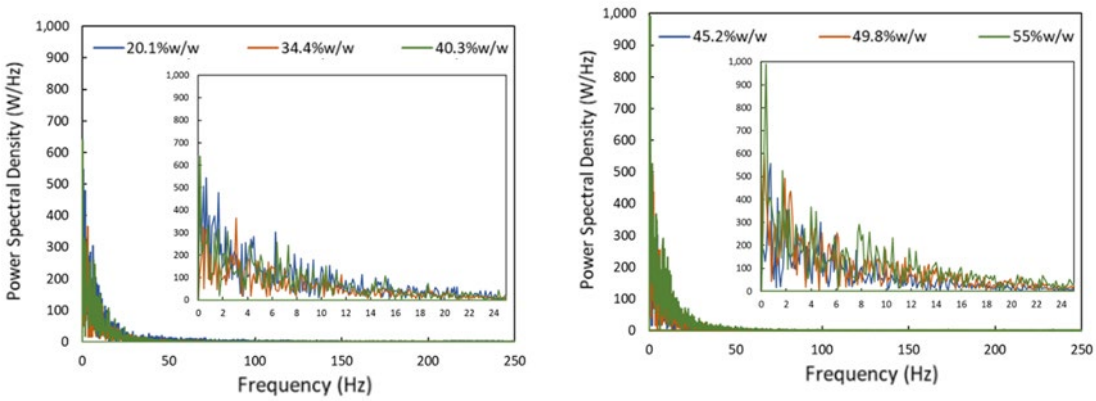

(a) 20.1w/w – 40.3w/w steam injection (b) 45.2w/w – 55w/w steam injection

Figure 6.8 Flame signals in the frequency domain for different steam injections.

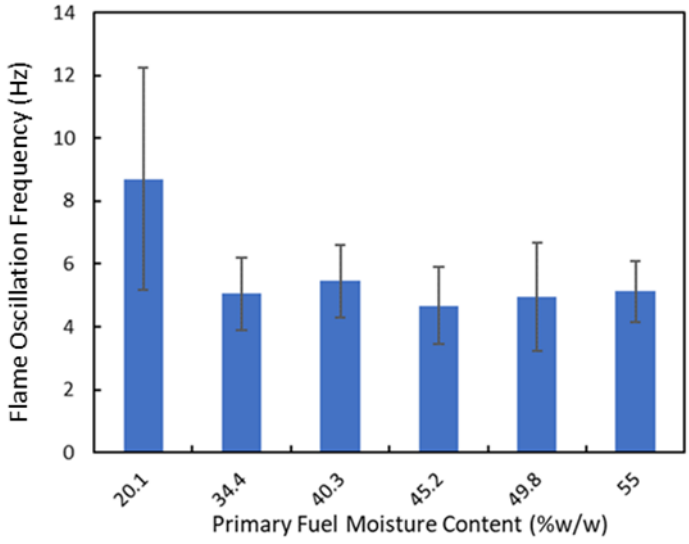

Figure 6.9 Flame oscillation frequency for different steam injections.

6.3.1.4 Flame Spectra

Two different analyses were taken from each spectrometer measurement. A total of 400 samples were taken from each test condition to maximise the data collected. The averaged radiative intensities of the flame spectrum across the visible range was normalised to that of the baseline condition, i.e., Test 2. The peak value of the flame radical C_2^* at 590 nm is extracted from normalised flame spectral distribution. Figure 6.10 shows the normalised flame spectra under different steam injections. A grey straight line is shown across these graphs represents the baseline values (Test 2). It can be seen that only the spectral signal of 20.1%w/w flame is stronger than that of the baseline signal under all the test conditions. It has been demonstrated in Sections 6.3.1.1 and 6.3.1.2 that the flame with steam injection below 20.1%w/w shows a significant drop off in temperature and oscillation frequency. This overall spectrum data continues this trend through the analysis of the flame using a second sensor, further proving that this is the case under high moisture fuel content.

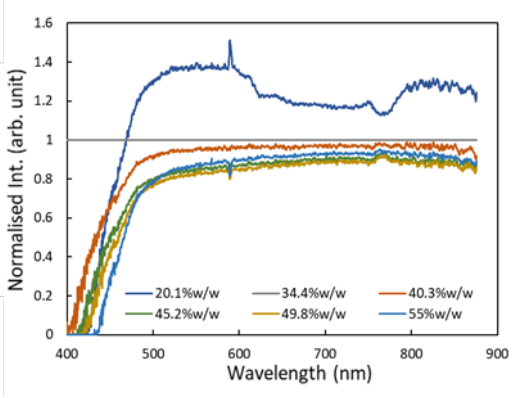

Figure 6.10 Normalised flame spectra for different steam injections.

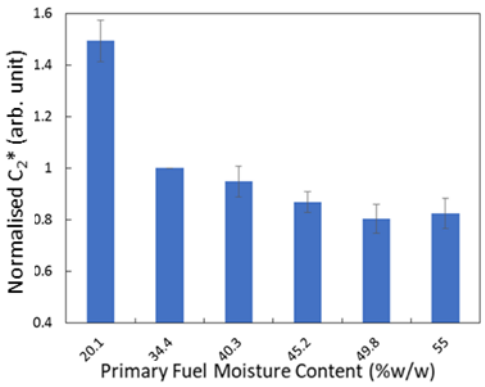

Figure 6.11 Normalised intensity of C_2^* for different steam injections.

Figure 6.11 shows the variations of average peak intensity of C_2^* (590 nm) for different steam injections. It has been discussed that the emissive intensity of C_2^* increases significantly with the equivalence ratio approaching and passing beyond stoichiometric conditions [112]. This should also suggest that under poor combustion state, a low C_2^* value would be presented. It would appear once more that the flame with the steam injection of 20.1%w/w shows the highest C_2^* intensity over all test conditions. There is a gentle decreased trend in the C_2^* intensity of the flame between 34%w/w and 55%w/w.

6.3.2 Variation in Burner Zone Stoichiometry

The burner zone stoichiometry (BZS) was varied giving a total of 4 test conditions (refer to Table 6.2). The purpose of this test is to discover if changing the stoichiometry of the burner would add an impact on the combustion performance.

6.3.2.1 Flame Area

Figure 6.12 shows the images of flame for different BZS settings, whilst Figure 6.13 gives the variation of flame area under such conditions. The variation of flame area for different burner zone stoichiometry levels show that the flame areas are more similar over these testing conditions, indicating that changing the BZS has less of a significant effect on the flame size. Now that the total areas of the flame are graphed it is clear to see that the flame area is quite consistent with the burner settings, tending to increase in size as the burner zone stoichiometry increases. This is most evident between Test 7 with a stoichiometry of 0.69 a.u to Test 9 with a stoichiometry of 0.83 a.u where the flame size increases from a normalised value of 13% to 16%.

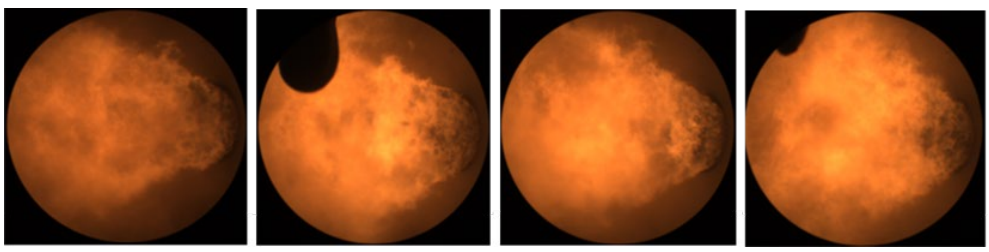

0.69 0.81 0.83 0.89

Figure 6.12. Flame images for different BZS settings.

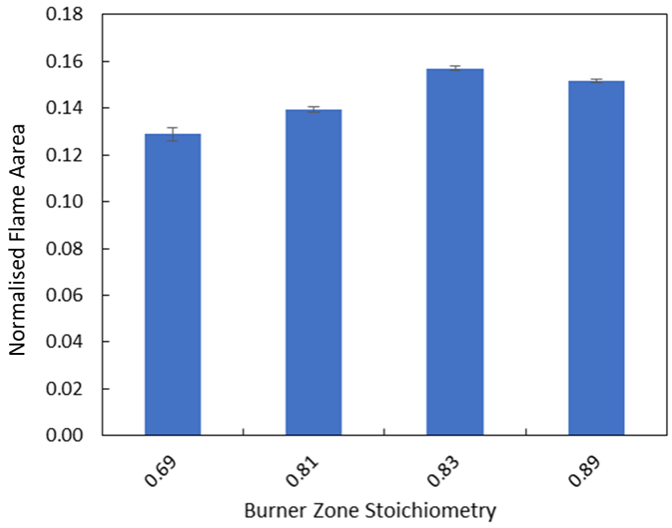

Figure 6.13 Flame area for different BZS settings.

6.3.2.2 Flame Temperature

Figure 6.14 shows the flame temperature distributions for different BZS settings, whilst Figure 6.15 shows the variation of flame temperature for such conditions. It is clear that there is a sharp increase from the flame temperature (1447 °C) in BZS 0.69 (Test 7) to 1496 °C in BZS 0.81 (Test 8). The flame reduced slighted when the BZS continued increasing to 0.89 (Test 10) and remains very similar. However, the standard deviations of the average temperature at the high BZS levels (i.e., 11.81 °C@ BZS 0.81, 24.53 °C@ BZS 0.83 and 11.88 °C@0 BZS.89) is much greater than that of BZS 0.69 (1.08 °C).

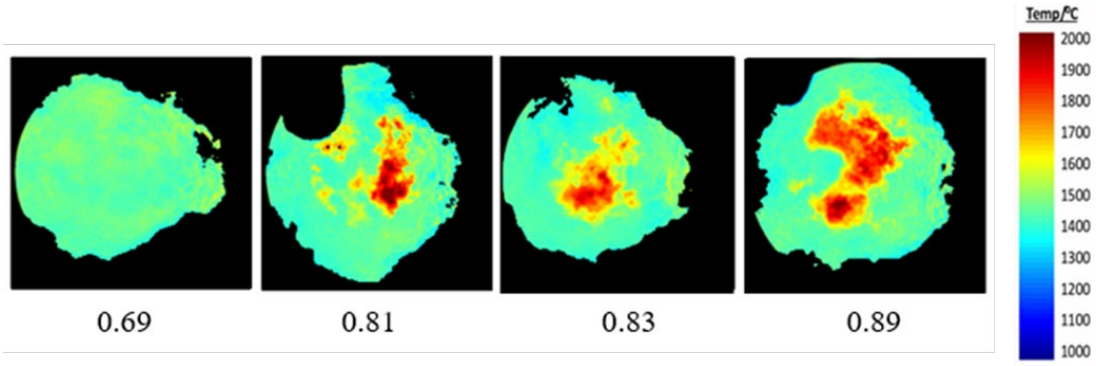

Figure 6.14 Temperature distribution for different BZS settings.

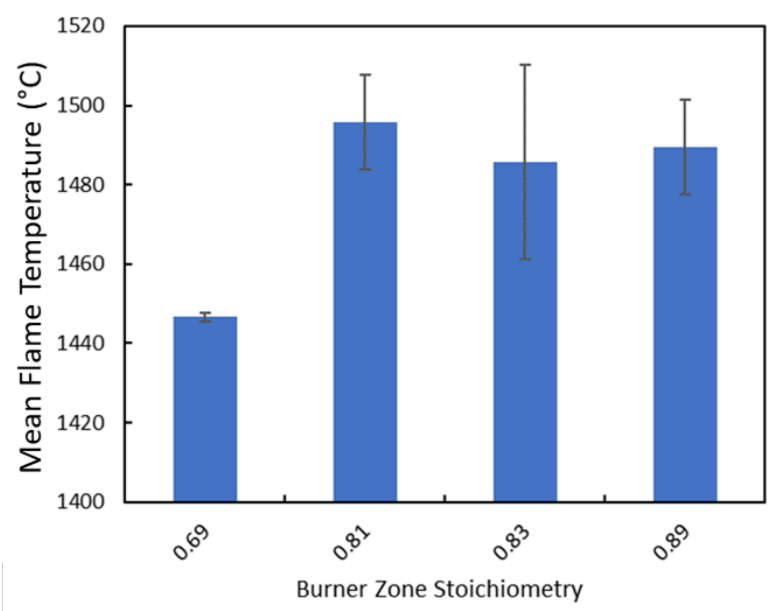

Figure 6.15 Flame temperature for different BZS settings.

6.3.2.3 Flame Oscillation Frequency

The same camera settings and parameters of analysis were used to create these results as Section 6.3.1.3. It can be seen from the time domain in Figure 6.16 that the flame signal of BZS 0.89 has a large variation between -7000 a.u. and 4000 a.u. The intensity of the flame under BZS 0.89 appears to be more uniform with a small variation between -3000

a.u. and 2000 a.u. It can be seen from the frequency domain results in Figure 6.17 that the power spectral density of the flame signal of BZS 0.89 appears to dominate heavily over the other conditions particularly between 0 and 30 Hz.

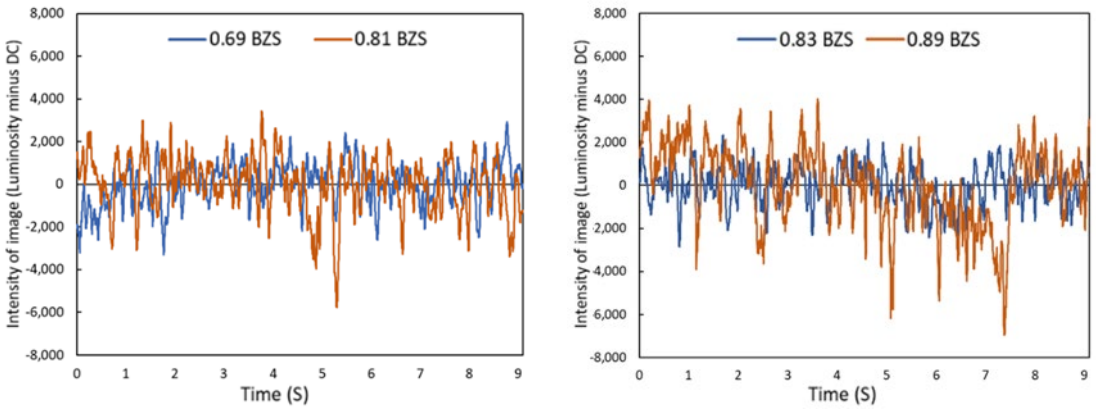

(a) 0.69 BZS to 0.81 BZS stoichiometry (b) 0.83 BZS to 0.89 BZS stoichiometry

Figure 6.16 Flame signals in time domain for different BZS settings

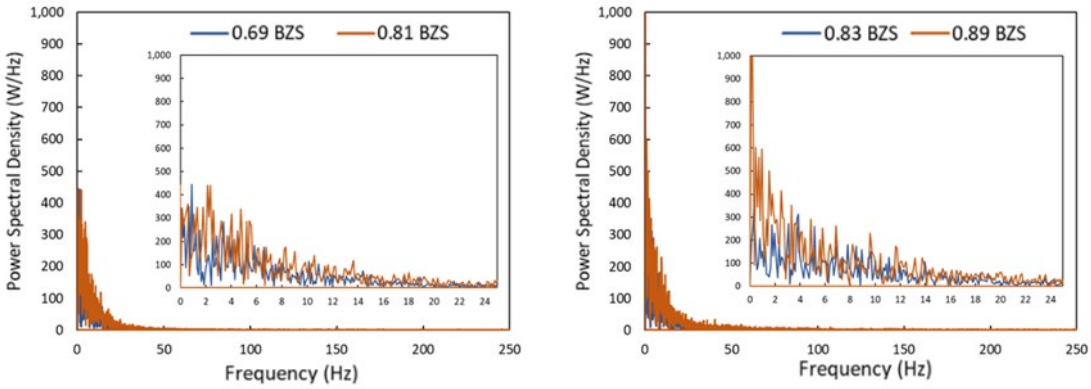

(a) 0.69 BZS to 0.81 BZS stoichiometry (b) 0.83 BZS to 0.89 BZS stoichiometry

Figure 6.17 Flame signals in the frequency domain for different BZS settings.

Figure 6.18 shows the oscillation frequency of the flame for different BZS conditions. The average frequencies are quite uniform with the highest frequency of 6.83 Hz being present under BZS 0.89, it can, however, be seen that the flames under BZS 0.81 and 0.83 have high standard deviations of 1.96 Hz and 3.21 Hz, respectively. This is could indicate that there is an operation performance under such conditions.

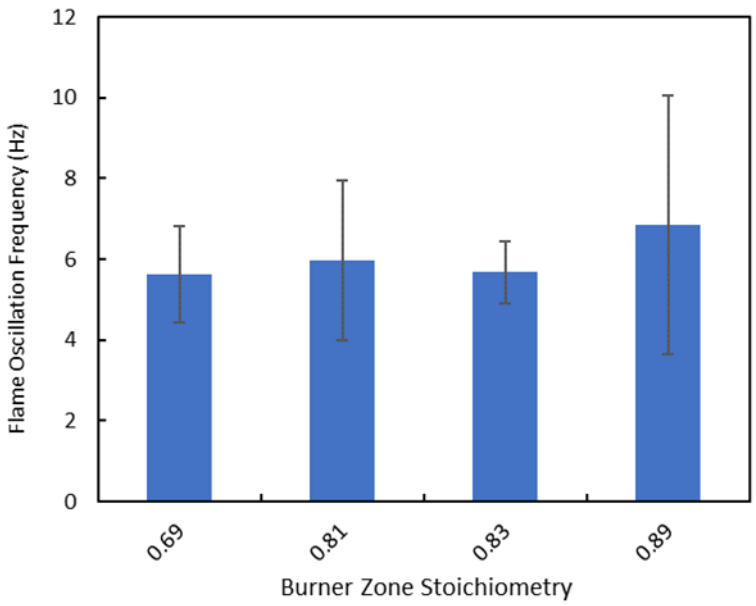

Figure 6.18 Flame oscillation frequency for different BZS settings.

6.3.2.4 Flame Spectra

Figure 6.19 shows the normalised flame spectra under the different BZS settings. A grey straight line is shown across these graphs representing the baseline values taken from BZS 0.81 (i.e., the baseline). The normalised intensity of the light emitted by the flames show that the condition with the lowest levels of stoichiometry, i.e., BZS 0.69 has the weakest signal. Figure 6.20 shows the variations of average peak intensity of C_2^* (590 nm) under the different BZS settings. It is known that the high levels of stoichiometry,

the combustion rate of the coal should be high and therefore the emissive radiation of flame radicles such as C_2^* should also increase. This is evident across these results, as the BZS increases from 0.69 to 0.81 and 0.83 the normalised C_2^* increases to 0.79, 1 and 1.37, respectively. It would then appear that the combustion levels out at BZS 0.89 with a C_2^* radiation of 1.38.

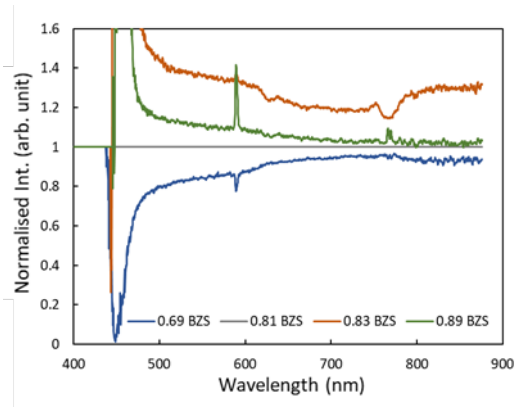

Figure 6.19 Normalised flame spectra for different BZS settings.

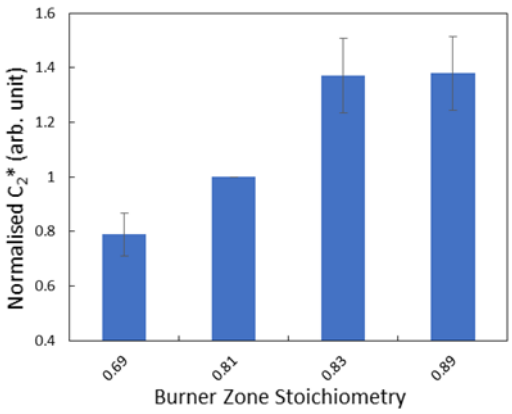

Figure 6.20 Normalised intensity of C_2^* for different BZS settings.

6.4 Prediction of NO_x Emission Using ANN

To effectively evaluate the emission prediction capabilities of the ANN model the data from the eight standard tests are divided into 80% training and 20% performance (the performance set is divided further into 50% validation and 50% testing). The model for this ANN is the same design as the model from 5.4. Only the training data is changed. The training subset is used to compute the gradient, the network weights and biases, while the validation and testing subsets are not included in the initial network development, they are used in two unique ways to ensure there is no overfitting. The validation subset (10% of the overall data size) is monitored during the training process and the errors are

calculated to make adjustments to the network, while the testing subset (10% of the overall data size) is used only after all training is completed to analyse the performance of the network against a set of blind data. 400 data points were used for each input and output parameter. The 14 tests listed below in Table 6.3 were used to train the model, giving a total number of data points of 5600, and therefore, 22400 total inputs when all four parameters are considered.

During this study, it was chosen to analyse the performance of the network, by comparing a similar NO_x emission performance of 0.826 and 1.326, this flame data was obtained from the burner outside the times used within the training data sets. If the model is successfully trained it should be able to yield accurate NO_x predictions.

Figure 6.21 shows the performance of the model trained for the emission prediction of the furnace under the steam injection operating conditions when applied to the validation, training and repeat data subsets. The ideal fit and the relative error lines are plotted as a dash, the results show that the predicted results including 0.826 and 1.326 are extremely close to the idea and none of the predictions fall outside of the 3% error margin, including.

The relative errors of each data point are shown in Figures 6.22 and 6.23 both of these plots show that the majority of the errors for the validation, testing and repeated tests fall below 10%, with validation and testing following a similar trend across the data, it can be seen that the error of 0.826 and 1.326 (test conditions outside of the training matrix) have a very similar and accurate prediction, with only a handful of the 400 test conditions over 5% relative error.

Table 6.3 Test matrix of NO_x predication.

Test No	Load (MW)	Burner outlet PA:Fuel	BZS	PA steam injection (kg/h)	PF Moisture (%w/w)	**NO@6% O_2 (ppm), normalised**
Experimentation	Variation in NOx emission					
1	40.2	3.21	0.81	797	20.1	**1.067**
2	40	3.64	0.79	2015	34.4	**1.000**
3	40	3.97	0.8	2696	40.3	**1.178**
4	40	4.07	0.79	3373	46.2	**1.139**
5	40	4.33	0.78	4125	49.8	**1.184**
6	40	4.8	0.8	5169	55	**1.551**
7	40.2	3.88	0.69	2700	40.3	**0.826**
8	40.2	3.86	0.81	2700	40.3	**1.326**
10	40.2	3.83	0.89	2700	40.3	**1.739**
11	40.2	3.68	0.8	2111	35.2	**1.158**
12	40.2	3.34	0.82	2023	34.4	**0.817**
13	40.2	3.69	0.8	2038	34.5	**0.942**
14	40.1	4.29	0.78	5181	56.1	**1.057**
15	40.2	4.82	0.8	5194	56.2	**1.528**
Rep 1 (7)	40.1	3.84	0.77	2690	40.2	**0.826**
Rep 2 (8)	40.2	3.9	0.83	2700	40.3	**1.326**

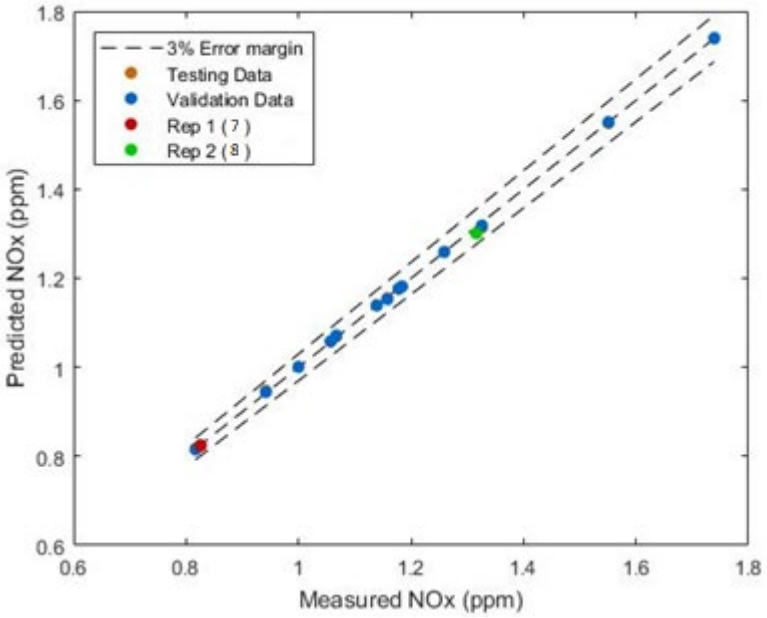

Figure 6.21 Comparison between predicted and measured NO_x emissions.

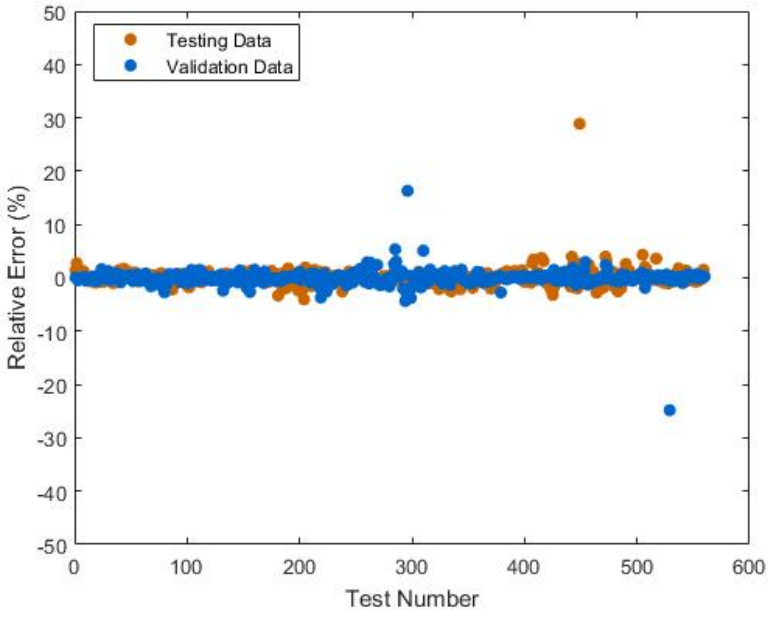

Figure 6.22 Relative error of NO_x prediction for training and validation data

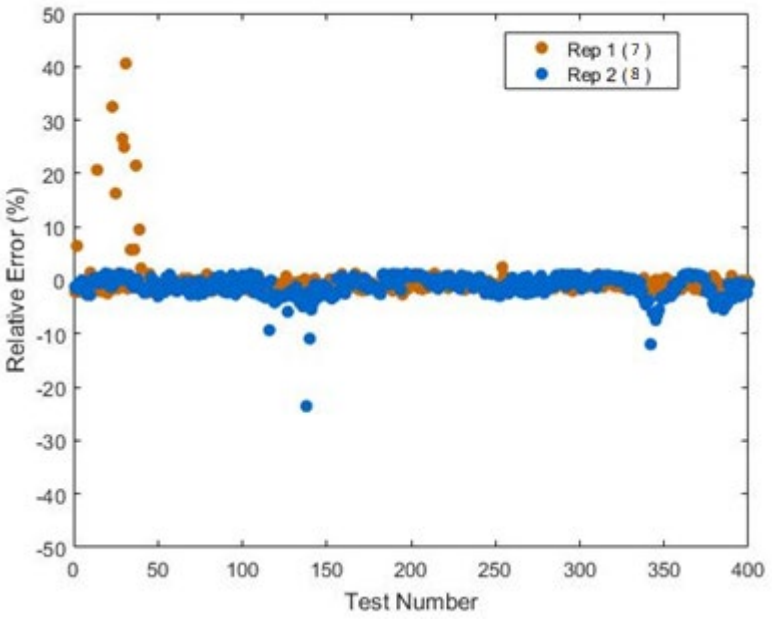

Figure 6.23 Relative error of NO_x prediction for repeat tests.

6.5 Summary

A range of different combustion tests have been explored on the 40 MW_{th} industry-scale coal-fired Combustion Test Facility. The tests have demonstrated the ability to determine flame state with the prototype system and the computational algorithms. It has been demonstrated that the temperature, oscillation frequency and flame radicals such as C_2^* can give a reasonable assessment of the flame.

In addition, the test results were used to train a modest ANN model to discover the best results of NO_x emission prediction. It was therefore discovered that the performance as well as the other benefits such as training time indicate that the ANN is suitable for flame NO_x prediction and errors around 3% have been witnessed.

Chapter 7

Conclusions and Recommendations for Future Work

7.1 Introduction

The research work presented in this thesis is concerned with the development of a methodology for the burner condition monitoring and NO_x prediction in fossil-fuel-fired furnaces. A prototype instrumentation system, combined with digital imaging, spectrometric analysis, image processing and soft computing techniques, has been designed, implemented and evaluated. The system has been tested on a 120 MW_{th} gas-fired heat recovery boiler and a 40 MW_{th} coal-fired CTF. Test results have demonstrated that the system is capable of providing the quantitative measurement of a number of flame characteristic parameters including area, temperature, and oscillation frequency, and intensity of flame radicals (such as C_2^*, OH^*, CH^*, CN^*) under a wide range of combustion conditions, and give the effective prediction of NO_x emissions in the furnaces.

This chapter presents the conclusions that have been drawn from the research programme conducted and makes recommendations for future work in the field.

7.2 Conclusions

7.2.1 Instrumentation System

The instrumentation system developed is mainly comprised of an integrated probe housing a rigid optical probe, fibre optics and a thermocouple, a camera house containing a digital camera, a spectrometer, a thermocouple PCB and a mini-motherboard with associated application software. The system is capable of monitoring simultaneously flame characteristic parameters using a digital camera and a spectrometer. The integration of the optical and electronic components as a single sealed unit has offered the system excellent portability, accessibility to the furnace and robustness. The digital camera and the spectrometer have been proven to be capable of monitoring the flames of industrial furnaces across a wide range of flame radiation intensities with the aid of dedicated software. The mini-motherboard, as the computing core of the system, has shown a high performance in data processing and transmission (to the host computer system).

The accuracy of the temperature measurement has been verified by applying the system to measuring the true of a standard blackbody temperature source in a temperature range from 800 °C C to 1500 °C in the research laboratory. The maximum error of the temperature measurement has been found to be 0.76% occurring at 1225 °C. The performance of the oscillation frequency has also been evaluated by using a standard frequency-varying light source. It has been found that the relative error is no greater than 0.93% in a frequency range of 0 to 300 Hz.

Results obtained on an full-scale boiler and an industrial-scale combustion test facility have demonstrated that the developed system, including all optical, mechanical,

electronic and computing elements, as well as the application software, is operational and reliable in hostile industrial environments.

7.2.2 Tests on the 120 MW_{th} Boiler

A range of burner configurations under two gas turbine power inputs have been explored on the 120 MW_{th} boiler to investigate the flame characteristics of gas-fired flames using the instrumentation system developed. The experimental results have further demonstrated the effectiveness of the system for the burner condition monitoring and NO_x prediction on a full-scale industrial boiler.

7.2.2.1 Burner Condition Monitoring

The results presented in Section 5.3 have demonstrated that the parameters selected for the monitoring of the burners in an industrial boiler are repeatable and reliable. Section 5.4 revealed that the different GT loads and burner configurations have significant impact on the flame stability and combustion state. Flame area under GT 33 MW_{th} tended to increase in size as well as stability as the standard deviation increased as the boiler setting changed from Gun to Spud, while all parameters seemed to remain more uniform under 25 MW_{th}, indicating that the change in gas turbine load affects the combustion state far more greatly. The results have also shown that the flame temperature decreases with the amount of fuel, and the oscillation frequency continues the trend where it could be seen that the lowest average oscillation frequencies are still sampled from tests with the Spud burners ignited on Burner 4.

7.2.2.2 NO_x Prediction

The results obtained from the NO_x prediction using inputs such as temperature, area, normalised average spectral intensity across the whole broadband of the miniature spectrometer and the normalised average peak value of wavelength 568 nm related to C_2^* to train a Bayesian regularised ANN has produced relative errors of around 3%, and maximum relative errors of 8% under real industrial conditions, even when predicting flame data from test conditions that were not ever shown to the network during the training procedure. This demonstrates that this off the shelf hardware with machine learning can be used as an online prediction method for NO_x.

It was also observed in these experiments that the emissive intensity of C_2^* is low in air rich combustion mixtures, with the value increasing significantly with the equivalence ratio approaching and passing beyond the stoichiometric conditions. It was demonstrated through the spectral analysis that the highest value incorporated two Spud burners.

It can therefore be concluded that the poor flame stability may be caused by single Spud burners igniting and using a disproportional amount of the fuel and/or there is a pre-existing problem within the fourth burner itself. In order to achieve the best rates of combustion while emitting the lowest NO_x amounts efforts should be directed to a fault within the Spud burners of Burner 4 as well as ensuring to maintain relatively even fuel flow across the burners.

7.2.3 Tests on the 40 MW_{th} Coal-fired Combustion Test Facility

Extensive industrial trials have been conducted on a 40 MW_{th} coal-fired CTF under a wide range of combustion conditions, including variations in steam injection (to simulate high moisture content), and variations in burner zone stoichiometry. For each test, flame images and spectral signals were acquired, and the flame parameters were quantified based on the proposed computational algorithms. Those include the flame area, temperature, oscillation frequency, and flame radical intensities over the UV and visible (VIS) spectral ranges. As a result of the tests, a better understanding of the flame of coal with high moisture has been achieved. A number of conclusions can be drawn from the presented results.

7.2.3.1 Burner Condition Monitoring

The moisture content of the coal affects significantly the stability of the flame and thus the overall combustion process. It has been found that a high moisture content of the coal gives rise to a smaller flame area, lower flame temperature, but decreased oscillation frequency. Inversely, the results of varied burner zone stoichiometry show a greater flame area, temperature and oscillation frequency. The flame spectra analysis has suggested an improved flame stability with a higher level of stoichiometry. In addition, it has been found the radiative intensity of the detected flame radicals is an important indicator for NO_x production. Reduced NO_x emissions have also been observed when the stoichiometry reaches 0.81, indicating an increase in prompt NO_x formation.

Moreover, a correlation has been found between the flame stability (expressed by the standard deviation of each parameter and the oscillation frequency) and each flame

parameter. It is suggested that maintaining a stable state of stability within these monitored flame parameters is crucial for a stable flame, and therefore reduced NO_x emission.

In summary, the experimental results have demonstrated the satisfactory sensitivity of the system to the variations in combustion conditions tested. It has been proven that the power spectral density, oscillation frequency, flame temperature and spectral analysis can be used as effective parameters for assessing the burner condition.

7.2.3.2 NO_x Prediction

A range of flame characteristics have been extracted from flame images and UV-VIS spectra. These flame characteristics have then been used as the inputs to construct an artificial neural network (ANN) for the NO_x prediction. The results presented in Section 6.6 have demonstrated the effectiveness of the developed Backpropagation ANN for the NO_x prediction, showing that the maximum prediction error is around 3% for all the experimental conditions. Compared to other soft-computing algorithms such as Deep Learning where a great deal of input data are required for constructing the model, the ANN has achieved a similar success rate with reduced flame data for constructing the model, which is particularly important for industrial applications where a great of input data are normally not available. The better performance of the Bayesian regularisation based ANN is believed to be attributed to the use of the Means Squared Error (MSE) and R-Number which regulate effectively the network to ensure less over-fitting. In addition, it should be noted that, although the present work focused on the prediction of NO_x emissions from boilers, the developed soft computing technique is expected to be applicable for predicting the emissions from other pollutants such as SO_2 and CO_2.

In conclusion, the test results have demonstrated the effectiveness of the constructed ANN model as well as the selected flame characteristics and the soft computing techniques for NO_x prediction.

7.3 Recommendations for Future Work

The potential uses of the outcomes of this research programme have been presented and demonstrated within this thesis. However, the monitoring of burner conditions and prediction of NO_x emissions still possess possibilities for improvement. There are a number of areas that require further research and development. This section outlines the areas that should be pursued over the next few years.

One of the possible hardware improvements is the camera. Throughout the course of this research programme a camera with two different modes, i.e., high- resolution and one high-speed, or two cameras, one having a high- resolution and another high-speed, were used for different analysis (i.e., the high resolution camera for the geometric and temperature measurement and the high-speed camera for the oscillation frequency measurement. A camera with both high resolution and fast sampling rate would help to reduce the need for compromise and allow for both measurements to be taken simultaneously. In addition, the use of a high-speed 3CCD camera could potentially provide a true spatial colour distribution, and therefore a more accurate temperature distribution measurement. The modular spectrometer incorporated within this research has a resolution of 2048 and a bandwidth across the UV and VIS spectra (180-900 nm). These parameters could be improved further for a better resolution in order to obtain a higher accuracy of the flame radical measurement. There are also UV-VIS-NIR

spectrometers which can be helpful for monitoring flame radicals over a wider spectral range simultaneously.

During the cause of this research programme, it was discovered that the intensities of radicals such as Sodium (Na) and Potassium (K) where quite profound and prevalent within the spectrum readings. The characteristics of these alkali chlorides are noted as the main cause of furnace fouling and corrosion and could be used for monitoring these concentrations and hence predicting furnace slagging and corrosion. These radicals could also be monitored for on-line fuel tracking, due to their link with the composition of the fuel burnt.

There is also a potential to integrate acoustic techniques alongside the optical/imaging techniques for further flame monitoring. It has been demonstrated that the acoustic information inside the furnace is related to the heat release characteristics of the combustion process and the peak frequency of such an acoustic signal could derive an average temperature of the furnace. Therefore, acoustic flame monitoring could assist the current incorporated two-colour pyrometry approach to achieve more accurate measurements of the flame and thus a better understanding of the combustion process.

Furthermore, in the present study, the calibration of the system was conducted using a blackbody furnace in a laboratory for the temperature measurement as well as the subtraction of blackbody radiation for the spectroscopic analysis. It is worth to calibrate the system under more realistic industrial environments to investigate the effects of industrial environments on these system measurements over a long duration. During the course of this study, the system was only examined on gas- and coal-fired industrial

furnaces. It is worth to evaluate the system under a wider range of combustion conditions over a longer duration.

In addition, it has been previously expressed that the measurement of flame radical emissions through a spectrometer is more efficient when placed as close to the flame front as possible. The separation of individual burner flames has proven to be very complex and difficult if the flames overlapped within the images captured. It would desirable to monitor the flames through the sight-tube of each individual burner, where the existing flame detector is installed. For this to be achieved, it is foreseen that the durability and robustness of the system would have to be improved.

Another possible hardware improvement involves the mini-motherboard. It is reasonable to assume that, with the inclusion of such devices in the industrial environment, many of these devices may be required, which would significantly increase the system complexity and cost. There is a possibility to construct a centralised computing module to control simultaneously multiple cameras/spectrometers to provide a more reliable and robust solution, and more importantly, an alternative that is cheaper and has lower power consumption.

Finally, the work reported in this thesis concludes that the information provided by the system offers very useful quantitative data regarding the combustion state of the furnace, this could therefore be used either, automatically, by a control system to drive a control if it is linked with a combustion parameter such as air-to-fuel ratio and equivalence ratio online. Alternatively, manually through an operator to diagnose the burner condition, NO_x emissions or indication of the occurrence of abnormal combustion events to ensure immediate actions to be taken.

The work demonstrated in this thesis has shown the potential of advanced flame monitoring and emission prediction through digital imaging and spectrometry. It is more than feasible that such techniques will lead to a robust instrumentation system for the control and diagnosis of industrial combustion facilities.

References

[1] M. Moinul Hossain, G. Lu, Y. Yan, and D. Sun, “Three-dimensional reconstruction of flame temperature and emissivity through tomographic imaging and pyrometric measurement,” *IST 2012 - 2012 IEEE Int. Conf. Imaging Syst. Tech. Proc.*, pp. 13–17, 2012.

[2] H. Zhou, Q. Tang, L. Yang, Y. Yan, G. Lu, and K. Cen, “Support vector machine based online coal identification through advanced flame monitoring,” *Fuel*, vol. 117, no. PARTB, pp. 944–951, 2014.

[3] D. Sun, G. Lu, and Y. Yan, “An embedded imaging and signal processing system for flame stability monitoring and characterisation,” *2010 IEEE Int. Conf. Imaging Syst. Tech. IST 2010 - Proc.*, pp. 210–213, 2010.

[4] J. Ballester, R. Hernández, A. Sanz, A. Smolarz, J. Barroso, and A. Pina, “Chemiluminescence monitoring in premixed flames of natural gas and its blends with hydrogen,” *Proc. Combust. Inst.*, vol. 32, no. 2, pp. 2983–2991, 2009.

[5] G. Lu, Y. Yan, and M. Colechin, “A digital imaging based multifunctional flame monitoring system,” *IEEE Trans. Instrum. Meas.*, vol. 53, no. 4, pp. 1152–1158, 2004.

[6] J. Ballester and T. Garc??a-Armingol, “Diagnostic techniques for the monitoring and control of practical flames,” *Prog. Energy Combust. Sci.*, vol. 36, no. 4, pp. 375–411, 2010.

[7] X. Li, D. Sun, G. Lu, J. Krabicka, and Y. Yan, “Prediction of NOx emissions throughflame radical imaging and neural network based soft computing,” *IST 2012 - 2012 IEEE Int. Conf. Imaging Syst. Tech. Proc.*, vol. 44, no. 0, pp. 502–505, 2012.

[8] D. Sun, “Flame Stability and Burner Condition Monitoring through Optical Sensing and Digital Imaging,” *Ph.D. Thesis, Univ. Kent*, no. November, 2012.

[9] Y. Yan, T. Qiu, G. Lu, M. M. Hossain, G. Gilabert, and S. Liu, “Recent advances in flame tomography,” *Chinese J. Chem. Eng.*, vol. 20, no. 2, pp. 389–399, 2012.

[10] N. Li *et al.*, “Prediction of Pollutant Emissions of Biomass Flames Using Digital Imaging , Contourlet Transform and Radial Basis Function Network Techniques,” 2014.

[11] N. Li, G. Lu, X. Li, Y. Yan, and D. Arts, “Prediction of NOx Emissions from a Biomass Fired Combustion Process through Digital Imaging , Non- negative Matrix Factorization and Fast Sparse Regression,” vol. 44, no. 0, 2015.

[12] L. R. Boeck, M. Kellenberger, G. Rainsford, and G. Ciccarelli, “Simultaneous OH-PLIF and schlieren imaging of flame acceleration in an obstacle-laden channel,” vol. 000, pp. 1–8, 2016.

[13] D. Sun, G. Lu, H. Zhou, X. Li, and Y. Yan, “A Simple Index Based Quantitative Assessment of Flame Stability,” vol. 44, no. 0, pp. 2–5, 2013.

[14] D. Sun, G. Lu, H. Zhou, and Y. Yan, “Flame stability monitoring and

characterization through digital imaging and spectral analysis," *Meas. Sci. Technol.*, vol. 22, no. 11, p. 114007, 2011.

[15] N. Li, G. Lu, X. Li, and Y. Yan, "Prediction of NOx Emissions from a Biomass Fired Combustion Process Based on Flame Radical Imaging and Deep Learning Techniques," *Combust. Sci. Technol.*, vol. 2202, no. October, p. 151005142401005, 2015.

[16] and J. B. Jackson, P., "Enhancing Techniques for Flame Monitoring.," *Control and Instrumentation*, vol. 19, no. 9. 1987.

[17] L. Arias, S. Torres, D. Sbarbaro, and O. Farias, "Photodiode-based sensor for flame sensing and combustion-process monitoring," no. November, 2008.

[18] Forney, "HD Flame Detector Manual," *Publ. 372001-17 Rev. A*, 2018.

[19] F. Xu and X. Zhang, "Test on application of flame detector for large space environment," *Procedia Eng.*, vol. 52, pp. 489–494, 2013.

[20] a R. Jones, "Flame failure detection and modern boilers," *J. Phys. E.*, vol. 21, pp. 921–928, 2000.

[21] T. E. Willson, P. M., & Chappell, "Pulverised Fuel Flame Monitoring in Utility Boilers.," *Measurement and Control*, vol. 18, no. 2. pp. 66–72, 1985.

[22] "Thermocouples and sample probes for combustion studies," *Prog. Energy Combust. Sci.*, vol. 19, no. 3, pp. 259–278, 1993.

[23] R. Souri, A. Negarestani, S. Souri, M. Farzan, and M. Mahani, "Design and construction of a new ultraviolet sensor using CsI deposition in the ionization chamber," *Nucl. Eng. Technol.*, vol. 50, no. 5, pp. 751–757, 2018.

[24] C. Kranz, "A new flame detection method for two channels infrared flame detectors," pp. 209–213, 2002.

[25] G. Heskestad and J. S. Newman, "Fire detection using cross-correlations of sensor signals," *Fire Safety Journal*, vol. 18, no. 4. pp. 355–374, 1992.

[26] O. Lloyd, "Method of and Apparatus for Flame Monitoring." UK patent No 2085253, 1981.

[27] D. P. Nolan, "Fire and Gas Detection and Alarm Systems," *Handb. Fire Explos. Prot. Eng. Princ.*, pp. 181–201, 2010.

[28] K. Kim and D. W. Hahn, "Interaction between iron based compound and soot particles in diffusion fl ame," *Energy*, vol. 116, pp. 933–941, 2016.

[29] D. Gu, Z. Sun, G. J. Nathan, P. R. Medwell, Z. T. Alwahabi, and B. B. Dally, "Improvement of precision and accuracy of temperature imaging in sooting flames using two-line atomic fluorescence (TLAF)," *Combust. Flame*, vol. 167, pp. 481–493, 2016.

[30] Z. W. Jiang, Z. X. Luo, and H. C. Zhou, "A simple measurement method of temperature and emissivity of coal-fired flames from visible radiation image and its application in a CFB boiler furnace," *Fuel*, vol. 88, no. 6, pp. 980–987, 2009.

[31] H. W. Huang and Y. Zhang, "Flame colour characterization in the visible and infrared spectrum using a digital camera and image processing," *Meas. Sci.*

Technol., vol. 19, no. 8, 2008.

[32] K. Sujatha, D. Pappa, and A. Kalaivani, "Combustion Quality Estimation in Power Station Boilers using Median Threshold Clustering Algorithms," *Int. J. Eng. Sci. Technol.*, vol. 2, no. 7, pp. 2623–2631, 2010.

[33] F. Wang *et al.*, "The research on the estimation for the NO x emissive concentration of the pulverized coal boiler by the flame image processing technique q," vol. 81, no. x, pp. 2113–2120, 2002.

[34] G. Lu, Y. Yan, Y. Huang, and A. Reed, "Intelligent vision system for monitoring and control of combustion flames," *Meas. Control*, vol. 32, no. 6, pp. 164–168, 1999.

[35] L. Xu and Y. Yan, "A new flame monitor with triple photovoltaic cells," *IEEE Trans. Instrum. Meas.*, vol. 55, no. 4, pp. 1416–1421, 2006.

[36] C. Romero, X. Li, S. Keyvan, and R. Rossow, "Spectrometer-based combustion monitoring for flame stoichiometry and temperature control," *Appl. Therm. Eng.*, vol. 25, no. 5–6, pp. 659–676, 2005.

[37] T. Parameswaran, R. Hughes, P. Gogolek, and P. Hughes, "Gasification temperature measurement with flame emission spectroscopy," *Fuel*, vol. 134, pp. 579–587, 2014.

[38] M. M. Hossain, G. Lu, and Y. Yan, "Measurement of flame temperature distribution using optical tomographic and two-color pyrometric techniques," *2012 IEEE I2MTC - Int. Instrum. Meas. Technol. Conf. Proc.*, pp. 1856–1860, 2012.

[39] Y. taik Han, K. hyeon Lee, and K. doug Min, "A study on the measurement of temperature and soot in a constant-volume chamber and a visualized diesel engine using the two-color method," *J. Mech. Sci. Technol.*, vol. 23, no. 11, pp. 3114–3123, 2010.

[40] Y. Huang, Y. Yan, and G. Riley, "Vision-based measurement of temperature distribution in a 500-kW model furnace using the two-colour method," *Meas. J. Int. Meas. Confed.*, vol. 28, no. 3, pp. 175–183, 2000.

[41] D. Sun, G. Lu, H. Zhou, and Y. Yan, "Measurement of soot temperature, emissivity and concentration of a heavy-oil flame through pyrometric imaging," *2012 IEEE I2MTC - Int. Instrum. Meas. Technol. Conf. Proc.*, pp. 1865–1869, 2012.

[42] H. Li *et al.*, "Simultaneous identification of multi-combustion-intermediates of alkanol-air flames by femtosecond filament excitation for combustion sensing," *Sci. Rep.*, vol. 6, no. February, pp. 1–7, 2016.

[43] Y. Su, H. Song, and Y. Lv, "Recent advances in chemiluminescence for reactive oxygen species sensing and imaging analysis," vol. 146, no. December 2018, pp. 83–97, 2019.

[44] Y. Liu, J. Tan, H. Wang, and L. Lv, "Characterization of heat release rate by OH* and CH* chemiluminescence," *Acta Astronaut.*, vol. 154, no. August 2018, pp. 44–51, 2019.

[45] Y. Yuan, S. Li, F. Zhao, Q. Yao, and M. B. Long, "Characterization on hetero-

homogeneous ignition of pulverized coal particle streams using CH* chemiluminescence and 3 color pyrometry," *Fuel*, 2015.

[46] D. Alviso, M. Mendieta, J. Molina, and J. C. Rolon, "Image representation of flames from data processing of an optical multichannel analyzer spectrometer," *Symp. Signals, Images Artif. Vis. - 2013, STSIVA 2013*, 2013.

[47] J. Krabicka, G. Lu, and Y. Yan, "Profiling and characterization of flame radicals by combining spectroscopic imaging and neural network techniques," *IEEE Trans. Instrum. Meas.*, vol. 60, no. 5, pp. 1854–1860, 2011.

[48] S. Karnani and D. Dunn-rankin, "Visualizing CH* chemiluminescence in sooting flames," *Combust. Flame*, vol. 160, no. 10, pp. 2275–2278, 2013.

[49] T. Dreier and C. Schulz, "Simultaneous measurement of localized heat-release with OH / CH 2 O – LIF imaging and spatially integrated OH * chemiluminescence in turbulent swirl flames," *Proc. Combust. Inst.*, vol. 34, no. 2, pp. 3549–3556, 2013.

[50] B. Li, D. Zhang, M. Yao, and Z. Li, "Strategy for single-shot CH 3 imaging in premixed methane / air flames using photofragmentation laser-induced fluorescence," vol. 000, pp. 1–9, 2016.

[51] C. D. Carter, S. Hammack, and T. Lee, "High-speed flamefront imaging in premixed turbulent flames using planar laser-induced fluorescence of the CH C − X band," vol. 168, pp. 66–74, 2016.

[52] B. Zhou, J. Kiefer, J. Zetterberg, Z. Li, and M. Aldén, "Strategy for PLIF single-shot HCO imaging in turbulent methane / air flames," *Combust. Flame*, vol. 161, no. 6, pp. 1566–1574, 2014.

[53] J. Kiefer, F. Ossler, Z. S. Li, and M. Ald??n, "Spectral interferences from formaldehyde in CH PLIF flame front imaging with broadband B-X excitation," *Combust. Flame*, vol. 158, no. 3, pp. 583–585, 2011.

[54] D. Gu, Z. Sun, G. J. Nathan, P. R. Medwell, Z. T. Alwahabi, and B. B. Dally, "Improvement of precision and accuracy of temperature imaging in sooting flames using two-line atomic fluorescence (TLAF)," *Combust. Flame*, vol. 0, pp. 1–13, 2015.

[55] T. Kathrotia, U. Riedel, and J. Warnatz, "A numerical study on the relation of OH*, CH*, and C2* chemiluminescence and heat release in premixed methane flames," *Proc. Eur. Combust. Meet.*, pp. 2–6, 2009.

[56] N. Lamoureux, K. Marschallek-watroba, P. Desgroux, J. Pauwels, M. D. Sylla, and L. Gasnot, "Measurements and modelling of nitrogen species in CH 4 / O 2 / N 2 flames doped with NO , NH 3 , or NH 3 + NO," *Combust. Flame*, vol. 176, pp. 48–59, 2017.

[57] Z. Ruzheng, S. Wenyu, T. Tao, and Y. Bin, "Species diagnostics and modeling study of laminar premixed flames fueled by acetone – butanol – ethanol," *Proc. Combust. Inst.*, vol. 000, pp. 1–8, 2016.

[58] T. Nishimura, A. Yamamoto, T. Torii, and K. Matsumoto, "Development of Laser Ionization Mass Spectrometer for detection of unstable species in fl ames," *Microchem. J.*, vol. 95, no. 1, pp. 50–56, 2010.

[59] G. Magnotti and R. S. Barlow, “Dual-resolution Raman spectroscopy for measurements of temperature and twelve species in hydrocarbon – air flames,” pp. 1–9, 2016.

[60] S. Ihantola, J. Sand, K. Peräjärvi, J. Toivonen, and H. Toivonen, “Fluorescence-assisted gamma spectrometry for surface contamination analysis,” *IEEE Trans. Nucl. Sci.*, vol. 60, no. 1, pp. 305–309, 2013.

[61] Y. Toya, T. Itagaki, and K. Wagatsuma, “Spectrochimica Acta Part B Correlation between the Gas Temperature and the Atomization Behavior of Analyte Elements in Flame Atomic Absorption Spectrometry Estimated with a Continuum-light-source Spectrometer System,” *Spectrochim. Acta Part B At. Spectrosc.*, vol. 125, pp. 146–151, 2016.

[62] N. R. Canada, N. R. Canada, N. R. Canada, and N. R. Canada, “Petroleum coke gasification temperatures and flame spectra at high pressure,” 2015.

[63] C. Tung and S. Hochgreb, “Flame structure , spectroscopy and emissions quantification of rapeseed biodiesel under model gas turbine conditions,” *Appl. Energy*, vol. 185, pp. 1383–1392, 2017.

[64] A. J. Ferrer-Riquelme, “1.04 - Statistical Control of Measures and Processes.” Elsevier, pp. 97–126, 2009.

[65] D. G. M. J. F. P. V. G. Sainz, *Fault Detection and Diagnosis using Multivariate Statistical Techniques in a Wastewater Treatment Plant* ., vol. 42, no. 11. IFAC, 2004.

[66] W. A. Shewhart, “Application of statistical methods to manufacturing problems.” Journal of the Franklin Institute, Volume 226, Issue 2, pp. 163–186, 1938.

[67] E. S. Page, “Continuous Inspection Schemes,” *Biometrika*, vol. 41, no. 1/2, pp. 100–115, 1954.

[68] R. Abujiya, M. Riaz, and M. H. Lee, “Enhanced Cumulative Sum Charts for Monitoring Process Dispersion,” pp. 1–22, 2015.

[69] J. S. Hunter, “The Exponentially Weighted Moving Average,” *J. Qual. Technol.*, vol. 18, no. 4, pp. 203–210, Oct. 1986.

[70] A. Bakdi and A. Kouadri, “A new adaptive PCA based thresholding scheme for fault detection in complex systems,” *Chemom. Intell. Lab. Syst.*, vol. 162, no. August 2016, pp. 83–93, 2017.

[71] S. J. Qin, “Annual Reviews in Control Survey on data-driven industrial process monitoring and diagnosis,” *Annu. Rev. Control*, vol. 36, no. 2, pp. 220–234, 2012.

[72] B. Scholkopf, A. Smola, and K. R. Muller, “Nonlinear Component Analysis as a Kernel Eigenvalue Problem,” no. 44, 1996.

[73] J. Lee, C. Yoo, S. Wook, P. A. Vanrolleghem, and I. Lee, “Nonlinear process monitoring using kernel principal component analysis,” vol. 59, pp. 223–234, 2004.

[74] H. W. Huang and Y. Zhang, “Imaging based chemiluminescence characterisation of partially premixed syngas flames through DFCD technique,” *Int. J. Hydrogen*

Energy, vol. 38, no. 11, pp. 4839–4847, 2013.

[75] D. Sbarbaro, O. Farias, and A. Zawadsky, "Real-time monitoring and characterization of flames by principal-component analysis," *Combust. Flame*, vol. 132, no. 3, pp. 591–595, 2003.

[76] R. Hernández and J. Ballester, "Flame imaging as a diagnostic tool for industrial combustion," *Combust. Flame*, vol. 155, no. 3, pp. 509–528, 2008.

[77] O. John and S. Prince, "Classification of flame and fire images using feed forward neural network," *2014 Int. Conf. Electron. Commun. Syst. ICECS 2014*, no. 1, pp. 1–6, 2014.

[78] L. Xu, Y. Yan, S. Cornwell, and G. Riley, "On-line Fuel Tracking by Combining Principal Component Analysis and Neural Network Techniques," vol. 54, no. 4, pp. 1640–1645, 2005.

[79] Y. Lv, T. Yang, and J. Liu, "An adaptive least squares support vector machine model with a novel update for NOx emission prediction," *Chemom. Intell. Lab. Syst.*, vol. 145, pp. 103–113, 2015.

[80] S. S. Mane, "Temperature Measurement Based on Image Processing & Neural Network," 2015.

[81] Z. Hao, C. Kefa, and M. Jianbo, "Combining neural network and genetic algorithms to optimize low NO x pulverized coal combustion," vol. 80, no. x, pp. 2163–2169, 2001.

[82] J. Ma, F. Xu, K. Huang, and R. Huang, "Improvement on the linear and nonlinear auto-regressive model for predicting the NOx emission of diesel engine," *Neurocomputing*, vol. 207, pp. 150–164, 2016.

[83] N. Li, G. Lu, S. Member, X. Li, and Y. Yan, "Prediction of Pollutant Emissions of Biomass Flames Through Digital Imaging , Contourlet Transform , and Support Vector Regression Modeling," vol. 64, no. 9, pp. 2409–2416, 2015.

[84] E. Lughofer, V. Macián, C. Guardiola, and E. Peter, "Identifying static and dynamic prediction models for NOx emissions with evolving fuzzy systems," *Appl. Soft Comput. J.*, vol. 11, no. 2, pp. 2487–2500, 2011.

[85] A. Senegac, "Multi-step-ahead prediction of NOx emissions for a coal-based boiler," vol. 106, no. 2013, pp. 89–99, 2016.

[86] F. Wang, S. Ma, H. Wang, Y. Li, and J. Zhang, "Control Engineering Practice Prediction of NO X emission for coal-fired boilers based on deep belief network," *Control Eng. Pract.*, vol. 80, no. X, pp. 26–35, 2018.

[87] Henke Sass Wolf, "Technische Endoskope," *Tec-line*, 2016.

[88] P. Class, O. Size, S. Model, and G. Shutter, "Specification Sensor UI-3280CP-C-HQ Rev . 2 (AB00851) Pin assignment I / O connector," vol. 2, pp. 1–2, 2019.

[89] Ocean Optics, "USB2000+ Data Sheet," pp. 1–38, 2016.

[90] T. C. C. Inc.(COMMELL), "LP-173 User Manual," 2017.

[91] F. Bore and S. S. Body, "PN16 Flanged Stainless Steel Wafer Ball Valve – LV6340," *Leengate Valve*, 2016.

[92] J. C. Frakes, “SeaBreeze Manual,” *Ocean Opt.*, pp. 1–16, 2016.

[93] J. G. K. J. F. K. L. Zucherman, “Digital image analysis of a turbulent flame,” vol. 6, no. 1, pp. 16–24, 1998.

[94] M. Hossain, G. Lu, Y. Yan, and A. S. Brief, “Tomographic Imaging Based Measurement of Three- Dimensional Geometric Parameters of a Burner Flame,” *Ieee*, pp. 3–6, 2014.

[95] H. Zhao and N. Ladommatos, “Optical diagnostics for soot and temperature measurement in diesel engines,” *Prog. Energy Combust. Sci.*, vol. 24, no. 3, pp. 221–255, 1998.

[96] Y. Huang, Y. Yan, G. Lu, and A. Reed, “On-line flicker measurement of gaseous flames by image processing and spectral analysis,” *Meas. Sci. Technol.*, vol. 10, no. 8, pp. 726–733, 1999.

[97] M. Shimura, T. Ueda, G. M. Choi, M. Tanahashi, and T. Miyauchi, “Simultaneous dual-plane CH PLIF, single-plane OH PLIF and dual-plane stereoscopic PIV measurements in methane-air turbulent premixed flames,” *Proc. Combust. Inst.*, vol. 33, no. 1, pp. 775–782, 2011.

[98] H. W. Huang and Y. Zhang, “Syngas combustion radiation profiling through spectrometry and DFCD processing techniques,” *Int. J. Hydrogen Energy*, vol. 37, no. 6, pp. 5257–5267, 2012.

[99] C. Poynton, “Digital Video and HD - Colour science for video,” *Morgan Kaufmann Ser. Comput. Graph.*, no. 26, pp. 287–314, 2012.

[100] H. D. Cheng, X. H. Jiang, Y. Sun, and J. Wang, “Color image segmentation : advances and prospects,” vol. 34, no. September 2000, 2001.

[101] Y. Wang, Y. Cui, S. Chen, and P. Zhang, “Study on HSI Color Model-Based Fruit Quailty Evaluation,” *2010 3rd Int. Congr. Image Signal Process.*, vol. 6, pp. 2677–2680, 2010.

[102] S. Ling, “SpectraSuite Installation Installation and Operation Manual,” *Ocean Opt.*, no. 000, 2009.

[103] J. Meseguer, I. Pérez-Grande, and A. Sanz-Andrés, “Thermal radiation heat transfer,” *Spacecr. Therm. Control*, pp. 73–86, 2012.

[104] F. Li, L. Xu, Z. Cao, and M. Du, “A Chemi-ionization Processing Approach for Characterizing Flame Flicklering Behavior,” 2015.

[105] R. B. King, “Relative Transition Probabilities of the Swan Bands of Carbon,” *Astrophys. Journal.*, vol. 108, no. 752, pp. 429–433, 1948.

[106] A. Smithells and R. K. Dekosky, “The swan band spectrum of carbon,” *Proc. Phys. Soc.*, vol. 40, no. 1, pp. 71–78, 1927.

[107] T. Li, J. Sun, Y. Yuan, C. Xu, Y. Shuai, and H. Tan, “Simulation of calibration process in fl ame measurement by plenoptic camera,” *Appl. Therm. Eng.*, vol. 135, no. October 2017, pp. 179–187, 2018.

[108] J. Smart, G. Lu, Y. Yan, and G. Riley, “Characterisation of an oxy-coal flame through digital imaging,” *Combust. Flame*, vol. 157, no. 6, pp. 1132–1139, 2010.

[109] S. Zhang, G. Shen, L. An, and Y. Niu, “Online monitoring of the two-dimensional temperature fi eld in a boiler furnace based on acoustic computed tomography,” *Appl. Therm. Eng.*, vol. 75, pp. 958–966, 2015.

[110] F. D. Foresee and M. T. Hagan, “Gauss-Newton approximation to Bayesian learning,” *Proc. Int. Conf. Neural Networks*, 1997.

[111] C. E. Rasmussen, C. K. I. Williams, G. Processes, M. I. T. Press, and M. I. Jordan, *Gaussian Processes for Machine Learning*. 2006.

[112] J. Krabicka, G. Lu, and Y. Yan, “A spectroscopic imaging system for flame radical profiling,” *2010 IEEE Int. Instrum. Meas. Technol. Conf. I2MTC 2010 - Proc.*, pp. 1387–1391, 2010.

Appendix 1: Program for Computation of Flame Parameters

```
%************************************************************%
%File name:          computeFlameParameters.m
%Synopses:           1)Load video
%                        2)Take individual frames
%                        3)Carry out thresholding
%                        4)Create Binary mask
%                        5)Map boundaries to Burners
%                        6)Convert to HSI
%                        7)Calculate Temperature distribution
%                        8)Mask individual flames
%                        9)save images and data
%Programmer:         James Cugley, EDA, University of Kent
%Date:               August 1, 2016
%************************************************************%

clear all; close all; clc;

P1 = 0.3093;%  (183.8, 236)
P2 = -1.123;%  (-1813, -1538)
P3 = 1.872;%  (4013, 4368)

TEMPERATURE_MAX = 1800;         % maximum temperature(unit: °C)
TEMPERATURE_MIN = 900;          % minimum temperature(unit: °C)

OFFSET         = 2/256;         % noise intensity grey level (default: 2; gain boost: 5)
NOISE_THRESHOLD = 15/256;       % threshold

expT = 1; %set exposure time in ms.

optional = 1;
TempImg = 0;
write = 1;
output = 1;

cd 'I:\August2018\Camera\High Res'
PathName = uigetdir;
cd('I:\Code\Temperatre');
 dataMeanFFT = [];
 dataMeanPSD = [];
%OFFSET = 15/256;

Mmax = 0;
Count = 0;
Count2 = 0;
```

```
Count3 = 0;
TempCount = 0;

Gslide = 0.24; % Full GT
%Gslide = 0.25; % Low GT


nhood = true(19);

%normalizedThresholdValue = 0.1;

FileNames = getAllFilesAvi(PathName);
%AveTemp = zeros(size(FileNames)-1);
for iFileName = 1:size(FileNames,1)
   disp(FileNames{iFileName});
end
cd(PathName);
%mkdir('Analysis')

   for iImg = 1:size(FileNames,1)
   PathFileName = char(FileNames(iImg));
%% Initialize variables
FileName = strsplit(char(FileNames(iImg)),'\');
FileName = char(FileName(end));


if (any(PathName ~= 0) && any(FileName ~=0))
   vidObj    = VideoReader([PathFileName]);
   vidFrames = vidObj.NumberOfFrames;
   vidHeight = vidObj.Height;
   vidWidth  = vidObj.Width;
   vidFormat = vidObj.VideoFormat;
   disp(['Loading FIle... ' FileName]);

else
   disp('File selection has been cancelled');
   return;
end
    vidFPS    = vidObj.FrameRate;
%N = vidFPS;       %Set Framerate for a second
imgSum = [];
N = floor(vidFrames);                    %Set Framerate for a second
S = [];

AveTemp = []; F1AveTemp = []; F2AveTemp = []; Ms = []; F1Ms = []; F2Ms = []; Mh
= []; F1Mh = []; F2Mh = []; Mi = []; F1Mi = []; F2Mi = []; Ch = []; F1Ch = []; F2Ch =
[]; Cs = []; F1Cs = []; F2Cs = []; Ci = []; F1Ci = [];F2Ci = [];

blobAreaTot = [];
F1blobAreaTot = [];
F2blobAreaTot = [];
```

```
%% Extract images from video and calculate the intensity(brightness) of each image
   disp(['Extracting ' num2str(N) ' frames from video...']);
   for jImage = 1:15:N % one second capture

                sortCentroid = [];
            index2 = [];
            MaxCentroid = [];
            M = [];
            I = [];

          imgRgb = im2double(read(vidObj,jImage));
          %Calibration
           imgG = rgb2gray(imgRgb);
           %imgSG = rgb2gray(imgSat);
             cd('I:\Code\Temperatre\New');
           imgB = createMask(imgRgb,Gslide);
           imgBfull = bsxfun(@times, imgB, cast(imgSatR,class(imgB)));

 labeledImage = bwlabel(imgB, 8);
 blobMeasurements = regionprops(labeledImage, imgG, 'all');
 numberOfBlobs = size(blobMeasurements, 1);

 coloredLabels = label2rgb (labeledImage, 'hsv', 'k', 'shuffle'); % pseudo random color
lab
allAreas = [blobMeasurements.Area];
[sortedAreas, sortIndexes] = sort(allAreas, 'ascend');

 disp(['F1: ' num2str(sortedAreas(end))])
 disp(['F2: ' num2str(sortedAreas(end-1))])
% TempCount = TempCount +1;

 disp(Count2);

while sortedAreas(end) > 70000 || sortedAreas(end-1) < 2000

 disp(['F1: ' num2str(sortedAreas(end))])
 disp(['F2: ' num2str(sortedAreas(end-1))])

 Count3 = Count3 + 0.01;
 imgB = createMask(imgRgb,Gslide+Count3);

    imgBfull = bsxfun(@times, imgB, cast(imgSatR,class(imgB)));

labeledImage = bwlabel(imgB, 8);
blobMeasurements = regionprops(labeledImage, imgG, 'all');
numberOfBlobs = size(blobMeasurements, 1);

coloredLabels = label2rgb (labeledImage, 'hsv', 'k', 'shuffle'); % pseudo random color
lab
allAreas = [blobMeasurements.Area];
[sortedAreas, sortIndexes] = sort(allAreas, 'ascend');
```

```
end
Count3 = 0;
for k = 1:size(sortIndexes,2)
   sortCentroid(k) = blobMeasurements(sortIndexes(k)).Centroid(2);
end
MaxCentroid = sortCentroid(end-1:end);
[M,I] = max(MaxCentroid);
[M2,I2] = min(MaxCentroid);
MaxCentroidIndex = sortIndexes(end-1:end);

 for i = 1:size(sortIndexes,2)-2
    [c2(i) index2(i)] = min(abs(MaxCentroid-sortCentroid(i)));
 end

 for l = 1: size(index2,2)
index2(l) = MaxCentroidIndex(index2(l));
end

 for j = 1:size(index2,2)
    labeledImage(labeledImage == sortIndexes(j)) = index2(j);
 end

 blobMeasurements2 = regionprops(labeledImage, imgG, 'all');

 thisBlob1 = ismember(labeledImage, MaxCentroidIndex(I2));
 thisBlob2 = ismember(labeledImage, MaxCentroidIndex(I));

  coloredLabels2 = label2rgb (labeledImage, 'hsv', 'k', 'shuffle'); % pseudo random color
lab

  cd('I:\Code\Temperatre');
%[BW1,maskedRGBImage] = createMask(imgRgb);

F1imgBfull = thisBlob1;
F2imgBfull = thisBlob2;

          F1imgRgb = bsxfun(@times, imgRgb, cast(F1imgBfull,class(imgRgb)));
          F2imgRgb = bsxfun(@times, imgRgb, cast(F2imgBfull,class(imgRgb)));

imgRgb2 = bsxfun(@times, imgRgb, cast(imgB, 'like', imgRgb));


  cd('I:\Code\Temperatre\New');

      imgHSI = rgb2hsiD(imgRgb);
      imgHSI2 = bsxfun(@times, imgHSI, cast(imgB, 'like', imgHSI));
      F1imgHSI = bsxfun(@times, imgHSI, cast(F1imgBfull,class(imgHSI)));
      F2imgHSI = bsxfun(@times, imgHSI, cast(F2imgBfull,class(imgHSI)));
      F1imgRgb2 = bsxfun(@times, imgRgb2, cast(F1imgBfull,class(imgRgb2)));
      F2imgRgb2 = bsxfun(@times, imgRgb2, cast(F2imgBfull,class(imgRgb2)));
```

```
      %imgHSI3 = bsxfun(@times, imgHSI2, cast(imgB,class(imgHSI2)));
      imgG2 = bsxfun(@times, imgG, cast(imgB,class(imgG)));
      F1imgG2 = bsxfun(@times, imgG2, cast(F1imgBfull,class(imgG2)));
      F2imgG2 = bsxfun(@times, imgG2, cast(F2imgBfull,class(imgG2)));
      %imgG3 = bsxfun(@times, imgG2, cast(imgB,class(imgG2)));
      [F2tempDis,F2TempImg,F1tempDis,F1TempImg,tempDis,imgTempDis,TempImg]
=
get2dtd_New(imgRgb,imgB,F1imgBfull,F2imgBfull,P1,P2,P3,OFFSET,NOISE_THRE
SHOLD,WINDOW_SIZE,TEMPERATURE_MIN,TEMPERATURE_MAX);


      F1imgTempDis = bsxfun(@times, imgTempDis,
cast(F1imgBfull,class(imgTempDis)));
      F2imgTempDis = bsxfun(@times, imgTempDis,
cast(F2imgBfull,class(imgTempDis)));

%       figure(1) to visually inspect threshold
%  drawnow
%
%        subplot(3, 3, 1)
%             imshow(imgRgb);
%        subplot(3, 3, 2)
%              imshow(imgB);
%        subplot(3, 3, 3)
%            imshow(imgTempDis);
%        subplot(3, 3, 4)
%             imshow(F1imgBfull);
%        subplot(3, 3, 5)
%             imshow(F2imgBfull);
%        subplot(3, 3, 6)
%             imshow(F1imgTempDis);
%        subplot(3, 3, 7)
%             imshow(F2imgTempDis);

Count = Count +1;
    Count2 = Count2 +1;
     S = vertcat(S,Count2);
    if write == 1
 %if Count == 5
    cd([PathName '\Thesis\Images' ])
    mkdir(char(FileName(1:end-4)))
    cd(char(FileName(1:end-4)))


 imwrite(imgRgb2,['Test ' char(FileName(1:end-4)) ' Image '  int2str(Count2) '
RGB.png']);
   imwrite(F1imgRgb2,['Test ' char(FileName(1:end-4)) ' Image '  int2str(Count2) ' F1
RGB.png']);
   imwrite(F2imgRgb2,['Test ' char(FileName(1:end-4)) ' Image '  int2str(Count2) ' F2
RGB.png']);
 imwrite(imgG2,['Test ' char(FileName(1:end-4)) ' Image '  int2str(Count2) ' GS.png']);
```

```
   imwrite(F1imgG2,['Test ' char(FileName(1:end-4)) ' Image '  int2str(Count2) ' F1
GS.png']);
   imwrite(F2imgG2,['Test ' char(FileName(1:end-4)) ' Image '  int2str(Count2) ' F2
GS.png']);
 imwrite(imgB,['Test ' char(FileName(1:end-4)) ' Image '  int2str(Count2) ' BI.png']);
   imwrite(F1imgBfull,['Test ' char(FileName(1:end-4)) ' Image '  int2str(Count2) ' F1
BI.png']);
   imwrite(F2imgBfull,['Test ' char(FileName(1:end-4)) ' Image '  int2str(Count2) ' F2
BI.png']);
imwrite(imgHSI2,['Test ' char(FileName(1:end-4)) ' Image '  int2str(Count2) '
HSI.png']);
   imwrite(F1imgHSI,['Test ' char(FileName(1:end-4)) ' Image '  int2str(Count2) ' F1
HSI.png']);
   imwrite(F2imgHSI,['Test ' char(FileName(1:end-4)) ' Image '  int2str(Count2)  ' F2
HSI.png']);
 imwrite(imgTempDis,['Test ' char(FileName(1:end-4)) ' Image '  int2str(Count2) '
T.png']);
   imwrite(F1imgTempDis,['Test ' char(FileName(1:end-4)) ' Image '  int2str(Count2) '
F1 T.png']);
   imwrite(F2imgTempDis,['Test ' char(FileName(1:end-4)) ' Image '  int2str(Count2) '
F2 T.png']);

Count = 0;
cd('I:\Code\Temperatre');
 end

if sum(F1imgBfull(:) == 1) > 0 && sum(F2imgBfull(:) == 1) > 0
F1blobAreaTot(Count2,1) = sum(F1imgBfull(:) == 1);
F2blobAreaTot(Count2,1) = sum(F2imgBfull(:) == 1);

cd(PathName);
end


nfft = (floor(vidFPS)); % WIndow size set to sample rate
nwft = N/nfft; % data split into windows


cd 'I:\Code\Temperatre'

    F1imgH = F1imgHSI(:,:,1);
    F1imgS = F1imgHSI(:,:,2);
    F1imgI = F1imgHSI(:,:,3);
    F1Hnan = F1imgH;F1Hnan(F1Hnan==0)=NaN;
    F1Snan = F1imgS;F1Snan(F1Snan==0)=NaN;
    F1Inan = F1imgI;F1Inan(F1Inan==0)=NaN;

    F2imgH = F2imgHSI(:,:,1);
    F2imgS = F2imgHSI(:,:,2);
    F2imgI = F2imgHSI(:,:,3);
    F2Hnan = F2imgH;F2Hnan(F2Hnan==0)=NaN;
```

```
F2Snan = F2imgS;F2Snan(F2Snan==0)=NaN;
F2Inan = F2imgI;F2Inan(F2Inan==0)=NaN;

F1HrowMean = sum(F1imgH,2) ./ sum(F1imgH~=0,2);
F1HrowMean(isnan(F1HrowMean))=0;
F1Mh(Count2,1) = sum(F1HrowMean,1) ./ sum(F1HrowMean~=0,1);
F1Mh(isnan(F1Mh))=0;

F1SrowMean = sum(F1imgS,2) ./ sum(F1imgS~=0,2);
F1SrowMean(isnan(F1SrowMean))=0;
F1Ms(Count2,1) = sum(F1SrowMean,1) ./ sum(F1SrowMean~=0,1);
F1Ms(isnan(F1Ms))=0;

F1IrowMean = sum(F1imgI,2) ./ sum(F1imgI~=0,2);
F1IrowMean(isnan(F1IrowMean))=0;
F1Mi(Count2,1) = sum(F1IrowMean,1) ./ sum(F1IrowMean~=0,1);
F1Mi(isnan(Mi))=0;

F2HrowMean = sum(F2imgH,2) ./ sum(F2imgH~=0,2);
F2HrowMean(isnan(F2HrowMean))=0;
F2Mh(Count2,1) = sum(F2HrowMean,1) ./ sum(F2HrowMean~=0,1);
F2Mh(isnan(F2Mh))=0;

F2SrowMean = sum(F2imgS,2) ./ sum(F2imgS~=0,2);
F2SrowMean(isnan(F2SrowMean))=0;
F2Ms(Count2,1) = sum(F2SrowMean,1) ./ sum(F2SrowMean~=0,1);
F2Ms(isnan(F2Ms))=0;

F2IrowMean = sum(F2imgI,2) ./ sum(F2imgI~=0,2);
F2IrowMean(isnan(F2IrowMean))=0;
F2Mi(Count2,1) = sum(F2IrowMean,1) ./ sum(F2IrowMean~=0,1);
F2Mi(isnan(Mi))=0;



F1Ch(Count2,1) = nanstd(F1Hnan(:),[],1);
F1Ch(isnan(F1Ch))=0;
F1Cs(Count2,1) = nanstd(F1Snan(:),[],1);
F1Cs(isnan(F1Cs))=0;
F1Ci(Count2,1) = nanstd(F1Inan(:),[],1);
F1Ci(isnan(F1Ci))=0;

F2Ch(Count2,1) = nanstd(F2Hnan(:),[],1);
F2Ch(isnan(F2Ch))=0;
F2Cs(Count2,1) = nanstd(F2Snan(:),[],1);
F2Cs(isnan(F2Cs))=0;
F2Ci(Count2,1) = nanstd(F2Inan(:),[],1);
F2Ci(isnan(F2Ci))=0;

 cd(PathName);
```

```
blobAreaTot(jImage,1) = sum(imgB(:) == 1);
 flameIntensity(jImage,1) = sum(sum(imgG2)); % Overall Intensity
 flameBrightness(jImage,1)    = flameIntensity(jImage,1)/blobAreaTot(jImage,1); %
Brightness
 flameNonuniformity(jImage,1) = sum(sum(abs(imgG) -
flameBrightness(jImage,1)*255))/(flameBrightness(jImage,1)*blobAreaTot(jImage,1)*
255); % Nonuniformity
 flameNonuniformityABS(jImage,1) = abs(flameNonuniformity(jImage,1));
F1AveTemp(Count2,1) = F1TempImg;
F2AveTemp(Count2,1) = F2TempImg;

    end
    blobAreaTot = horzcat(F1blobAreaTot,F2blobAreaTot);
    AveTemp = horzcat(F1AveTemp,F2AveTemp);
    Mh = horzcat(F1Mh,F2Mh);
    Ms = horzcat(F1Ms,F2Ms);
    Mi = horzcat(F1Mi,F2Mi);
    Ch = horzcat(F1Ch,F2Ch);
    Cs = horzcat(F1Cs,F2Cs);
    Ci = horzcat(F1Ci,F2Ci);
Count2 = 0;
disp('Complete.');

input = 0;
output = 0;

  Label1 = ["F1 Area","F2 Area","F1 Mh","F2 Mh","F1 Ms","F2 Ms","F1 Mi","F2
Mi","F1 Ch","F2 Ch","F1 Cs","F2 Cs","F1 Ci","F2 Ci"];

 Label3 = ["Frame"];

 Label4 = ["F1 Temperature","F2 Temperature"];


 Out1 = [blobAreaTot,Mh,Ms,Mi,Ch,Cs,Ci];

  Out3 = vertcat(Label3,S);

 Out4 = vertcat(Label1,Out1);

 Out6 = vertcat(Label4,AveTemp);
 Par2 = horzcat(Out3,Out4,Out6);
     if write == 1
  xlswrite(['Test ' char(FileName(1:end-4)) ' with ' num2str(N) ' Frames New Parameters
2 '],Par2);
     end
     end
disp('Complete.');
```

Appendix 2: Program for Computation of Flame Temperature

```
%************************************************************%
%File name:          get2dtd_New.m
%Synopses:           1)Load video
%                    2)Take individual frames
%                    3)Create temperature distribution
%                    4)mask flame 1 and 2
%                    5)create image of pseudo colour map
%                    6)output image and data of flames
%Programmer:         James Cugley, EDA, University of Kent
%Date:               August 1, 2016
%************************************************************%

function
[F2tempDis,F2TempImg,F1tempDis,F1TempImg,tempDis,imgTempDis,TempImg,Tem
pImgMin,TempImgMax] =
get2dtd_New(imgRgb,imgBfull,F1imgBfull,F2imgBfull,P1,P2,P3,OFFSET,NOISE_T
HRESHOLD,WINDOW_SIZE,TEMPERATURE_MIN,TEMPERATURE_MAX)

colorMode      = 64;          % 16, 32, 64, 128 or 256
colorCode      = jet(colorMode);% from blue to red, low temperature to high
temperature
                        % if only part of color space is required, then e.g., colorCode =
colorCode(33:end,:); colorMode   = 32;
imgColorBar    = imrotate(repmat(reshape(colorCode,colorMode,1,3),1,4),180);


tIncrement     = (TEMPERATURE_MAX-TEMPERATURE_MIN)/colorMode;

height  = size(imgRgb,1);
width   = size(imgRgb,2);

lamda1 = 0.62 ; % Wave lenght for Red Channel in micrometers (610 nm) 3130
lamda2 = 0.54;  % Wave lenght for Green Channel in micrometers (540 nm)3130

deltalamda1 = 0.0525; % Band With for Red Channel Deltlamda1 in micrometers (95
nm) 3130
deltalamda2 = 0.15; % Band With for Green Channel Deltlamda2 in micrometers(90
nm)     3130

C2 = 14388; % Planck's second constant C2 = 1.4388*10^(-2)mK

K1 = C2*(1.0/lamda2-1.0/lamda1);
K2 = (lamda1/lamda2).^5;
```

```
BndRatio = deltalamda2/deltalamda1; %Band width Ratio

%% Smooth flitering
if WINDOW_SIZE>1
   %disp('Smooth filtering...');
   w       = ones(WINDOW_SIZE,WINDOW_SIZE);
   w       = w/sum(w(:));
   imgRgbF = zeros(height,width);

   imgRgbF(:,:,1) = filter2(w,imgRgb(:,:,1),'same');
   imgRgbF(:,:,2) = filter2(w,imgRgb(:,:,2),'same');
   imgRgbF(:,:,3) = filter2(w,imgRgb(:,:,3),'same');

   imgRgb = imgRgbF;
end


%% Compute temperature (matched with PC application)
% disp('Computing temperature...');
tempDis = zeros(height,width);
for jRow=1:height
   for iColumn=1:width

      g1 = imgRgb(jRow,iColumn,1);   % g1 = R
      g2 = imgRgb(jRow,iColumn,2);   % g2 = G

      if ( (g1>NOISE_THRESHOLD) && (g2>NOISE_THRESHOLD) )          %
remove offset (dark response)
         g1 = g1 - OFFSET;
         g2 = g2 - OFFSET;

                        ratio = g1/g2;    % intensity ratio of g1 to g2
         temp = K1/[log(ratio) + log(P1*ratio + P2 + P3) + log(K2)+log(BndRatio)];

          if ( (temp<=TEMPERATURE_MAX) && (temp>=TEMPERATURE_MIN) )
% results beyond [MIN,MAX] are considered as error [0°C]
             tempDis(jRow,iColumn) = temp;
          elseif (temp<=TEMPERATURE_MIN)
             tempDis(jRow,iColumn) = 0;
          elseif (temp>=TEMPERATURE_MAX)
             tempDis(jRow,iColumn) = 0;
          end
      else
         tempDis(jRow,iColumn) = 0;
      end
   end
end
tempDis = bsxfun(@times, tempDis, cast(imgBfull,class(tempDis)));
TempImg = mean2(tempDis(tempDis>0));

F1tempDis = bsxfun(@times, tempDis, cast(F1imgBfull,class(tempDis)));
```

```
F1TempImg = mean2(F1tempDis(F1tempDis>0));

F2tempDis = bsxfun(@times, tempDis, cast(F2imgBfull,class(tempDis)));
F2TempImg = mean2(F2tempDis(F2tempDis>0));


%% Map temperature to color
imgTempDis = zeros(size(tempDis,1),size(tempDis,2),3);
%if optional == 1
   %disp('Map temperature to color...');
   for jRow = 1:height
      for iColumn = 1:width
         if tempDis(jRow,iColumn)==0
            imgTempDis(jRow,iColumn,:) = 0;
         else
            if tempDis(jRow,iColumn)<=TEMPERATURE_MIN
               imgTempDis(jRow,iColumn,:) = colorCode(1,:);
            else
               if tempDis(jRow,iColumn)>=TEMPERATURE_MAX
                  imgTempDis(jRow,iColumn,:) = colorCode(end,:);
               else
                  colorIndex = ceil((tempDis(jRow,iColumn) -
TEMPERATURE_MIN)/tIncrement);
                  imgTempDis(jRow,iColumn,:) = colorCode(colorIndex,:);
               end
            end
         end
      end
   end
end
```

Appendix 3: Program for Computation of Flame Oscillation Frequency

```
%************************************************************%
%File name:          computeOscillationFrequency.m
%Synopses:           1)Load video
%                        2)Take indivisual frames
%                        3)Compute luminosity
%                        4)Calculate PSD
%                        5)Display oscillation frequency graphs
%                        6)Save flame data
%Programmer:         James Cugley, EDA, University of Kent
%Date:               August 1, 2016
%************************************************************%

clear all; close all; clc;

LoadP = 'I:\August2018\Camera\High Speed\GT full load\Results';
cd(LoadP);
dwtmode('per')

count4 = 0;
input = 1;
output = 0;
Level = 2;

sumA = 0;sumA2 = 0;
sumB = 0;sumB2 = 0;

%Generate Sine Wave Time Specifications
if input ~= 1
Fs = 900;             % samples per second
N = Fs;
dt = 1/Fs;            % seconds per sample
S = 6;               % seconds
t = (0:dt:S-dt);
%Sine wave
Fa = 300;
 Fa1 = 6.5; % hertz
 Fa2 = 12.3; % hertz

x = 10*sin(2*pi*Fa*t);
%x = 20*sin(2*pi*Fa1*t)+10*sin(2*pi*Fa2*t);
end

%% Load data
if input == 1
```

```
[fname,pname] = uigetfile('*.txt','Select a file');
if (any(pname ~= 0) && any(fname ~=0))
   data = load([pname fname]);
else
   disp('File selection has been cancelled');
   return;
end

disp(['Loading FIle... ' fname]);
disp('Calculating Mean, FFT and PSD');
fname2 = fname(1:end-4);
InfoExt = strsplit(fname2);
fname3 = str2double(InfoExt(end));
Z = str2double(erase(InfoExt(1),"Hz"));
N = fname3;

else
data = x;
   pname = char([LoadP '\' num2str(Fa) 'Hz']);
   fname = char([num2str(Fa) 'Hz.txt']);
end

M = length(data); %FFT BLOCK LENGTH

cfd = zeros(Level,M);
nbcol = 128;
WaveLet = 'db8';
S = M/N;
Fc = N/2;
Fs = N;
dt = 1/Fs;
t = (0:dt:S-dt);
%t2 = (0:M-1)*dt;              % Time vector
% Calculate DC
imgIntMean  = mean(data(:)); % DC
%Remove DC
data2(:) = data(:) - imgIntMean;
% % %Normalise Signal
   dataNorm = data2/(max(data2));
dataWL = data2;
L = zeros(Level,(Level+2));
cA = zeros(Level,(M/2));
freq = zeros(Level,(M));
[Ctemp, Ltemp] = wavedec(dataWL,Level,WaveLet);
C = zeros(Level,length(Ctemp));
count = 0;
count2 = 0;
check1 = 0;
count3 = 0;

figure(10)
```

```
set(gcf, 'Units', 'Normalized', 'OuterPosition', [0 0 1 1]);

for i = 1:Level
   hold on
[Ctemp, Ltemp] = wavedec(dataWL,i,WaveLet);

[C(i,1:length(Ctemp)),L(i,1:i+2)] = wavedec(dataWL,i,WaveLet); %perform a level i
decomposition of the signal
cA(i,(1:ceil(M/2^i))) = appcoef(C(i,1:length(Ctemp)),L(i,1:i+2),WaveLet,i); %extract
the level i approximation coefficients
cD(i,(1:ceil(M/2^i))) = detcoef(C(i,1:length(Ctemp)),L(i,1:i+2),i); %extract the levels 3,
2, and 1 detail coefficients
A(i,:) = wrcoef('a',C(i,1:length(Ctemp)),L(i,1:i+2),WaveLet,i); %reconstruct the level i
approximation
D(i,:) = wrcoef('d',C(i,1:length(Ctemp)),L(i,1:i+2),WaveLet,i); %reconstruct the details
at levels 1 - i

count = count + 1;
 subplot(Level,2,count); plot(A(i,:));
 title(['Approximation A' num2str(i)])
 xlim([0 M/2]);
 count = count + 1;
 subplot(Level,2,count); plot(D(i,:));
 title(['Detail D' num2str(i)])
  xlim([0 M/2]);

ANorm = A(i,:)/(max(A(i,:)));
ANorm(ANorm<0)=[];
dataNorm(dataNorm<0)=[];

if check1 == 0
if mean(ANorm) > mean(dataNorm) * 0.6
   count2 = count2 + 1;
else
   check1 = 1;
end
end

end
if count2 == 0;
   count2 = count2 + 1;
end

hold off
cfdw2 = wcodemat(D,nbcol,'row');

figure(11)
set(gcf, 'Units', 'Normalized', 'OuterPosition', [0 0 1 1]);
colormap(pink(128));
image(cfdw2);
tics = 1:Level;
```

```
labs = int2str(tics');
ax = gca;
ax.YTickLabelMode = 'manual';
ax.YDir = 'normal';
ax.Box = 'On';
ax.YTick = tics;
ax.YTickLabel = labs;
title('Discrete Transform, absolute coefficients');
ylabel('Level');

% Perform fft
imgIntFft = abs(fft(data2(:)));

imgIntFftAi = abs(fft(A(count2,:)));
% Compute the square magnitude of the complex FFT output array
imgIntPsd = imgIntFft.^2/M; % Calculates better weighted frequency
imgIntPsdAi = imgIntFftAi.^2/M; % Calculates better weighted frequency
imgIntPsd2 = 2*imgIntFft/M; % Calculates better power for plotting
 imgIntPsd(1) = imgIntPsd(1)/2;
  imgIntPsdAi(1) = imgIntPsdAi(1)/2;
imgIntPsd2(1) = imgIntPsd2(1)/2;
% Find frequency Bin that has the largest energy
[pkB,MaxFreqB] = findpeaks(imgIntPsd,'NPeaks',1,'SortStr','descend');
% Compute frequency (Hz) of the largest spectral component
peakFrequency = MaxFreqB(1);
peakFrequencyflicker = ((peakFrequency-1)*N)/M;

% average Psd into seconds to plot
M2 = ceil(M/2);
freq = [0:M2-1]*(1/S);

% compute rolling fft.
nfft = N; % WIndow size set to sample rate
nwft = M/nfft; % data split into windows

for i = 1:nwft
    m = 1+(i-1)*nfft;%set start position of window
    n = m-1+nfft; %set end position of window
    y1(m:n) = data2(m:n); % creates rolling data points (y1 = data2);
    yAi(m:n) = A(count2,m:n); % creates rolling data points (y1 = data2);
    yf = fft(y1(m:n)); % creates rolling fft
    yAif = fft(yAi(m:n)); % creates rolling fft
    yfa = abs(yf); % magnitude
       yAifa = abs(yAif); % magnitude
    yfas = (yfa*2) / nfft;
       yAifas = (yAifa*2) / nfft;
    yfaPSD = yfa.^2 / nfft;
       yAifaPSD = yAifa.^2 / nfft;
    yfaPSD(1) = yfaPSD(1)/2;
       yAifaPSD(1) = yAifaPSD(1)/2;
    yyf(i,1:nfft/2) = yfas(1:nfft/2); % calculates final fft for window i
```

```
      yyAif(i,1:nfft/2) = yAifas(1:nfft/2); % calculates final fft for window i
   yyfPSD(i,1:nfft/2) = yfaPSD(1:nfft/2);
      yyAifPSD(i,1:nfft/2) = yAifaPSD(1:nfft/2);
end

% Compute demoninator
  for i = 1:size(yyfPSD,1)
  Flicker3(i,1) = (sum(yyfPSD(i,:).*[1:length(yyfPSD)])/sum(yyfPSD(i,:)))-1;
  end
  for i = 1:size(yyfPSD,2)
  yyfPSDm(1,i) = sum(yyfPSD(:,i))/size(yyfPSD,1);
  end

    for i = 1:size(yyAifPSD,1)
  FlickerAi2(i,1) = (sum(yyAifPSD(i,:).*[1:length(yyAifPSD)])/sum(yyAifPSD(i,:)))-1;
    end

  for i = 1:size(yyAifPSD,2)
  yyAifPSDm(1,i) = sum(yyAifPSD(:,i))/size(yyAifPSD,1);
  end

maxi = max(yyfPSDm); % largest value within windows
yyfPSDm = yyfPSDm/maxi; % normalises fft to maximum (1)

% Compute demoninator
  for i = 1:M2
  sumB(i) =  imgIntPsd(i);
  sumBAi(i) = imgIntPsdAi(i);
  sumB2(i) =  imgIntPsd2(i);
  end
% Compute numerator
  for i = 1:M2
  sumA(i) =  imgIntPsd(i)*i-1;
  sumAAi(i) =  imgIntPsdAi(i)*i-1;
  sumA2(i) =  imgIntPsd2(i)*i;
  end
% Compute total sum of demoninator and numerator
TotSumA = sum(sumA);
TotSumB = sum(sumB);
TotSumAAi = sum(sumAAi);
TotSumBAi = sum(sumBAi);
 TotSumA2 = sum(sumA2);
 TotSumB2 = sum(sumB2);
% Compute flicker
for i = 1:M2
flickerTEST(i) =  sumA(i)/sumB(i);
end
flickerTEST2 = mean(flickerTEST(2:900))
flicker =  ((((TotSumA/TotSumB))*N)/M);
flicker2 =  ((((TotSumA2/TotSumB2))*N)/M);
flickerAi =  ((((TotSumAAi/TotSumBAi))*N)/M);
```

```
for i = 1:Level
imgIntFftAi2(i,:) = abs(fft(A(i,:)));
imgIntPsdAi2(i,:) = imgIntFftAi2(i,:).^2/M;
imgIntPsdAi2(i,1) = imgIntPsdAi2(i,1)/2;

  for j = 1:M2
  sumBi2(i,j) =  imgIntPsdAi2(i,j);
  end

  for j = 1:M2
  sumAi2(i,j) =  imgIntPsdAi2(i,j)*j;
  end

TotSumAi2(i) = sum(sumAi2(i,:));
TotSumBi2(i) = sum(sumBi2(i,:));

flickeri2(i) =  ((((TotSumAi2(i)/TotSumBi2(i))-1)*N)/M);
disp(flickeri2(i))

end

flickeri2v = flickeri2';

%compute frequency
[pkC,MaxFreqC] = findpeaks(imgIntPsd,'NPeaks',1,'SortStr','descend');
fprintf('The largest peak is %.2f. Hz\n',MaxFreqC(1) -1);
fprintf('The calculated frequency of the largest component is %.2f.
Hz\n',peakFrequencyflicker);
fprintf('The calculated flicker 1 is %.2f. Hz\n',flicker);
fprintf('The calculated flicker 2 is %.2f. Hz\n',flicker2);
fprintf('The calculated wavelet transform approximation flicker is %.2f.
Hz\n',flickerAi);
fprintf('The calculated mean rolling flicker  is %.2f. Hz\n',mean(Flicker3));
t_rounded = round(t,3);

%Plot Graphs
f = figure(12);
set(gcf, 'Units', 'Normalized', 'OuterPosition', [0 0 1 1]);
p = uipanel('Parent',f,'BorderType','none');
p.TitlePosition = 'centertop';
p.FontSize = 16;
p.FontWeight = 'bold';

 subplot (1,2,1,'Parent',p);

plot(data2(1:100)); %Plot Frame Number

xlabel('Time (S)');%Plot Time
ylabel('Intensity of image (Luminosity) Minus DC');
```

```
xticklabels([t_rounded(1:10:110)]);
freq(1,numel(data)) = 0;
freqv=freq';

subplot(1,2,2,'Parent',p);
plot(freqv(1:M2),abs(imgIntPsd2(1:M2)),'b')
xlabel('Frequency (Hz)');
ylabel('Power Spectral Density (W/Hz)');
xlim([0 15]);

figure(13)
set(gcf, 'Units', 'Normalized', 'OuterPosition', [0 0 1 1]);
yyf(:,1) = [];
surf(yyf)
shading interp
title('Frequency and Spectra captured from High Speed Camera over Time')
ylabel('Time (S)')
xlabel('Frequency (Hz)')
zlabel('Spectrum (Magnitude)')

figure(14)
set(gcf, 'Units', 'Normalized', 'OuterPosition', [0 0 1 1]);
yyfPSD(:,1) = [];
surf(yyfPSD)
shading interp
title('PSD captured from High Speed Camera over Time')
ylabel('Time (S)')
xlabel('Frequency (Hz)')
zlabel('Power spectral density (W/Hz)')

if output == 1

data2v = data2';
datav = data';
Asave = A';
Dsave = D';
cAsave = cA';cAsave(numel(datav),1) = 0;
cDsave = cD';cDsave(numel(datav),1) = 0;

 labels1 = ["Image Intensity","Image Intensity (minusDC)","FFT","PSD
(FFT^2)","Power (FFT*2)"];
 for j = 1:Level
 labelsD(j) = string(['Detail (Reconstruction) ' num2str(j)]);
 labelsA(j) = string(['Approx (Reconstruction) ' num2str(j)]);
 labelscD(j) = string(['Detail (Coefficient) ' num2str(j)]);
 labelscA(j) = string(['Approx (Coefficient) ' num2str(j)]);
 labelsWT(j) = string(['Wavelet Transform Approximation Flicker ' num2str(j)]);
 end

 labelsOut = horzcat(labels1,labelscD,labelscA,labelsD,labelsA);
```

```
labelFreq = string("Frequency");
labelFFT = string("Moving Window FFT");
labelPSD = string("Moving Window PSD");
FFTdist = size(yyf);FFTdist = FFTdist(2);
labelFFTdist = char(['A' num2str(FFTdist+2)]);
PSDdist = char(['A' num2str(FFTdist+3)]);
labelDatadist = char(['A' num2str(M+2)]);
labelDatadist2 = char(['A' num2str(M+8)]);

labels2a = ["FPS";"Largest Peak";"Frequency of the Largest Component";"Flicker"];
labels2b = labelsWT;
labels2c = ["Rolling FFT Flicker"];
labels2 = vertcat(labels2a,labels2b');

Results1 =
horzcat(datav,data2v,imgIntFft,imgIntPsd,imgIntPsd2,cDsave,cAsave,Dsave,Asave);
Out1 = vertcat(labelsOut,Results1);

freqv = vertcat(labelFreq,freqv);

Out1 = horzcat(freqv,Out1);

Results2 = vertcat(Fs,(MaxFreqC(1)-1),peakFrequencyflicker,flicker,flickeri2v);
Out2 = horzcat(labels2,Results2);
Flicker3Std = std(Flicker3);
Out3 = horzcat(labels2c,Flicker3',Flicker3Std);

cd(pname)

end

dwtmode('sym')
disp('Complete.')
```

Appendix 4: Program for Computation of Flame Spectral Signals

```
%*************************************************************%
%File name:          collectSpectra.m
%Synopses:                  1)Load txt
%                           2)Extract wavelengths
%                           3)Compute Relative irradiance
%                           4)extract flame radicals
%                           5)Save flame data
%Programmer:         James Cugley, EDA, University of Kent
%Date:               August 1, 2016
%*************************************************************%

clear all;close all;clc;

output = 1;

h = 6.626068e-34;
c = 2.99792458e8;
k = 1.38064852e-23;
Tc = 3100;
n = zeros(2048,1);
n(1:2048) = 1;

SReads1 = 0;
SReads2 = 0;

Wl1 = 689; %CH*1 (432nm)
Wl2 = 698; %C2* (436nm)
Wl3 = 342; %OH*1 (306nm)
Wl4 = 571; %CN* (390nm)
Wl5 = 1141; %Na (589nm)
Wl6 = 1686; %K (390nm)

%% Load Dark Scan and wavelengths.
cd('I:\Doosan 041017\Calibration\Spectrometer');
disp('load DARK spectrum FILE');
[DarkFile,DarkPath] = uigetfile('*.txt;');
DarkFullPath = fullfile(DarkPath,DarkFile);
cd('X:\Data\Sheffield\Sheffield 29032017\Data\Processing\matlab');
FID = fopen(DarkFullPath);
%FID = fopen('X:\Data\Spectrometer Calibration\10000 Int\VIS_DARK_10000Int.txt');
DarkCell = textscan(FID, '%*s %f', 'HeaderLines', 17, 'CollectOutput', 2);
FID2 = fopen(DarkFullPath);
%FID2 = fopen('X:\Data\Spectrometer Calibration\10000
Int\VIS_DARK_10000Int.txt');
WaveCell = textscan(FID2, '%f %*s', 'HeaderLines', 17, 'CollectOutput', 2);
```

```
fclose(FID);
Dark = DarkCell{1};
Wave = WaveCell{1};
WaveM = Wave*1e-9;
%% Load Light Scan.
cd(DarkPath);
disp('load LIGHT spectrum FILE');
[LightFile,LightPath] = uigetfile('*.txt;');
LightFullPath = fullfile(LightPath,LightFile);
cd('X:\Data\Sheffield\Sheffield 29032017\Data\Processing\matlab');
FID = fopen(LightFullPath);
%FID = fopen('X:\Data\Spectrometer Calibration\10000
Int\VIS_LIGHT_10000Int.txt');
LightCell = textscan(FID, '%*s %f', 'HeaderLines', 17, 'CollectOutput', 2);
fclose(FID);
Light = LightCell{1};
%% Calculate Bw
for i = 1:size(Wave)
Therm{i} = ( (h*c) / (WaveM(i)*k*Tc) );
Therm2{i} = exp(Therm{i});
%Therm3{i} = Therm2{i} - 1;
BlackRef{i} = ( (2*h*(c.^2)) / ( ((WaveM(i).^5) * Therm2{i}) ) -1 );
end
Bw = cell2mat(BlackRef);
Bw(Bw<0) = 0;
Bw = Bw.';
Therm = Therm.';
BlackRef = BlackRef.';
BLNorm = 100 / max(Bw) ;
BLmax = bsxfun(@times, Bw,BLNorm);
BwNorm = bsxfun(@rdivide, Bw,max(Bw));

%% Load folder and find files.
disp('load BASELINE spectrums PATH');
cd('I:\Doosan 041017');
pathName = uigetdir;
cd('X:\Data\Sheffield\Sheffield 29032017\Data\Processing\matlab');
FileNames = getAllFilesTxt(pathName);
Size =  60;%size(FileNames,1); % Set limit of number of files (10, 50, 100, 250,
Current is ALL)
cd(pathName);
sb = regexp(pathName, '\', 'split');
sb1 = sb(length(sb)-1);

%% Open first file and capture Wavelength.
%disp(FileNames{1});
FID=fopen(FileNames{1});
datacell = textscan(FID, '%f%*f', 'HeaderLines', 17, 'CollectOutput', 2);
fclose(FID);
```

```
Scans = [];ScansRelIrr = [];ScansMinusDark = [];ScansMinusLight =
[];ScansMinusDarkBase = [];normalisedBWNormRelIrr =
[];numDivScansMinusDarkBase = [];
fprintf('Reading %d Files.\n',Size)

iFileName1 = 1;
iFileName2 = 1;

%% Open Baseline.
while SReads1 < Size
%for iFileName = 1:Size
   FID = fopen(FileNames{iFileName1});
   %SampleCell = textscan(FID, '%*s %f', 'HeaderLines', 17, 'CollectOutput', 2); %if
header
   SampleCell = textscan(FID, '%*s %f', 'HeaderLines', 0, 'CollectOutput', 2); % no
header
   Sample = SampleCell{1};
   fclose(FID);

   numBase = Sample(:,1) - Dark(:,1); %creates dark subtract
   numBase(numBase<0) = 0;
   OnesnumBase = find(numBase==0);

   ScansMinusDarkBase = horzcat(ScansMinusDarkBase,numBase);
   ScansMinusDarkBase(ScansMinusDarkBase<0) = 0;
   SReads1 = SReads1 + 1;

iFileName1 = iFileName1 + 1;
end

%% Load folder and find files.
disp('load SAMPLE spectrums PATH');
cd('I:\Doosan 041017');
pathName = uigetdir;
cd('X:\Data\Sheffield\Sheffield 29032017\Data\Processing\matlab');
FileNames = getAllFilesTxt(pathName);
%Size =  30;%size(FileNames,1); % Set limit of number of files (10, 50, 100, 250,
Current is ALL)

cd(pathName);

%% Open all remaining selected files calculate relative irradiance.
while SReads2 < Size
%for iFileName = 1:Size
   %disp(FileNames{iFileName});
   FID = fopen(FileNames{iFileName2});
   %SampleCell = textscan(FID, '%*s %f', 'HeaderLines', 17, 'CollectOutput', 2); %if
header
   SampleCell = textscan(FID, '%*s %f', 'HeaderLines', 0, 'CollectOutput', 2); % no
header
   Sample = SampleCell{1};
```

```
fclose(FID);

num = Sample(:,1) - Dark(:,1); %creates dark subtract
MinusLight = Sample(:,1) - Light(:,1); %creates light subtract
num(num<0) = 0;
Onesnum = find(num==0);

dom = Light(:,1) - Dark(:,1); %used in full RelIrr
dom(dom<1) = 1;
Onesdom = find(dom==0);

num2 = num(:,1) - dom(:,1); %creates dark and light subtract
num2(num2<0) = 0;
Onesnum2 = find(num2==0);

Tot = bsxfun(@rdivide, num,dom);
Tot(isnan(Tot))=0;
RelIrr = bsxfun(@times, Bw,Tot);
 RelIrr(isnan(RelIrr))=0;
BWNormRelIrr = bsxfun(@times, BwNorm,Tot);
 BWNormRelIrr(isnan(BWNormRelIrr))=0;

largestTot = max(Tot);
smallestTot = min(Tot);
minmaxTot = largestTot - smallestTot;
numTot = bsxfun(@minus, Tot, smallestTot);
MinMaxTot = bsxfun(@rdivide, numTot, minmaxTot);

NormThenRelIrr = bsxfun(@times, BwNorm,MinMaxTot);
NormThenRelIrr(isnan(NormThenRelIrr))=0;

largestNum = max(num);
smallestNum = min(num);
minmaxNum = largestNum - smallestNum;
numDec = bsxfun(@minus, num, smallestNum);
MinMaxNum = bsxfun(@rdivide, numDec, minmaxNum);

ave = mean(num);
normalisedAve = bsxfun(@rdivide, num, ave);

largestNumL = max(num2);
smallestNumL = min(num2);
minmaxNumL = largestNumL - smallestNumL;
numDecL = bsxfun(@minus, num2, smallestNumL);
MinMaxNumL = bsxfun(@rdivide, numDecL, minmaxNumL);

aveL = mean(num2);
normalisedAveL = bsxfun(@rdivide, num2, aveL);

largestRelIrr = nanmax(RelIrr);
ILmax = 100 / largestRelIrr;
```

```
    smallestRelIrr = min(RelIrr);
    minmaxRelIrr = largestRelIrr - smallestRelIrr;
    RelIrrDec = bsxfun(@minus, RelIrr, smallestRelIrr);
    MinMaxRelIrr = bsxfun(@rdivide, RelIrrDec, minmaxRelIrr);
    BLmaxRelIrr = bsxfun(@times, RelIrr,BLmax);

    ILmaxRelIrr = bsxfun(@times, RelIrr,ILmax);

    aveRelIrr = mean(RelIrr);
    normalisedRelIrr = bsxfun(@rdivide, RelIrr, aveRelIrr);

    ScansMinusDark = horzcat(ScansMinusDark,num);
    ScansMinusLight = horzcat(ScansMinusLight,MinusLight);
    ScansRelIrr = horzcat(ScansRelIrr,RelIrr);
    normalisedBWNormRelIrr = horzcat(normalisedBWNormRelIrr,BWNormRelIrr);

    ScansRelIrr(ScansRelIrr<0) = 0;
    ScansMinusDark(ScansMinusDark<0) = 0;
    ScansMinusLight(ScansMinusLight<0) = 0;
    normalisedBWNormRelIrr(normalisedBWNormRelIrr<0) =0;

    SReads2 = SReads2 + 1;

iFileName2 = iFileName2 + 1;
end

    for i = 1:size(ScansMinusDark,2)
    numDivScansMinusDarkBase(:,i) = (ScansMinusDark(:,i) ./
ScansMinusDarkBase(:,i));
    end
    numDivScansMinusDarkBase(isnan(numDivScansMinusDarkBase))=1;
    [ii,jj]=find(isinf(numDivScansMinusDarkBase));
    numDivScansMinusDarkBase(ii,jj) = ScansMinusDark(ii,jj);

    for i = 1:size(ScansMinusDark,1)
        ScansMinusDarkAve(i,1) = mean(ScansMinusDark(i,:));
        ScansMinusLightAve(i,1) = mean(ScansMinusLight(i,:));
        numDivScansMinusDarkBaseAve(i,1) = mean(numDivScansMinusDarkBase(i,:));
        ScansRelIrrAve(i,1) = mean(ScansRelIrr(i,:));
        normalisedBWNormRelIrrAve(i,1) = mean(normalisedBWNormRelIrr(i,:));
    end

    numDivScansMinusDarkBase =
horzcat(numDivScansMinusDarkBase,numDivScansMinusDarkBaseAve);
    ScansRelIrr = horzcat(ScansRelIrr,ScansRelIrrAve);
    normalisedBWNormRelIrr =
horzcat(normalisedBWNormRelIrr,normalisedBWNormRelIrrAve);
    ScansMinusDark = horzcat(ScansMinusDark,ScansMinusDarkAve);
    ScansMinusLight = horzcat(ScansMinusLight,ScansMinusLightAve);

    for i = 1:size(ScansMinusDark,2)
```

```
                ScansMinusDarkInt(1,i) = sum(ScansMinusDark(:,i));
        ScansMinusDarkMax(1,i) = max(ScansMinusDark(:,i));
        ScansMinusDarkK(1,i) = ScansMinusDark(Wl6,i);
        ScansMinusDarkNa(1,i) = ScansMinusDark(Wl5,i);
        ScansMinusDarkCH(1,i) = ScansMinusDark(Wl1,i);
        ScansMinusDarkC2(1,i) = ScansMinusDark(Wl2,i);
        ScansMinusDarkOH(1,i) = ScansMinusDark(Wl3,i);
        ScansMinusDarkCN(1,i) = ScansMinusDark(Wl4,i);
                ScansMinusLightInt(1,i) = sum(ScansMinusLight(:,i));
        ScansMinusLightMax(1,i) = max(ScansMinusLight(:,i));
        ScansMinusLightK(1,i) = ScansMinusLight(Wl6,i);
        ScansMinusLightNa(1,i) = ScansMinusLight(Wl5,i);
        ScansMinusLightCH(1,i) = ScansMinusLight(Wl1,i);
        ScansMinusLightC2(1,i) = ScansMinusLight(Wl2,i);
        ScansMinusLightOH(1,i) = ScansMinusLight(Wl3,i);
        ScansMinusLightCN(1,i) = ScansMinusLight(Wl4,i);
                numDivScansMinusDarkBaseInt(1,i) =
sum(numDivScansMinusDarkBase(:,i));
        numDivScansMinusDarkBaseMax(1,i) = max(numDivScansMinusDarkBase(:,i));
        numDivScansMinusDarkBaseK(1,i) = numDivScansMinusDarkBase(Wl6,i);
        numDivScansMinusDarkBaseNa(1,i) = numDivScansMinusDarkBase(Wl5,i);
        numDivScansMinusDarkBaseCH(1,i) = numDivScansMinusDarkBase(Wl1,i);
        numDivScansMinusDarkBaseC2(1,i) = numDivScansMinusDarkBase(Wl2,i);
        numDivScansMinusDarkBaseOH(1,i) = numDivScansMinusDarkBase(Wl3,i);
        numDivScansMinusDarkBaseCN(1,i) = numDivScansMinusDarkBase(Wl4,i);
                ScansRelIrrInt(1,i) = sum(ScansRelIrr(:,i));
        ScansRelIrrMax(1,i) = max(ScansRelIrr(:,i));
        ScansRelIrrK(1,i) = ScansRelIrr(Wl6,i);
        ScansRelIrrNa(1,i) = ScansRelIrr(Wl5,i);
        ScansRelIrrCH(1,i) = ScansRelIrr(Wl1,i);
        ScansRelIrrC2(1,i) = ScansRelIrr(Wl2,i);
        ScansRelIrrOH(1,i) = ScansRelIrr(Wl3,i);
        ScansRelIrrCN(1,i) = ScansRelIrr(Wl4,i);
                 normalisedBWNormRelIrrInt(1,i) =
sum(normalisedBWNormRelIrr(:,i));
        normalisedBWNormRelIrrMax(1,i) = max(normalisedBWNormRelIrr(:,i));
        normalisedBWNormRelIrrK(1,i) = normalisedBWNormRelIrr(Wl6,i);
        normalisedBWNormRelIrrNa(1,i) = normalisedBWNormRelIrr(Wl5,i);
        normalisedBWNormRelIrrCH(1,i) = normalisedBWNormRelIrr(Wl1,i);
        normalisedBWNormRelIrrC2(1,i) = normalisedBWNormRelIrr(Wl2,i);
        normalisedBWNormRelIrrOH(1,i) = normalisedBWNormRelIrr(Wl3,i);
        normalisedBWNormRelIrrCN(1,i) = normalisedBWNormRelIrr(Wl4,i);
    end

   Rads = ["Integral";"Max";"K";"Na";"CH";"C2";"OH";"CN"];
   Rads2 = ["Integral STD";"Max STD";"K STD";"Na STD";"CH STD";"C2 STD";"OH
STD";"CN STD"];


for j = 1:2048
MaxScansMinusDark{j,1} = max(ScansMinusDark(j,:));
```

```
MinScansMinusDark{j,1} = min(ScansMinusDark(j,:));
AveScansMinusDark{j,1} = mean(ScansMinusDark(j,:));

MaxScansRelIrr{j,1} = max(ScansRelIrr(j,:));
MinScansRelIrr{j,1} = min(ScansRelIrr(j,:));
AveScansRelIrr{j,1} = mean(ScansRelIrr(j,:));

end

MaxScansMinusDark = cell2mat( MaxScansMinusDark );
MinScansMinusDark = cell2mat( MinScansMinusDark );
AveScansMinusDark = cell2mat( AveScansMinusDark );

MaxScansRelIrr = cell2mat( MaxScansRelIrr );
MinScansRelIrr = cell2mat( MinScansRelIrr );
AveScansRelIrr = cell2mat( AveScansRelIrr );

MaxScansMinusDark(MaxScansMinusDark<0) = 0;
MinScansMinusDark(MinScansMinusDark<0) = 0;
AveScansMinusDark(AveScansMinusDark<0) = 0;


MaxScansRelIrr(MaxScansRelIrr<0) = 0;
MinScansRelIrr(MinScansRelIrr<0) = 0;
AveScansRelIrr(AveScansRelIrr<0) = 0;

ScansMinusDarkNum = bsxfun(@minus,ScansMinusDark,MinScansMinusDark);
ScansMinusDarkDom = bsxfun(@minus,MaxScansMinusDark,MinScansMinusDark);

ScansScansRelIrrNum = bsxfun(@minus,ScansRelIrr,MinScansRelIrr);
ScansScansRelIrrDom = bsxfun(@minus,MaxScansRelIrr,MinScansRelIrr);

   ScansMinusDark =
vertcat(ScansMinusDark,ScansMinusDarkInt,ScansMinusDarkMax,ScansMinusDarkK,
ScansMinusDarkNa,ScansMinusDarkCH,ScansMinusDarkC2,ScansMinusDarkOH,Sca
nsMinusDarkCN);
   numDivScansMinusDarkBase =
vertcat(numDivScansMinusDarkBase,numDivScansMinusDarkBaseInt,numDivScansM
inusDarkBaseMax,numDivScansMinusDarkBaseK,numDivScansMinusDarkBaseNa,nu
mDivScansMinusDarkBaseCH,numDivScansMinusDarkBaseC2,numDivScansMinusD
arkBaseOH,numDivScansMinusDarkBaseCN);
   ScansRelIrr =
vertcat(ScansRelIrr,ScansRelIrrInt,ScansRelIrrMax,ScansRelIrrK,ScansRelIrrNa,Scans
RelIrrCH,ScansRelIrrC2,ScansRelIrrOH,ScansRelIrrCN);
   normalisedBWNormRelIrr =
vertcat(normalisedBWNormRelIrr,normalisedBWNormRelIrrInt,normalisedBWNormR
elIrrMax,normalisedBWNormRelIrrK,normalisedBWNormRelIrrNa,normalisedBWNor
mRelIrrCH,normalisedBWNormRelIrrC2,normalisedBWNormRelIrrOH,normalisedB
WNormRelIrrCN);
   ScansMinusLight =
vertcat(ScansMinusLight,ScansMinusLightInt,ScansMinusLightMax,ScansMinusLight
```

```
K,ScansMinusLightNa,ScansMinusLightCH,ScansMinusLightC2,ScansMinusLightOH,
ScansMinusLightC2);

  IntnumSTD = std(ScansMinusDark(2049,1:Size)); MaxnumSTD =
std(ScansMinusDark(2050,1:Size)); KnumSTD = std(ScansMinusDark(2051,1:Size));
NanumSTD = std(ScansMinusDark(2052,1:Size)); CHnumSTD =
std(ScansMinusDark(2053,1:Size)); C2numSTD = std(ScansMinusDark(2054,1:Size));
OHnumSTD = std(ScansMinusDark(2055,1:Size)); CNnumSTD =
std(ScansMinusDark(2056,1:Size));
  IntnumDarkBaseSTD = std(numDivScansMinusDarkBase(2049,1:Size));
MaxnumDarkBaseSTD = std(numDivScansMinusDarkBase(2050,1:Size));
KnumDarkBaseSTD = std(numDivScansMinusDarkBase(2051,1:Size));
NanumDarkBaseSTD = std(numDivScansMinusDarkBase(2052,1:Size));
CHnumDarkBaseSTD = std(numDivScansMinusDarkBase(2053,1:Size));
C2numDarkBaseSTD = std(numDivScansMinusDarkBase(2054,1:Size));
OHnumDarkBaseSTD = std(numDivScansMinusDarkBase(2055,1:Size));
CNnumDarkBaseSTD = std(numDivScansMinusDarkBase(2056,1:Size));
  IntRelIrrSTD = std(ScansRelIrr(2049,1:Size)); MaxRelIrrSTD =
std(ScansRelIrr(2050,1:Size)); KRelIrrSTD = std(ScansRelIrr(2051,1:Size));
NaRelIrrSTD = std(ScansRelIrr(2052,1:Size)); CHRelIrrSTD =
std(ScansRelIrr(2053,1:Size)); C2RelIrrSTD = std(ScansRelIrr(2054,1:Size));
OHRelIrrSTD = std(ScansRelIrr(2055,1:Size)); CNRelIrrSTD =
std(ScansRelIrr(2056,1:Size));
  IntBWNormRelIrrSTD = std(normalisedBWNormRelIrr(2049,1:Size));
MaxBWNormRelIrrSTD = std(normalisedBWNormRelIrr(2050,1:Size));
KBWNormRelIrrSTD = std(normalisedBWNormRelIrr(2051,1:Size));
NaBWNormRelIrrSTD = std(normalisedBWNormRelIrr(2052,1:Size));
CHBWNormRelIrrSTD = std(normalisedBWNormRelIrr(2053,1:Size));
C2BWNormRelIrrSTD = std(normalisedBWNormRelIrr(2054,1:Size));
OHBWNormRelIrrSTD = std(normalisedBWNormRelIrr(2055,1:Size));
CNBWNormRelIrrSTD = std(normalisedBWNormRelIrr(2056,1:Size));
  IntMinusLightSTD = std(ScansMinusLight(2049,1:Size)); MaxMinusLightSTD =
std(ScansMinusLight(2050,1:Size)); KMinusLightSTD =
std(ScansMinusLight(2051,1:Size)); NaMinusLightSTD =
std(ScansMinusLight(2052,1:Size)); CHMinusLightSTD =
std(ScansMinusLight(2053,1:Size)); C2MinusLightSTD =
std(ScansMinusLight(2054,1:Size)); OHMinusLightSTD =
std(ScansMinusLight(2055,1:Size)); CNMinusLightSTD =
std(ScansMinusLight(2056,1:Size));

  Rads2valnum =
vertcat(IntnumSTD,MaxnumSTD,KnumSTD,NanumSTD,CHnumSTD,C2numSTD,OH
numSTD,CNnumSTD);
  Rads2valRelIrr =
vertcat(IntRelIrrSTD,MaxRelIrrSTD,KRelIrrSTD,NaRelIrrSTD,CHRelIrrSTD,C2RelIr
rSTD,OHRelIrrSTD,CNRelIrrSTD);
  Rads2valBWNorm =
vertcat(IntBWNormRelIrrSTD,MaxBWNormRelIrrSTD,KBWNormRelIrrSTD,NaBW
NormRelIrrSTD,CHBWNormRelIrrSTD,C2BWNormRelIrrSTD,OHBWNormRelIrrST
D,CNBWNormRelIrrSTD);
```

```
   Rads2valDarkBase =
vertcat(IntnumDarkBaseSTD,MaxnumDarkBaseSTD,KnumDarkBaseSTD,NanumDark
BaseSTD,CHnumDarkBaseSTD,C2numDarkBaseSTD,OHnumDarkBaseSTD,CNnum
DarkBaseSTD);
   Rads2valMinusLight =
vertcat(IntMinusLightSTD,MaxMinusLightSTD,KMinusLightSTD,NaMinusLightSTD,
CHMinusLightSTD,C2MinusLightSTD,OHMinusLightSTD,CNMinusLightSTD);

   Rad2valnum2 = horzcat(Rads2,Rads2valnum);
   Rads2valRelIrr2 = horzcat(Rads2,Rads2valRelIrr);
   Rads2valBWNorm2 = horzcat(Rads2,Rads2valBWNorm);
   Rads2valDarkBase2 = horzcat(Rads2,Rads2valDarkBase);
   Rads2valMinusLight2 = horzcat(Rads2,Rads2valMinusLight);

    Wave = vertcat(Wave,Rads);

 %% Export Scans
 if output == 1
 mkdir('Analysis 2')
 s1 = '\Analysis 2';
 s = strcat(pathName,s1);
 s2 = regexp(s, '\', 'split');
 s3 = s2(length(s2)-1);

 cd(s);

% %concatenate with wavelengths
    ScansnumDivScansMinusDarkBase = horzcat(Wave,numDivScansMinusDarkBase);
    ScansRelIrr = horzcat(Wave,ScansRelIrr);
    ScansMinusDark = horzcat(Wave,ScansMinusDark);
    ScansMinusLight = horzcat(Wave,ScansMinusLight);

    normalisedBWNormRelIrr = horzcat(Wave,normalisedBWNormRelIrr);

% %scans normalised across readings of each single scan

  xlswrite([char((s2(length(s2)-2))) ' ' num2str(Size),' Scans Minus
Dark'],ScansMinusDark);
  xlswrite([char((s2(length(s2)-2))) ' ' num2str(Size),' Scans Minus Dark'],Rad2valnum2,
1, 'A2057');

  xlswrite([char((s2(length(s2)-2))) ' ' num2str(Size),' Scans Minus
Light'],ScansMinusLight);
  xlswrite([char((s2(length(s2)-2))) ' ' num2str(Size),' Scans Minus
Light'],Rads2valMinusLight2, 1, 'A2057');

  xlswrite([char((s2(length(s2)-2))) ' ' num2str(Size),' Scans Relative
Irradiance'],ScansRelIrr);
  xlswrite([char((s2(length(s2)-2))) ' ' num2str(Size),' Scans Relative
Irradiance'],Rads2valRelIrr2, 1, 'A2057');
```

```
  xlswrite([char((s2(length(s2)-2))) ' ' num2str(Size),' Scans Relative Irradiance Norm
BWNorm'],normalisedBWNormRelIrr);
  xlswrite([char((s2(length(s2)-2))) ' ' num2str(Size),' Scans Relative Irradiance Norm
BWNorm'],Rads2valBWNorm2, 1, 'A2057');

 %scan normalised across each wavelength from every scan
  xlswrite([char((s2(length(s2)-2))) ' ' num2str(Size),' Scans Normalised by Baseline ',
char((sb(length(sb)-1)))],ScansnumDivScansMinusDarkBase);
  xlswrite([char((s2(length(s2)-2))) ' ' num2str(Size),' Scans Normalised by Baseline ',
char((sb(length(sb)-1)))],Rads2valDarkBase2, 1, 'A2057');
 end
 disp('Complete.');
```

Appendix 5: Program for Training Artificial Neural Network

```
%************************************************************%
%File name:          TrainNetwork.m
%Synopses:                   1)Load Training Data
%                            2)Select Network Parameters
%                            3)Train Network
%                            4)Evaluate Network
%                            5)Repeat until best performance found
%Programmer:         James Cugley, EDA, University of Kent
%Date:               August 1, 2016
%************************************************************%

x = InputScaled'; % scaled input of parameters
t = NoxIP';       % NOx values

BestHidden = 0;
count = 0;
count2 = 0;

 net = [];
ErrBest=1;
TotErrBest = 200;
   performanceOut1Best = 10;
   performance = [];
   performanceOut1 = [];
   performanceOut2 = [];
   performanceOut3 = [];

   BestPar = [];
   BestNet = [];

   BestTrain = [];
   BestVal   = [];
   BestTest  = [];

for Hidden1 = 5:1:12

for ValR = 10:5:15

for TestR = 10:5:15

for Num = 1:10

   TrainR = 100 - (ValR + TestR);
```

```
trainFcn = 'trainbr';  % Choose a Training Function, Bayesian Regularization
backpropagation.

hiddenLayerSize = Hidden1;% Create a Fitting Network

net = fitnet(hiddenLayerSize,trainFcn);

net.input.processFcns = {'removeconstantrows','mapminmax'};% Choose Input and
Output Pre/Post-Processing
net.output.processFcns = {'removeconstantrows','mapminmax'};

net.divideFcn = 'dividerand';  % Divide data randomly % Setup Division of Data for
Training, Validation, Testing
net.divideMode = 'sample';  % Divide up every sample
net.divideParam.trainRatio = TrainR/100;
net.divideParam.valRatio = ValR/100;
net.divideParam.testRatio = TestR/100;

net.performFcn = 'mse';  % Mean Squared Error % Choose a Performance Function

net.plotFcns = {'plotperform','plottrainstate','ploterrhist', ...
    'plotregression', 'plotfit'};% Choose Plot Functions

net.trainParam.max_fail = 6;

[net,tr] = train(net,x,t);% Train the Network

y = net(x); % Test the Network

e = gsubtract(t,y);
performance = perform(net,t,y);

% Recalculate Training, Validation and Test Performance
trainTargets = t .* tr.trainMask{1};
valTargets = t .* tr.valMask{1};
testTargets = t .* tr.testMask{1};
trainPerformance = perform(net,trainTargets,y);
valPerformance = perform(net,valTargets,y);
testPerformance = perform(net,testTargets,y);


TotPerformance = trainPerformance + valPerformance + testPerformance;

TestOP1 = net(Test1IP1scale');
TestOP2 = net(Test1IP2scale');
%TestOP3 = net(Test2IP1scale');
%TestOP4 = net(Test2IP2scale');

NetOut1 = mean(TestOP1);
NetOut2 = mean(TestOP2);
%NetOut3 = mean(TestOP3);
```

```
%NetOut4 = mean(TestOP4);

performanceOut1 = perform(net,Noxtest1IP1,TestOP1);
performanceOut2 = perform(net,Noxtest1IP2,TestOP2);
%performanceOut3 = perform(net,Noxtest2IP1,TestOP3);
%performanceOut4 = perform(net,Noxtest2IP2,TestOP4);

Err = abs(NetOut1-Noxtest1IP1(1,1))/Noxtest1IP1(1,1);
TotErr = 0;

for i = 1:size(TestOP1,2)
TotErr = TotErr + abs(TestOP1(1,i)-Noxtest1IP1(1,1))/Noxtest1IP1(1,1);
end

AllPerformance = TotPerformance + performance + performanceOut1 +
performanceOut2;

count = count+1;
AllTests(count,:) =
[Hidden1,ValR,TestR,Num,performance,trainPerformance,valPerformance,testPerform
ance,performanceOut1,performanceOut2,performanceOut3];

if Num == 10
   count2 = count2+1;
   AllTestsAve(count2,:) = mean(AllTests(count-9:count,:));
end

if performance + performanceOut1 + performanceOut2 < performanceOut1Best
%if AllPerformance < performanceOut1Best %+ performanceOut2 + performanceOut3
< performanceOut1Best
   %if performance < performanceOut1Best

   TotErrBest = TotErr;
   %performanceOut1Best = performance + performanceOut1 + performanceOut2 +
performanceOut3;
   performanceOut1Best = performance + performanceOut2 + performanceOut3;
   %performanceOut1Best = performance;
   ErrBest = Err;
   BestPar = [Hidden1,ValR,TestR];

   BestNet = net;

   BestTrain = trainTargets;
   BestVal   = valTargets;
   BestTest  = testTargets;

   BestResult(1,1) = NetOut1;

   BestErr (1,1) = abs(NetOut1-Noxtest1IP1(1,1))/Noxtest1IP1(1,1);

   y = BestNet(InputScaled');
```

```
    y2 = BestNet(Test1IP1scale');
    y3 = BestNet(Test1IP2scale');
    %y4 = BestNet(Test2IP1scale');
    %y5 = BestNet(Test2IP1scale');

end

if (false)
    genFunction(net,'myNeuralNetworkFunction');
    y = myNeuralNetworkFunction(x);
end
if (false)
    genFunction(net,'myNeuralNetworkFunction','MatrixOnly','yes');
    y = myNeuralNetworkFunction(x);
end
if (false)
    gensim(net);
end
end
end
end
end
end
%end

mkdir('Results')
cd('Results')

save('performanceOut1Best','performanceOut1Best')
save('BestPar','BestPar');
save('BestNet','BestNet');
save('BestTrain','BestTrain');
save('BestVal','BestVal');
save('BestTest','BestTest');
save('BestResult','BestResult');
save('BestErr','BestErr');

disp('Complete.')
```

Publications and Dissemination

The following publications were produced during the work leading to the preparation of this thesis.

[1] V. G. Narushina, G. Lu,M. N. Romanovc, **J. Cugley** and D. K. Griffinc, "A 2-D Imaging-assisted geometrical transformation method for non-destructive evaluation of the volume and surface area of avian eggs", *Food Science & Technology*, 2019 (under review).

[2] **J. Cugley**, G. Lu, Y. Yan and I. Searle, "Visualisation and measurement of flames in a gas-fired multi-burner boiler", *IMEKO 2018 (The XXII World Congress of the International Measurement Confederation)*, 3rd- 6th Sept 2018, Belfast, UK.

[3] Md. M. Hossain, **J. Cugley**, G. Lu and Y. Yan, "Burner condition monitoring based on flame imaging and data fusion techniques" 1*2th ECCRIA (The European Conference on Fuel and Energy Research and its Applications),* 5th-7th Sept 2018, Cardiff University, Cardiff, UK.

[4] Md. M. Hossain, **J. Cugley**, G. Lu and Y. Yan, "Investigations into the impact of coal moisture on burner performance through flame imaging and spectrometric analysis" *12th ECCRIA (The European Conference on Fuel and Energy Research and its Applications)*, 5th-7th Sept 2018, Cardiff University, Cardiff, UK.

[5] **J. Cugley**, G. Lu, Y. Yan and I. Searle, "Flame monitoring and characterisation through digital imaging and spectrometry", *IFRF 2018 Conference- Clean, Efficient and Safe Industrial Combustion*, 30th-31st May 2018, Sheffield, UK.

[6] **J. Cugley**, G. Lu, Y. Yan and I. Searle, "Advanced flame monitoring and emissions prediction through digital imaging and spectrometry", *BF2RA Energy Science Lecture*, Sept 2017.

[7] **J. Cugley**, G. Lu, Y. Yan and G. Marshall, "Flame monitoring and emission predication through digital imaging and spectrometry" *11th ECCRIA* (The European Conference on Fuel and Energy Research and its Applications), *5th-7th Sept* 2016, University of Sheffield, Sheffield, UK.